

Modelling the Denmark Strait Overflow During the Last Interglacial Cycle

From Regional Dynamics to Basin Wide Impacts

Dissertation
zur Erlangung des Doktorgrades
der Mathematisch-Naturwissenschaftlichen Fakultät
der Christian-Albrechts-Universität zu Kiel



vorgelegt von
Frank Kösters

Kiel
November 11, 2004

Referent:	Prof. Dr. Rolf Käse
Korreferent:	Prof. Dr. Mojib Latif
Tag der mündlichen Prüfung:	28. Oktober 2004
Zum Druck genehmigt:	Kiel, 28. Oktober 2004

Der Dekan

Zusammenfassung

Die Dänemarkstraße ist unter heutigen klimatischen Bedingungen die wichtigste Meerenge für kalte Wassermassen die aus dem Nordmeer stammen und in den Nordatlantik fließen. Der Schwerpunkt dieser Studie liegt auf der regionalen und beckenweiten Dynamik des Dänemarkstraßen-Überstroms unter heutigen klimatischen Bedingungen sowie denen des letzten glazialen Maximums. Die Studie ist Teil der Forschergruppe Ozeanpassagen an der Universität Kiel, die sich mit dem Einfluss von Meerengen auf das Klima in der Vergangenheit beschäftigt.

Der Volumentransport des Überstroms wird durch hydraulische Gesetze bestimmt, das heißt der Transport ergibt sich aus dem relativen Dichtekontrast nördlich und südlich der Dänemarkstraße sowie der Dicke des kalten Wassers oberhalb der Meeresschwelle im Norden. Mithilfe von hochauflösenden numerischen Modellen wird untersucht wie der Transport am besten auf der Grundlage bestehender hydraulischer Gesetze beschrieben werden kann. Es konnte gezeigt werden, dass die hydraulischen Gesetze in einem großen Parameterbereich gültig sind und damit auch für glaziale Bedingungen angewendet werden können. Unter Verwendung des hochauflösenden numerischen Ozeanmodells können die jeweiligen Einflüsse der Änderungen von Wassermassen und Meerestiefen während des letzten glazialen Maximums abgeschätzt und separiert werden. Daraus ergibt sich für das letzte glaziale Maximum, dass der Rückgang des globalen Meeresspiegels und die Vereisung der Schelfbereiche in der Dänemarkstraße einen kleineren Einfluss als der verringerte Dichtekontrast hatten.

Neben dem dichtegetriebenen Transport kann die Windschubspannung den Überstromtransport beeinflussen, wie in einem hochauflösenden Modell des Grönland-Schottland Rückens gezeigt. Daher ist anzunehmen, dass die Änderungen im Windfeld im Zusammenhang mit unterschiedlichen Phasen der Nordatlantischen Oszillation dem Überstrom eine zwischenjährliche Variabilität aufprägen. Das gleiche Argument gilt für die Änderungen im Windfeld unter glazialen Randbedingungen. Doch trotz erhöhter Windschubspannungen war der Dänemarkstraßen-Transport von kaltem Wasser aufgrund des stark verminderten Dichtekontrastes während des glazialen Sommers vermutlich auf unter 0.5 Sv reduziert. Wahrscheinlich war der erhöhte Windschub jedoch ein wichtiger Faktor, der zu einem eisfreien Nordmeer während des glazialen Sommers beigetragen hat. Insgesamt war der nordwärtige Wärmetransport während des Glazials stark vermindert, insbesondere für den Fall einer geschlossenen Dänemarkstraße, zum Beispiel durch eine Eisbergblockade.

Die den Transport bestimmenden Gesetze wurden als Überstrom-Parameterisierung in ein globales, grob auflösendes Ozeanmodell eingebaut, um den Dänemarkstraßen-Transport realistischer darstellen zu können. Die Parameterisierung führt zu einer verstärkten meridionalen Umwälzbewegung im Nordatlantik und dementsprechend zu einem erhöhten nordwärtigem Wärmetransport. Daraus ergibt sich, dass die mittlere Oberflächentemperatur in Europa und der Dänemarkstraßen-Transport von kaltem Wasser eng miteinander verknüpft sind. Dies wiederum stellt die besondere Bedeutung der Dänemarkstraße heraus, auch wenn die Änderungen in der meridionalen Umwälzbewegung kleiner sind als von vorherigen Studien erwartet. Ferner ergibt sich kein stabilisierender Effekt für eine Frischwasseranomalie über den ganzen Nordatlantik und nur eine kleine Stabilisierung für eine lokale Störung in der Labradorsee.

Abstract

The Denmark Strait overflow is the major gateway for dense water from the Nordic Seas into the North Atlantic and thus it constitutes an important part of the thermohaline circulation under present-day climate conditions. This study focuses on the regional to basin wide dynamics of the Denmark Strait overflow for present-day and Last Glacial Maximum conditions. It contributes to the Research Unit Ocean Gateways located at the University of Kiel which addresses the question how ocean gateways might have affected climate in the past.

The volume transport of the overflow is likely to be controlled by hydraulic constraints, thus the transport is set by the relative density contrast between the water masses north and south of the Denmark Strait and the height of dense water above sill level. By using high resolution numerical models it is investigated how the volume transport can be best described using existing hydraulic theories. Hydraulic constraints are shown to be valid over a wide parameter range which allows to transfer this theory to LGM conditions. During the LGM both bathymetry and hydrography have been different and the relative importance of the individual effects is disentangled using a high-resolution numerical model. The drop in eustatic sea-level and glaciated shelves in this area had a comparable smaller effect than the reduced density contrast.

In addition to buoyancy forcing wind stress might play a role in setting the overflow transport. In a regional model of the Greenland-Scotland Ridge an influence of wind stress on the overflow can be shown. Therefore, wind stress changes due to different phases of the NAO are expected to imprint a signal on the overflow transport. The same holds for wind field changes from Last Glacial Maximum to present-day conditions. Even though the wind stress was increased the density difference between Nordic Seas and North Atlantic supports almost no buoyancy forcing of the overflows thus the Denmark Strait overflow was probably reduced to less than 0.5 Sv during Last Glacial Maximum summer. However, it is proposed that the increased LGM wind stress is an important factor in keeping the Nordic Seas ice free during summer. The heat transport associated with the volume transport is generally reduced for the Last Glacial Maximum with a pronounced reduction if the Denmark Strait is additionally closed e.g. by iceberg blocking.

The relation connecting hydraulic constraints and volume transport was implemented in a global climate model to improve the representation of the Denmark Strait overflow in that model. It results in an increased Atlantic meridional overturning and the associated northward heat transport. A close correlation between overflow representation and climate in northern Europe can be shown. This emphasises the impact of the Denmark Strait overflow on climate even though the response in overturning due to the representation is less than expected from previous studies. There is nearly no stabilising effect of the overflow for large scale freshwater perturbations but a weak effect if the system is perturbed locally in the Labrador Sea.

Table of Contents

1. Introduction	1
1.1. The Denmark Strait - A high latitude ocean gateway	1
1.2. Present-day circulation patterns	1
1.2.1. Northern North Atlantic	1
1.2.2. Observations for the Denmark Strait overflow	3
1.2.3. Coupling of the Faroe Bank Channel and Denmark Strait overflows	4
1.2.4. Hydraulic Control	5
1.2.5. Interannual variability - the North Atlantic Oscillation	6
1.3. Geological setting	7
1.4. The Glacial North Atlantic	9
1.4.1. Paleoceanographic reconstruction of the Denmark Strait overflow	10
1.4.2. Long-term climate variability	12
1.5. The modelling perspective	12
1.6. Objectives and thesis outline	13
2. Tools and methods for ocean and overflow modelling	15
2.1. The Regional Ocean Modelling System	16
2.2. Model configurations	19
2.2.1. The Denmark Strait overflow process model	19
2.2.2. The Greenland-Scotland Ridge regional ocean model	21
2.2.3. The northern North Atlantic regional ocean model	22
2.3. The University of Victoria Earth System Coupled Model (UVic ESCM)	24
2.4. Data processing	25
3. A process modelling study of the Denmark Strait overflow	27
3.1. Theory of rotating hydraulics	28
3.1.1. Hydraulically controlled flow	28
3.1.2. The Deep-Upstream-Basin	29
3.1.3. Extension to realistic topography	30
3.1.4. Finite basin and upstream influence	31
3.2. Comparing model results and hydraulic transport estimates	32
3.2.1. Model validation	32
3.2.2. Modelled dense water transport	34
3.2.3. Conditions for hydraulic control	37
3.2.4. Dependence of transport on reservoir height	40
3.2.5. Sensitivity to changes in density contrast	41
3.2.6. Validation for different meridional positions	43
3.2.7. Comparison of different theoretical hydraulic limitations	43
3.2.8. Limitations of the hydraulic theory	46
3.3. Influence of boundary conditions	46

3.3.1.	Sensitivity to the upstream circulation	46
3.3.2.	Extension to continuous stratification	50
3.3.3.	Comments on tides and barotropic forcing	55
3.4.	Summary and conclusions	57
4.	Paleoclimate sensitivity experiments for the last glacial-interglacial cycle	59
4.1.	LGM sensitivity experiments	60
4.1.1.	Effects of changes in gateway depth and aperture	60
4.1.2.	LGM density contrast and transport	64
4.1.3.	Realistically stratified glacial conditions	66
4.2.	Dansgaard/Oeschger stadial and interstadial experiments	68
4.3.	Overflow plume and pathway	69
4.3.1.	Descent of the overflow	69
4.3.2.	Mesoscale processes	71
4.3.3.	Sedimentation patterns	71
4.4.	Summary and conclusions	72
5.	The Dense Northern overflows for present-day and Last Glacial Maximum conditions	75
5.1.	Present-day circulation	76
5.1.1.	Model validation	76
5.1.2.	Changing wind forcing	79
5.1.3.	Application to the North Atlantic Oscillation	81
5.1.4.	Comparison of Faroe Bank Channel and Denmark Strait overflow	84
5.2.	Last Glacial Maximum Circulation	85
5.2.1.	LGM experiments	85
5.2.2.	The role of wind driven heat transport for ice free glacial Nordic Seas	91
5.3.	Blocking Denmark Strait	94
5.4.	Dispersal of marine biota	99
5.5.	Summary and conclusions	103
6.	Long-term, Basin Scale Impact of the Denmark Strait overflow	105
6.1.	Evaluation of an overflow parameterisation based on hydraulic constraints	106
6.1.1.	Artificial overflow in the high-resolution Denmark Strait model	106
6.1.2.	A northern North Atlantic test case	106
6.2.	Evaluation of the overflow parameterisation in a global model	110
6.2.1.	Including the overflow parameterisation	110
6.2.2.	Sensitivity experiments	112
6.2.3.	Including a bottom boundary layer	119
6.2.4.	Extension to include a parameterisation for the Faroe Bank Channel outflow	123
6.2.5.	Summarising the thermohaline transports	123
6.3.	Influence on the stability of the thermohaline circulation	126
6.3.1.	Overview and experimental set-up	126
6.3.2.	Response of the overturning and hysteresis loops	129
6.4.	Beyond the northern overflows	131
6.4.1.	The importance of wind stress	132
6.4.2.	Horizontal and vertical diffusion	133

6.5. Summary and conclusions	135
7. Summarising discussion	137
7.1. Regional dynamics	137
7.2. Basin wide impact	140
8. Conclusions	143
A. Appendices	145
A.1. List of acronyms	145
A.2. Model formulation	146
A.2.1. Equations of motion	146
A.2.2. Stretched vertical coordinate system and horizontal curvilinear coordinates	146

List of Figures

1.1. Main current system of the North Atlantic and the Nordic Seas	2
1.2. Schematic representation of the Denmark Strait overflow	4
1.3. Bathymetry of Denmark Strait for LGM and PD	8
1.4. Key data for the time slice from 30 ka BP to present-day	11
2.1. Stretched vertical grid	17
2.2. Bathymetry of the Denmark Strait overflow process model	19
2.3. Bathymetry for the Greenland-Scotland Ridge experiment	21
2.4. Bathymetry for the northern North Atlantic experiment	23
2.5. Bathymetry of the global model	25
3.1. Schematic representation of the Denmark Strait overflow	28
3.2. Snapshot of the descending overflow plume and bathymetry of the Denmark Strait	32
3.3. Bottom density field from model and observations	33
3.4. Thickness of the overflow	34
3.5. Along-stream section of model and observations	35
3.6. Cross-stream section through Denmark Strait for model and observations	36
3.7. Modelled transport as a function of squared upstream reservoir height	36
3.8. Comparison of different Froude number definitions for experiment DS-Res-0ka	38
3.9. Composite Froude number G for experiments with different effective height	39
3.10. Potential vorticity distribution at the sill	39
3.11. Transport time series of the modelled transport and the theoretical transports	40
3.12. Theoretical transport as function of modelled transport	42
3.13. Dense water transport as a function of cross-ridge density contrast	43
3.14. Modelled DSO transport as a function of the inverse Coriolis parameter	44
3.15. Ratio of modelled to theoretical transport for the sill and upstream area	44
3.16. Theoretical shape of the DSO from theory and model	45
3.17. Hovmöller diagram of the cumulative cold water transport	48
3.18. Hovmöller digram of transport for different source configurations	49
3.19. Ratio of theoretical to modelled transport	49
3.20. Bottom density field from model snapshot and observations	51
3.21. Along-stream section of the initial model conditions from model and observations	52
3.22. East-West cross-stream density section	53
3.23. The effect of stratification on the cumulative transport	53
3.24. Transport in four density classes as function of along stream distance	54
3.25. Amplitude of M2 tide with tidal ellipse	56

4.1. East-west cross-stream section of the velocity field for different LGM bathymetries	61
4.2. Composite Froude number for LGM and PD experiments	61
4.3. Dense water transport as a function of squared effective height for different bathymetries	62
4.4. Two-layer model from average density contrast across DS	65
4.5. The density and velocity structure of the experiment with LGM stratification	67
4.6. LGM transport in four density classes as function of along stream distance	68
4.7. Dense water transport as function of density bin	69
4.8. The descent of the overflow plume for different density contrasts	70
4.9. Sediment bed thickness from a sediment model for PD	72
5.1. PD volume transport in density classes	77
5.2. Depth of the 27.8 isopycnal	77
5.3. Temperature and velocity field at the sill and for the Hornbanki section	78
5.4. Relation between wind forcing and volume transport	79
5.5. Annual mean amplitude of standardised wind stress	83
5.6. Transport of DSOW as predicted from NCEP/NCAR wind stress anomaly	83
5.7. Spin-down of the overflow transport for a given reservoir	84
5.8. Time series of transport and lagged correlation	86
5.9. LGM dense water transport across the GSR in density classes	88
5.10. Glacial summer sea-surface temperature and schematic surface circulation	91
5.11. Wind stress for LGM and PD	92
5.12. Sverdrup volume transport for LGM and PD	93
5.13. PD volume transport for an open, partially blocked and fully blocked Denmark Strait	95
5.14. LGM volume transport for an open, partially blocked and fully blocked Denmark Strait	96
5.15. Depth and velocity of the 27.8 isopycnal for PD winter conditions	97
5.16. Depth and velocity of the 28.75 isopycnal for LGM summer conditions	98
5.17. Float distribution for PD winter and LGM summer	100
5.18. LGM and PD surface temperature, circulation and Lagrangian drifter pathways	101
5.19. The M2 tidal amplitude for PD and glaciated shelves	102
6.1. Evaluation of the overflow parameterisation in high-resolution model	107
6.2. Average temperature and velocity of the lowest 6 σ -layers for parameterised overflow	108
6.3. Time-series of the transport of cold water for medium-resolution model	109
6.4. Schematic representation of the overflow parameterisation	111
6.5. AMOC and MLD for reference and parameterised model experiments	113
6.6. MLD from model and observations	114
6.7. Barotropic mass transport streamfunction for reference and parameterised model experiments	115
6.8. Structure of the deep western boundary currents	116
6.9. Circulation and water mass properties at the GSR region for reference and parameterised model experiments	117
6.10. Annual mean northward heat transport vs. latitude in PW for reference and parameterised model experiments	118

6.11. Changes in SAT and snow cover due to parameterised overflows	118
6.12. Zonally integrated overturning streamfunction at 58° N for reference and parameterised model experiments	119
6.13. Comparison of bottom cell densities for reference and parameterised model experiments	120
6.14. AMOC and MLD for experiments with BBL	121
6.15. Changes in density profile of the central Labrador Sea due to parameterisation	122
6.16. AMOC and MLD for experiments with parameterised FBC	124
6.17. Meridional transport in the Atlantic at 36° N	125
6.18. AMOC and MLD for experiments without GSR	127
6.19. Location and magnitude of freshwater perturbation	128
6.20. Hysteresis curves for a freshwater perturbation experiment with an amplitude of 0.3 Sv/500 yrs.	129
6.21. Hysteresis curves with 0.15 Sv/500 yrs.	130
6.22. Self recovery of the AMOC for a transient freshwater pulse	131
6.23. AMOC and Hysteresis curve for experiments without wind forcing	132
6.24. Vertical diffusivity profile and dependence of AMOC on diffusivity	134
6.25. Dependence of AMOC on grid Peclet number	135
A.1. Schematic representation of the Arakawa C-grid.	147

List of Tables

1.1. Overview of studies on hydraulic control	5
2.1. Configuration of the Denmark Strait overflow process model	20
2.2. Configuration for the regional Greenland-Scotland Ridge model	22
2.3. Configuration for the North Atlantic model	23
3.1. Notations for different transport definitions	31
3.2. Overview of the ratio of experimental to theoretical transports	41
4.1. Overview of dam-break experiments	62
4.2. Ratio of modelled to theoretical transport for paleoclimate experiments	63
4.3. Density contrast across Denmark Strait between average north and south profiles	65
4.4. Overview of experiments employing a continuous density stratification	66
4.5. Overview of paleoclimate experiments employing a continuous density stratification	68
5.1. Overview of experiments with average density profiles and wind forcing	79
5.2. Mean volume transport for varying wind stress from the GSR-0ka experiments	80
5.3. Minimum, maximum and difference of wind stress curl	82
5.4. Overview of experiments with average density profiles and wind forcing	87
5.5. Volume transport from the GSR-21ka experiments	87
5.6. Estimates of LGM heat fluxes	89
5.7. Overview of experiments assessing the influence of closing or partially blocking DS	94
5.8. Estimates on heat fluxes across the GSR	99
6.1. Transport of cold water for medium-resolution model	110
6.2. Overview of global model experiments	110
6.3. Overview of AMOC and NADW for individual experiments	124
6.4. Summary of the freshwater perturbation experiments	128

1. Introduction

1.1. The Denmark Strait - A high latitude ocean gateway

The formation of North Atlantic Deep Water (NADW¹) ventilates the deep ocean and is an important part of the thermohaline circulation (THC) for present-day climate conditions [Schmitz, 1995; Marshall and Schott, 1999]. The driving force for the flow associated with the THC is most likely set by the pressure gradient due to deep ventilation at high latitudes and downward mixing of heat at low-latitudes (see Rahmstorf [2003] for an outline). However, it has been argued that the THC is entirely driven by wind stress and abyssal tides [Wunsch and Ferrari, 2004]. The circulation patterns due to buoyancy and wind forcing are intimately linked and cannot be disentangled from observations. However, the combination of both sets the Meridional Overturning Circulation (MOC) which will be used as a representative of the THC henceforth.

NADW is mainly originating from the cold and dense water masses formed in the Nordic Seas and is subsequently crossing the Greenland-Scotland Ridge (GSR) to enter the North Atlantic basin [Hansen *et al.*, 2004]. The Denmark Strait, situated between Greenland and Iceland (Figure 1.1), plays a major role for this process as a dense water gateway connecting the Nordic Seas and the North Atlantic [Dickson and Brown, 1994]. The water mass properties of Denmark Strait Overflow Water (DSOW) influence the strength of the Atlantic Meridional Overturning Circulation (AMOC) [Gerdes and Köberle, 1995; Döscher and Redler, 1997] and, through the relation between the AMOC and the northward heat transport, climate in the North Atlantic realm [Böning *et al.*, 1996]. Therefore, changes in the overflow transports have an impact on the basin wide horizontal and meridional circulation so that the Denmark Strait can be regarded as a key region for assessing climate change. Various field programmes have tried to measure the overflow strength [e.g. Worthington, 1969; Ross, 1973; Dickson and Brown, 1994; Girton *et al.*, 2001], its pathway downstream [Girton and Sanford, 2003] and its sources [Rudels *et al.*, 1999; Jónsson, 1999; Rudels *et al.*, 2002]. The northern overflows have recently obtained renewed attention due to an observed freshening of the overflowing water mass [Dickson *et al.*, 1999] as part of an overall change in the Atlantic freshwater balance [Curry *et al.*, 2003]. This could be a sign of a weakening of the THC.

1.2. Present-day circulation patterns

1.2.1. Northern North Atlantic

The path of the North Atlantic Current (NAC) can be traced from the trajectories of Lagrangian drifters [Orvik and Niiler, 2002; Jakobsen *et al.*, 2003] and can be seen in hydrographic sections [Orvik *et al.*, 2001]. Warm and salty Atlantic water, originating from the NAC, enters the Nordic Seas in the upper layers (Figure 1.1). The western most branch,

¹Acronyms used in this study are listed in Appendix A.1.

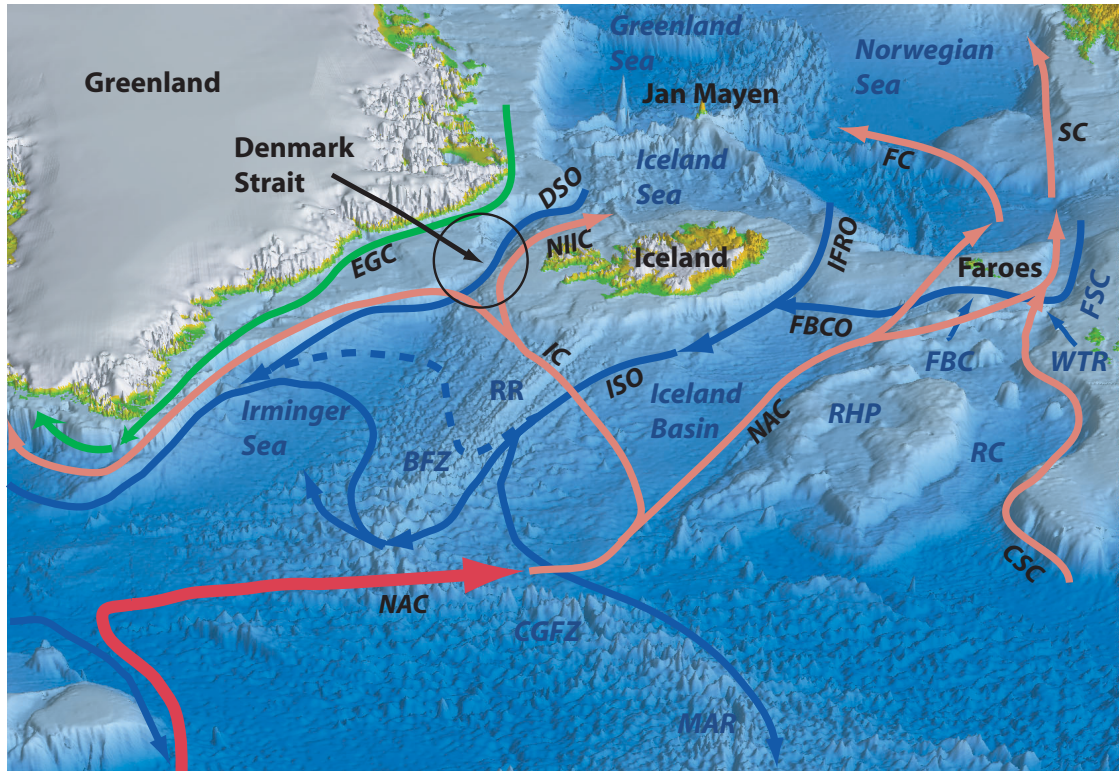


Figure 1.1.: Main current system of the North Atlantic and the Nordic Seas (modified from *Hansen and Østerhus* [2000]). There is northward flow of warm water in the upper layers (red arrows) originating from the the North Atlantic Current (NAC) and following the Continental Slope Current (CSC), the Irminger Current (IC), the Faroe Current (FC), the North Icelandic Irminger Current (NIIC) and the Shetland Current (SC). In southward direction there is cold and fresh surface outflow (green arrow) with the East Greenland Current (EGC). The cold and dense overflows (blue arrows) are the Denmark Strait overflow (DSO), the Faroe Bank Channel overflow (FBCO) and the Iceland Faroe Ridge overflow (IFRO). FBCO and IFRO form together the Iceland-Scotland overflow (ISO). Moreover, the main bathymetry features are indicated (blue labels) such as the Bight Fracture Zone (BFZ), the Charlie-Gibbs Fracture Zone (CGFZ), the Faroe Bank Channel (FBC), the Faroe-Shetland Channel (FSC), the Mid-Atlantic Ridge (MAR), the Rockall-Hatton Plateau (RHP), the Reykjanes Ridge (RR) and the Wyville-Thomson Ridge (WTR).

west of Iceland, is the North Icelandic Irminger Current (NIIC). In the eastern part of the GSR the Shetland Current flows east and the Faroe Current west of the Faroes [Hansen *et al.*, 2003] into the Nordic Seas. There and subsequently in the Polar Ocean this water is modified by cooling and freezing to a number of distinct polar and arctic water types which flow back to the Atlantic Ocean [e.g. Mauritzen, 1996a]. Part of this return flow takes place at deeper levels as an overflow through the Denmark Strait into the Irminger Sea [Dickson and Brown, 1994]. Another main path is the overflow through the Faroe Bank Channel [Borenäs and Lundberg, 1988; Borenäs *et al.*, 2001]. Minor overflows take place across the Iceland-Faroe Ridge into the Iceland Basin and across the Wyville Thomson Ridge into the Rockall Trough. The combined Iceland-Faroe Ridge and Faroe Bank Channel overflows form a homogenous water mass, the Iceland Scotland Overflow Water (ISOW) [van Aken and de Boer, 1995]. From the Iceland Basin a part of the ISOW enters the western Atlantic through the Charlie-Gibbs Fracture Zone and the Bight Fracture Zone where it joins the Denmark Strait overflow on its way into the Western Basin of the North Atlantic as part of the NADW. The latter path, a fracture zone of the Reykjanes Ridge north of the Charlie-Gibbs fracture zone, was only recently observed by Zenk *et al.* [2003, ARGO Science Workshop] based on the distribution of ARGO floats. The other part of the ISOW follows the Mid-Atlantic Ridge further south into the eastern basin of the North Atlantic. The structure of the North Atlantic-Nordic Seas exchange is described in detail by Hansen and Østerhus [2000]. They have also calculated the volume fluxes across the GSR with a water mass balance and found an Irminger Current of 1 Sv, a Faroe Current of 3.3 Sv and a Shetland Current 3.7 Sv. In addition, they estimated a Bering Strait inflow of 1 Sv. This inflow is compensated by the overflows through the Denmark Strait (3 Sv) and between Iceland and Scotland (3 Sv) in addition to surface outflows following the East Greenland Current (EGC) (1.3 Sv) and the Canadian Archipelago (1.7 Sv).

1.2.2. Observations for the Denmark Strait overflow

The sources of the Denmark Strait and Faroe Bank Channel (FBC) overflows are not deep water but intermediate water masses of the Nordic Seas. The traditional view on the formation of overflow water masses is that it takes place because of the winter surface cooling in the Iceland Sea and subsequent export to the Denmark Strait following the EGC [Swift *et al.*, 1980]. This idea was questioned by Mauritzen [1996b]. She argued that the deepwater formation rate in the Iceland Sea would be too low to produce enough dense water to feed the overflow. Instead, Mauritzen [1996b] proposed an Arctic source, with the overflow water formed by a mixture of recirculating Atlantic Water which flows westward in the Fram Strait and Arctic Atlantic Water [Mauritzen, 1996a]. This view was modified by the study of Rudels *et al.* [2002] based on a detailed comparison of water mass properties, from which they proposed the lower part of the EGC as the major constituent of DSOW. Thus, according to their view, DSOW is created by a mixture of Polar Intermediate Water and Arctic Atlantic Water with contributions from the Greenland and Iceland Seas. The relative contribution of the Iceland Sea is again under debate after Jónsson and Valdimarsson [2004] have found a direct path from the Iceland Sea to the Denmark Strait. This direct path suggests that a significant amount of overflow water has its origin in the Iceland Sea.

The volume transport of the overflow shows variability over short time scales between 2 to 10 days [Saunders, 2001] but the average transport is fairly constant over seasonal and interannual timescales at about 2.7 - 2.9 Sv [Dickson and Brown, 1994; Girton *et al.*, 2001].

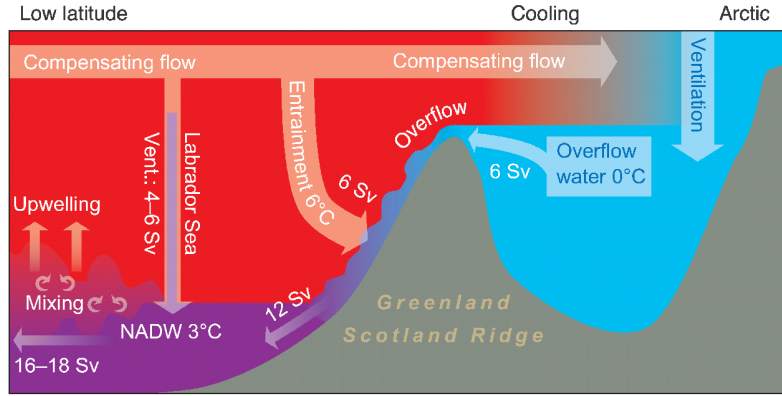


Figure 1.2.: Schematic representation of the Denmark Strait overflow as part of the thermohaline circulation [Hansen *et al.*, 2004]. Deep Water is formed north of the Greenland Scotland Ridge and overflows the ridge doubling its volume flux by entrainment of ambient water. This water mass, together with convective water from the Labrador Sea, forms the North Atlantic Deep Water which is subsequently exported to the south constituting an important part of the thermohaline circulation.

Therefore, it was suggested that the transport is limited by hydraulic constraints [Whitehead, 1998], an observation supported by numerical modeling [Käse and Oschlies, 2000]. Besides buoyancy forcing, wind stress can influence the inflow of warm Atlantic Water (AW) to the Nordic Seas and hence the outflow of cold fresh water into the North Atlantic. Biastoch *et al.* [2003] have shown in a high-resolution regional ocean model study of the heat and volume transport across the GSR that wind stress curl and heat transport are directly correlated. Seasonal variations have not been detected so far in measurements but there is evidence for a correlation of DSOW transport and the North Atlantic Oscillation [Blindheim *et al.*, 2000]. According to the latest current measurements carried out within the framework of the SFB 460 at Kiel University, there is growing evidence for an interannual variability in overflow transport [Macrandar *et al.*, *subm.*].

1.2.3. Coupling of the Faroe Bank Channel and Denmark Strait overflows

Observations of a decreasing overflow through the Faroe Bank Channel since 1950 [Hansen *et al.*, 2001] have risen the question how the Denmark Strait overflow acted over the same period of time and how the individual overflows are coupled. Nilsen *et al.* [2003] have obtained in a coarse resolution (30-40 km) ocean model an in-phase relation for the long term correlation (interannual timescales) and a fast (3 days) direct barotropic adjustment to wind changes. They obtain a positive correlation between the Denmark Strait overflow and Faroe Bank Channel overflow on interannual timescales but a negative correlation between the Denmark Strait overflow and the Iceland-Faroe Ridge overflow. An in-phase relation between Denmark Strait and Faroe Bank Channel overflows could also be expected from a coupled hydraulic system in which the overflows are fed by the same reservoir. However, the response to changes in the North Atlantic wind forcing for the individual overflows can be different. Biastoch *et al.* [2003] have found that for an overall increase in wind stress DSOW export increases whereas that of ISOW decreases. From these two studies one would expect a different behaviour for wind stress changes.

1.2.4. Hydraulic Control

The Denmark Strait overflow has to go through a channel, it does not show seasonal variations and is strongly influenced by rotation. Therefore, it is likely to be hydraulically or critically² controlled. Overflows have an asymmetric shape, this is a level interface upstream and a rapid descend at the sill, which is called overflow (Figure 1.2). *Whitehead et al.* [1974] have first applied the theory of rotating hydraulics to describe the overflow as flow over a weir following principles of engineering hydraulics. Subsequently, the field of rotating hydraulics has evolved with various theories of increasing complexity accompanied from numerical modelling studies (Table 1.2.4).

Study	Theory
<i>Whitehead et al.</i> [1974]	Zero potential vorticity, laboratory study, rot.
<i>Gill</i> [1977]	Constant potential vorticity, upstream currents necessary, rot.
<i>Armi</i> [1986]	Two-layer flow
<i>Farmer and Armi</i> [1986]	Barotropic net flow
<i>Pratt</i> [1986]	Effects of bottom friction
<i>Killworth</i> [1992a]	Transport maximum for a stratified fluid
<i>Killworth</i> [1992b]	Zero potential vorticity, different sill shapes, rot.
<i>Killworth</i> [1994]	Zero potential vorticity yields maximum, rot.
<i>Helfrich</i> [1995]	Time dependent flow, tides
<i>Pratt and Chechelnitsky</i> [1997]	Upstream circulation effects, rot.
<i>Pratt and Llewellyn-Smith</i> [1997]	Basin-sill coupling, rot.
<i>Borenäs and Whitehead</i> [1998]	Upstream separation, rot.
<i>Borenäs and Nikolopoulos</i> [2000]	Real bathymetry, rot.
<i>Pratt et al.</i> [2000]	Towing experiment, dependence on boundary layers, rot.
<i>Käse and Oschlies</i> [2000]	Numerical modelling and flow criticality for DS, rot.
<i>Shi et al.</i> [2001]	Numerical modelling of DSO variability, downstream mixing, rot.
<i>Whitehead</i> [2003]	Influence of passage shape, rot.
<i>Nikolopoulos et al.</i> [2003]	Real bathymetry for DS, constant potential vorticity, observations, rot.
<i>Garrett and Gerdes</i> [2003]	Shear flow
<i>Käse et al.</i> [2003]	Modelling and observations combined, rot.
<i>Helfrich and Pratt</i> [2003]	Upstream circulation in a finite basin, rot.
<i>Stern</i> [2004]	Constrained transport maximum, rot.
<i>Kösters</i> [2004]	Comparing hydraulic estimates and numerical modelling, rot.

Table 1.1.: Overview of studies on hydraulic control (extended from the review of [*Whitehead*, 1998]). The abbreviation rot. indicates that the study takes into account for rotation.

²To get an idea of what is meant by critical control consider water flowing along a channel. If it encounters a sill the cross sectional area is decreasing, in order to conserve mass the fluid has to speed up locally over the sill. This reduces in turn the pressure and the surface is depressed (Venturi effect). If the sill height increases eventually the situation will be met where the fluid cannot flow any faster since the cross sectional area would be too small or the surface depressed too much. That is the sill critically controls the flow and the upstream conditions have to adjust to the setting at the sill.

Analytical models are idealised descriptions of the overflow processes with associated intrinsic difficulties for quantitative transport estimates using hydrographic data. *Helfrich and Pratt* [2003] pointed out that the possible reduction of the Faroe Bank Channel overflow [*Hansen et al.*, 2001] and its climatic implications may be due to changes in the upstream circulation instead of a decrease in the actual dense water transport. This example emphasises the need for a better understanding, testing and modelling of hydraulic laws. The observed asymmetry of the flow alone does not necessarily mean that hydraulic control is active, because frictional effects could also lead to a similar appearance [*Pratt*, 1986]. Therefore, it is essential to determine whether the flow is critical by using numerical models. *Käse and Oeschlies* [2000] have corroborated the theory of *Whitehead et al.* [1974] with numerical modelling experiments and have shown that the flow is critically controlled by the sill (hydraulic control). This emphasises the role of model experiments which cannot only be used to find out whether the flow is critical or not but they also play an important role in assessing the overflow dynamics ranging from transport estimates to the decent and modification of the overflow plume.

1.2.5. Interannual variability - the North Atlantic Oscillation

On interannual timescales the North Atlantic Oscillation (NAO) is a major mode of atmospheric variability in the Northern Hemisphere and is associated with wind-stress changes. The NAO can be considered as part of the Arctic Oscillation (AO) and affects the whole North Atlantic region [e.g. *Marshall et al.*, 2001]. When dealing with paleoclimate studies the origin of the NAO becomes important in order to determine whether this feature was present in the past. The origin of the NAO is not completely understood yet but there is evidence from AGCMs that it is an internal mode of variability influenced by air-sea interaction [*Bojariu and Gimeno*, 2003]. The NAO is not uniquely defined³ but for reasons of simplicity it is taken in this study as the difference of normalised sea level pressure between the anti-correlated Azores High and the Iceland Low [*Hurrell*, 1995]. During phases of a positive NAO the westerly flow is enhanced, the cyclone paths and precipitation are shifted northeastward, and the temperature is higher than usual in central and northern Europe. The opposite behaviour holds for a negative NAO. Even though there have been signs of transport changes in the Deep Western Boundary Current at Cape Farewell on interannual timescales [*Bacon*, 1998] they have not been observed in the Denmark Strait until recently [*Macrande et al.*, *subm.*].

In climate reconstructions, the NAO can be seen as an intermittent climate oscillation with temporally active and passive phases [*Appenzeller et al.*, 1998]. Different proxies (tree-ring, snow accumulation and $\delta^{18}\text{O}$ isotopes from ice cores) yield estimates back to A.D. 1400 [*Glueck and Stockton*, 2001; *Cook et al.*, 2002]. If it is an intrinsic mode of atmospheric variability, the mechanism can be transferred to glacial time. The importance of the NAO on multi-centennial timescales is supported by a source analysis of ice rafted debris (IRD) from a sediment core of the Beaufort Gyre [*Darby and Bischof*, 2004]. The IRD composition indicates the origin of the transpolar drift and records the AO back to the last deglaciation (9-11 ka BP). This shows that an NAO-like mode of variability was active since at least the late Holocene. In contrast to that *Bond et al.* [2001] has shown that IRD events in the North Atlantic cannot be linked to different NAO phases but rather to a shift in the subpolar front. Long-term trends in the NAO have been reconstructed by *Rimbu et al.* [2003] derived from a

³See *Hurrell et al.* [2003] for an extensive overview on the NAO.

comparison of temperature trends based on alkenone data of sediment cores and an AGCM model. The results indicate a long-term decreasing trend from early to late Holocene which they attribute to an increase in solar insolation in the tropics. This suggests that the NAO is not only a source of interannual variability but may contribute to climate variability on multi-centennial to millennial timescales [Schulz and Paul, 2002].

1.3. Geological setting

The geological evolution of the GSR and the Denmark Strait in particular are important for the hydraulically controlled flow investigated here since it is very sensitive to changes in bathymetry. For present-day conditions, the model bathymetry is provided at a high resolution of 5' from ETOPO5 [NGDC, 1988] (Fig. 1.3 A). The maximum sill depth in the model is 580 m which is slightly less than the observed maximum sill depth of 630 m [e.g. Jónsson, 1999] due to the 5 km resolution in the model. The Last Glacial Maximum (LGM) bathymetry can be estimated from the present-day bathymetry by accounting for eustatic sea-level change. Clark and Mix [2002] review different estimates for the LGM sea-level lowering and find a range from 118 m to 130 m based on ice-dynamic reconstructions that are in accordance with the CLIMAP minimum model of 127.5 m. In this study the global sea level lowering is taken as 120 m for the LGM as in Peltier [2002]. Changes in bathymetry are also due to the advance and retreat of the land-based ice sheets and the accompanying isostatic adjustment. The contribution of glacial-isostatic adjustment (GIA) to changes in the bathymetry of the Denmark Strait was found by Fleming [2004] with a numerical model developed at the Research School of Earth Sciences, the Australian National University [Lambeck et al., 1998]. The ice models employed have been constrained from geological evidence, especially relative sea-level data. Geological evidence points towards glaciated shelves between Greenland and Iceland, even though the maximum extent remains uncertain. Seismic sections detect the greatest extent of the ice sheet off the SE Greenland shelf [Larsen, 1983] with a depth of grounded ice extending from 200 m to 400 m below present-day sea level. However, it is not certain if this extension is related to the last glaciation or the previous one.

Using carbonate accumulation rates and seafloor properties, Mienert et al. [1992] have developed a qualitative model that indicates an almost fully glaciated shelf. For an improved chronology of the ice-sheet extent, better time control is necessary. It may be obtained using ^{14}C dates of marine and terrestrial biotopes [e.g. Funder and Hansen, 1996]. Funder and Hansen [1996] find that the extension of the ice margin was roughly at the 300 m depth isobath of present-day bathymetry suggesting that ca 70% of the shelf was ice covered during the LGM. Their reconstruction indicates a distance of only 150 km between the ice sheets of Iceland and Greenland. However, this estimate may be too conservative since the oldest shells found on the shelf were formed at 17 ka BP [Bennike and Björck, 2002] suggesting a fully glaciated shelf during the LGM. From ice-dynamic modeling Huybrechts [2002] found that the Greenland Ice Sheet may have extended beyond the present-day coastline between 25 ka and 15 ka BP. By 10 ka BP, the ice sheet had retreated close to the current coastline and was approximately at the current ice margin at 4.5 ka BP. The GIA mentioned earlier was used to determine changes in the Denmark Strait's bathymetry [Fleming, 2004] and provided data for the LGM (21.5 ka BP) and the glacial-interglacial transition (11.3 ka BP) (Fig. 1.3 B,C). The geodynamic model combines eustatic and glacial isostatic effects resulting from fluctuations in the global ice regime. Since a GIA model that accommodates

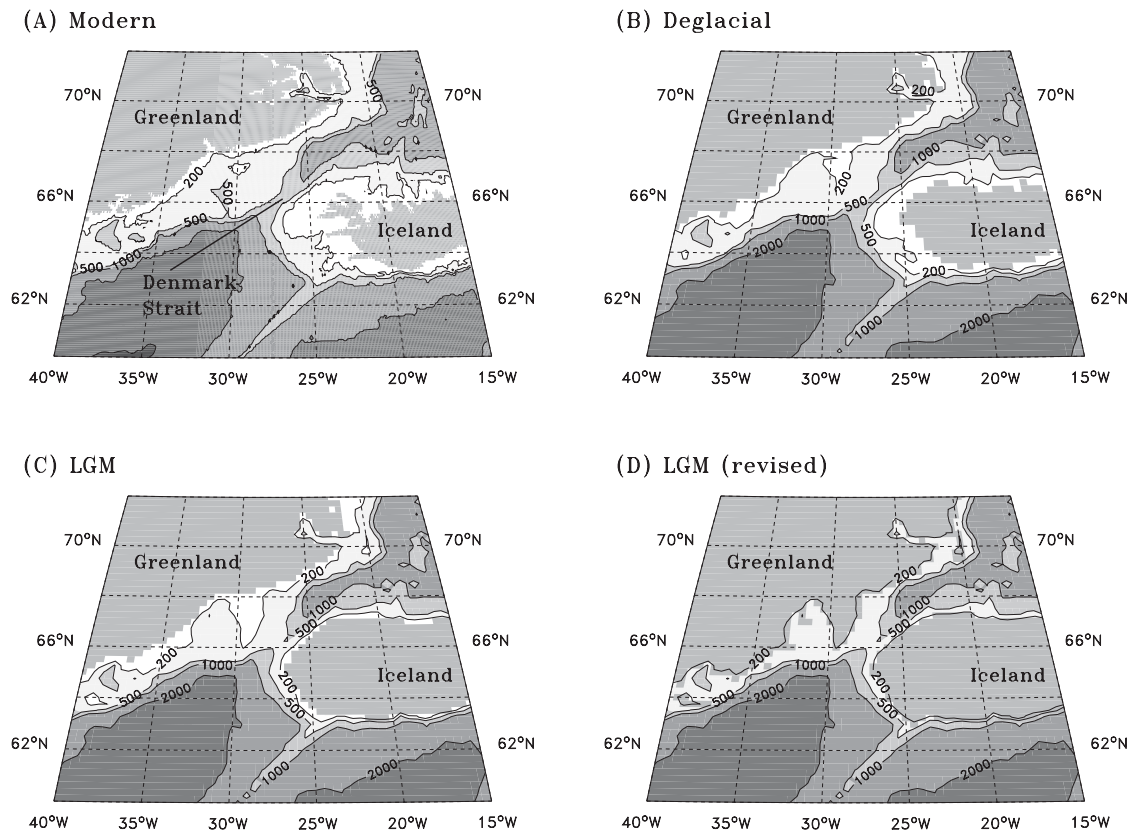


Figure 1.3.: Bathymetry of Denmark Strait for A) the present (0 ka BP), B) the glacial-interglacial transition (11.3 ka BP), C) and D) the Last Glacial Maximum (21.5 ka BP). Bathymetries B, C and D are based on the GIA models. C is the favoured model of *Fleming* [2004] while D includes a more extensive and possibly more realistic ice extent.

lateral variations in the earth's rheology parameter values was unavailable, the GIA response from the land-based ice sheets, excluding Iceland, was first determined using a global average earth model. In a further step, the response from Iceland, which was found separately using a more realistic structure for that area, was added. The Greenland ice model is from *Fleming* [2004] and was derived from the minimum and maximum ice sheets of *Denton and Hughes* [1981]. The Iceland model is from the maximum model of *Denton and Hughes* [1981] with timing from *Ingolfsson et al.* [1994]. Using these models, an LGM sill depth of ca 509 m was found compared to 581 m in the present. Although the LGM model underestimates the extent of the ice-sheet slightly, the overall agreement between the geodynamic model and geological field studies is satisfactory. In order to test the sensitivity of the Denmark Strait overflow to the lateral extension of the ice-sheet, an additional bathymetry (Fig. 1.3 D) was used where the ice extent was increased to match the reconstruction by *Funder and Hansen* [1996].

1.4. The Glacial North Atlantic

Under a different climatic situation, such as the LGM, one would expect changes in the strength of NADW formation and accordingly the AMOC. The response of coarse resolution climate models is ambiguous. Some numerical models simulate a weaker overturning during glacial times [*Ganopolski et al.*, 1998; *Schmittner et al.*, 2002a; *Prange et al.*, 2002; *Kim et al.*, 2003] while others indicate a strengthening [*Hewitt et al.*, 2001; *Kitoh et al.*, 2001]. The strengthening is usually attributed to the increased wind stress over the sub-polar North Atlantic in glacial times as found in atmospheric GCMs driven by reconstructed SSTs [*Lohmann and Lorenz*, 2000] and coupled climate models [*Shin et al.*, 2003]. Moreover, the increase in tidal amplitudes due to lowered sea-level and thus the removal of the highly dissipative shelves as an energy sink is likely to increase the abyssal mixing [*Munk and Wunsch*, 1998], which in turn may have led to an increased MOC. However, reconstructions of glacial $\delta^{13}\text{C}$ ventilation rates imply a weakened formation of NADW [*Sarnthein et al.*, 1994], a shallower overturning cell [*Boyle*, 1995] and an increased northward intrusion of Antarctic Bottom Water (AABW) [*Skinner and Shackleton*, 2004]. Less export of NADW to the Southern Ocean can be inferred from neodymium isotopes [*Rutberg et al.*, 2000]. Additional evidence for a reduced overturning circulation comes from a kinematic proxy ($^{231}\text{Pa}/^{230}\text{Th}$) [*McManus et al.*, 2004] which is directly correlated to the deep water export. A weaker Gulf Stream, as inferred from geostrophic estimates based on temperature and salinity reconstructions [*Lynch-Stieglitz et al.*, 1999a], is consistent with a reduced meridional overturning. However, it has been shown that tracer distributions do not uniquely constrain the circulation [*LeGrand and Wunsch*, 1995].

An important factor for the circulation in the North Atlantic is the location of deep-water formation during the glacial. In the current climate the deep water formation is the driving force for the overflows by setting up a pressure gradient across the GSR. This hydrostatic pressure gradient is maintained by the vertical density structure and therefore set by the buoyancy forcing (surface heat and freshwater fluxes). Under present-day climate conditions most of the deep water is formed in the Greenland Sea and Labrador Sea by open ocean convection [*Marshall and Schott*, 1999]. In the Labrador Sea boundary convection might play a role as well [*Spall*, 2001]. Moreover, there is evidence for deep water formation in the Irminger Sea [*Pickart et al.*, 2003] forced by the Greenland tip jet. Another deep water formation mechanism, especially in the Arctic shelf areas, is brine release which creates

highly saline water. This water is subsequently sinking from the shelf towards greater depths [Meincke *et al.*, 1997].

An agreement on the glacial location of deep water formation has not been reached yet. Some models indicate a shift of the formation areas to locations south of the GSR [Ganopolski *et al.*, 1998] whereas others suggest ongoing convection in the Nordic Seas [Schäfer-Neth and Paul, 2001; Paul and Schäfer-Neth, 2003]. As coarse resolution models often fail to reproduce present-day deep water formation north of the GSR the LGM estimates should be taken with caution. Paleoceanographic reconstructions suggest ongoing convection in the Nordic Seas for the last part of the last glacial, even though the individual deep water forming mechanisms have varied [Dokken and Jansen, 1999]. Open ocean convection is likely for the warmer interstadials, whereas during the colder stadials the main deep water formation mechanism was probably accomplished by brine release. Concentrating on the LGM, sea-ice reconstructions from the Glacial Atlantic Ocean Mapping (GLAMAP) project [Sarnthein *et al.*, 2003a], based on foraminiferal paleo-temperature estimates [Sarnthein *et al.*, 2003b; Norgaard-Pedersen *et al.*, 2003] and the earlier study of Weinelt *et al.* [1996], show that the Nordic Seas were ice-free during the LGM summer. Ongoing inflow of Atlantic water [Rasmussen *et al.*, 1996] suggests at least modest deep water formation by convection in the Nordic Seas during glacial summer. Moreover, there is evidence from carbonate accumulation rates [Henrich, 1998] that there was deep-water formation in the Norwegian-Greenland Seas during the LGM. Nevertheless, there is also evidence for a cessation of Norwegian Sea Overflow Water (NSOW) in glacial times (prior to 13.4 ka) suggesting the formation of NADW in subpolar regions [Kuijpers *et al.*, 1998]. The areas of deep-water formation may influence the direction of the overflows so that a reversed flow of deep water from the Atlantic to the Nordic Seas has been proposed [Vogelsang, 1990; Sarnthein *et al.*, 1992]. This is an idea that certainly needs to be tested in a physically consistent way, e.g. by numerical modelling.

1.4.1. Paleoceanographic reconstruction of the Denmark Strait overflow

It is still a point of debate whether the DSO played a similarly important role in deep water formation during the last 21 ka as it does today [e.g. Sarnthein *et al.*, 2001]. Considering LGM conditions, there are no direct transport estimates. From the lithofacies and chronology of sediment cores at the southern end of the Denmark Strait an indirect measure of overflow strength can be obtained. It indicates that the overflow had its present strength from around 12 ka BP on [Völker, 1999; Andrews and Cartee-Schoolfield, 2003]. Commonly, $\delta^{13}\text{C}$ values are used as ventilation proxies for identifying water masses [Duplessy *et al.*, 1988; Curry *et al.*, 1988] and the overflow strength is inferred from these. The benthic $\delta^{18}\text{O}$ and $\delta^{13}\text{C}$ records from core JM96-1225 (Figure 1.4), located at the southern exit of the Denmark Strait, help to distinguish between the different formation processes of NADW. Freshly ventilated NADW is enriched in $\delta^{18}\text{O}$ and $\delta^{13}\text{C}$ in contrast to depleted brine and Southern Ocean water. Based on these different isotopic characteristics, Hagen and Hald [2002] used the combined information of $\delta^{18}\text{O}$ and $\delta^{13}\text{C}$ to reconstruct glacial water masses and deep water formation processes.

The Denmark Strait is not only important as dense water gateway, but it might have had a more pronounced influence on the pacing of events in the past. Based on the analysis of IRD and the correlation of sediment cores north and south of the Denmark Strait *van Kreveld et al.* [2000] suggest that the Denmark Strait could have acted as a critical element

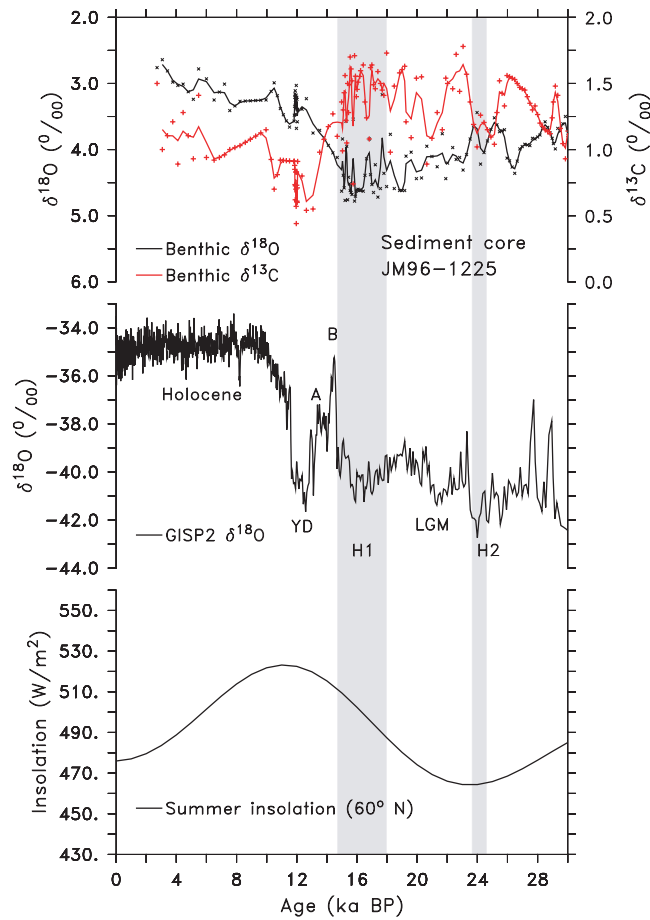


Figure 1.4.: Key data for the time slice from 30 ka BP to present-day.

Upper panel: Surface and deep-water conditions at the southern exit of the Denmark Strait as recorded in benthic $\delta^{18}\text{O}$ and $\delta^{13}\text{C}$ records from deep-sea core JM96-1225 [Hagen and Hald, 2002].

Middle panel: Surface temperature at the Greenland summit as reflected in the $\delta^{18}\text{O}$ record of the GISP2 ice core [Grootes and Stuiver, 1997]. The most important periods are the Holocene, the Younger Dryas (YD) cold phase, the Bølling-Allerød warm phase (B, A) and the Last Glacial Maximum (LGM).

Lower panel: Variation in summer (June mid-month) insolation at 60° N from orbital parameters [Berger and Loutre, 1991].

The light gray bands indicate the occurrence of Heinrich events 1 (14.67-18.1 ka BP) and 2 (23.4-24.2 ka BP) with timing of Sarnthein *et al.* [2001].

in generating Dansgaard-Oeschger (D-O) cycles by iceberg blocking of the strait. This raises the question which processes are associated with a closure of the Denmark Strait, an issue not addressed so far by modelling experiments.

1.4.2. Long-term climate variability

In many paleoceanographic studies the focus is on the millennial scale variability reflected in $\delta^{18}\text{O}$ values of foraminifera found in sediment cores and the GISP2 ice core [Grootes and Stuiver, 1997]. The ice core record clearly shows the exceptional stable conditions for the Holocene (from about 9 ka BP) and the rapid climate transitions which took place before. After the Last Glacial Maximum (LGM, 18-21.5 ka BP) [Mix et al., 2002], intense calving of icebergs occurred leading to Heinrich Event 1 (HE1, 18.1-14.67 ka BP) [Heinrich, 1988; Sarnthein et al., 2001]. This was followed by the Bølling-Allerød interstadial (14.7-12.9 ka BP) warm phase which ended with the Younger Dryas (12.9-11.6 ka BP) [Severinghaus et al., 1998].

One of the most widely discussed questions in Paleoceanography is that of Dansgaard-Oeschger (D/O) cyclicity. D/O events are rapid transitions from stadial to interstadial conditions and vice versa with a fundamental pacing period of 1470 years and multiples thereof [Schulz, 2002]. They were first found in a Greenland ice core [Johnsen et al., 1992; Dansgaard et al., 1993] and then linked to sea-surface temperatures [Bond et al., 1993] and deep circulation [Rasmussen et al., 1996]. The typical structure [Alley, 1998] is saw tooth-like. A rapid warming (O(10) years) is followed by a gradual cooling (O(100) years) and ending with a rapid transition to cool conditions which may last longer (O(100-1000) years). Three to four D/O events can be grouped in a Bond-cycle in a long-term cooling trend. The abrupt cooling at the end of the Bond cycle is associated with a so-called Heinrich event which is a massive discharge of icebergs to the North Atlantic. These events are therefore evident in ocean sediments as layers rich in ice rafted debris (Heinrich layers). The origin of the D/O cycles is controversial and ranges from external (solar) forcing [Bond et al., 2001] to internal oscillations of the ice sheets [MacAyeal, 1993a, b], deep decoupling oscillations of the ocean system [Schulz et al., 2002; Timmermann et al., 2003] or stochastic resonance of freshwater noise [Ganopolski and Rahmstorf, 2002].

1.5. The modelling perspective

Overflow dynamics act on Rossby Radius length scale which cannot be resolved by present-day global climate models. Even in eddy-permitting regional North Atlantic models the representation of overflows, especially the Denmark Strait, is still an issue [Willebrand et al., 2001]. The sensitivity of coarse resolution z -level models to bathymetry variations is well known [Roberts and Wood, 1997] and in coarse-resolution climate models one hardly obtains realistic transport rates for the Denmark Strait overflow without tuning of the model bathymetry [Gerdes, 1993b]. These bathymetry changes lack a physical basis and are subjective decisions. Transport rates are also model dependent, e.g. σ vs z -level models, which may cause serious problems since the exact overflow representation presumably has not only local impact but can change the horizontal circulation patterns [Beismann and Barnier, 2004].

These problems can be overcome only theoretically with an increase in horizontal and vertical resolution [Winton et al., 1997]. The necessary resolution is prohibitive for global

climate models due to increasing computational costs. Another way to handle this problem is to employ a rotated grid with one pole over Greenland to increase the resolution locally [Thorpe *et al.*, 2004] or to employ a grid focused on the North Atlantic [Nilsen *et al.*, 2003]. Still, the overflow dynamics on the Rossby radius scale cannot be resolved yet. The alternative approach to artificially increase the resolution in the North Atlantic, for instance in the Bergen Climate Model [Nilsen *et al.*, 2003], may have limitations. Important processes in the Southern Ocean might be underrepresented or inappropriately resolved. An ideal solution would be an overflow parameterisation which allows uniform coarse resolution but is based on physical constraints.

The main motivation to improve the representation of the northern overflows in coarse-resolution models is the often underestimated rate of deep water formation north of the GSR. It can be expected that stronger overflow leads to increased advection of warm and salty surface water to the north, thus preconditioning deep-convection in the Nordic seas. Thus, a strong impact on the simulated large scale overturning could result from better represented overflow processes as found in earlier studies [e.g. Döscher *et al.*, 1994; Böning *et al.*, 1996].

The modelling study of Lohmann [1998] suggests that the stability of the AMOC strongly depends on the representation of the overflow. He found that after a fresh water perturbation, which caused a collapse of the AMOC, it resumes only if an additional bottom boundary layer (BBL) model is used to improve the representation of the overflows. This emphasises the importance of a realistic overflow representation for climate models which investigate the stability of the THC.

Moreover, the Denmark Strait has not been investigated with an eddy resolving resolution for LGM conditions which is needed to represent adequately the governing dynamics. Even though coarse resolution numerical models of the glacial North Atlantic compare well with proxy data [Paul and Schäfer-Neth, 2003; Meissner *et al.*, 2003], the Denmark Strait is not properly resolved in these models and hence transport estimates are not reliable. The validity of hydraulic theory as demonstrated for present-day conditions from numerical modelling results and observations [Käse and Oschlies, 2000; Girton *et al.*, 2001] has given rise to the question as to whether this is also a useful tool for studying the Denmark Strait overflow under different climatic conditions, e.g. the LGM. In case of the Mediterranean outflow, hydraulic constraints on maximum overflow strength based on hydrography and bathymetry have already been applied successfully [Matthiesen and Haines, 2003].

1.6. Objectives and thesis outline

This thesis is part of the DFG funded “Research Unit Ocean Gateways” which focuses on the climatic impact of ocean gateways on climate. Particularly in this thesis, the Denmark Strait will be studied concerning the influence of gateway aperture and throughflow and on regional and basin wide ocean circulation.

Today’s coarse resolution climate models cannot resolve overflow processes across the GSR appropriately. This complicates model based estimates of deep water formation for climates different from today’s. To circumvent the problem a high resolution regional ocean model is used to study the northern overflows under present-day and Last Glacial Maximum conditions. The governing dynamics controlling the exchange across the ridge were determined from sensitivity experiments using idealised forcing changes and could then be parameterised and included into a global climate model.

The structure of this study is as follows:

Chapter 2 describes the basic modelling approach.

Chapter 3 discusses the DSO as an buoyancy driven flow with an idealised set-up to evaluate different theories describing hydraulically controlled flows [Kösters, 2004]. The basic model approach is extended to take into account a more realistic water mass structure.

Chapter 4 extends the approach of the previous section to the past, especially the Last Glacial Maximum and estimates Denmark Strait overflow transports based on hydraulic constraints [Kösters *et al.*, 2004]. The influence of variations in gateway depth and aperture on throughflow are disentangled.

Chapter 5 addresses the influence of wind stress and the connection between Faroe Bank Channel overflow and Denmark Strait overflow. A comparison of the present-day winter and LGM summer ocean circulation is made concerning volume and heat transport. Moreover, the spreading of marine biota is addressed.

Chapter 6 presents the results from the hydraulic parameterisation in the global model for the equilibrium state and for freshwater perturbation experiments. The influence of the DSO is compared to other factors determining the strength of the AMOC.

Chapter 7 jointly discusses the results of the previous chapters.

2. Tools and methods for ocean and overflow modelling

For the modelling of overflows, different techniques have been successfully applied so far, ranging from laboratory studies [*Whitehead et al.*, 1974] and simple one-dimensional representations of the overflow [*Price and Baringer*, 1994] to three-dimensional numerical models [*Käse and Oschlies*, 2000]. In an early study, *Whitehead et al.* [1974] employed rotating tank experiments to model the transport of dense water through a constriction with application to the Denmark Strait. More recently, *Cenedese et al.* [2003] found in laboratory studies the transition from laminar to wave like flow in density-driven currents by increasing the slope angle or density contrast as well as the transition to an eddy forming regime by increasing the rotation rate. The theoretical approach of *Price and Baringer* [1994] treats the overflow as a slab of dense water influenced by gravity, rotation and friction. The flow is taken as stationary and is integrated over its width leaving a “streamtube” for which entrainment and mean transport can be readily assessed. From such essentially one-dimensional streamtube models the descent of the plume can be predicted [*Killworth*, 2001] but the lateral structure remains unclear. The interaction of topography and flow was addressed by *Jungclaus and Backhaus* [1994] in a two-dimensional plume model based on reduced gravity assumptions. Adding a further dimension, *Jiang and Garwood Jr.* [1996] could show in experiments with a three-dimensional primitive equations model the break-up of large plumes into sub-plumes for overflows on a continental slope. Following this, *Käse and Oschlies* [2000] combined the laboratory studies of *Whitehead et al.* [1974] with numerical process studies of dam break experiments in which the overflow was represented as a purely density driven flow and appeared to be hydraulically controlled. *Biastoch et al.* [2003] extended the process model to include wind forcing in addition to hind-cast experiments driving the model with realistic heat fluxes and wind stress in a closed domain representing the northern North Atlantic.

For this study, a combined regional and process modelling approach has been chosen similar to that of *Käse and Oschlies* [2000] and *Biastoch et al.* [2003]. For the regional modelling a terrain-following (σ -coordinate) ocean model seems most appropriate due to the smooth representation of topography and the ability to simulate interactions between flows and topography [*Ezer et al.*, 2002]. In contrast, z -level models have difficulties in simulating overflow processes and bottom boundary layer dynamics because of the step-like representation of topography [*Gerdes*, 1993a; *Beckmann and Döscher*, 1997; *Winton et al.*, 1997]. On the other hand, the numerical error in the pressure gradient calculation over steep topography has been an area of concern for terrain-following ocean models [*Mellor et al.*, 1998]. In this study the accurate overflow representation is most important and hence a σ -coordinate model, the Regional Ocean Modelling System (ROMS), is used for which the model description and set-ups are given below.

In addition to the regional model, a coupled atmosphere-ocean global model of intermediate complexity is utilised to determine the importance of the overflow for long-term integrations in climate models. For this reason, the dynamics identified in the high-resolution

model are parameterised and included in the global model, the University of Victoria Earth system coupled model (UVic ESCM).

2.1. The Regional Ocean Modelling System

The model in most of the following experiments is ROMS, a primitive equations σ -coordinate model developed by the ocean modelling groups at Rutgers University (USA) and the University of California in Los Angeles (USA). ROMS has been successfully employed for a number of different applications ranging from modelling coastal areas [Penven *et al.*, 2001; Marchesiello *et al.*, 2003], to process [She and Klinck, 2000] and basin wide studies [Haidvogel *et al.*, 2000; Malanotte-Rizzoli *et al.*, 2000] as well as in intercomparison with other σ -coordinate models or z - and isopycnal-models [Chassignet *et al.*, 2000; Willebrand *et al.*, 2001].

Evolutionary, ROMS is a descendent of the S-coordinate Rutgers University Ocean Model (SCRUM) [Song and Haidvogel, 1994] but was completely rewritten to be computationally more efficient in single and multi-threaded computer architectures. It was also expanded to include a variety of new features including high-order advection schemes, accurate pressure gradient algorithms and several sub-grid scale parameterisations. As SCRUM it solves the incompressible, hydrostatic, primitive equations with a free surface¹. The prognostic variables are the surface elevation ζ , barotropic velocities (\bar{u}, \bar{v}) , baroclinic velocities (u, v) , potential temperature θ_T and salinity S as tracers. The density ρ is derived either from a linear equation of state or from the nonlinear UNESCO equation of state [UNESCO, 1981]. For computational economy, the momentum equations are solved using a split-explicit time-stepping scheme, which requires a special treatment and coupling between barotropic and baroclinic modes. A finite number of barotropic time steps are carried out within each baroclinic step. In order to avoid aliasing errors associated due to the higher sampling frequencies of the barotropic mode relative to the baroclinic, the barotropic fields are time averaged with a cosine-like filter [Shchepetkin and McWilliams, *subm.*]. ROMS is optimised for shared memory parallel computer architectures such as the NEC-SX5, compiler dependent directives (OpenMP) are only in the main routines of the computational code. Parallelisation is done by partitioning the full domain into two-dimensional subdomains. Then multiple sub-domains can be assigned to each processor in order to optimise the use of processor cache memory. The horizontal discretisation is with boundary fitted, orthogonal curvilinear coordinates on a staggered Arakawa C-grid, thus the grid can follow the coastal boundaries. Alternatively, a coastline can be specified by land/sea masking. In the vertical a generalised terrain-following coordinate is used [Song and Haidvogel, 1994], which allows to focus the resolution on the sea-surface or both sea-surface and seafloor (Figure 2.1).

Currently, all 2D and 3D equations are time discretised using a third-order accurate predictor (Leap-Frog) and corrector (Adams-Molton) time-stepping algorithm which is very robust and stable. The time-step Δt is commonly restricted by the grid spacing Δx and fastest mode of information propagation following the Courant-Friedrich-Levy (CFL) criterion as $\frac{c\Delta t}{\Delta x} < 1$. The external (barotropic) time step t_E can be calculated from the model

¹The model formulation and equations of motion, a description of the σ -coordinate system and the horizontal curvilinear coordinates is given in Appendix A.2 and in more detail in the technical SCRUM manual [Hedström, 1997].

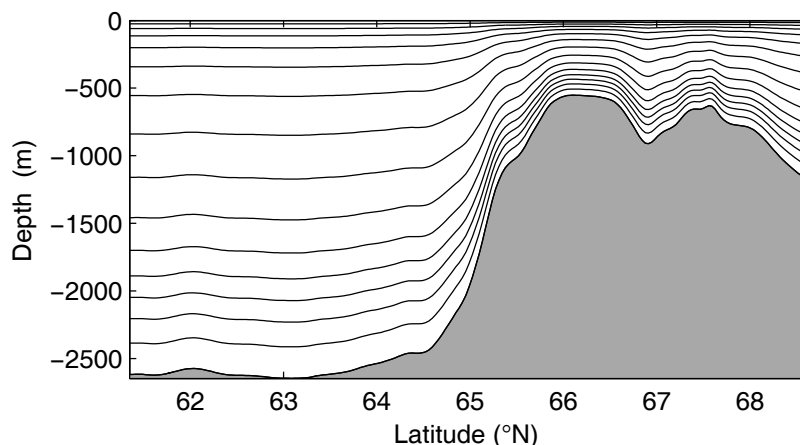


Figure 2.1.: The stretched vertical grid for σ -coordinates on a section across Denmark Strait. Note the increased resolution at the sea-surface and seafloor.

grid following *Ezer et al.* [2002] as

$$\Delta t_E \leq c^{-1} [(\Delta x)^{-2} + (\Delta y)^{-2}]^{-1/2}, \quad c = 2(gH)^{1/2} + u_{\max}. \quad (2.1)$$

Here, H is depth, g is gravitational acceleration and u_{\max} is the maximum velocity. The ratio of internal (baroclinic) step t_I to external time step should be $20 \leq N_{\text{fast}} = \frac{t_I}{t_E} \leq 80$. Due to the specially designed predictor-corrector time step algorithm used in ROMS, a substantial increase in the permissible time-step size is allowed of up to two times the CFL limitation.

The third-order, upstream-biased advection scheme allows the generation of steep gradients, enhancing the effective resolution of the solution for a given grid size [*Shchepetkin and McWilliams*, 1998]. The advection algorithm is quasi-monotone, consisting of a high-order, integrally conservative and non-dissipative, advection scheme followed by a low-order dissipation of excessive advection (overshooting). Due to the implicit diffusion no explicit lateral viscosity is necessary in the model domain except in sponge areas near the boundaries. In the vertical a conservative parabolic-spline discretisation reduces the pressure gradient truncation error. The vertical advection of tracers is by default a fourth-order advection scheme or alternatively based on Akima splines.

The pressure gradient error in topography following coordinates can be seen from the x -component of the pressure gradient force

$$\left. \frac{\partial p}{\partial x} \right|_z = \left. \frac{\partial p}{\partial x} \right|_\sigma - \frac{\sigma}{h} \frac{\partial p}{\partial \sigma} \frac{\partial h}{\partial x} \quad (2.2)$$

The first term on the right describes the pressure variation along a σ -surface and the second is the hydrostatic correction. In the presence of steep topography the two terms are large and of comparable magnitude, hence the residuals can be strongly affected by computational errors [*Beckmann and Haidvogel*, 1993]. In order to reduce the pressure gradient error inherent in σ -coordinate models, the bathymetry has to be smoothed after interpolating it to the model grid. A Shapiro filter [*Shapiro*, 1970] is weighted for smoothing of the topography with the bottom slope parameter r , defined as

$$r = \frac{\Delta h}{2h} = \frac{h^{+1/2} - h^{-1/2}}{h^{+1/2} + h^{-1/2}}. \quad (2.3)$$

Following suggestions from *Haidvogel and Beckmann [1999]* the filtering was applied until an r -value of less than 0.2 was reached, even though values of up to 0.4 are permissible [*Shchepetkin 2003, pers. comm.*]. After the bottom steepness is reduced, features with a wavelength of less than $2\Delta x$ are removed by applying a low-pass Shapiro filter.

The vertical mixing schemes in ROMS, which were used here, are a Brunt-Väisälä frequency (BVF) dependent scheme and the Large, McWilliams and Doney (LMD) parameterisation [*Large et al., 1994*]. The BVF scheme uses a constant background diffusivity, which is increased when unstable conditions are determined from the gradient Richardson number². The LMD parameterisation consists of a non-local, K-profile planetary (KPP) boundary layer scheme, which parameterises unresolved physical vertical sub-grid scale processes. It matches separate parameterisations for vertical mixing of the surface boundary layer and the ocean interior. A formulation based on boundary layer similarity theory is applied in the water column above a calculated boundary layer depth. This parameterisation is then matched at the interior with schemes to account for local shear, internal wave and double diffusive effects. Most importantly it allows the boundary layer to penetrate into the stable thermocline for convective and wind-driven situations.

If a lateral boundary faces the open ocean active boundary conditions instead of closed walls may be desirable. This can be done by including open boundaries based on radiation condition which connect the interior model solution to the surroundings [*Marchesiello et al., 2001*]. The direction of information propagation is determined and for inward flux a nudging term quickly (1 day) restores the model solution to climatological values and for outward flux the interior values are extrapolated to the boundary together with weak (60 days) nudging. The climatological forcing at the boundaries can be derived from other model experiments hence an effective one-way nesting can be implemented [e.g. *Penven et al., 2001*]. An extension of this approach is, as in the regional model study of the Gulf of Alaska [*Hermann et al., 2002*], to employ a telescoped grid with different nudging zones for barotropic (tidal) currents and tracers. The most recent development is the two-way nesting approach (ROMS-AGRIF). Here information can be exchanged between coarse and high resolution models running simultaneously. The successful validation for the California current system [*Penven et al., in revision*], suggests that this approach might be applicable in the future for the Denmark Strait as well.

Besides the main routines presented so far, ROMS has a number of modules for specific modelling questions. The optional modules include biological and sedimentological models coupled to ROMS. The sedimentological model regards suspending sediment in the water column like other tracers and solves the advection-diffusion equation with additional terms for the vertical settling velocity and source and sink terms related to erosion and deposition [*Warner et al., 2005*]. Moreover, the flow and suspended sediment concentration in the benthic boundary layer can be parameterised according to the wave-current interaction model of *Styles and Glenn [2000]*.

During the course of this study, the development of ROMS has continued from version 1.7.2 to 1.8, 2.0 (called TOMS) and finally 2.1. The differences in the numerical kernel between the individual versions are small. The different model versions mainly reflect the inclusion of additional modules, e.g. the sediment module in 2.0, and the switch from Fortran 77 to Fortran 90 with the release of ROMS 2.0.

²The gradient Richardson number is defined as $Ri_g = N^2 / \left(\left(\frac{\partial u}{\partial z} \right)^2 + \left(\frac{\partial v}{\partial z} \right)^2 \right)$, where N is the Brunt-Väisälä frequency.

2.2. Model configurations

2.2.1. The Denmark Strait overflow process model

ROMS 1.8 is set-up as a process model of the Denmark Strait, for a model domain (Fig. 2.2) extending from 60.5° N to 70.5° N and from 45° W to 16° W. 30 equally spaced

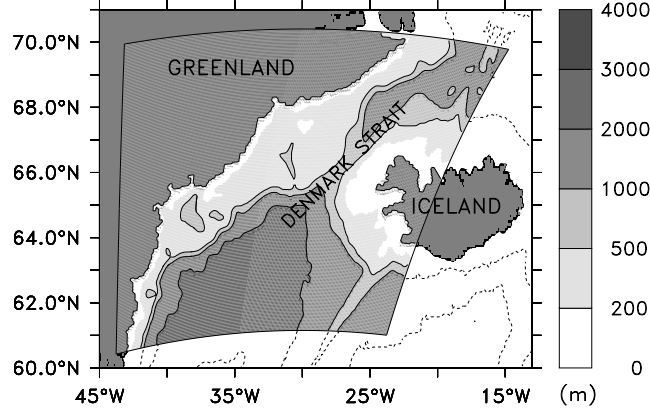


Figure 2.2.: Bathymetry (in m) of the Denmark Strait overflow process model. The Denmark Strait is located between Greenland and Iceland. The outlined domain shows the model area for the numerical experiments.

σ -layers are used in the vertical and an eddy resolving horizontal resolution of $5\text{ km} \approx 1/20^\circ$. In this case the grid stretching parameter (*tcline*) does not have an influence. The grid spacing was chosen to resolve the internal Rossby Radius $R_d \approx 10\text{ km}$. The topography of the model is obtained by bilinear interpolation of the 5-min ETOPO5 database [NGDC, 1988]. Depths shallower than 100 m are set to 100 m. After interpolation, the raw bathymetry was smoothed until an r -value of less than 0.2 was reached, but realistic values for the depth (580 m) and width (350 km) of the Denmark Strait were kept. The assumption that the pressure gradient error is negligible if the bathymetry is sufficiently smooth was assessed in a stability test with the smoothed bathymetry of Denmark Strait. The model was integrated from rest with uniform temperature (5°C) without surface forcing and in a closed domain. After 35 days of integration the maximum velocity was 0.24 cm/s and the maximum temperature deviation from initial conditions was $1.2 \cdot 10^{-4}\text{ }^\circ\text{C}$. These errors can be attributed to the pressure gradient error but are so small that they are neglected for the remainder of this study.

Only temperature is included as active tracer and hence a linear equation of state is used to derive density ρ from potential temperature θ_T as $\rho = 1027.96 \frac{\text{kg}}{\text{m}^3} - 0.08 \frac{\text{kg}}{^\circ\text{C m}^3} \cdot \theta_T$. The equation was derived from a linear regression of temperature and density (not shown), but the intercept was slightly adjusted from 1028.0 kg/m^3 to 1027.96 kg/m^3 , so that the overflow definitions $\sigma_\theta \geq 27.8$ and $T < 2^\circ\text{C}$ are equivalent here. For more accurate transport calculations an additional, passive tracer is added. The model is initialised with two water masses having a potential temperature of $\theta_T = -1^\circ\text{C}$ ($\rho = 1028.04 \frac{\text{kg}}{\text{m}^3}$) north of the sill and $\theta_T = +5^\circ\text{C}$ ($\rho = 1027.56 \frac{\text{kg}}{\text{m}^3}$) south of the sill, resembling the average two respective temperatures (densities). An overview for the model parameters is given in Table 2.1, for more details see below.

Initially, the model contains warm water south of the sill and in the upper layer, which

Model parameters	Values
Horizontal grid	5 km x 5 km resolution, isotropic grid 44° W - 15° W and 60° N - 70° N
Vertical grid	30 σ -levels, equidistant spacing with stretching parameters: $\theta_s = 1$, $\theta_b = 1$, $tcline = 100$ m
Boundary conditions	Closed boundaries at walls no-slip boundary conditions Land areas represented by a mask
Timestepping	$\Delta t_1 = 120$ s, $N_{fast} = 20$
Advection schemes	Third-order upstream bias horizontal advection for momentum and tracers Fourth-order centered tracer vertical advection Parabolic spline vertical reconstruction
Viscosity	No explicit
Diffusion	No explicit
Bottom drag	Quadratic law with $C_D = 1 \cdot 10^{-3}$
Pressure gradient	Quartic 2 Jacobian scheme
Mixing	Tracer and momentum mixing along S-surfaces
Interior mixing	Stability dependent Brunt-Väisälä frequency (BVF) scheme
Equation of state	Linear, density only temperature dependent
Forcing	Buoyancy forcing through source and sink terms No surface heat flux No wind stress forcing

Table 2.1.: Configuration of ROMS 1.8 for the Denmark Strait overflow process model.

thickness varies in the individual experiments from 0 to 580 m, and cold water below. The layer of cold water in the north is initially piled up behind an imaginary dam, which breaks when the the model is initialised, hence the experiments are called dam break experiments. Then the cold and dense water from the northern reservoir can flow southward. The experiment set-up will be called “two-layer model” in the following because the vertical density structure was chosen to approximate a two-layer system to better represent the theoretical approach. But note that 30 σ -layers were used in the vertical. The reservoir height is kept constant by replacing warm water advected from the south with cold water, using sinks and sources at the northern boundary. These source and sink terms are included in the horizontal tracer and momentum equation. A northward flow is prescribed in the top five layers whereas the flow is set to be southward in the bottom five layers. It thus resembles the advection of newly formed deep-water. This is different from SCRUM, as used in *Käse and Oschlies* [2000], where the source terms are added in the vertical momentum equations.

For advection of tracer and momentum the third- and fourth-order schemes were compared in sensitivity experiments. The standard third-order upstream biased advection scheme with no explicit viscosity gave stable results with only minor overshooting at the boundary between the two water masses in the dam break experiments. The disadvantage is that the amount of viscosity and diffusion cannot be controlled. Therefore, the fourth-order scheme was tested but it was found that it needs rather high values for the explicit viscosity. Due to the dam-break experimental set-up, there are large temperature contrasts and the model needs a biharmonic viscosity of $\nu_4 = 1 \cdot 10^9$ m⁴/s to be stable. The biharmonic viscosity implies a spindown time, i.e. the timescale where a given velocity is damped to 1/e of its initial strength, of $t = \frac{\Delta x^4}{\pi^4 \nu_4} = 0.074$ days. Compared to typical timescales of a quarter to half a day [*D. Haidvogel 2001, pers. comm.*] the spindown time seemed too short and

consequently the third-order upstream biased scheme was used for horizontal advection in all remaining experiments.

As time step limitation, derived from Equation (2.1) with a maximum bottom depth $H=3000$ m, one obtains a maximum external time step of $t_E=14$ s. With an external time step of $t_E=120$ s/20=6 s in the model this requirement is certainly met.

Bottom stress τ_b is calculated from the quadratic bottom drag equation as $\tau_b = \rho C_D |\mathbf{u}| \mathbf{u}$, with \mathbf{u} as the bottom velocity and density ρ . The constant, non-dimensional drag coefficient $C_D = 10^{-3}$ was chosen as in *Käse and Oschlies [2000]*.

2.2.2. The Greenland-Scotland Ridge regional ocean model

The domain of the DSO process model described above was extended to cover the full Greenland-Scotland Ridge from 42° W to 0° W and from 55° N to 74° N (Figure 2.3), thus both overflows, Denmark Strait and Faroe-Bank Channel, are included. For this model

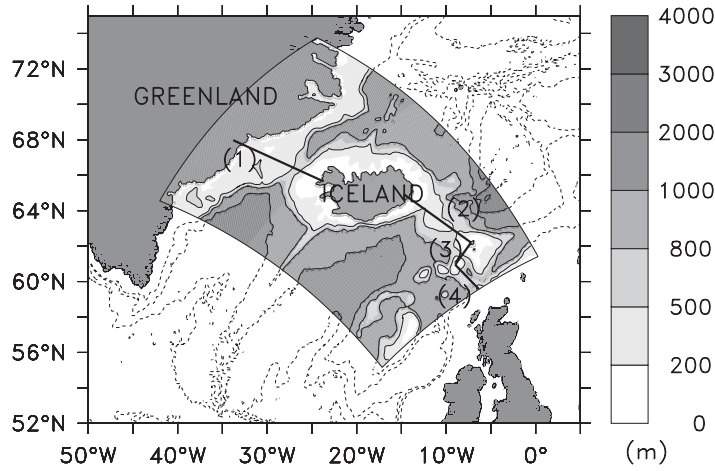


Figure 2.3.: Bathymetry (in meters) for the Greenland-Scotland Ridge experiment. The shading in the outlined box marks the model area. The sections labeled with 1 to 4 give the location of cross-sections used in later parts of this study, (1) is the Denmark Strait, (2) is the Iceland-Faroe Ridge, (3) is the Faroe Bank Channel and (4) is the Wyville-Thomson Ridge.

ROMS 2.1 is set-up with 30 σ -layers in the vertical, with higher resolution in bottom and surface layers. The resolution in the top 200 m is approximately uniform over the model domain ($tcline=200$ m). The minimum depth is set to be 100 m as in the previous model set-up. In the horizontal, the average resolution is 6 km on a rotated grid. The general set-up, as given in Table 2.2, is quite close to the DSO model, therefore only the main differences are described below.

Instead of two-water masses as before, realistic profiles representing the average conditions north and south of the ridge are used as in *Biastoch et al. [2003]*. These profiles are restored at the northern and southern boundary in 55 km wide nudging zones on a time-scale of 5 days at the boundary increasing to 60 days towards the interior domain. The eastern and western boundaries are closed and treated as walls. This can be justified since the western boundary coincides with Greenland and the eastern boundary is approximately the Scottish shelf, which is considered not to be important here. Density is calculated from potential temperature and salinity using the non-linear equation of state. Wind forcing

Model parameters	Values
Horizontal grid	6 km x 6 km resolution 42° W - 0° W and 55° N - 74° N
Boundary conditions	Closed boundaries at walls No-slip boundary conditions Temperature and salinity restoring zones at the northern and southern boundary
Vertical grid	30 σ -layers, higher resolution at bottom and surface Stretching parameter: $\theta_s = 5$, $\theta_b = 0.4$, $t_{\text{cline}} = 200$ m
Timestepping	$\Delta t_I = 144$ s, $N_{\text{fast}} = 20$
Advection scheme	Third-order upstream bias horizontal advection for momentum and tracers Fourth-order Akima vertical tracer advection Parabolic spline vertical reconstruction
Viscosity	No explicit
Diffusion	No explicit
Bottom drag	Quadratic law with $C_D = 1 \cdot 10^{-3}$
Pressure gradient	Splines density Jacobian
Mixing	Tracer and momentum mixing along S-surfaces
Interior mixing	LMD interior mixing (convective mixing due to shear instability, convective nonlocal transport, diffusivity due to shear instability) KPP surface boundary layer mixing
Equation of state	Non-linear [UNESCO, 1981]
Forcing	No surface heat flux Wind stress as body force

Table 2.2.: Configuration of ROMS 2.1 for the regional Greenland-Scotland Ridge model.

is applied at the surface, which for present-day conditions is the winter mean field of the European Centre for Medium range Weather Forecasts (ECMWF) reanalysis [Gibson *et al.*, 1997]. These forcing data were recommended by Myers [2003] based on an intercomparison of wind stress climatologies for the sub-polar North Atlantic. For a better representation of the surface mixed layer and the interior mixing the stability dependent BVF mixing scheme is replaced by the vertical mixing parameterization of Large *et al.* [1994]. The pressure gradient scheme with a density Jacobian scheme using monotonized cubic polynomials fits [Shchepetkin and McWilliams, 2003] was shown to yield slightly better results [Ezer *et al.*, 2002] with steep topography than the quadratic polynomial fit used before.

2.2.3. The northern North Atlantic regional ocean model

The circulation in the northern North Atlantic was assessed with ROMS 2.0 on a grid which spans from 42° N to 76° N and from 51° W to 11° E (Figure 2.4). The resolution is approximately 0.5° (50 km in zonal and meridional direction) and hence more closely to that of global climate models, which commonly have a resolution of about 2°. The bathymetry was designed to represent the sill depth realistically but the overall representation of the GSR is limited due to pressure gradient constraints on the maximum topographic slope. The general model set-up is given in Table 2.3 and is quite similar to the previous experiments, changes from that are described below.

The model is initialised with conditions from the World Ocean Atlas 2001 [Conkright *et al.*, 2003] and is restored to these values at the northern and southern boundary. It is integrated

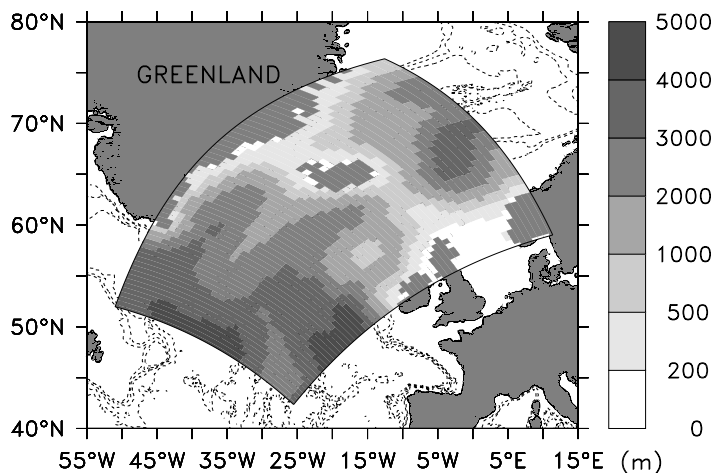


Figure 2.4.: Bathymetry (in meters) for the northern North Atlantic experiment. The shaded area represents the model domain.

Model parameters	Values
Horizontal grid	54 km x 52 km resolution Area: 42° N - 76° N and 51° W - 11 ° E
Boundary conditions	Closed boundaries at walls No-slip boundary conditions Temperature and salinity restoring zones at the northern and southern boundary
Vertical grid	25 σ -layers, higher resolution at surface and bottom Stretching parameter: $\theta_s = 3$, $\theta_b = 0.9$, $t_{cline} = 100$ m
Timestepping	$\Delta t_1 = 3600$ s, $N_{fast} = 40$
Advection scheme (momentum and tracer)	Third-order upstream bias horizontal advection Fourth-order centered vertical advection Parabolic spline vertical reconstruction
Viscosity	No explicit
Diffusion	No explicit
Bottom drag	Linear drag law with $C_D = 3 \cdot 10^{-4}$ m/s
Pressure gradient	Splines density Jacobian
Mixing	Tracer and momentum mixing along S-surfaces
Interior mixing	LMD interior mixing (convective mixing due to shear instability, convective nonlocal transport, diffusivity due to shear instability) KPP surface boundary layer mixing
Equation of state	Non-linear [UNESCO, 1981]
Forcing	Surface net heat and freshwater flux with a weak surface salinity restoring Wind stress forcing

Table 2.3.: Configuration of ROMS 2.0 for the North Atlantic model.

for 10 years starting from rest with the full seasonal cycle included. Temperature and salinity are nudged in 300 km wide restoring zones, on a time-scale of 5 days at the outer boundary increasing to 60 days towards the interior. Wind forcing, surface heat and freshwater fluxes are derived from the COADS climatology [DaSilva *et al.*, 1994]. In addition the heat flux sensitivity to sea surface temperature is utilized to represent the feedback between model SST and surface heat flux. The sea-surface salinity is relaxed to climatological values on a time-scale of 60 days.

2.3. The University of Victoria Earth System Coupled Model (UVic ESCM)

As global climate model the University of Victoria Earth System Climate Model (UVic ESCM) is used, which has been successfully employed for plaeoclimate studies before [e.g. Schmittner *et al.*, 2002b; Saenko *et al.*, 2003; Cottet-Puinel *et al.*, 2004]. A detailed model description and an evaluation for the present climate is given in Weaver *et al.* [2001]. A brief outline of the model design is given below.

All experiments presented in this study use version 2.6 of the UVIC ESCM consisting of coupled oceanic, sea-ice and atmospheric components. The ocean model is a fully three-dimensional general circulation model based on MOM 2.2 [Pacanowski *et al.*, 1993] with a resolution of 3.6° in zonal and 1.8° in meridional direction. In the vertical, the grid is discretized into 19 levels with varying resolution ranging from 50 m near the surface to 500 m at the sea floor. A convective adjustment scheme removes vertical instabilities through instantaneous mixing. Diffusion is on a rotated mixing tensor along isopycnals and the mixing effect of mesoscale eddies is parameterised with the Gent-McWilliams scheme [Gent and McWilliams, 1990] for eddy induced tracer transport. The formation of intermediate water is substantially improved through a parameterization for brine rejection during sea-ice formation. The sea-ice component is a thermodynamic/dynamic sea ice model with elastic-viscous plastic dynamics [Bitz *et al.*, 2001]. An energy balance model is used as reduced complexity atmosphere to reduce the computational costs. Atmospheric heat transport is parameterised through diffusion and moisture is transported through advection and diffusion. The advective transport is derived from the prescribed wind field. Precipitation occurs when the relative humidity exceeds 85%; the water vapor - planetary long wave feedback is parameterised. The seasonal cycle is resolved while the model does not exert higher frequency and interannual variability. One of the virtues of the coupled model is that no explicit flux adjustment is needed to keep the present-day simulations stable.

The flow across the sills of the Greenland-Scotland Ridge cannot be realistically modelled due to the coarse resolution of the model. For an improved northward transport of heat in the North Atlantic in the standard configuration the Denmark Strait was artificially made deeper and Iceland was removed. In the reference experiment presented here the GSR has been included again with a realistic sill depth of 600 m for the Denmark Strait and 1012 m for the Faroe-Shetland Channel (Figure 2.5).

The model is commonly integrated for 2000 years to be able to make a statistical analysis of the equilibrium state. Standard parameters used in all experiments include a CO₂ concentration of 365 ppm and present-day orbital parameters. Vertical diffusivities range from $6 \cdot 10^{-5} \text{ m}^2/\text{s}$ near the surface to $1.6 \cdot 10^{-4} \text{ m}^2/\text{s}$ at 5000 m depth. Diffusion is on isopycnals with $2 \cdot 10^3 \text{ m}^2/\text{s}$. The ocean model time step is 1125 s for barotropic and baroclinic velocities

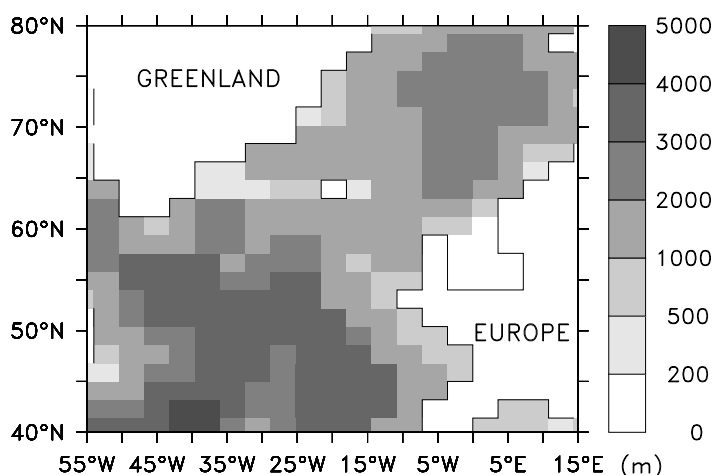


Figure 2.5.: Bathymetry (in meters) of the global model for the area of the northern North Atlantic. Only the ocean bathymetry is shown and land areas are masked white.

and 30 h for tracers. The atmospheric time step is 15 h. Due to the simplified atmosphere in comparison with coupled atmosphere-ocean general circulation models a much faster computation is feasible. In the standard set-up it takes about 215 hours on a single processor 2 GHz Xeon processor for 2000 years of integration. Thus the sensitivity associated to a particular process can be assessed for a wide parameter range.

2.4. Data processing

The common data format used with both models is the netCDF format [R*ew et al.*, 1996], which was found to be very comfortable to handle. Even though it can be an issue to create the appropriate files, large amounts of data can be handled very easily.

The initial quality control and much of the further analysis was done by using Ferret as a tool [H*ankin et al.*, 2000]. Originally intended for meteorologic applications it has become much more versatile during the course of this study, especially concerning the graphical output. The main pre- and post-processing tools for use with ROMS is intended to be Matlab. Only recently a whole suite of routines including an easy to use graphical front end was released as Roms_tools [P*enven*, 2003].

3. A process modelling study of the Denmark Strait overflow

The Denmark Strait overflow (DSO) is strongly influenced by topography and rotation. Such flows through straits and sills are known to be limited by hydraulic constraints [Pratt and Lundberg, 1991]. The criticality of the flow and hence whether it is hydraulically controlled can be determined by carrying out model experiments. Käse and Oschlies [2000] could corroborate the theory of Whitehead *et al.* [1974] with numerical modelling experiments and showed that the flow through Denmark Strait is critically controlled by the sill. Moreover, numerical models play an important role in assessing the overflow dynamics, ranging from transport estimates to the decent and modification of the overflow plume.

The main focus of this chapter will be on the description of the Denmark Strait as hydraulically controlled flow. Theoretical estimates and numerical model results are compared over a broad parameter range. After an introduction into the basics of rotating hydraulics, recent findings will be discussed. In the first part of this chapter, the theoretical approaches of Whitehead *et al.* [1974], Nikolopoulos *et al.* [2003] and Helfrich and Pratt [2003] are compared with model results from a high-resolution ocean general circulation model of the Denmark Strait. From this comparison the main mechanisms of the buoyancy driven overflow can be identified and the sensitivities to different parameters e.g. sill depth and density contrast can be evaluated. In the second part of this chapter, the sensitivity of the model for different initial conditions and forcing mechanisms, especially the effect of a continuous stratification will be investigated and compared to theoretical estimates. Thus, the fidelity of hydraulic theory is tested for the interpretation of oceanographic data and for applications concerning paleoceanographic questions of the Denmark Strait.

The main questions addressed in this chapter are:

- Is the description of the Denmark Strait overflow as two-layer system valid?
- What is the parameter sensitivity of the modelled overflow for changes in the dense water reservoir, e.g. a freshening of the Nordic Seas?
- Is the overflow hydraulically controlled for conditions different from today's?
- What kind of theories on hydraulic limitations do exist and which one describes the modelled overflow best?
- What will be the effect of a more realistic hydrographic structure compared to the two-layer process model?
- Do changes in the upstream circulation have an effect on the overflow? What about a barotropic net flow?

3.1. Theory of rotating hydraulics

3.1.1. Hydraulically controlled flow

Sidewall and bottom constrictions of the Denmark Strait show only small depth variations in along-stream direction, which allows to describe the transport using rotating hydraulic laws as in *Whitehead et al.* [1974] (WLK in the following). Furthermore, the hydrography may be simplified since the observed density structure [*Conkright et al.*, 2003] resembles that of a two-layer system of cool and dense Denmark Strait overflow Water (DSOW) underneath warm and less dense Modified North Atlantic Water (MNAW) [*Hansen and Østerhus*, 2000]. The reference system for investigating rotating hydraulics is commonly chosen as a rotating channel aligned in the y -direction with cross-channel direction x and bottom topography t positive upwards. To describe the overflow in a simple way, commonly a $1\frac{1}{2}$ -layer model is used, which consists of an upper, stagnant layer of density ρ and a lower, moving layer of density $\rho + \Delta\rho$ (Figure 3.1). The height of the interface above the sill is denoted as effective

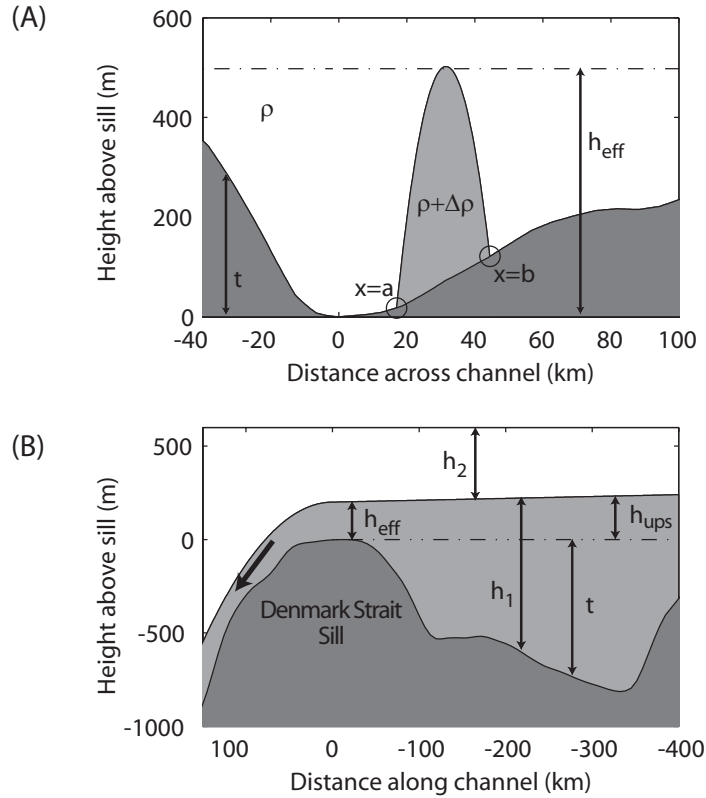


Figure 3.1.: Schematic representation of the Denmark Strait overflow with an idealised cross-stream section (A) as viewed from the North with Iceland to the left and Greenland to the right (adopted from *Nikolopoulos et al.* [2003]). The parabolic shape represents the overflow with the intersection points a and b of the parabola with the topography and with $t(a)$ and $t(b)$ as the corresponding height above sill level. The along-stream structure of the overflow is shown in the lower figure (B), with the characteristic asymmetric shape relative to the sill mentioned before. The effective height of the overflow layer above the sill is denoted as h_{eff} and the upstream height as h_{ups} .

height (h_{eff}), the depth of the lower layer is h_1 , the upper layer is h_2 and the topography is described by t , hence $h_1 = h_{\text{eff}} - t$ (Figure 3.1).

There are three different ways in which hydraulic control can be expressed, either in terms of information propagation by waves [Pratt and Lundberg, 1991], as maximisation (minimisation) of volume transport [Killworth, 1992a] or as asymmetries caused by hydraulic transitions [Armi, 1986]. Here hydraulic control is regarded to be important, if the information-propagation speed is comparable to the fluid advection speed u . The observed density and velocity structure at Denmark Strait [Girton *et al.*, 2001] suggests that this applies to the transport of DSOW (Section 3.2.3).

The governing equations in the following analysis are the momentum equation and the equation of continuity. Due to the slow variation in topography in along channel direction (y -axis) this velocity component (v) of the overflow can be seen as in geostrophic balance. For such semi-geostrophic flows the horizontal momentum equation is

$$u \frac{\partial v}{\partial x} + v \frac{\partial v}{\partial y} + fu = -g' \frac{\partial h_1}{\partial y}, \quad (3.1)$$

$$fv = g' \frac{\partial h_1}{\partial x}, \quad (3.2)$$

where u and v are the velocities in x and y direction, respectively, and f is the Coriolis parameter. The equation of continuity is taken as

$$\frac{\partial}{\partial x}(uh_1) + \frac{\partial}{\partial y}(vh_1) = 0. \quad (3.3)$$

From this, the conservation of potential vorticity G can be shown and yields

$$\frac{\zeta + f}{h_1} = G(\psi), \quad (3.4)$$

where $\zeta = \frac{\partial v}{\partial x} - \frac{\partial u}{\partial y}$ is the relative vorticity and ψ is the transport stream function, defined as

$$\frac{\partial \psi}{\partial x} = v, \quad \frac{\partial \psi}{\partial y} = -u. \quad (3.5)$$

This forms the basis for the following theoretical approaches which then mainly differ in the treatment of potential vorticity conservation (3.4). At first the classical WLK model is outlined, followed by a review of two recently published studies. *Borenäs and Nikolopoulos* [2000] extended the WLK approach to take into account for realistic bathymetry, which has already been applied to the Denmark Strait by *Nikolopoulos et al.* [2003]. The study of *Helfrich and Pratt* [2003] is essentially a revised version of the Gill model [Gill, 1977] for a finite upstream basin with emphasis on the upstream conditions.

3.1.2. The Deep-Upstream-Basin

At first, consider the case in which the upstream basin is deep and upstream velocities are negligible. Then the Bernoulli potential $B(\psi)$ is that of the upstream basin $B(\psi) = g' h_{\text{ups}}$, which is here assumed to be constant along a streamline and hence $\frac{dB}{d\psi} = G(\psi) = 0$. With little curvature in y , and therefore $\frac{\partial v}{\partial y} = 0$, this simplifies Equation (3.1) and one yields

$$\frac{\partial v}{\partial x} = -f. \quad (3.6)$$

Now the transport is calculated by integrating $v \cdot h_{\text{eff}}$ from the right hand wall to the intersection point a . The maximum value of h_{eff} is the undisturbed upstream value h_{ups} , which results in a maximum transport Q_{WLK} as

$$Q_{\text{WLK}} = \frac{1}{2} \frac{g' h_{\text{ups}}^2}{f}. \quad (3.7)$$

Note that assuming $G(\psi)$ is small is often referred to as zero-potential vorticity assumption but as *Pratt and Lundberg* [1991] have pointed out it should be referred to as deep-upstream-basin case, since $G(\psi)$ is dimensional and can be quite large even though the ratio of $h_{\text{eff}}/h_{\text{ups}} \ll 1$. With respect to experiments discussed below it should be pointed out that in case of a dynamically wide sill which is a sill width comparable to the Rossby radius one should use the following relation instead

$$Q_{\text{WLK-WIDE}} = \frac{2^{3/2}}{3} L \sqrt{g'} \left(h_{\text{ups}} - \frac{f^2 L^2}{8 g'} \right)^{3/2}, \quad (3.8)$$

where L is the width of the channel.

3.1.3. Extension to realistic topography

One basic simplification of the WLK model is that it assumes a rectangular cross-section. This restriction was lifted by *Borenäs and Nikolopoulos* [2000] who developed a method for calculating the maximum deep-water flow for real topography. From geostrophy (Equation (3.1)) and potential vorticity conservation (Equation (3.4)) an equation for the interface height h_{eff} can be obtained as

$$h_{\text{eff}} = -\frac{f^2 x^2}{2g'} + \frac{fV_0}{g'} x + h_0.$$

This equation contains two constants, the interface height h_0 and the velocity V_0 at $x = 0$, which can be determined from the intersection points a and b and their according depth $t(a)$ and $t(b)$ (Figure 3.1 A). To determine possible combinations of a and b consider the case of zero potential vorticity where the Bernoulli function is a constant $B(\psi) = g' h_{\text{ups}}$ for all streamlines and can then be written as

$$B(\psi) = \frac{1}{2} v^2 + g' h_{\text{eff}} = g' h_{\text{ups}}. \quad (3.9)$$

Now h_0 and V_0 can be combined using the Bernoulli equation. From this one obtains a defining function for the constants a and b and all combinations of intersection points a and b can be found. Due to the approximately parabolic cross-sectional topography of Denmark Strait permissible pairs of points a and b correspond to an inverse parabola shifted along the x -axis. *Nikolopoulos et al.* [2003] suggest two different transport limitations. The shape of h_{eff} implies return flow where the slope of h_{eff} is negative ($\frac{\partial h_{\text{eff}}}{\partial x} < 0$) and as *Killworth* [1994] has pointed out this area of reversed flow should be replaced with a stagnant water mass to evaluate maximum transport bounds. Therefore, two different transports are calculated, the transport including the recirculation area (Q_{NB}) by evaluating the integral from a to b

and the transport without recirculation (Q_{NB2}) by integrating from a to the maximum of h_{eff} , which yields:

$$\begin{aligned} Q_{\text{NB}} &= \int_a^b v h_1 dx \\ &= \frac{g'}{2f} [h_{\text{eff}}^2(b) - h_{\text{eff}}^2(a)] - \int_a^b vt dx, \end{aligned} \quad (3.10)$$

$$\begin{aligned} Q_{\text{NB2}} &= \int_a^{h_{\text{max}}} v h_1 dx \\ &= \frac{g'}{2f} [h_{\text{max}}^2 - h_{\text{eff}}^2(a)] - \int_a^{h_{\text{max}}} vt dx. \end{aligned} \quad (3.11)$$

Nikolopoulos et al. [2003] applied this approach to the Denmark Strait to obtain transport estimates from hydrographic sections. Moreover, the authors extended the zero potential vorticity assumption to the case of constant potential vorticity but found that the changes due to a finite value of potential vorticity are small and therefore only the zero potential vorticity case will be considered here.

3.1.4. Finite basin and upstream influence

The coupling of the upstream circulation with the hydraulic flow within the strait has been examined by *Helfrich and Pratt* [2003]. They extended the classical Gill model [*Gill*, 1977] to a finite upstream basin and compared it with results from a $1^{1/2}$ -layer reduced gravity model for different source types (inflow and downwelling) and the influence of the upstream circulation on the modelled transport across the sill. Using the basin potential vorticity budget (see Section 3.3.1) to investigate the basin-strait coupling *Pratt and Llewellyn-Smith* [1997] found that for interior downwelling an anticyclonic boundary current will develop, whereas a boundary inflow will split into two boundary currents. *Helfrich and Pratt* [2003] showed that their model correctly predicts the transport independent of the upstream circulation. The transport, as suggested in their model, can be calculated at the strait entrance region as:

$$Q = \frac{g'}{2f} (h_R^2 - h_L^2), \quad (3.12)$$

where h_R is the maximum and h_L is the minimum value of h_{eff} .

Q_{mo}	modelled transport
Q_{th}	theoretical transport
Q_{WLK}	from [<i>Whitehead et al.</i> , 1974]
Q_{WLK2}	same as Q_{WLK} but taken at the sill entrance
Q_{NB}	from <i>Nikolopoulos et al.</i> [2003]
Q_{NB2}	same as Q_{NB} but no recirculation
Q_{HPG}	from [<i>Helfrich and Pratt</i> , 2003], extended Gill model
Q_{p}	modelled transport (from passive tracer)
Q_{t}	modelled transport (from temperature)
Q_{td}	modelled transport (depth restricted, from temperature)

Table 3.1.: List of notations for different transport definitions.

3.2. Comparing model results and hydraulic transport estimates

3.2.1. Model validation

As model validation, the experiment which is most closely to present-day conditions (reservoir height of 480 m and a density contrast of $\Delta\rho = 0.48 \text{ kg/m}^3$) is compared to observations [Dickson and Brown, 1994; Girton *et al.*, 2001; Girton and Sanford, 2003]. The general model set-up is described in Section 2.2.1 and referred to as DS-Res-0ka. Even though the numerical model is simplified the main features from observations are reproduced. After the model is initialised (the dam break) a plume of cold water develops rapidly and flows southward, following the topography along the Greenland shelf break (Figure 3.2). After

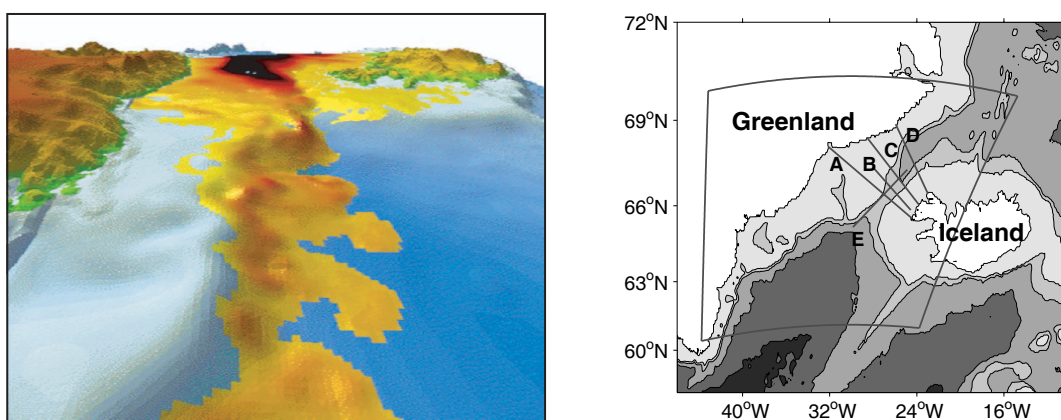


Figure 3.2.: *Left panel:* Snapshot of the descending overflow plume from the model experiment DS-Res-0ka. Greenland is at the left, Iceland at the right margin. The shading of the overflow indicates the overflow thickness, with increasing thickness as darker colours (yellow-red-black) and the full reservoir in the north.

Right panel: Bathymetry (in meters) of the Denmark Strait (shaded). The model area is outlined and the diagnostic cross-sections discussed in the text are labelled with A - E.

20 days the model is in quasi-steady state, that is the time averaged fields (dense water transport, effective height) are stationary and after 60 days the overflow plume reaches the southern boundary. Therefore, the model is integrated in all runs for 60 days, and days 20 to 60 are analysed. It is difficult to directly compare model and observations since both are snapshots of a non-stationary flow and mean observational sections are not readily available. As a first qualitative validation of the numerical model the simulated bottom density field is compared to that of observations from a Poseidon cruise [Käse *et al.*, 2003](Figure 3.3). Even though the two-layer model is a simplification of the the actual hydrography, one can clearly see the propagation of dense water from the northeast to the southwest with dilution effects due to entrainment on its way downstream as in the observations. The transport of overflow water is about 2.1 Sv in the model, as derived from the passive tracer, which is less than the estimates from observations of 2.7 Sv [Girton *et al.*, 2001] and 2.9 Sv [Dickson and Brown, 1994].

At the surface the DSO can be traced with remote sensing from eddies, which follow the path of the overflow at a translation speed of about 25 cm/s [Bruce, 1995], which agrees well

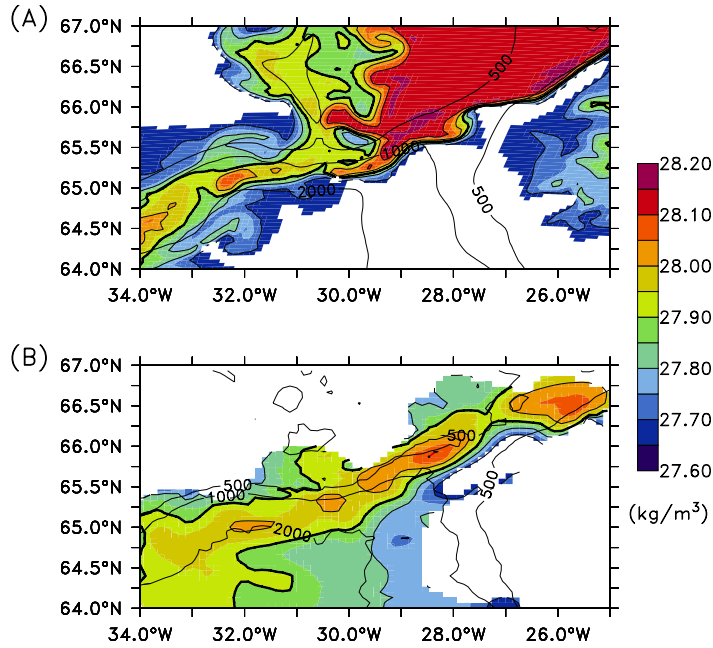


Figure 3.3.: Bottom density field (A) from a model snapshot ($h_{\text{eff}} = 480$ m, $\Delta\rho = 0.48$ kg/m³) and from observations (B) of Poseidon cruise of Käse *et al.* [2003]. The heavy line represents the 27.9 isopycnal and is included to outline the core of the overflow.

with the mean surface velocity along the overflow path in the model of 20 cm/s (not shown). The eddy generating process of vortex tube stretching is expected from observations [Krauss, 1996], modelling [Shi *et al.*, 2001] and is further discussed in data model comparisons by Krauss and Käse [1998] and Girton [2001].

With increasing distance from the sill, the overflow thickness reduces and the width increases due to mixing and entrainment of ambient warmer water (Figure 3.4 A). The plume structure resembles that of the observations (Figure 3.4 B) at least as far downstream as 64° N, further south the plume structure is influenced by the closed boundary.

From the models initial density distribution (Figure 3.5 A) a typical overflow plume structure develops very rapidly (< 15 days) (Figure 3.5 B) and the dense part of the modelled plume structure resembles the observations closely (Figure 3.5 C). Nevertheless, there are differences in the density field due to the missing background stratification of the model, which will be investigated in more detail in Section 3.3.2 where a model with background stratification is discussed. The modelled cross-stream density structure (Figure 3.6 A) is close to the observation (Figure 3.6 B) and the velocity field is as expected. It has a significant barotropic component of 70% at the sill, which agrees well with the study of Käse *et al.* [2003]. The relative importance of the barotropic fraction naturally depends on the upstream height h_{ups} and is decreasing with decreasing upstream height to values as low as 25% barotropic component for a 180 m reservoir of dense water. The non-barotropic part consists of an increase in velocity towards the bottom. The bottom velocity has a mean value of 25 cm/s in the model, reaching up to 60 cm/s at times. This is less than the observed maximum values of up to 1.3 m/s, but the overall velocity pattern agrees well with the observations.

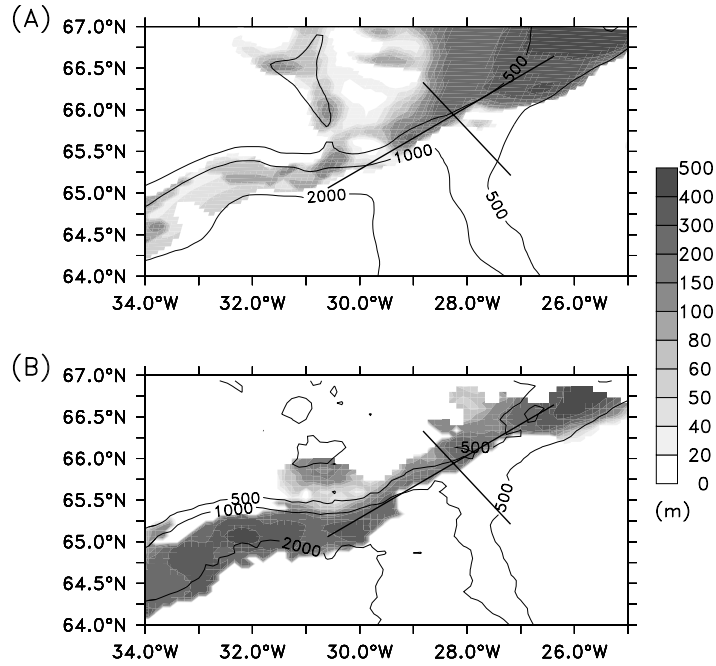


Figure 3.4.: Thickness of the overflow defined as the layer with a density $\sigma_\theta \geq 27.8$. In the upper figure (A) a snapshot (day 40) from a model run (with $h_{\text{eff}} = 480\text{ m}$ and $\Delta\rho = 0.48\text{ kg/m}^3$) is compared to observations (B) from a Poseidon cruise [Käse *et al.*, 2003]. The thick lines denote the location of the along- and cross-stream sections shown in Figure 3.6 and Figure 3.5, respectively.

3.2.2. Modelled dense water transport

The dense water transport through Denmark Strait is commonly defined as that of water colder than 2°C or from a density of $\sigma_\theta \geq 27.8$ and higher. Due to entrainment at the sill entrance this does not correctly measure the amount of dense water transported over the sill but is affected by recirculation. Therefore a passive tracer was used to calculate the transport in the model. Since the transport Q_p derived from the passive tracer does not rely on a temperature definition it results in a more accurate estimate of the mean transport. For comparison, the modelled transport is calculated across the sill at section A^1 using the passive tracer transport (Q_p), the transport of water colder than 2°C (Q_t) and the transport using the same temperature limitation but additionally restricted to that part of the sill where the depth exceeds 350 m (Q_{td}). All of these three definitions of volume transport show a quadratic relation with the upstream reservoir height h_{ups} . In Figure 3.7 this is represented as a linear regression of the volume transports and the squared upstream reservoir height (h_{ups}^2). For observations a passive tracer suitable for quantitative transport estimates is not available yet but it might be estimated in the future from analysing chlorofluorocarbon inventories [Smethie and Fine, 2001]. The results from the simulations suggest that the transport estimated with the temperature criterion (Q_t) underestimates the true overflow. Detailed inspection of the results indicate that the recirculation of cold water on the shelf and entrainment are responsible for this bias. It can be circumvented by restricting the calculations to a depth below 350 m. This is shown by Q_{td} which closely approximates the true transport Q_p .

¹The different section are shown in Figure 3.2.

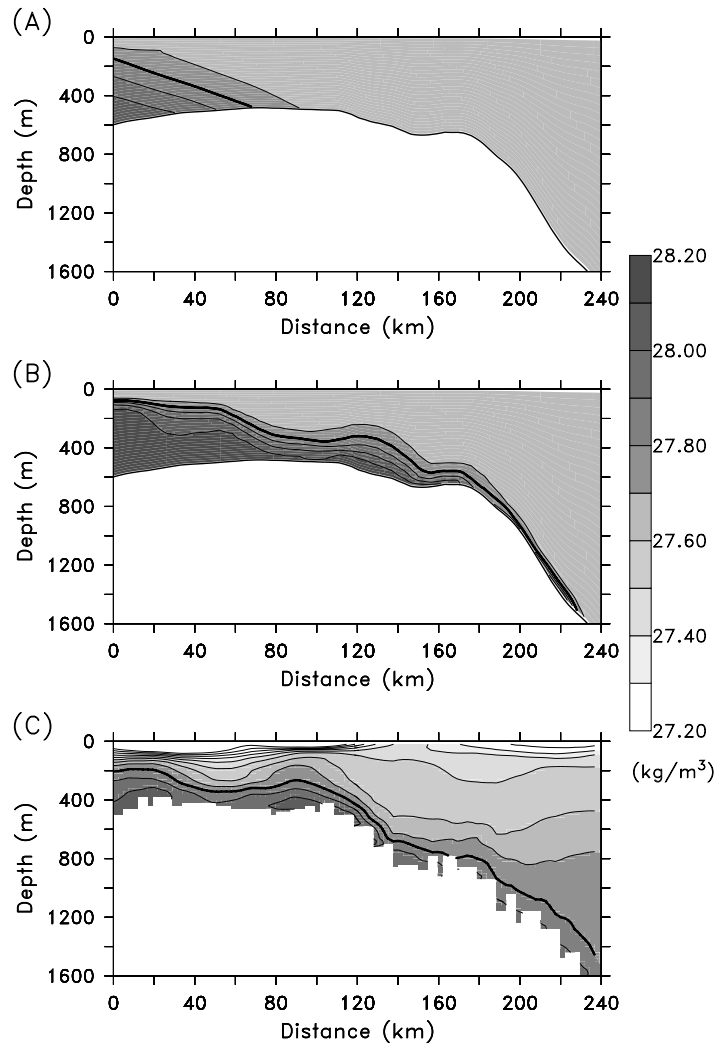


Figure 3.5.: Along-stream section (A) of the initial model conditions (day 1), a model snapshot (day 46) (B) and observations (C). The heavy line represents the overflow as defined from the 27.8 isopycnal.

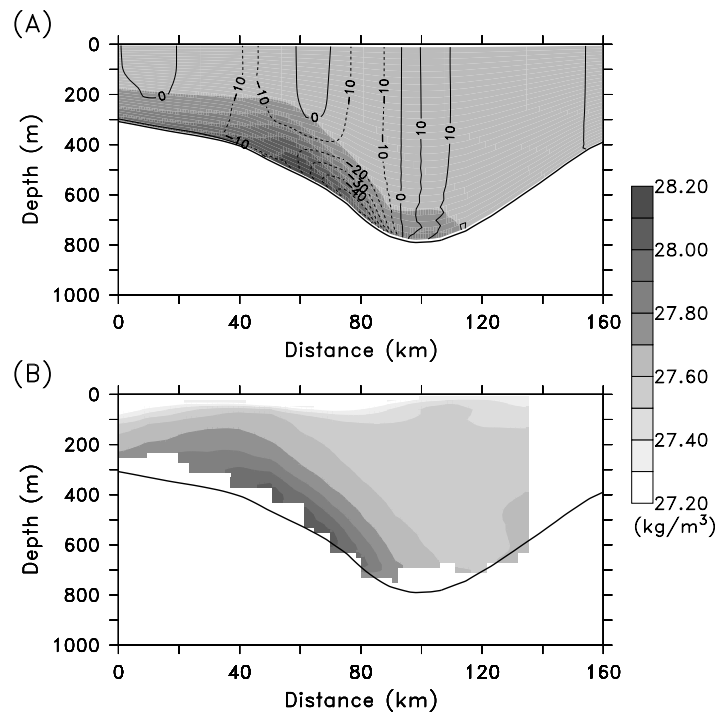


Figure 3.6.: Cross-stream section through Denmark Strait (Greenland to the left, Iceland to the right, E and W in the figure denote East and West, respectively) comparing modelled density (shaded) of a model snapshot (day 46) (A) and observations (B). The along-stream velocity (contours in cm/s , southward flow as dashed lines) is shown for the model only.

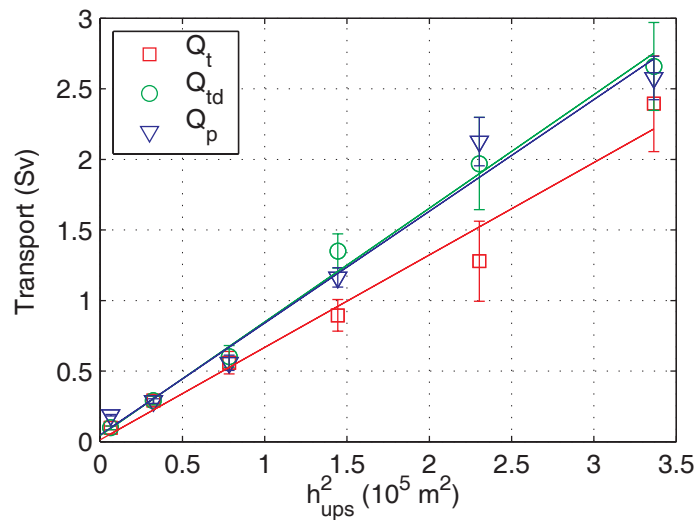


Figure 3.7.: Modelled transport as a function of squared upstream reservoir height h_{ups} for different transport definitions. Transport of water colder than 2°C (Q_t), transport for water colder than 2°C and a depth exceeding 350 m (Q_{td}) and calculated from the passive tracer (Q_p).

3.2.3. Conditions for hydraulic control

The asymmetry of Bernoulli streamlines [Armi, 1986] of the flow through Denmark Strait suggests that it is hydraulically controlled. However, frictional effects could lead to a similar appearance without hydraulic control being active [Pratt, 1986]. Therefore it is essential to determine the criticality of the flow.

Critical state of flow In a non-rotating channel information propagates at gravity wave speed $c = \sqrt{g'h_1}$, which has to be compared to the fluid advection speed in order to assess whether the flow is hydraulically controlled or not. This can be best expressed in terms of the composite Froude number G , which was defined for a two-layer system by Armi [1986] as

$$G^2 = F_1^2 + F_2^2 - \frac{\Delta\rho}{\rho} F_1^2 F_2^2, \quad (3.13)$$

with $F_i^2 = v_i^2/g'h_i$ as the Froude number of a single layer. For small density contrasts Equation (3.13) reduces to

$$G^2 = F_1^2 + F_2^2. \quad (3.14)$$

A Froude number smaller than unity ($G < 1$) indicates that the flow is subcritical, if bigger than unity ($G > 1$) it is supercritical and if equal unity ($G = 1$) it is critical. Control points are such critical points where long-wave disturbances (gravity waves) travel neither upstream nor downstream. Unfortunately rotation is important for Denmark Strait and the simple non-rotating assessment of flow criticality cannot be assumed to be valid a priori. Therefore, the validity of the assumption that the composite Froude number is valid in case of rotation is assessed next.

Stern [1974] has shown the following requirement for critical conditions in rotating channel flow

$$\int_{-w/2}^{w/2} \frac{1}{hv^2} \left(1 - \frac{v^2}{g'h}\right) dx = 0, \quad (3.15)$$

here w is the width of the channel. For Denmark Strait the width was taken to be the distance between the 350 m isobath, which is consistent with the definition of the overflow transport Q_{td} . Following Pratt *et al.* [2000] a generalised Froude number F_S can be defined from this as

$$F_S^2 = \int_{-w/2}^{w/2} h^{-2} dx \int_{-w/2}^{w/2} (v^2 h)^{-1} dx. \quad (3.16)$$

A different approach is to define a semi-geostrophic Froude number F_d [Gill, 1977; Helfrich and Pratt, 2003] as

$$F_d^2 = \frac{q \left(\left(\frac{1}{2}(h_R - h_L)/T \right)^2 \right)}{\frac{1}{2}(h_R + h_L) \left[1 - T^2 \left(1 - q \frac{1}{2}(h_R + h_L) \right) \right]} \quad (3.17)$$

with $T = \tanh(q^{1/2}w/2)$, h_R and h_L being the interface depth at the right- and left-hand side, respectively, of the channel looking downstream. A comparison of the different Froude numbers (Figure 3.8) shows that the in non-rotating systems commonly used composite Froude number G is still meaningful even in the case of strong rotation.

As the Denmark Strait is wide compared to the internal Rossby radius R_d information will be transmitted via Kelvin waves along the boundary of the sill. Baroclinic Kelvin waves

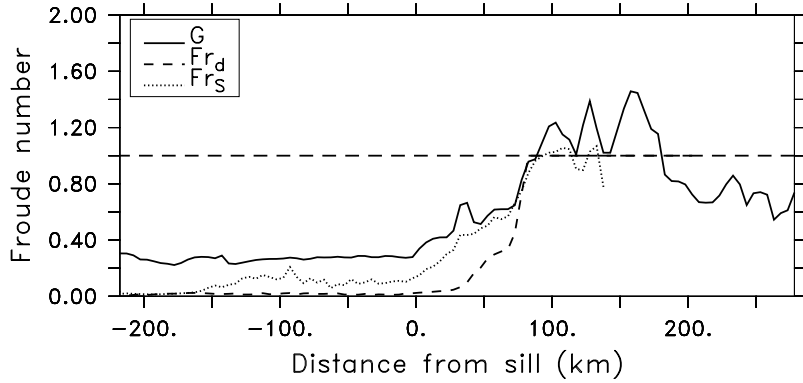


Figure 3.8.: Comparison of different Froude number definitions for experiment DS-Res-0ka representative for present-day. G is the composite, Fr_d is the semi-geostrophic and Fr_s is the Stern Froude number. Note that they all become unity at the same distance from the sill.

travel with a phase speed of internal gravity waves at $c = \sqrt{g' h_1}$ but decay away from the boundary at the scale of the deformation radius. With typical values for the Denmark Strait one yields as the gravity wave speed of $c = \sqrt{0.0033 \text{ ms}^{-2} \cdot 157 \text{ m}} = 0.72 \text{ m/s}$. Comparing this with the observed velocities at the sill of up to 1.3 m/s and a mean velocity of 0.56 m/s [Girton and Sanford, 2003] the fluid advection speed exceeds the gravity wave speed only at times. It does, however, exceed the gravity wave speed south of the sill where the advection speed increases. From Figure 3.8 one can conclude that the fluid advection speed is small when approaching the sill (negative distance) and therefore the Froude number is subcritical ($G < 1$), after passing through the sill the fluid accelerates when descending and reaches a critical Froude number ($G = 1$) at 80 km downstream. When descending further, the fluid can gain even more speed and gets supercritical at times.

Besides the effects of rotation, friction [Garrett and Gerdes, 2003] and stratification [Killworth, 1992a] will affect the overflow and alter the criterion for critical flow with no commonly agreed solution so far. Therefore, the following Froude number analysis is restricted to the definition given by Equation (3.14).

The position of the control point seems not to be dependent on the effective height (Figure 3.9 A). Even though the downstream behaviour is different, the flow reaches a critical state at roughly the same distance from the sill. In contrast to that, it slightly shifts for a changing density contrast (Figure 3.9 B) and moves towards the sill for an increasing density contrast. However, the main structure of generally critical conditions downstream (70-120 km) from the sill remains the same for all cases considered here.

Potential vorticity distribution The assumptions about the distribution of potential vorticity in the theoretical approaches of Whitehead *et al.* [1974] and Helfrich and Pratt [2003] outlined above (Section 3.1.2, Section 3.1.4) assume zero or constant potential vorticity, respectively. The assumption of zero potential vorticity as resulting from an infinite upstream basin depth does not hold for realistic topography with a maximum depth of 3000 m. However, as shown by Nikolopoulos *et al.* [2003] the extension to finite potential vorticity results in minor changes of the hydraulic limitation only. More important for the validity of the theoretical assumptions is that the potential vorticity has to remain constant along streamlines when approaching the control section (section where the flow is critical). As evident

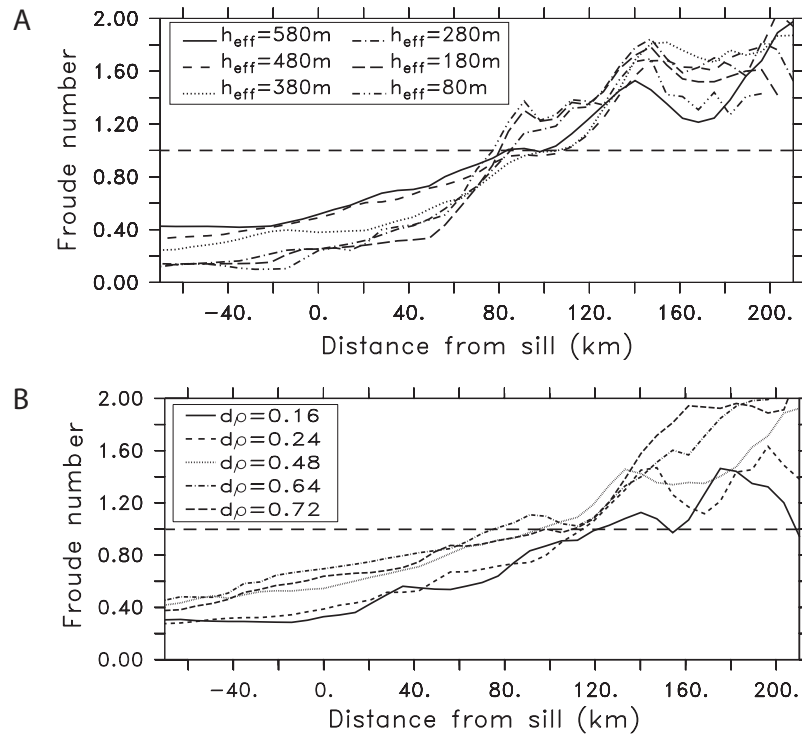


Figure 3.9.: Composite Froude number G for experiments with different effective height h_{eff} (A) and density contrast $d\rho$ (B). A Froude number equal to one (dashed line) represents critical conditions.

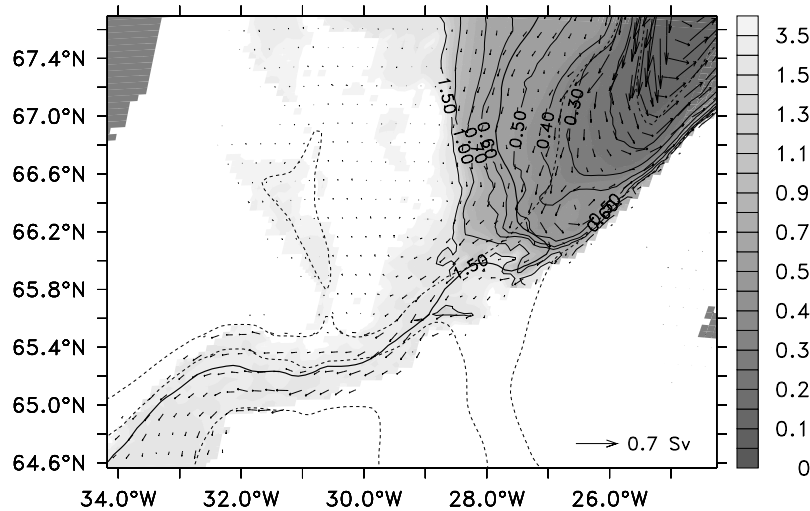


Figure 3.10.: Potential vorticity distribution at the sill (in $10^{-6}\text{m}^{-1}\text{s}^{-1}$) shaded and contoured. In addition the 500 m, 1000 m and 2000 m isobath are shown as dashed contours. The thick line is given as an example for the overflow streamlines derived from the 1.1 Sv mass transport stream-function.

from Figure 3.10 this assumption is only partly fulfilled. When following a streamline (thick, black line) the potential vorticity is in the range of $0.55 \cdot 10^{-5} \text{m}^{-1} \text{s}^{-1}$ when approaching the shallowest part of the sill at 66°N . After the fluid has moved through the shallowest section of the sill and separates from the left side of the channel (looking downstream), the potential vorticity is increasing significantly on the way downstream. When reaching the control section 80 km downstream of the sill, the potential vorticity has increased by a factor of three to $1.65 \cdot 10^{-5} \text{m}^{-1} \text{s}^{-1}$. This change can be understood when looking at the magnitude of the single terms contributing to the potential vorticity ($G = (\zeta + f)/h_1$). The Coriolis parameter f is nearly constant on the small spatial scales considered here. Moreover, f is relatively large compared to the relative vorticity ζ . Therefore one would need a strong increase of ζ to keep the potential vorticity constant for decreasing layer thickness h_1 . Frictional effects will counteract this increase of relative vorticity by dissipation of kinetic energy. These changes of the Bernoulli potential along a stream line, point out already that the underlying theory is idealised and one has to take into account for mechanisms not included. In the following it is assumed that the theory is valid in general but keeping in mind that the conversion of potential energy to kinetic energy is not complete, instead frictional effects will tend to decrease the overflow transport.

3.2.4. Dependence of transport on reservoir height

For hydraulically controlled flow the transport through the sill can be assessed from the upstream reservoir height and the density contrast alone. Here the three different methods explained above are used to determine the theoretical transports and compare them with the modelled transport Q_p . The model is analysed along the sections *A-D*, which are shown in Figure 3.2. For the deep-upstream basin approach two section are used, Q_{WLK2} is calculated at section *C* at the sill entrance, whereas for Q_{WLK} the upstream section *D* is taken. The extended Gill theory (Q_{HPG}) is employed at the sill entrance region along section *B*. At section *A*, the approach from Nikolopoulos is evaluated for both, the full width (Q_{NB}), and the part with a positive slope of the interface h_{eff} only (Q_{NB2}).

The upstream reservoir height is changed systematically from 80 m to 580 m in steps of 100 m to test the theoretical relations. As an example the transport time series for the case of $h_{\text{ups}} = 580 \text{ m}$ is shown in Figure 3.11. Q_{WLK} is clearly an upper bound on the

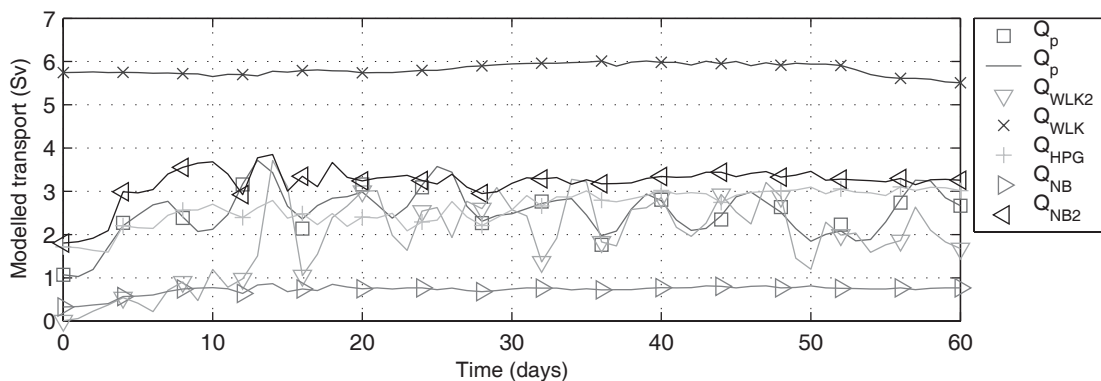


Figure 3.11.: Transport time series of the modelled transport (Q_p) and the theoretical transports ($Q_{\text{WLK2}}, Q_{\text{WLK}}, Q_{\text{HPG}}, Q_{\text{NB}}$ and Q_{NB2}) for an upstream height of $h_{\text{ups}} = 580 \text{ m}$. The modelled transport was smoothed with a 3 point running mean filter.

modelled transport, with very little variability in time. Q_{WLK} is already determined from the initial conditions for reservoir upstream height and density contrast. If the transport is evaluated closer to the sill ($Q_{\text{WLK}2}$) the values are initially similar to the upstream estimate but after the adjustment to steady state around day 15 it is close to the modelled transport. The variability is similar to that of the modelled transport, but the time mean is slightly underestimated. Q_{HPG} predicts transports close to that of the numerical model during the first 20 days but gradually increases towards too high values as the model approaches steady state. $Q_{\text{NB}2}$ overestimates the flow most of the time whereas Q_{NB} predicts too low values. Both estimates are only weakly variable and can be regarded as upper and lower bounds on the modelled transport.

Next, the time mean flow for different external conditions is considered by changing the reservoir height systematically. For each experiment the modelled transport is plotted versus the theoretical transport estimates (Figure 3.12), both are averaged over days 20 to 60. The variability is indicated by the error-bars indicating the 95% confidence bounds for the mean, which were calculated taking into account for the auto-correlation of the transport time series following *von Storch and Zwiers* [1999]. The relation between theoretical and modelled transports for different upstream heights, corroborates the results derived from the analysis of the time series of the individual experiment (Figure 3.11). The transport estimate from Q_{WLK} overestimates the modelled transport by far. $Q_{\text{NB}2}$ and Q_{HPG} slightly overestimate it and Q_{WLK} and Q_{NB} underestimate it. However, all of these theoretical predictions show a quadratic relationship of the transport and the dense water interface height and can be appropriately scaled to predict the correct time mean modelled transport (Table 3.2).

Theory	Exp./Theo.	Correl.coeff.
WLK	46 %	0.99
WLK2	111 %	1.00
NB	307 %	0.87
NB2	71 %	0.92
HPG	83 %	0.92

Table 3.2.: Overview of the ratio of experimental to theoretical transports.

3.2.5. Sensitivity to changes in density contrast

The hydraulically controlled transport through Denmark Strait depends not only on the effective height, but also on the density difference across the sill. A broad range of density contrasts from 0.16 to 0.72 kg/m³ has been employed, keeping the effective height fixed at 480 m. From this it is found that the assumed linear relation of density contrast and transport ($Q \propto \Delta\rho$) holds (Figure 3.13), and a linear regression yields a correlation coefficient of $R=0.94$. However, a non-linear component can be noticed, which might be due to changes in entrainment with varying temperature contrast. Nevertheless, when the observed transport of 2.7 Sv [*Girton et al.*, 2001] is placed at the observed density contrast of DSOW and MNAW of 0.48, it agrees well with the model.

The linear relationship of density contrast obtained from hydraulic theory emphasises the importance of observations of a reduced density or freshening of the overflows [*Dickson et al.*, 2002]. The model clearly shows that a decreased density contrast would lead to a reduced overflow strength and vice versa. This could in turn affect the overturning and heat transport in the North Atlantic [*Böning and Semtner*, 2001]. A freshening of the overflow

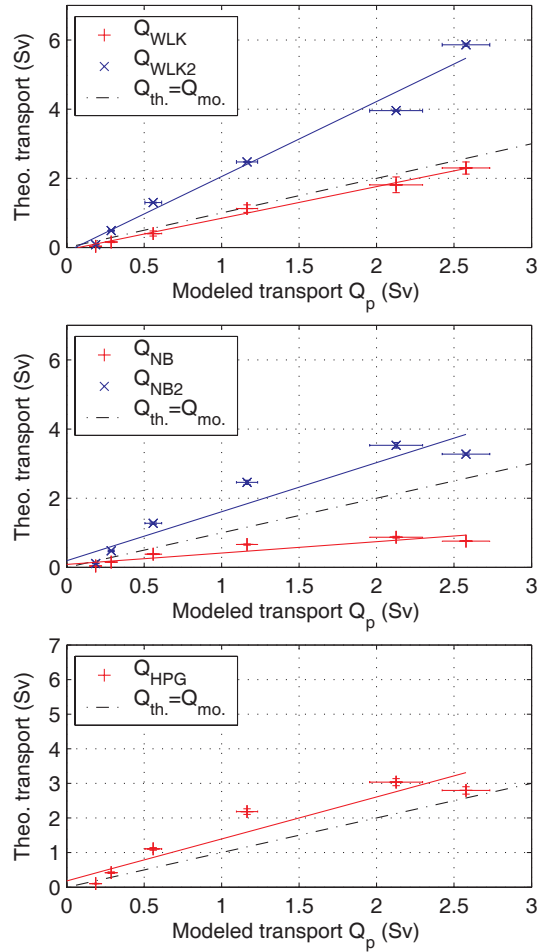


Figure 3.12.: Theoretical transport Q_{th} as function of modelled transport Q_{mo} . The theoretical transport is calculated comparing various approaches. In (A) it is derived from the classical WLK theory (Q_{WLK}) and from the proposed revised version Q_{WLK2} . In (B) the method from [Nikolopoulos et al., 2003] is used (Q_{NB} and Q_{NB2}) and in (C) the method from [Helfrich and Pratt, 2003] is applied (Q_{HPG}). The modelled transport has been obtained from the passive tracer in all cases Q_p . The error-bars indicate the 95% confidence bounds. The dash-dotted line represents the perfect theory $Q_{th} = Q_{mo}$.

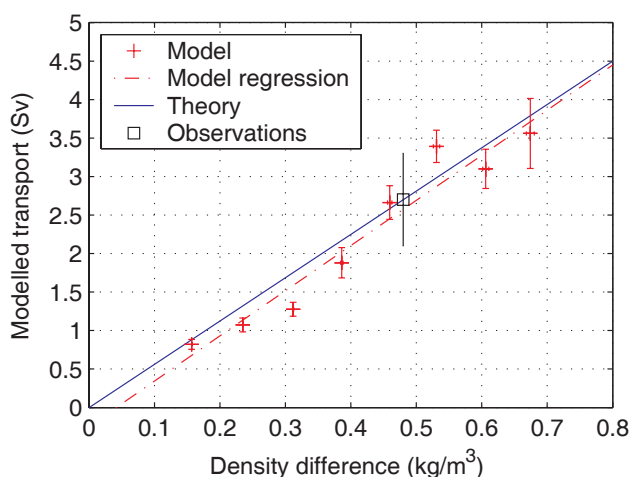


Figure 3.13.: Dense water transport as a function of cross-ridge density contrast. The density contrast was varied systematically and is compared with observations [Girton *et al.*, 2001].

and the corresponding salinity decrease is not explicitly included in the model but the resulting density change can be translated to an equivalent change in temperature. Dickson *et al.* [2002] found a decrease in salinity of the Denmark Strait overflow of 0.0415‰ in the last 30 years, which is equal to a density loss of approximately 0.033 kg/m^3 . As one can derive from Equation (3.7) this would cause a relative decrease in dense water transport from 2.9 Sv to 2.7 Sv by almost 7%.

3.2.6. Validation for different meridional positions

The Coriolis force depends on the lateral position of the sill and in order to generalise the theory for different meridional positions it has to be examined for different values of the Coriolis force. The minimum value for f is limited because the Rossby radius is changing with f and in the derivations above it is assumed that the sill width is large compared to the Rossby radius. Therefore, the variation of f are limited from 6.510^{-5} s^{-1} to 1.310^{-4} s^{-1} which relates to a meridional position of the sill from 26° N to 64° N . Figure 3.14 shows that a linear function of f^{-1} describes the transport for the parameter range considered here sufficiently well. A linear regression yields a correlation coefficient of $R=0.93$ and corroborates the assumed linear relationship. This generally confirms the validity of the hydraulic theory for different meridional positions of a sill structure like the Denmark Strait.

3.2.7. Comparison of different theoretical hydraulic limitations

The first approach was the deep-upstream basin estimate of Whitehead *et al.* [1974], which was found to be strongly depend on the position where it is taken. In order to evaluate how the theoretically predicted transport depends on the upstream site where it is evaluated, the theoretical estimate was calculated for all upstream points deeper than 350 m. This is represented as the ratio of modelled to theoretical transport in Figure 3.15. The transport estimate in the upstream area Q_{WLK} is constant over a broad spatial range with a ratio of modelled to theoretical transport of 46 %, which shows only little spatial variability and

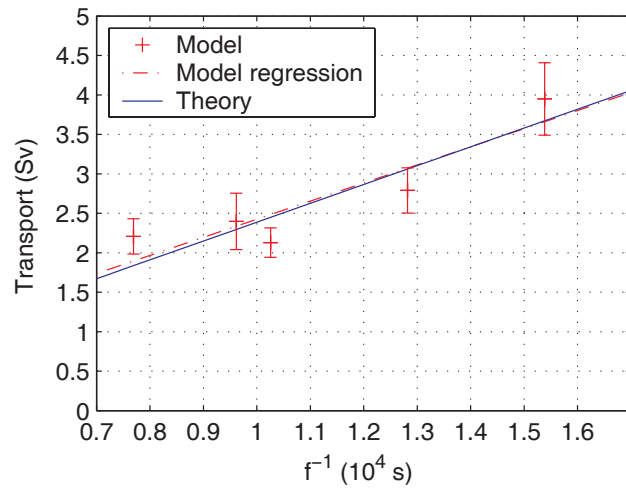


Figure 3.14.: Modelled DSO transport as a function of the inverse Coriolis parameter f^{-1} . The dash-dotted line was derived from a linear regression of the modelled data points, whereas the solid line has the theoretical slope of $1/f$ and only the intercept at the y-axis fitted to the data.

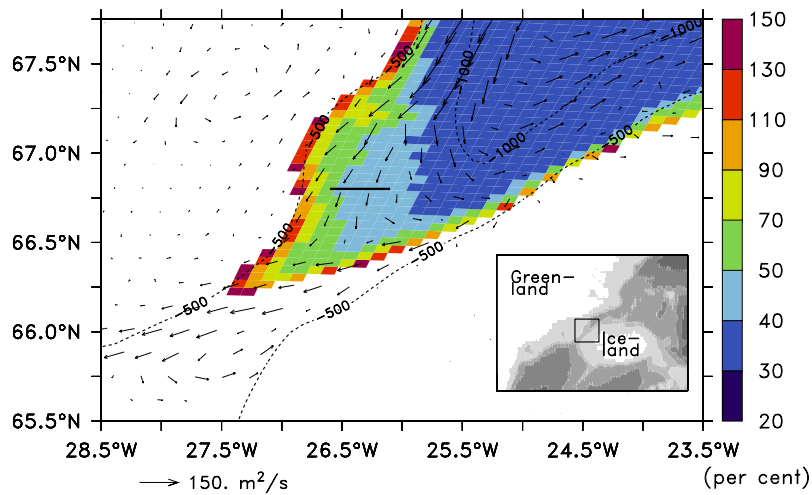


Figure 3.15.: Ratio of modelled transport Q_p to theoretical transport Q_{WLK} (in percent) calculated for the sill and upstream area. The vectors correspond to the vertically integrated velocity (in m^2/s) of water with $\sigma_\theta \geq 27.8$. The solid black line at a latitude of $66.8^\circ N$ depicts an ideal monitoring position of the upstream height as revealed from the model results.

provides a robust upper transport bound. Along the boundaries and at the sill the ratio is rapidly increasing. Close to the sill it is almost 100 % and the variability is close to that of the modelled transport (Figure 3.11). Q_{WLK2} was derived from the WLK theory but taken at the sill, it gave very convincing results when compared to model data but the method depends strongly on the hydrographic input data. As the interface height is determined in the sill entrance region it is variable in time. Due to the strong variability a snapshot of the density field as obtained from a field survey, might be very different from one taken a few days later. This difficulty could be overcome when the key regions identified from the model (Figure 3.15) are monitored with moorings. To shift the interest from the sill to the sill entrance region may help to solve problems with moorings directly at the Denmark Strait where high current velocities and heavy trawling lead to a very difficult environment for the equipment [Käse 2003, pers. comm.].

The overflow position at the sill, as determined from interface height and density contrast according to *Borenäs and Nikolopoulos* [2000], resembles the model results (Figure 3.16). The transport estimates from this method differ strongly depending if the reversed flow

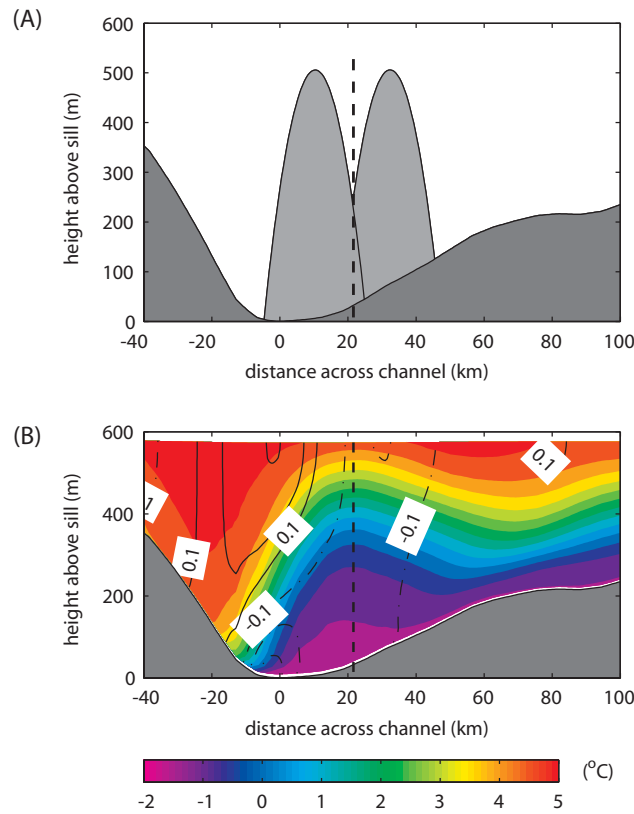


Figure 3.16.: Theoretical shape of the DSO (A) as determined from geostrophic relation [*Borenäs and Nikolopoulos, 2000*]. The left profile in the upper figure corresponds to Q_{NB} and the right profile to Q_{NB2} . In (B) the model results averaged over days 51-61 are shown along section A, with temperature shaded and velocity contoured (negative contours indicate southward flow).

is taken into account (Q_{NB}) or taken as stagnant (Q_{NB2}). This ambiguity complicates the application to modern hydrographic sections. But it is potentially useful when the hydrography is not well known as for paleoceanographic questions. The overflow position

and shape are best described with a mean of the shapes associated with Q_{NB} and Q_{NB2} as seen for the transport estimates. The mean position of the overflow core in the model coincides with the mean position from the theory (dashed line in Figure 3.16).

Finally, Q_{HPG} which is estimated at the sill entrance region, combines the virtues of the WLK approach at the sill and upstream, because it rather closely predicts the transport but is less variable than Q_{WLK2} .

3.2.8. Limitations of the hydraulic theory

There are some aspects which are not considered in the experiments above. The effect of a wind driven barotropic component was not included due to the limited model domain which would prevent barotropic flow around Iceland. This will be discussed in a following chapter in connection with the Greenland-Scotland Ridge regional model (Chapter 5).

The fact that the modelled transport did not reach the hydraulic limitation can be attributed to the fact that friction is not considered in the hydraulic theory. Frictional effects diminish the available kinetic energy for the overflow thereby reducing the transport as it was found in the model. One expects that an increase of friction drives the flow towards criticality [Pratt, 1986]. Bottom friction was kept constant at the value optimal for the Denmark Strait of $C_D = 10^{-3}$ as found by Käse and Oschlies [2000]. The internal friction in stratified flows will increase the entrainment, as shown by Gerdes *et al.* [2002] entrainment from vertical mixing caused by internal friction will drive the flow to criticality in the same way as friction does. Mixing due to instabilities occurs mainly downstream of the sill but can take place directly at the sill at times. This effect is not accounted for in the hydraulic theory and will increase the uncertainty of the predicted transport bounds if weak, or could lead to the situation where the theory is not applicable any more. This will be the case if the amount of turbulent kinetic energy input within the strait is so strong that considerable vertical momentum flux occurs. That turbulent mixing does play a minor role for the Denmark Strait can be seen from a scale analysis following Hogg *et al.* [2001]. They examine the transition from flows dominated by turbulent mixing to the hydraulic limit depending on the $Gr_T A^2$ scale. Here Gr_T is the Grashof number $Gr_T = g' h_1^3 / K_v^2$, with K_v the turbulent eddy viscosity and A the height to length scale of the mixing zone. With typical values for the Denmark Strait of $A = 500 \text{ m} / 200 \text{ km}$ and $Gr_T = 4.8 \cdot 10^{-3} \text{ m/s}^2 \cdot (500 \text{ m})^3 / (10^{-2} \text{ m}^2/\text{s})^2$ one obtains a scale in the order of 10^7 . Based on their analysis this indicates that turbulent mixing is insignificant and accounts for less than 5% of the transport and supports the approach based on hydraulic dynamics.

3.3. Influence of boundary conditions

3.3.1. Sensitivity to the upstream circulation

If the transport is sensitive to changes in the upstream region, this might be a way how remote forcing, such as a changing wind stress curl for different NAO situations, could affect the overflow. The upstream circulation is in turn intimately linked to the source of the DSO. As discussed in Section 1, there is no agreement yet where these sources are. There are two opposing ideas of an origin either mainly from the East Greenland Current (EGC) [Rudels *et al.*, 2002] or from convection in the Iceland Sea [Jónsson and Valdimarsson, 2004]. Obviously the related upstream currents are different in each case, mainly cyclonic if fed

from the EGC and anti-cyclonic if originating from the Iceland Sea, and do have different effects on DSO properties.

From rotating hydraulic theory, it can be shown that the circulation upstream depends on how exactly the mass flux into the upstream basin is included. For a downwelling source in the interior the circulation is different compared to inflow conditions at the wall. This can be seen from integrating the potential vorticity budget along a closed contour C at the basin boundary [Helfrich and Pratt, 2003], which results in

$$\oint_C \zeta h \mathbf{v} \cdot \mathbf{n} ds = \oint_C (\mathbf{M} - r \mathbf{v}) \cdot \mathbf{t} ds. \quad (3.18)$$

Equation (3.18) can be understood as the balance between the net potential vorticity (ζ) normal (\mathbf{n}) to the boundary and the net tangential (\mathbf{t}) sum of the interlayer momentum flux (M) and friction ($\mathbf{D} = -r\mathbf{v}$). When taking into account for $M \ll D$ the interlayer momentum flux can be neglected. This simplifies Equation (3.18) and one finds that on average an anticyclonic circulation takes place for downwelling sources in the interior of the basin, because the only way for the system to lose potential vorticity now is through the strait. For a boundary inflow the current will split into two parts instead, with the ratio of the two parts depending on the relative position of source and strait. For an inflow opposite of the strait and a symmetrical basin the flow would be symmetrical, in the case of realistic topography the splitting will be asymmetrical.

One can think of five different test cases to investigate the upstream circulation, which differ on how exactly the overflowing water masses are replenished. This can be done as (1) an interior source applied to the horizontal momentum equations resembling an EGC origin, (2) a boundary inflow resembling an EGC origin, (3) a surface cooling which contributes to deep-water formation in the Iceland Sea, (4) an interior downwelling resembling local deep-water production or (5) no new deep-water at all (spin-down).

The upstream circulation for these experiments is expected to be different as seen from the discussion of Equation (3.18). These scenarios were investigated in a series of three different model experiments. From preliminary experiments it was found that the surface cooling is very closely approximated by the interior downwelling source using a vertical momentum source (case A henceforth). The second experiment is the case of no dense water sources (case B), which represents a spin-down of the Nordic Sea deep water production. Finally, the third experiment has a boundary inflow, which is quite well reflected by the horizontal momentum source and will be referred to as case C from now on.

The temporal evolution of the upstream circulation is shown in Figure 3.17. Comparing the three different experiments the first thing to notice is that the structure remains the same for all of them for approximately the first 10 days. It is exactly the expected structure for a dam break scenario. Kelvin waves propagate along the boundary and initiating the flow, which follows the lefthand wall, then separates from the wall and feeds the evolving overflow. After that initial phase the structure differs significantly. In case (A), with a vertical momentum source, the upstream structure does not change significantly in accordance with the experiments of Helfrich and Pratt [2003], the overflow is fed from a source at the lefthand side throughout the time. This is in contrast to case (C) where a horizontal momentum source has been implemented. There the upstream circulation evolves as cyclonic circulation with the source of the overflow shifted to the west and with significant recirculation in the interior. The spin-down experiment (B), without momentum source, is essentially similar to (C) but with a less pronounced shift to the west in the beginning,

which becomes more evident after day 35. Due to the decreasing volume flux the strong recirculation cell of case (C) is absent. It is noteworthy that the associated transports through

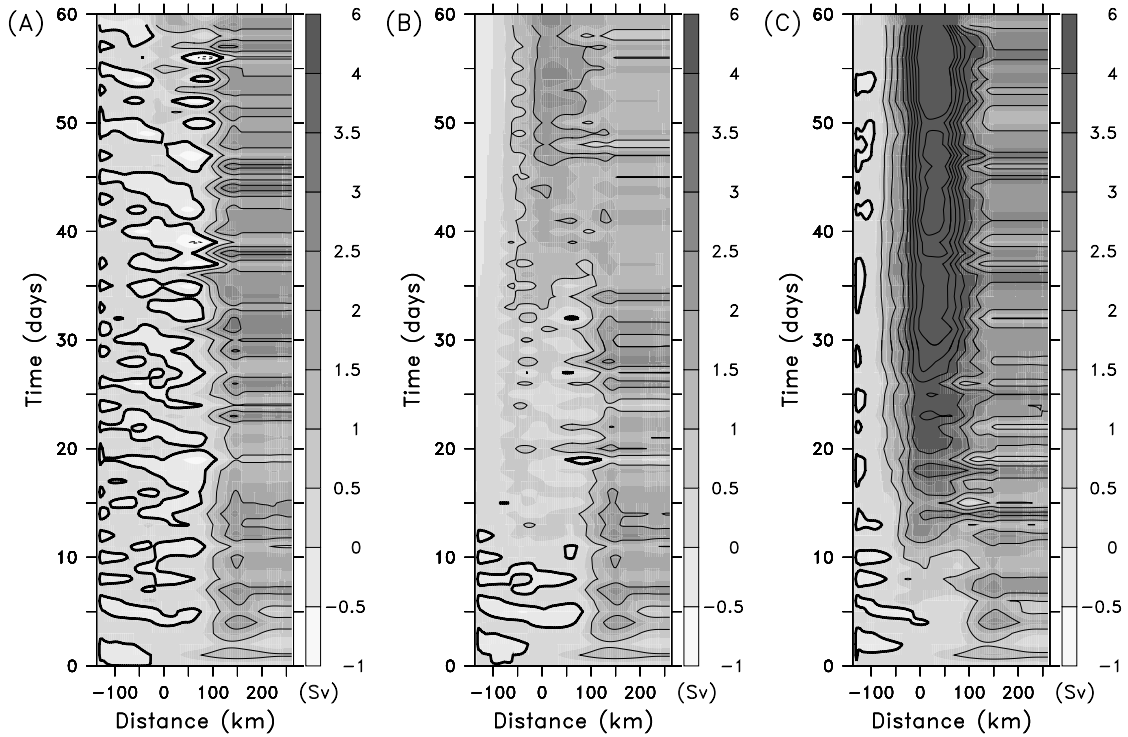


Figure 3.17.: Hovmöller diagram of the cumulative cold water transport (in Sverdrup) across section D for (A) vertical momentum source, (B) no momentum source and (C) the horizontal momentum source.

the section are surprisingly similar for (A) and (C) (Figure 3.18) with a difference for the mean transport of less than 0.2 Sv. The transport time series for the spin down experiment shows the expected decrease of transport with time due to the decreasing reservoir of cold water. The cyclonic circulation and associated left-hand side contribution of overflow water masses is in harmony with the theoretical basin potential vorticity integral (3.18) whereas the changed circulation for a different source needs further discussion.

Using the horizontal momentum source the change from anti-cyclonic to cyclonic upstream circulation after 12 days corresponds to the time interval Kelvin waves need to propagate from the momentum source to the upstream section. Therefore the anti-cyclonic mode can be regarded as natural upstream mode and the transition to cyclonic circulation is due to the momentum source. In so far the horizontal momentum corresponds to the boundary inflow concerning the potential vorticity budget and is therefore the appropriate setting to simulate an EGC fed overflow.

The different upstream circulations were more closely inspected by changing the source locations along the northern and western boundary (Figure 3.19). The different source locations caused changes in the upstream circulation. When positioned at the Greenland Shelf a strong boundary currents develops and the associated circulation is predominantly cyclonic whereas a gradual shift to the west causes the circulation to be anti-cyclonic. Much of this can be understood when considering the potential vorticity budget again. For a flat bottom the inflow will split as in *Helfrich and Pratt [2003]* but since there are topographic features

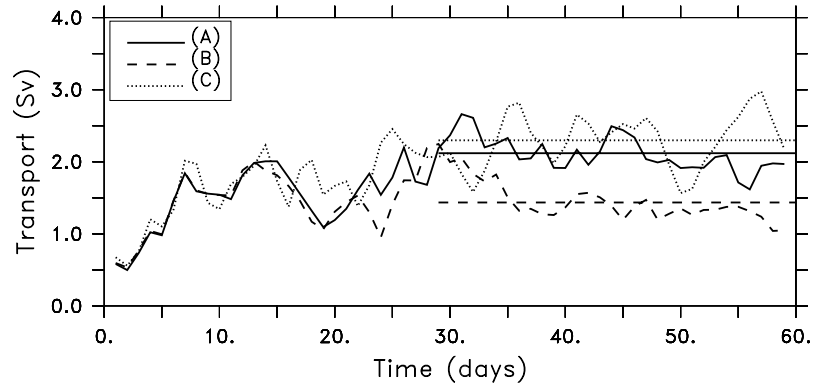


Figure 3.18.: Transport times series across section D for (A) vertical momentum source, (B) no momentum source and (C) horizontal momentum source. The transport corresponds to the cumulative sum from the Hovmöller diagrams shown in Figure 3.17.

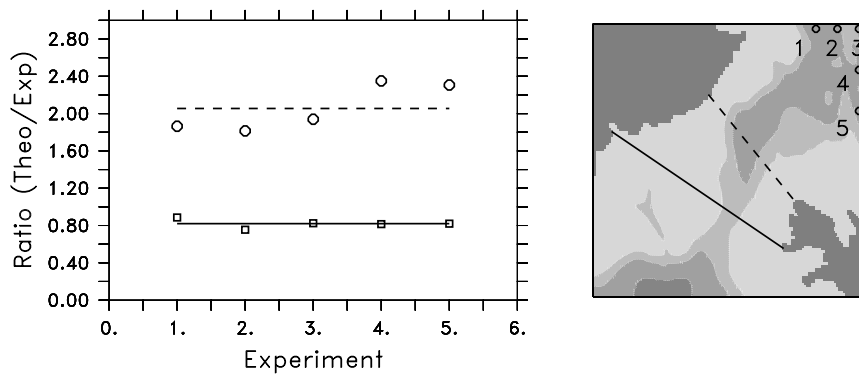


Figure 3.19.: Ratio of theoretical to modelled transport for different upstream source locations (corresponding to experiments 1-5, with experiment 1 furthest to the west). The dashed line represents the upstream estimates and the solid line corresponds to the sill estimate.

close to the inflow position, this will influence the circulation. The currents associated to sources 1 to 3 follow f/H contours along the western boundary. For source locations 4 and 5 the β -effect becomes important and due to the decreasing depth at the inflow location the current is deflected to the south.

Even though the initial conditions are the same in all experiments, the different upstream circulations result in different modelled transports and different theoretical transport estimates. This provides the ideal test for the transport estimate of *Helfrich and Pratt* [2003], which should be valid for different upstream circulations. Indeed it is found that the transport estimate taken close to the sill predicts the transport very closely, whereas the upstream estimates differ and are obviously influenced by the circulation (Figure 3.19).

The influence of the upstream circulation was assessed by comparing interior downwelling (vertical momentum source), boundary inflow (horizontal momentum source) and spindown experiments. The resulting equilibrium upstream circulation was found to be cyclonic for boundary inflow and spindown, whereas it was anti-cyclonic for the interior downwelling experiment. It might be tempting to relate these findings to a DSOW source either from the EGC [*Rudels et al.*, 2002] or the Iceland Sea [*Jónsson and Valdimarsson*, 2004]. Unfortunately, both observational based theories on the origin of DSOW are in harmony with the model results and none can be rejected. For interior downwelling in the Iceland Sea an anti-cyclonic circulation as found by *Jónsson and Valdimarsson* [2004] is expected and for a boundary inflow as with the EGC in *Rudels et al.* [2002] a cyclonic circulation would be regarded as likely.

3.3.2. Extension to continuous stratification

The approximation of the continuously stratified ocean as a two-layer system as done in the theories discussed before is obviously a simplification. The hydraulic properties of stratified fluids have been investigated by *Killworth* [1995, 1992b] and concerning the hydraulically controlled volume transport little difference can be expected compared to the two-layer model. The main differences will be downstream where entrainment and cyclogenesis become more important.

The effects of a continuous density stratification are assessed in sensitivity experiments with a continuous stratification. The general model set-up is described in Section 2.2.2, but the model grid is the high-resolution Denmark Strait bathymetry of experiment DS-Res-0ka described in Section 2.2.1. The density profiles are derived from the climatology of *Conkright et al.* [2003] and represent a mean of the regions north and south of the sill.

The modelled bottom density field (Figure 3.20) shows that the inclusion of background stratification leads to much more realistic results downstream. The lateral extent of the overflow plume (the heavy line denotes the 27.8 isopycnal) agrees well with observations [*Käse et al.*, 2003] as does the general density distribution.

The most prominent difference between the experiments with continuous stratification and without, is that the overflow signal can be better preserved downstream and comes closer to the observations when continuous background stratification is present (Figure 3.21), as compared to the two-layer set-up (Figure 3.5), which tends to entrain too strongly.

The cross-stream section does not show significant differences in the overflow plume but naturally reflects the ambient stratification better. The structure of the velocity field is similar with a barotropic component of the southward flow but increasing velocities towards the bottom (Figure 3.22).

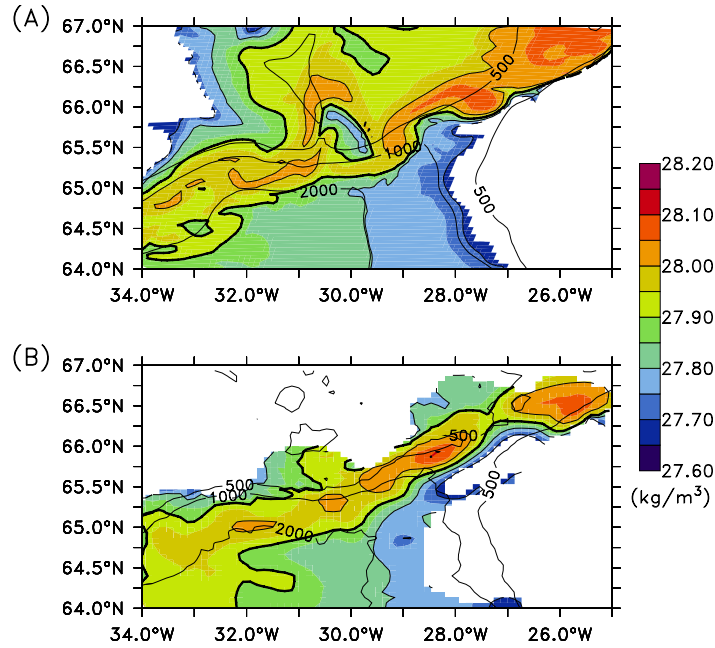


Figure 3.20.: Bottom density field from model snapshot (day 70) (A) and observations (B). The thick line represents the 27.9 isopycnal to outline the core of the overflow. Note that most of the shelf area was ice covered at the time of the observations and was not accessible.

The transport as function of contributing density classes (Figure 3.23) clearly shows the differences in transport of water mass properties. First, compare the two-layer case (DS-Res100-0ka) with the stratified profile (DS-Lev-0ka). The general shape of the two-layer set-up is limited by the densities of the two water masses (layer 1: 27.56 kg/m^3 and layer 2: 28.04 kg/m^3). In contrast to that the stratified case includes less dense fluids, which explains the more pronounced side lobe, and due to the employed density profiles the core of the overflow is not as dense as expected. In the two-layer case, the maximum transport of 1.6 Sv is found for the 27.8 kg/m^3 density class, whereas it is found in the 27.7 kg/m^3 density class at 1.9 Sv for the stratified case. The increased transport in DS-Lev-0ka is primarily due to the slightly higher effective height compared to DS-Res100-0ka. Note that the net transport including all density classes has to be zero in both cases since the domain just extends across the DS and is closed, hence neither barotropic net flow nor circulation around Iceland are included.

The transport of DSOW increases in along-stream direction from the point of overflow to the southern tip of Greenland from 2.9 Sv to 13.3 Sv [Dickson and Brown, 1994]. Warm water is entrained into the plume thereby reducing the average density of the plume but increasing the volume transport of water defined as DSOW from its density. This increase of DSOW due to entrainment of warmer water into the plume is more closely investigated below. The differences between the two-layer and the stratified case concerning the entrainment are more pronounced downstream of the sill (Figure 3.24). The rate of entrainment, as implied by the increasing transport with distance from the sill, for the stratified experiments (Figure 3.24 A) is in good agreement with observations Girton and Sanford [2003]. As seen before the core of the overflow at the sill is slightly less dense as observed but the rate of transport increase with distance from the sill is in agreement with the observed structure from the sill to

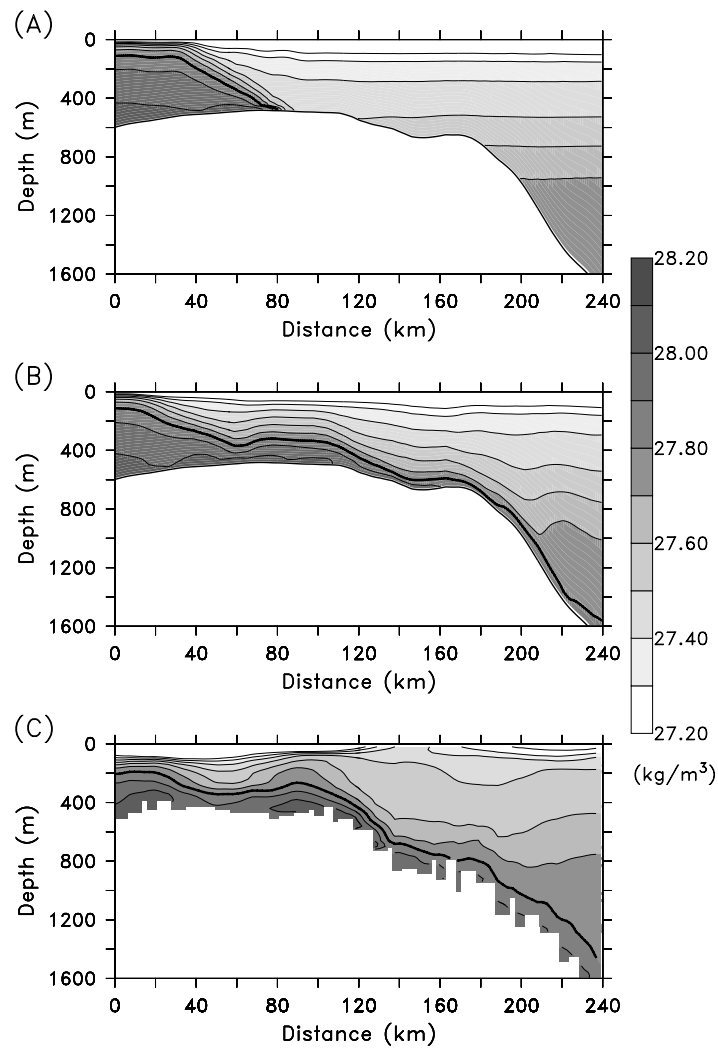


Figure 3.21.: Along-stream section of the initial model conditions (day 1) (A), a model snapshot (day 49) (B) and observations (C). The thick contour line represents the 27.8 isopycnal.

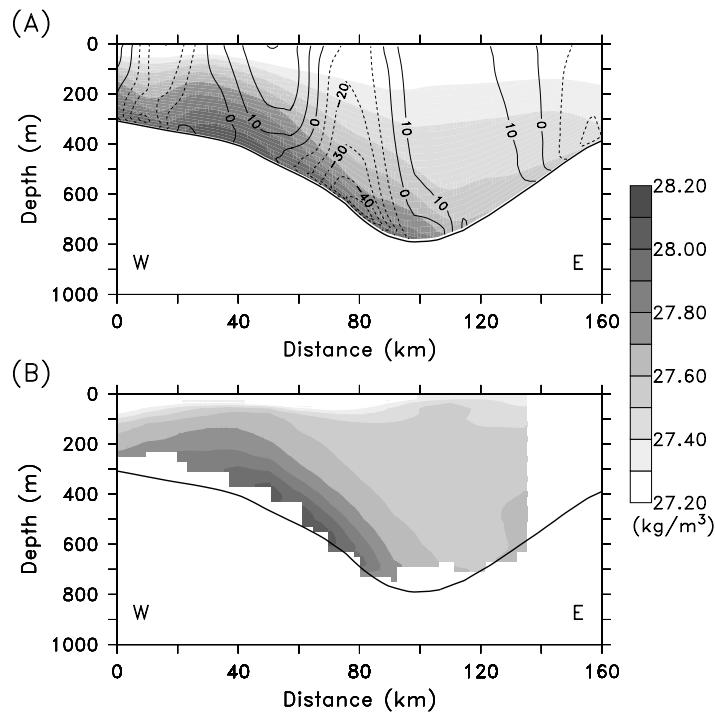


Figure 3.22.: East-West cross-stream density section (shaded) comparing a model snapshot (day 49) (A) and observations (B). The along-stream velocity (contours in cm/s, southward flow as dashed lines) is shown for the model only.

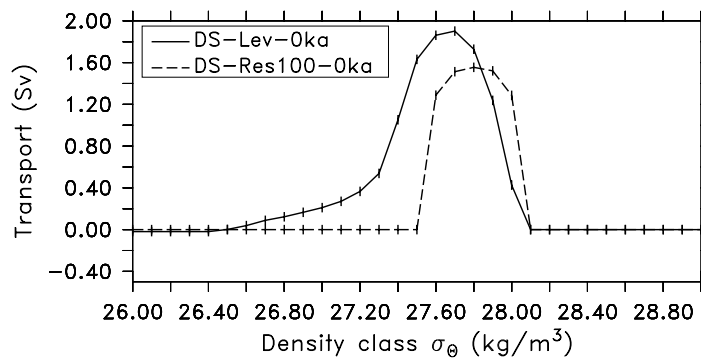


Figure 3.23.: The effect of stratification (solid line) on the cumulative transport in density classes as compared to the two-layer experiment (dashed line). The transport is integrated from high to low densities and the density class is associated to the lower bound. The midpoint of the 0.1 σ_θ wide density bins is indicated as vertical line.

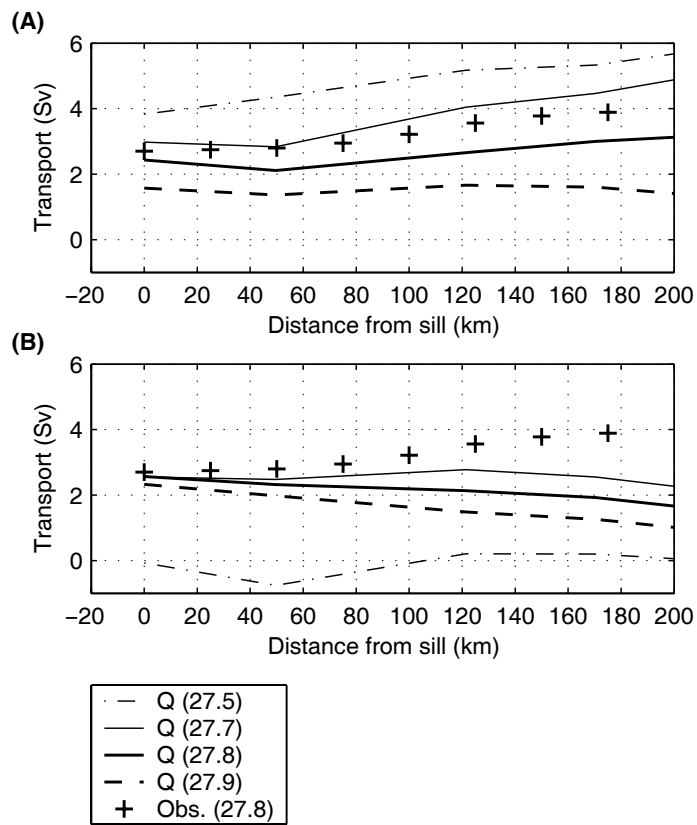


Figure 3.24.: Transport in four density classes (27.5, 27.7, 27.8 and 27.9 kg/m³) as function of along stream distance from the sill comparing the entrainment of the continuously stratified (A), the two-layer experiments (B) and observations [*Girton, 2001*]. Note that the transport of water with e.g. $\sigma_\theta \geq 27.8\text{kg/m}^3$ is denoted as $Q(27.8)$.

200 km downstream. Compared to that, the two-layer experiments (Figure 3.24 B) cannot reproduce the entrainment that well. Even though model and observations agree at the sill, the transport in the overflow density class $Q(27.8)$ is reduced from the sill onwards and moreover the transport of less dense water $Q(27.7)$ which is expected to increase, reduces after 100 km from the sill. This reduced transport of dense water can be explained in terms of a too high entrainment close to the sill. The density contrast between overflow plume and ambient water in the two-layer case is higher than for the stratified case, therefore the entrainment is too high and the associated entrainment stress affect the momentum balance of the overflow and drain too much of the available potential energy².

After these model experiments with two water masses, the set-up was refined to account for a more realistic stratification. The experiments with two average density profiles gave convincing results in terms of better representing the entrainment and down-stream behaviour. The question arises if the two-layer approach in the first place can capture the main effects of the descending overflow. The background stratification has an influence on the entrainment downstream but the effects on the dense water transport and descent of the plume close to the sill can be assumed to be small. As shown from the cross-sections investigating the entrainment downstream, the main features close to the sill are represented well and the transport estimates are not significantly altered. However, the experiments show that the background stratification is essential for a correct representation of entrainment and if missing the overflow transport downstream of the sill will be underestimated.

3.3.3. Comments on tides and barotropic forcing

The hydraulic transport estimates discussed so far, did not consider a barotropic background flow, such as the effect of tides or wind forcing. The effect of tides in the DS is small compared to the observed velocities accounting for 2-10% of the variance in the current meter velocities [Girton, 2001] but they probably alter the hydraulic constraints. From a global inverse model (TPX0.6) of barotropic ocean tides [Egbert and Erofeeva, 2002] one can derive that the largest tidal velocities are about 25 cm/s at the sill, decreasing north and south of it to less than 10 cm/s (Figure 3.25). In the model, tides are not accounted for and therefore it will be briefly discussed here what would be expected from tidal forcing. To estimate the effect of tides on the DSO the better known tidal influence on the exchange through the Strait of Gibraltar [Bryden *et al.*, 1994], where in contrast to the DS rotation does not play a role, is briefly reviewed. It is important to distinguish between volume and mass transport here. Even though the net volume transport can be small, the time averaged exchange can lead to an exchange of water masses which is due to the depth variations with tides of the isohaline. For inflow the interface depth is deeper than for outflow conditions and hence there is a net export of salt from the Mediterranean to the Atlantic. For the Denmark Strait the effect will be smaller due to a smaller tidal amplitude and a greater sill depth hence variations in interface depth are relatively small. It might be more important for the Iceland-Faroe Ridge where tidal currents are amplified by pulses of overflow water [Perkins *et al.*, 1994].

The effects of tides on the equations of hydraulics have been presented by Farmer and Armi [1986] for the Strait of Gibraltar. Even though the main ideas will be similar for the Denmark Strait it has to be kept in mind that their study can provide only limited

²See Girton and Sanford [2003] for an extensive discussion on the mechanisms of descent and entrainment for the DSO.

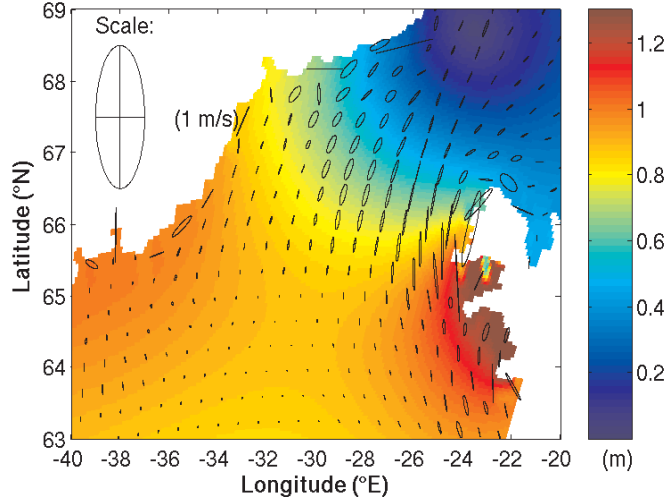


Figure 3.25.: Amplitude of M2 tide with tidal ellipse from inverse, tidal model [Egbert and Erofeeva, 2002]. The scale shown in the upper left corner corresponds to a maximum tidal velocity of 1 m/s of a tidal ellipse.

insight for the Denmark Strait since rotation is not taken into account. The main effect of the barotropic component will be to change the interface height and currents at the control section affecting the criticality of the flow. For very strong barotropic flow the two-layer system would eventually act as one moving layer, whereas for small to moderate forcing as considered here the effects will be small. The barotropic forcing creates a second “virtual” control point [Farmer and Armi, 1986], which is directed towards the origin of the barotropic current.

The time dependence of non-rotating barotropic exchange flows, which is important for tides, has been investigated in the study by Helfrich [1995]. There it was shown that the net flow depends on a dynamic length scale $\gamma = (g'H)^{1/2}T/L$ and a measure of the forcing strength $q_{b0} = u_{b0}/(g'H)^{1/2}$ with T , L and u_{b0} as the strait depth and length scales and the barotropic velocity, respectively. With typical values for the DSO one finds that hydraulic transport bounds do not change by more than 5%. Interestingly, the overflow through the Faroe Bank Channel for which the non-rotating theory is more applicable, is likely to be more affected due to higher barotropic tidal velocities. The effects of rotation will probably slightly change the results of Helfrich [1995] when applied to the DSO but the main features will remain. The maximum transport is reached for very slowly varying forcing ($\gamma \rightarrow \infty$) and the transport is minimised for rapidly varying forcing ($\gamma \rightarrow 0$). If the forcing q_{b0} grows stronger the transport bounds will increase. For the present-day situation the effects due to tides are assumed to be small, this was probably different for glacial and deglacial times (see Chapter 5). Besides the effect of tides as barotropic forcing, the overflow is influenced by wind stress. The mean wind stress produces a slowly varying forcing compared to tides ($\gamma \rightarrow \infty$) and hence the hydraulic transport is maximised.

Due to the lack of a theory for barotropic forcing under the influence of rotation, one could think of employing the non-rotating theory. This is done here and it is assumed that the total transport, as limited by hydraulic constraints, can be split into a barotropic and a baroclinic part. This idea was tested by estimating the influence of barotropic forcing in

a sensitivity experiment (DS-Lev-0ka-bar). A uniformly high background flow of 2.0 Sv was prescribed in a model which otherwise follows the set-up of experiment DS-Lev-0ka. The hydraulic estimate yields for the standard case 4 Sv and with barotropic net flow nearly the same value of 3.9 Sv, but the actual dense water transport increases from 1.7 Sv to 3.7 Sv. This apparent splitting of the total flow of 3.7 Sv into 1.7 Sv buoyancy driven and 2 Sv barotropic net flow gives first support for the assumption that the non-rotating theory is valid in case of rotation as well. It seems that the underlying mechanism is sufficiently well described simply as the sum of unforced flow and net barotropic flow. The implications of this finding will be further investigated in Section 5.1.2, examining the effects of changing wind stress.

An interesting implication which arises from the present-day tides in the DS, is that the faunal exchange not necessarily needs a net flow (DSOW or IC) but it is sufficient to have tidal fluctuation $\langle u'v' \rangle$. As explained for the Strait of Gibraltar mass transport does not necessarily needs volume transport and so biota from the north may be transported to the south by tidal currents and vice versa. This mechanism might not be that important for present-day but it certainly is more pronounced at times with a smaller DSO as in glacial times (Section 5.4).

3.4. Summary and conclusions

The transport of dense water across the Denmark Strait has been considered in a hydraulic framework comparing model experiments for a buoyancy driven overflow with realistic topography and existing theories. In dam break experiments with two water masses, it could be shown that the overflow reaches critical conditions and is likely to be hydraulically controlled. If this result is valid, changes in the Irminger Basin do not affect the overflow, whereas changes upstream of the control point set the overflow transport. Moreover, for hydraulically controlled flows an upper transport bound exists which can be used to predict the actual transport. Here the theories of *Whitehead et al.* [1974], *Nikolopoulos et al.* [2003] and *Helfrich and Pratt* [2003] were evaluated by using the results from a high-resolution model with respect to their skill in predicting the mean transport.

- The Denmark Strait overflow can be approximately described as a two-layer system. A detailed Froude number analysis has shown that it is likely to be limited by hydraulic constraints. The flow reaches critical conditions at about 80 km from the sill independent of reservoir height and only weakly variable with density contrast, getting closer to the sill for an increased density contrast.
- Three different hydraulic theories were applied to the DSO to predict the transport.
 - The estimate of *Whitehead et al.* [1974] is spatially variable and it imposes an upper bound on the transport if taken far upstream with a mean modelled transport of only about 46% of that predicted by hydraulic limitations. The variability is small far upstream and increases towards the sill, therefore the upstream value is even applicable when the reservoir height and density contrast are only approximately known as for paleoceanographic questions. If it is evaluated at the sill entrance region, the theoretical value reproduces the observed variability and magnitude well with a scaling factor of 1.1.

- The estimate Q_{NB2} from *Nikolopoulos et al.* [2003] defines an upper transport bound whereas Q_{NB} sets the lower transport bound. Both estimates are only weakly variable and seem to define the model transport extrema well. As a drawback, this leaves quite an uncertainty which makes this method less applicable for the interpretation of hydrographic sections.
- The approach of *Helfrich and Pratt* [2003] might be most useful for the interpretation of hydrographic sections and future monitoring arrays because Q_{HPG} yields good estimates of the mean transport with small variability only.
- The expected linear relation between transport and density contrast ($0.16 - 0.72 \text{ kg/m}^3$) holds. Therefore, a freshening of the Nordic Seas relative to the North Atlantic leads to a directly proportional decrease in overflow transport.
- The hydraulic theory was validated for different meridional positions ($>26^\circ \text{ N}$) of the Denmark Strait sill.
- The upstream circulation changes dependent on the boundary conditions. The circulation is cyclonic for a boundary inflow and anti-cyclonic for interior downwelling. Moreover, the DSO does depend on the upstream circulation, but the hydraulic estimate at the sill correctly predicts the transport.
- Taking into account for a realistic stratification can significantly improve the representation of entrainment, which is too strong in the two-layer model.
- Based on model experiments it is suggested that non-rotating treatment of barotropic flow can be applied to rotating hydraulics.

4. Paleoclimate sensitivity experiments for the last glacial-interglacial cycle

The validity of hydraulic theory as demonstrated for present-day conditions from numerical modelling results and observations [*Käse and Oeschies, 2000; Girton et al., 2001*] has given rise to the question as to whether this is also a useful tool for studying the Denmark Strait Overflow for different climatic conditions, e.g. the Last Glacial Maximum. In case of the Mediterranean outflow, hydraulic constraints on maximum overflow strength based on hydrography and bathymetry have been already successfully applied [*Matthiesen and Haines, 2003*]. That past climate changes have affected the Denmark Strait overflow (DSO) is commonly agreed. The leading questions in this chapter is how the different boundary conditions quantitatively changed the overflow. The effect of the DSO on climate in turn can only be indirectly assessed, since a regional model of the Denmark Strait only is used.

In order to assess the paleoclimatic sensitivity of the DSO for the last glacial-interglacial cycle, the theory of rotating hydraulics, introduced and validated for present-day in the previous chapter, is extended to paleoclimate conditions. The idealised and process oriented set-up allows to study the overflow mechanisms for different parameters, such as glacial-interglacial sea-level changes, isostatic movements and the associated gateway depth and aperture changes. The time slice specifically considered in the numerical experiments are present-day, Last Glacial Maximum (LGM) and Dansgaard-Oeschger (D/O) stadial-interstadials (30 ka BP, 70 ka BP). From this conclusions can be drawn how the DSO has responded to changes in the boundary conditions in the past and to some extent how the overflow has in turn affected climate.

The main objectives of this chapter are:

- to obtain hydraulic transport estimates for different bathymetries in order to determine changes in the overflow, which are only due to variations in gateway depth and aperture,
- to assess the influence of different density contrasts and stratifications representing present and past climatic conditions on the overflow,
- to investigate the existence of peculiarities of the overflow at times with pronounced D/O cyclicity,
- to determine changes in the path and descent of the overflow due to variations in the density contrast.

4.1. LGM sensitivity experiments

4.1.1. Effects of changes in gateway depth and aperture

The most pronounced changes in gateway depth and aperture are related to sea-level drops during glacial times. At the LGM the global sea-level was decreased by about 120 m [Clark and Mix, 2002]. In the DS the eustatic sea-level drop was partly compensated by downward isostatic movements [Fleming, 2004] due to the ice loading on Greenland and Iceland. In the sensitivity experiments presented here, two realistic LGM bathymetries (Figure 1.3 C, D) are considered, which cover the likely extremes for glacial times. In bathymetry LGM-1 there are only minor glaciations on the shelf whereas in bathymetry LGM-2 the shelf is fully glaciated. The glaciation of the shelf corresponds to a reduction in gateway aperture of 34% from 61 km² to 40 km². As experimental set-up in the sensitivity experiments investigating the two LGM bathymetries, the density contrast was taken as that of present-day. The effective height is that of the maximum dense water reservoir, hence dense water reaching the surface ($h_2=0$ m). Note that the effective height is reduced from 580 m to 509 m due to the combining effects of a lowered sea-level and isostatic movements.

The velocity structure obtained at the sill, shows the expected adjustment of the currents to the bathymetry. For a less glaciated shelf (Figure 4.1 A) the velocity field is close to that of present-day (Figure 3.6). The overflow dominates most of the sill (about 100 km), with an area of weak recirculation in the west and strong northward flow representing the Irminger Current in the east. In contrast to that, the narrow gateway (Figure 4.1 B) causes higher velocities for both overflow and recirculation area. From a hydraulic point of view this behaviour was expected. Initially, there is the same potential energy available in both cases but because the conversion to kinetic energy takes place over a larger region, if the shelf is ice free, the resulting velocities are smaller.

As one can see from the density contours, the isopycnals are generally deeper when the shelf is glaciated thus the dense water signal is less well preserved southwards. In the upstream area (not shown) the depth of the 27.8 isopycnal is the same for both cases but the deepening of the isopycnals on approaching the sill is faster when the shelf is glaciated. However, the general velocity structure seems to be maintained, the overflow is attached to the western side of the sill with recirculation areas east and west of it. However, the overflow is compressed in width and extends over 40 km only. In the upstream area the glaciers on the shelf force the current, when it approaches from the north-east, to recirculate which explains the strong recirculation and earlier deepening of the isopycnals.

The fraction of the dense water transport explained by the barotropic velocity does not show a consistent picture but varies between 50% to 70% in both cases, if the upstream height h_{ups} is varied. The critical point where the Froude number becomes equal to one slightly shifts away from the sill to a position 100 km downstream if the shelf is glaciated and slightly towards the sill (60 km) if not, but both values are close to the present-day value of 80 km (Figure 4.2).

Overall the differences of the overflow dynamics due to the glaciated sill do not seem to be significant. Therefore it is suggested that the hydraulic relation does not differ between the LGM scenarios, which is tested with sensitivity experiments in the same way as before for present-day conditions (Table 4.1). The upstream height is changed systematically and modelled and theoretical transports are compared. The aim is to establish a relation between transport Q and effective height h_{eff} for four bathymetries resembling the conditions at present-day (0 kaBP), glacial-interglacial transition (11.3 kaBP) and LGM (21.5 kaBP)

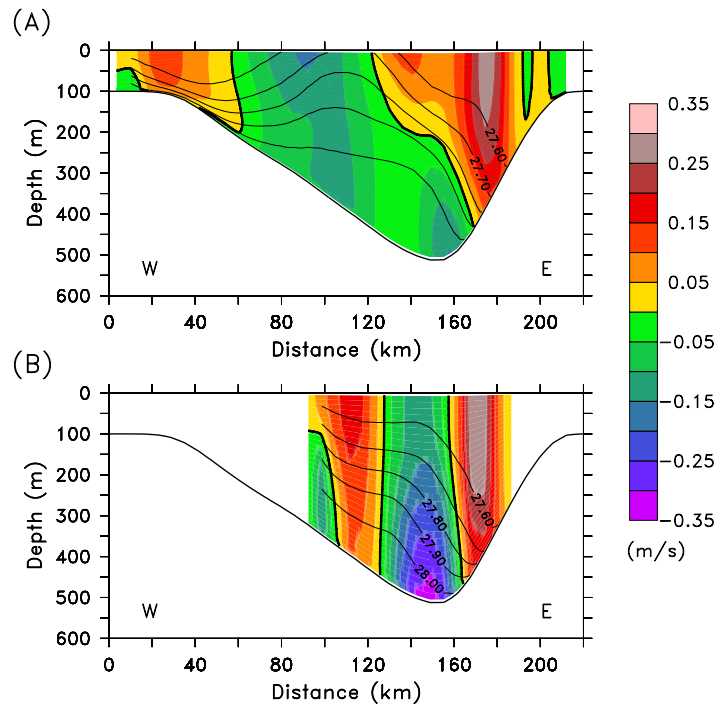


Figure 4.1.: East-west cross-stream section of the velocity field (shaded) and isopycnals (contour lines) for two different LGM bathymetries. The bathymetry from the isostatic rebound model (A) predicts a shallow sill but only minor glaciations on the shelf. Hence the overflow can extend over most of the sill. The modified version (B) takes into account for geological evidence of a glaciated shelf, which narrows the sill and causes higher velocities at the sill.

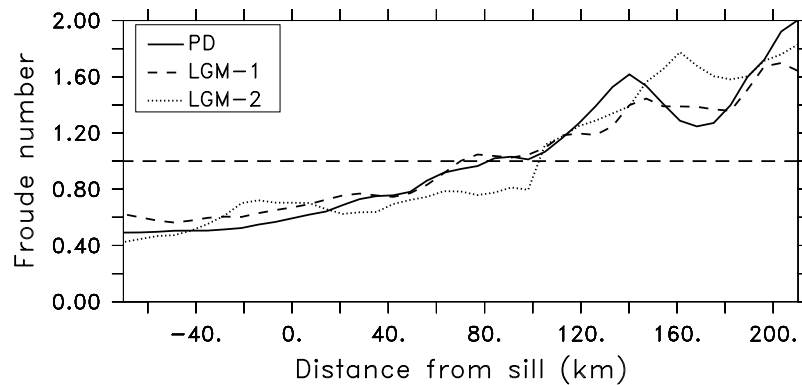


Figure 4.2.: Composite Froude number G for experiments with bathymetries representing conditions of present-day (PD), the LGM with minor glaciations on the shelf (LGM-1) and the LGM with a fully glaciated shelf (LGM-2). The intersection of the individual curves with the dashed line at a Froude number of one indicates where the flow gets critical and hence the location of the control section.

(Chapter 1). The thickness of the warm layer on top of the cold reservoir was changed systematically from 0 m to 500 m in steps of 100 m for all bathymetries.

Experiment	Time Slice	Bathymetry
DS-Res-0ka	modern	ETOPO5
DS-Res-10ka	deglacial	GFZ 11.3 ka BP
DS-Res-21ka1	LGM	GFZ 21.5 ka BP
DS-Res-21ka2		modified GFZ 21.5 ka BP

Table 4.1.: Overview of dam-break experiments for paleoclimate studies based on realistic bathymetries for modern (0 ka BP), deglacial (11.3 ka BP) and glacial conditions (21.5 ka BP).

The transport is plotted versus the squared effective height in order to better show the assumed quadratic relation ($Q \propto h_{\text{eff}}^2$). The theoretical transport is calculated from the mean upstream effective height and the mean density difference upstream versus downstream. As earlier pointed out (Section 3.2.4), this does not give the best fit to the transport in terms of reflecting variability, but provides a robust estimate of the mean transport. Using this simplified method has the advantage that it can provide a template to calculate transport from sparse information, such as the geological record, or coarse information, such as from global GCMs. From Figure 4.3 one can see that the theoretical transport provides the

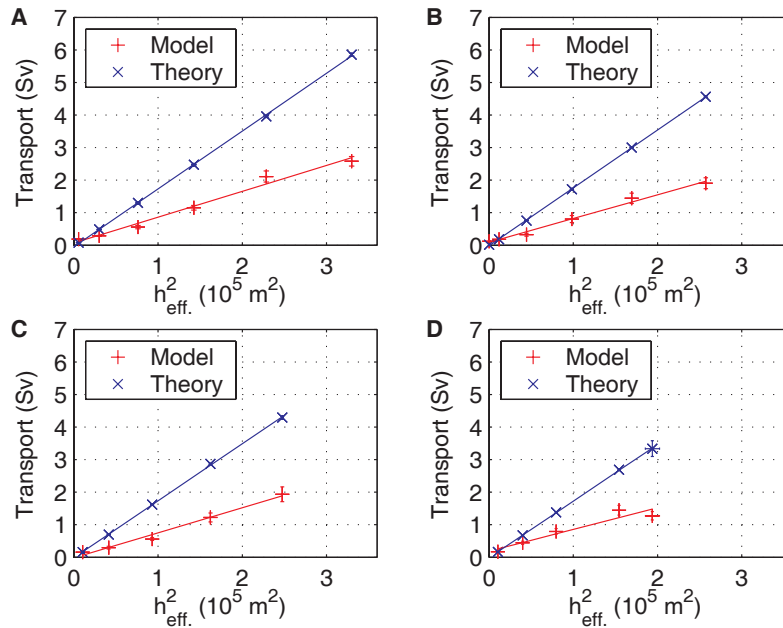


Figure 4.3.: Dense water transport as a function of squared effective height investigating the transport of DSOW for different bathymetries, representing conditions for present-day (A: DS-Res-0ka), deglacial times (B: DS-Res-10ka) and the LGM with partially (C: DS-Res-21ka1) and fully glaciated shelves (D: DS-Res-21ka2).

expected upper limit on the modeled transport for all experiments. The expected quadratic relation of effective height and transport shows high correlation in all experiments and an average ratio of modeled to theoretical transport of 0.46 ± 0.15 is obtained (Table 4.2). Thus,

Experiment	Time slice	Ratio Model/Theory	Correlation R^2
DS-Res-0ka	0 ka BP	0.47	0.98
DS-Res-10ka	11.4 ka BP	0.44	0.99
DS-Res-21ka1	21.5 ka BP	0.44	0.99
DS-Res-21ka2	21.5 ka BP	0.47	0.91

Table 4.2.: Ratio of modelled to theoretical transport for paleoclimate experiments based on realistic bathymetry. The correlation coefficient is that of the linear regression of modelled and theoretical transport estimates.

the theoretical limit can be linearly scaled to give a best fit on the modelled transport, which then allows to predict the transport from the effective height and density contrast only. It should be pointed out that, in Figure 4.3, transport is plotted against reservoir height. Due to the reduced sill depth for the LGM the cold water interface must be higher to achieve the same reservoir height. Hence, for the same density profile, the upper LGM transport limit is reduced by 33% due to the decrease in sill depth from 581 m to 509 m alone, when using the observed present-day effective height of 400 m. The geodynamic model for the glacial transition (11.3 ka BP) results in a similar sill depth (513 m) as for the LGM (509 m) and the largest differences are restricted to the shelf. This implies that the overflow was still reduced by 31% due to topography during deglacial times.

The systematic variation of the upstream height in sensitivity experiments with bathymetries representing present-day, deglacial and glacial times could corroborate the theoretical model of *Whitehead et al.* [1974] already shown to be valid for present-day in the previous chapter. As before a scaling factor could be found to predict the overflow transport from reservoir height and density contrast. Moreover, the differences between scaling factors of different experiments are small and it is suggested to utilise an average value of 0.5 ± 0.2 over the geological times considered. Here it is especially interesting that the differences between experiments with fully and only partially glaciated shelves are small and thus the initially raised hypothesis that the hydraulic transport limitation is not sensitive to changes on the shelf is corroborated. Moreover, the simple hydraulic relation allows to easily estimate the effect of changes in sill depth and density contrasts for other climatic states than those considered here. As a further application the validation of the model of *Whitehead et al.* [1974] for a different topographic boundary conditions supports the idea to use the hydraulic transport limitation as a parameterisation in coarse-resolution models. Since it was shown to work reliably for a fixed setup, this gives some confidence in using this approach to improve the representation of the Denmark Strait overflow in GCMs. However, one must be aware that by choosing a scaling factor; assumptions about a fixed upstream circulation are made. This is a restriction but because of the poor performance of GCMs in this region uncertainties related to the scaling factor pose a secondary problem. However, some effects changing the buoyancy driven flow are not taken into account here. Differences between glaciated and non-glaciated shelves could be due to frictional and boundary effects. This is briefly discussed below following *Stewart* [2002].

First, the increased velocities of north- and southward flow through the strait increase the relative importance of the non-linear terms in the momentum equation. This is best expressed as a higher Reynolds number $Re = \frac{VL}{\nu}$, with the along-stream velocity scale V , the across-stream length scale L and the kinematic viscosity ν . In case of a glaciated shelf, V is strongly increasing, L is decreasing and ν is constant. This will slightly increase the amount

of turbulent kinetic energy created by enhanced Reynolds stresses and produce horizontal mixing. In the model this is not included, since the Reynolds stresses are parameterised as a fixed eddy viscosity term in the horizontal momentum equation. Second, the glaciated shelf increases the area where lateral friction can be active, in the model included as no-slip boundary condition. Together with the secondary circulation in the channel [Johnson and Ohlsen, 1994] from bottom and interfacial Ekman layers this will increase the lateral mixing. The condition for the depth averaged velocity to yield strong vertical mixing in a curved channel, following Seim and Gregg [1997], is

$$u^2 \geq \frac{1}{\alpha} \frac{R}{B} \frac{g h}{\rho_0} \Delta\rho. \quad (4.1)$$

Here R is the radius taking into account for the curvature of the channel. The radius of the Denmark Strait is approximately 12500 km assuming a depth of 400 m and width of 100 km. B is the width and h the depth, α is a factor describing the vertical shear, here taken as 0.55 following Seim and Gregg [1997]. This yields that the depth integrated velocity during the LGM had to exceed 1 m/s in order for strong vertical mixing to occur. This cannot be ruled but is assumed to be unlikely and therefore the effects of lateral boundaries will not change the vertical mixing, at least in this respect.

4.1.2. LGM density contrast and transport

The hydraulically controlled transport through Denmark Strait not only depends on the effective height, but also on the density difference across the sill. In Section 3.2.5 it was shown for a broad range of density contrasts extending from $\Delta\rho = 0.16 - 0.72 \text{ kg/m}^3$, that the assumed linear relation of density contrast and transport ($Q \propto \Delta\rho$) holds. In order to assess possible LGM transports, a rough estimate on the LGM density contrast was obtained from coarse resolution global GCM data [Paul and Schäfer-Neth, 2003; Meissner et al., 2003]. The Greenland-Scotland Ridge topography is not properly resolved in these models, and hence the representation of the observed water mass structure close to the Denmark Strait is limited. The two global models differ significantly with respect to the representation of the Greenland-Scotland Ridge. In Meissner et al. [2003] the depth of the GSR is increased to 2000 m and Iceland is removed, whereas in Paul and Schäfer-Neth [2003] the ridge is more realistically included with a depth of about 1100 m and it includes Iceland. Thus quite a different behaviour was expected initially on how the density structure is represented. However, taking into account for the coarse resolution of the models the representation of the observed data is fairly good (Figure 4.4).

The two global models differ but not as strongly as one would expect from the bathymetry representation. Due to a higher vertical resolution the model of Paul and Schäfer-Neth [2003] yields a vertical stratification closer to observations whereas the model of Meissner et al. [2003] only roughly resembles the observations. The changes from LGM to present-day seem to be consistent in the models, showing a pronounced reduction in density contrast.

In order to obtain a transport estimate from observational and model data, a two-layer model was fitted to the top 800 m of the density contrast profiles (Table 4.3). The fit was constrained by a minimisation of the sum of squares of residuals. The density contrast found from the climatology based on observations (0.28 kg/m^3) is less than what would usually taken as density contrast (0.48 kg/m^3) when higher resolution data from observations or models is taken. However, here the same algorithm had to be used to calculate the

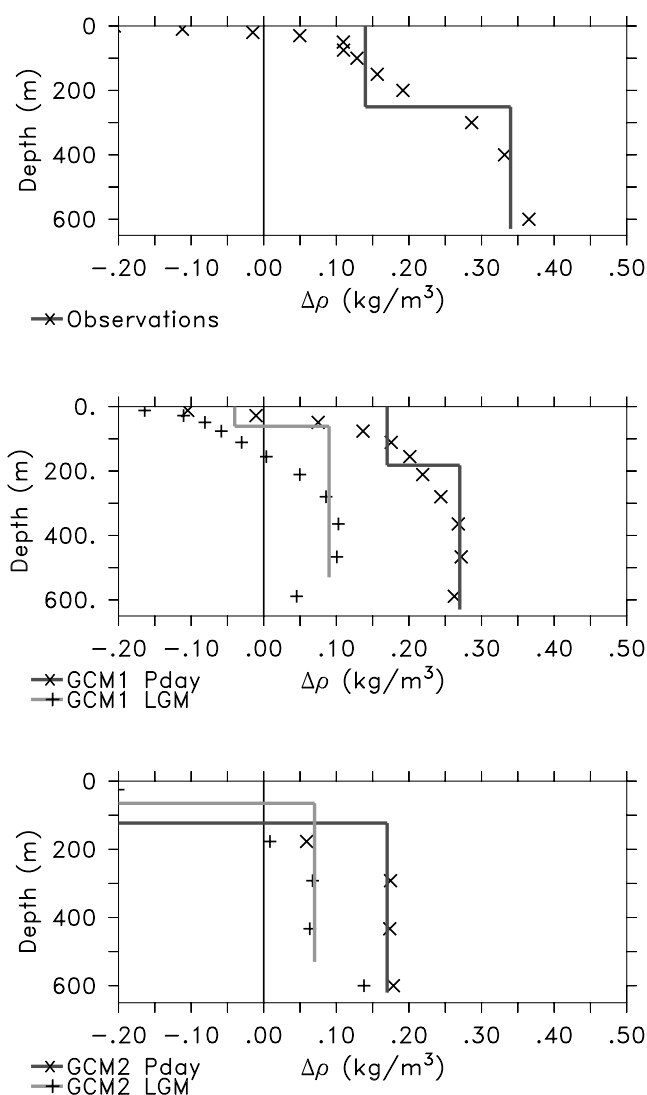


Figure 4.4.: Two-layer model from average density contrast across DS from models (GCM1 is from *Meissner et al.* [2003] and GCM2 from *Paul and Schäfer-Neth* [2003]) and observations from *Conkright et al.* [2003]. The straight lines represent a two-layer model fit to the data, which was used to determine hydraulic transport estimates.

Data	$\Delta\rho$ (kg/m ³)	h_{eff} (m)	Q (Sv)	Data
GCM1-PD	0.26	470	2.1	<i>Paul and Schäfer-Neth</i> [2003]
GCM1-LGM	0.08	390	0.4	<i>Paul and Schäfer-Neth</i> [2003]
GCM2-PD	0.17	420	1.1	<i>Meissner et al.</i> [2003]
GCM2-LGM	0.08	340	0.3	<i>Meissner et al.</i> [2003]
Observations	0.28	520	2.9	<i>Conkright et al.</i> [2003] and <i>Dickson and Brown</i> [1994]

Table 4.3.: Density contrast across Denmark Strait between average north (30° W - 20° W, 67° N - 68° N) and south (30° W - 25° W, 64° N - 65° N) profiles. The transport follows from Eq.(3.7) where the sill depth is taken as 620 m for present-day and 540 m for LGM.

density contrast and effective height from model data and observations to make the results comparable. This resulted in a broad averaging of densities and a reduction in density contrast. The average density contrast for present-day conditions is slightly underestimated in the models when compared to observations and will probably be underestimated for LGM conditions, too. Nevertheless, the results show a consistent picture.

After the hydraulic theory was corroborated it was applied to assess the glacial DSO quantitatively. The transport calculated from the two-layer fit (Table 4.3) cannot be taken as realistic value as such but it can show a general trend only and provide an estimate on the relative change. From the results shown here, one would expect that the greatly reduced across-sill density difference diminishes the hydraulic LGM transport by more than a factor of four in addition to the reduction due to the reduced sill depth. Unfortunately, the reduction of the density contrast for the LGM is uncertain; but different models [Meissner *et al.*, 2003; Paul and Schäfer-Neth, 2003] show the same tendency of a greatly reduced contrast. Furthermore, the recent glacial SST reconstructions of Pflaumann *et al.* [2003], showing a greatly reduced gradient due to a southward shift of the polar front, support this view. Using these data the hydraulic theory predicted a ceased DSO transport.

4.1.3. Realistically stratified glacial conditions

The two-layer model of the previous section focused on the changes in bathymetry using an idealised hydrography. Here the transport variations due to the combined effect of changes in bathymetry and density contrast are investigated in detail for a realistic stratification. The model set-up was described for present-day conditions in Section 3.3.2 and is here extended towards glacial conditions. Note that the present-day profile of Conkright *et al.* [2003] underestimates the density contrast and hence the estimate for buoyancy forced transport is probably slightly too low. The density stratification for the mean profiles representing the areas north and south of the sill is based on global model results [Paul and Schäfer-Neth, 2003; Meissner *et al.*, 2003]. The LGM bathymetries LGM-1 and LGM-2 from the isostatic rebound model described before are both employed to investigate the effects of a glaciated shelf. In order to be able to separate topographic and buoyancy effects the density profiles have been implemented for different bathymetries (Table 4.4).

Experiment	Bathymetry	BC	Q_{\max} (Sv)	σ_{θ} (kg/m ³)
DS-Lev-0ka	Modern (ETOPO5)	Levitus	1.9	27.7
DS-LGM1-0ka		LGM-1	0.2	28.7
DS-LGM2-0ka		LGM-2	0.4	27.6
DS-Lev-21ka2	LGM (modified GFZ 21.5 ka BP)	Levitus	1.6	27.6
DS-LGM1-21ka2		LGM-1	0.2	28.7
DS-LGM2-21ka2		LGM-2	0.3	27.6

Table 4.4.: Overview of experiments employing a continuous density stratification. The *time slice* column denotes the bathymetry which was implemented (Chapter 1). Column *BC* lists the boundary condition for the buoyancy forcing, Levitus is based on Conkright *et al.* [2003], LGM-1 is based on [Paul and Schäfer-Neth, 2003] and LGM-2 relies on [Meissner *et al.*, 2003]. σ_{θ} denotes the density bin where the maximum transport Q_{\max} was observed.

The experiments representing the LGM hydrography indicate that the overflow has almost vanished and an along-stream overflow structure is not longer apparent (Figure 4.5). In cross-

stream direction there is a weak velocity signal but a pronounced plume as for present-day is not visible as such. The descent of the plume does take place but does not show up as distinct as for present-day. One might ask if the flow is still hydraulically controlled.

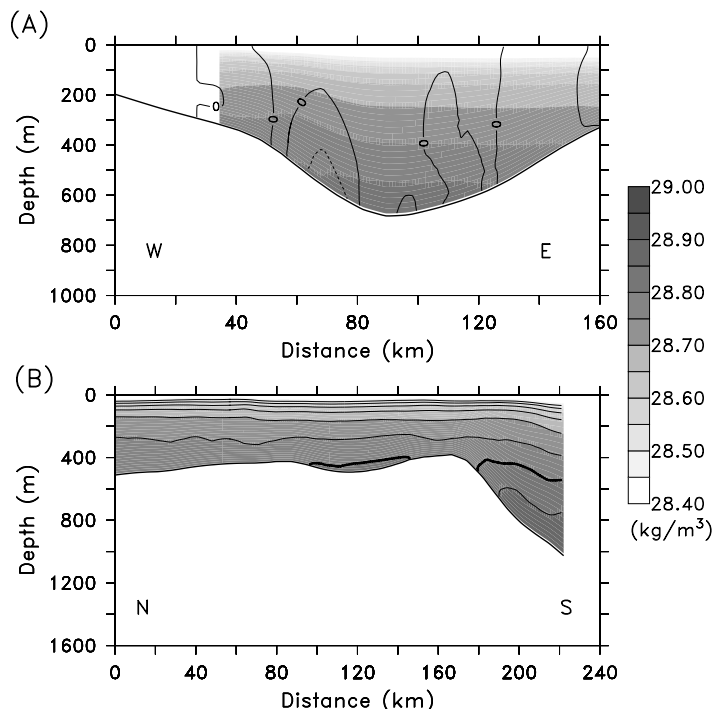


Figure 4.5.: The density (shading) and velocity (contoured with interval 10 cm/s) structure of the experiment with LGM stratification (DS-LGM1-21ka2) shows only a weak overflow in cross-stream (W: West, E: East) direction (A). In the along-stream (N: North, S: South) density section (B) the characteristic overflow is almost vanished. For an exact location map of the sections see Figure 3.4.

The pressure gradient and the associated potential energy are reduced, which causes less conversion to kinetic energy and hence a slower velocity of the plume. Nevertheless, there is good evidence that the flow is still critically controlled. As shown in the Froude number analysis (Section 3.2.3) the flow was still critical for $\Delta\rho = 0.16 \text{ kg/m}^3$.

The LGM experiment preserves the overflow plume to a distance 170 km downstream of the sill (Figure 4.6). Due to the small density contrast of the overflow plume, it reaches fairly quickly a depth where the ambient water has the same density and the remaining kinetic energy is lost in mixing processes.

The difference in transport (Table 4.4) between present-day (DS-Lev-0ka) and LGM (DS-Lev-21ka2) bathymetries with the same density structure is small and can be explained by the change in sill depth alone. Moreover, the change in width due to the glaciated shelf does not seem to play a role. The strongest changes occur when the LGM density profiles (DS-LGM1-0ka, DS-LGM2-0ka) are used. The reduction in transport as a result of the diminished density contrast is as expected from the two-layer fit of the previous section.

Concerning the LGM density stratification, it should be noted that the stratification was weaker as it is today. The average static stability E as derived from the potential density

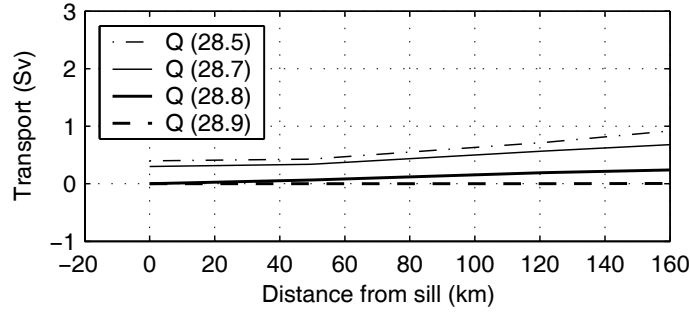


Figure 4.6.: Transport in four density classes (28.5, 28.7, 28.8 and 28.9 kg/m³) as function of along stream distance from the sill for the continuously stratified LGM experiment DS-LGM1-21ka2. The transport of water with e.g. $\sigma_\theta \geq 28.8$ kg/m³ is denoted as $Q(28.8)$.

variation with depth

$$E = -\frac{1}{\rho} \frac{\partial \sigma_t}{\partial z} \quad (4.2)$$

averaged over the the top 1000 m of the North Atlantic changes from $E = 750 \cdot 10^{-8} \text{m}^{-1}$ for the LGM to $E = 850 \cdot 10^{-8} \text{m}^{-1}$ for present-day¹. This indicates a weakened stratification during the LGM, which was additionally diminished due to a higher input of tidal mixing energy [Wunsch, 2003]. Therefore both were weaker, horizontal density contrast and vertical stratification.

4.2. Dansgaard/Oeschger stadial and interstadial experiments

The following sensitivity experiments address the two time slices where D/O cyclicity became first pronounced (30 ka) or is best expressed (70 ka). These are based on realistic bathymetries from the isostatic-rebound model (Chapter 1). Boundary conditions for the density structure are those from the previous section with present-day conditions representing interstadials and LGM conditions representing stadials (Table 4.5).

Experiment	Time Slice	BC	Q_{\max} (Sv)	σ_θ (kg/m ³)
DS-Lev-30ka	interstadial (30 ka)	Levitus	1.6	27.6
DS-LGM1-30ka	stadial (30 ka)	LGM-1	0.1	28.7
DS-Lev-70ka	interstadial (70 ka)	Levitus	1.9	27.7
DS-LGM1-70ka	stadial (70 ka)	LGM-1	0.2	28.7

Table 4.5.: Overview of experiments employing a continuous density stratification. The bathymetry is derived from the isostatic rebound models discussed earlier (Chapter 1). Buoyancy profile Levitus is based on *Conkright et al.* [2003], LGM-1 is based on [Paul and Schäfer-Neth, 2003].

The results concerning the topographic influence on transport can be translated to glacial-interglacial conditions in general as shown in Figure 4.7. It can clearly be seen that the effect of a reduction in sill depth (interglacial vs. glacial bathymetry) on the transport is small. The

¹The data are from *Meissner et al.* [2003].

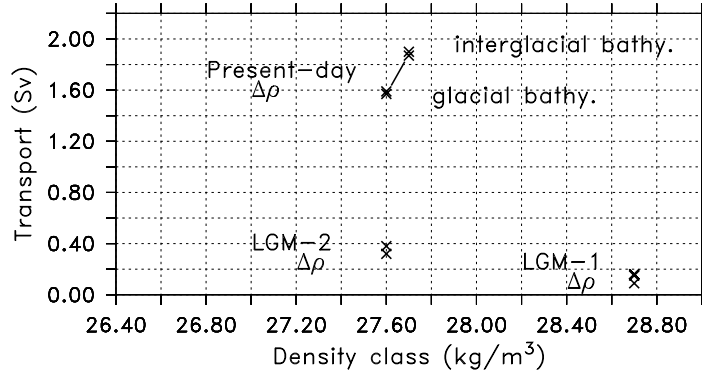


Figure 4.7.: Dense water transport Q_{max} as function of density bin σ_θ where the maximum transport was observed. The graph includes results from Table 4.4 and Table 4.5.

transport is reduced by about 0.3 Sv which is much less than the effects of a changed density contrast. A change in density contrast from present-day to LGM results in a transport reduction of 1.6 Sv.

The intention of the experiments was to find if there are any peculiarities in the timeslice with strongly expressed D/O cyclicity. Based on the experiments discussed before it can be stated that there is no significant difference between the different glacial and interglacials considered here. The drop in transport associated with the fall in glacial sea-level and the corresponding shallower sill depth is a consistent feature throughout the last two glacial-interglacial cycles. There are no striking differences which are due to the bathymetry. The main factor influencing the transport is the density contrast, which shows strong glacial-interglacial changes. This could only be tested for present-day and LGM since information for 30 ka and 70 ka was absent.

4.3. Overflow plume and pathway

4.3.1. Descent of the overflow

For the interpretation of paleoceanographic data derived from sediment cores, it is important to know the path of the overflow. Changes in the overflow path are not commonly discussed when interpreting sediment core records, instead it is often assumed that the path of the overflow has been the same throughout the last glacial-interglacial cycle. This assumption is supported by the theoretical approach of *Killworth* [2001] who found from a force balance that the overflow should descent at a constant rate of 250 m per 100 km pathway. However, this model is in contrast to observations [*Girton and Sanford*, 2003] and stream-tube models [*Jungclauss and Backhaus*, 1994]. In the stream-tube model the descent dz with along-stream distance ds is a function of combined bottom and interfacial stress τ , density anomaly ρ' and overflow thickness H

$$\frac{dz}{ds} = \frac{\tau}{\rho'gH}. \quad (4.3)$$

The bottom friction in turn depends on the velocity of the overflow, in the numerical model this is expressed as a quadratic drag law in the form of $\tau_b = \rho C_D v^2$, with the bottom drag at a constant value of $C_D = 10^{-3}$. From this one would expect changes in the overflow path

for LGM conditions since the density anomaly and velocity were probably reduced. These changes may in part compensate each other and it is difficult to draw conclusions from the stream tube model for different climatic states. Therefore the path of the overflow from the numerical model is compared for experiments with different density contrasts, where high density contrasts resemble interglacial and low density contrasts resemble glacial conditions.

The path of the overflow can be best described following *Girton and Sanford* [2003] as the position of the overflows center of gravity (COG)

$$COG = \frac{\int \Delta\rho x dx}{\int \Delta\rho dx} = C_D Fr^2. \quad (4.4)$$

The position of the COG was determined from the model results at cross-sections along the overflow path (Figure 4.8), which show that the position of the plume is sensitive to the density contrast. For a decreasing density contrast the speed of the plume is decreasing

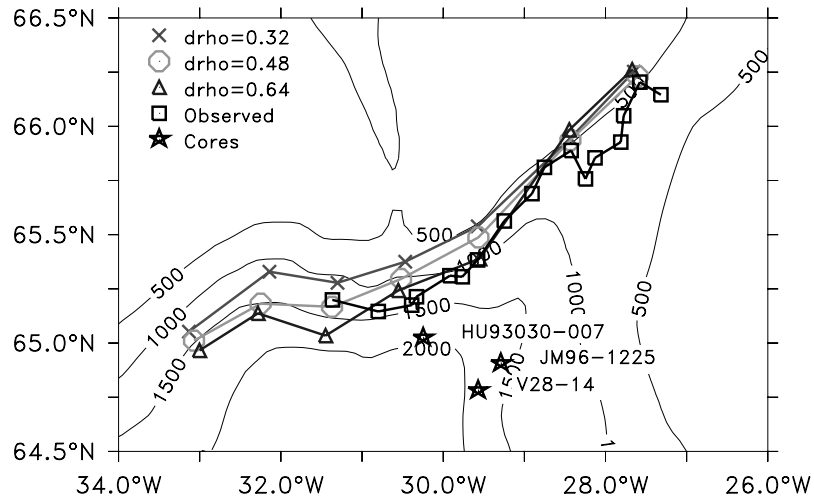


Figure 4.8.: The descent of the overflow plume for different density contrasts ($\Delta\rho = 0.32, 0.48, 0.64 \text{ kg/m}^3$) and the observed overflow path [*Girton and Sanford, 2003*]. The sediment cores from the locations shown are commonly used to derive overflow properties (HU93030 from *Andrews et al. [1998]*, JM96-1225 from *Hagen and Hald [2002]* and V28-14 from *Curry et al. [1988]*).

and the overflow position is shifted upwards towards shallower depths and vice versa for an increasing density contrast. This can be understood in terms of the Froude number which is increasing for increasing density contrast (cf. Figure 3.9). The observed overflow path from observations [*Girton and Sanford, 2003*] is fairly well represented by the experiment for present-day conditions ($\Delta\rho = 0.48 \text{ kg/m}^3$). It agrees at the sill and further downstream but it slightly underestimates the initial descent at the sill exit region (65.3°N). Moreover, it can be clearly seen that the core locations intended to sample the overflow lay far away from the actual overflow core. The reason for this is that the coring positions are dependent on adequate sedimentation patterns, which will be absent close to the overflow core (further discussed below). Nevertheless, the spatial distance to the overflow needs to be taken into account when inferring overflow properties from these cores.

The descent downstream of the overflow core is in good agreement with the observed path [*Girton and Sanford, 2003*] and stream tube models [*Jungclauss and Backhaus, 1994; Killworth, 2001*]. This yields some confidence for the modelling results, nevertheless there

are shortcomings. As suggested by *Wåhlin* [2004], small-scale topographic features may force a downward channelling of dense water. Topographic corrugations such as canyons only a few kilometres wide could force nearly geostrophic flow towards greater depths. This mechanism might act at the exit of the Denmark Strait where a rapid descent is observed but could not be modelled.

A common assumption inherently made in many paleoceanographic studies seems to be that the position of the overflow core in the past was not different from today's. In contrast to that, the examination of the overflow path in the model for varying density contrasts has shown this is not necessarily the case. The core of the overflow shifts to shallower depth with reduced density contrast, hence it is likely that the outflow at the LGM took place at shallower depth. Therefore it is essential to consider the variable admixture of Irminger Current water to DSOW, a shift of the DSO core to shallower depth increases the portion of MNAW in the sediment record which could easily be misinterpreted as an apparent warming of DSOW.

4.3.2. Mesoscale processes

Short term variability and mesoscale processes are intimately linked to the descent of the overflow and may therefore be of interest for paleoceanographic questions even though they cannot be directly reconstructed. *Jungclauss et al.* [2001] have shown that the formation of eddies in the Denmark Strait can be explained as originating from baroclinic instabilities disturbing the stable stratification. The overflow plume develops with anti-cyclonic eddies upslope, transporting original overflow water masses, and cyclonic eddies downslope, entraining ambient water. The position of the overflow plume as intensified bottom jet is stabilised by the vortices which tend to move along-slope. From a wavenumber stability analysis they obtained that the most unstable waves depend on the bottom slope (s) and the density contrast ($\Delta\rho$). Hence, for a reduced density contrast the growth rate of unstable waves shifts to higher wavenumbers or shorter wavelengths. From this one would expect a reduced eddy size for LGM conditions as a consequence of the reduced density contrast, which in turn has an influence on the horizontal mixing [*Gent et al.*, 1995]. Furthermore, a changed density contrast will alter the mean translation speed of eddies, which can be approximated by the Nof speed c_{Nof} [*Nof*, 1983] as

$$c_{Nof} = g's/f. \quad (4.5)$$

Since the maximum bottom slope will remain fairly constant through time, $s \approx 1.2 \cdot 10^{-2}$ for present-day, the reduced LGM density contrast will tend to reduce the translation speed.

4.3.3. Sedimentation patterns

The overflows high velocity causes sediment erosion along the path of descent. The resulting sedimentation pattern was simulated with a basic sedimentation model [*Warner et al.*, 2005] of a homogeneous, 1 m thick sediment bed, which can be eroded and redeposited. Suspended sediment is carried by diffusion and advection in the lowest layer within the water column.

The overflow causes a realistic change in the sediment bed and the resulting sedimentation patterns (Figure 4.9) have some remarkable features. First of all the high current speed of the overflow leads generally to erosion directly underneath the plume and redeposition on

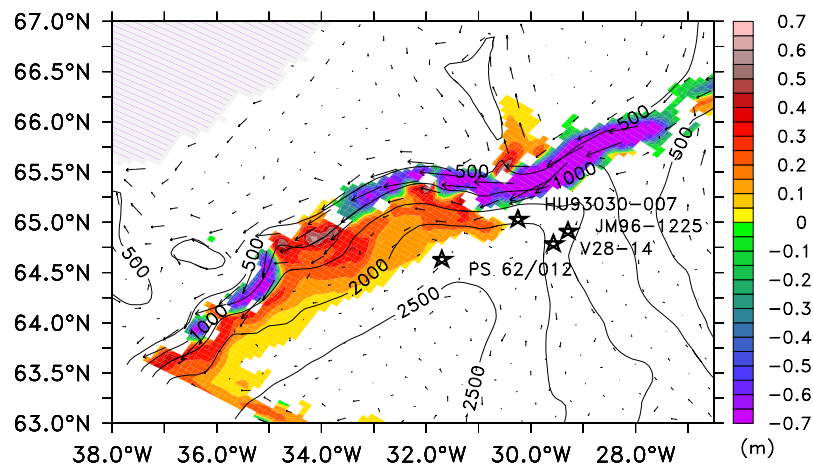


Figure 4.9.: Sediment bed thickness from a sediment model for the present-day overflow. Note the erosion along the path of the overflow and the redeposition downslope.

the downslope side. This agrees well with data obtained from the parasound system during cruise ARK XVIII [Sarnthein *et al.*, 2003c] to the Denmark Strait. The high-resolution acoustostratigraphy showed that the sea-floor is eroded to bedrock along the path of the overflow. The redeposition of eroded material in the model is close to the actual coring sites (Figure 4.9) and supports the assumption that the cores sample primarily the overflow. On the other hand, the redeposition potentially limits the accuracy of the stratigraphy of the cores. A noteworthy feature is the high redeposition rate along the path of the overflow where the isobath is rapidly turning to the west and back to the east again (34° W, 65° N). This causes a rapid decrease in depth along-stream, which in turn creates high rates of redeposition and might be of interest for future cruises.

4.4. Summary and conclusions

The dense water transport through Denmark Strait for changing gateway depths and apertures, resembling present-day, deglacial and LGM bathymetries were investigated. Observed and maximum hydraulically predicted flows were compared and it was found that the theoretical values fit the observed ones when linearly scaled. A range in the scaling factor of hydraulic theory from 0.4 - 0.8 was found, with 0.5 being a reasonable value for the parameterisation when implemented into a GCM. Moreover, hydraulic control may also be a useful tool for estimating the LGM overflow strength from geological records, once density fields are resolved.

The main scientific question of the experiments presented above was to evaluate if the overflow description as rotating hydraulic system proposed in the previous chapter is valid under different climatic conditions. Specifically, the time from LGM to present-day was considered in terms of bathymetry and hydrography changes affecting the volume transport and descent of the overflow.

Comparing the LGM and present-day results, the overflow was changed during the LGM due to the following factors:

- The overflow strength was reduced due to a change in gateway depth and aperture arising from glacial-isostatic adjustment, leading to a significant reduction in volume transport of ca. 30%.

- A reduced density contrast by more than 60% as suggested from global-model results yields a decrease in overflow strength by the same amount.
- Changes in gateway aperture (glaciated vs. non-glaciated shelves) have a minor impact on the transport only but influence the local density and velocity structure.
- Based on experiments with realistically stratified conditions it is suggested that the buoyancy driven Denmark Strait overflow during the LGM was at least reduced by a factor of 5 to no more than 0.3 Sv.
- Besides changes in volume transport, a shift to shallower depth by up to 500 m due to the changed force balance of the descending plume was found.
- The differences between present-day and LGM could be corroborated for different glacial-interglacial bathymetries and stadial-interstadial density structures based on experiments representing 30 and 70 ka BP.

5. The Dense Northern overflows for present-day and Last Glacial Maximum conditions

The previous chapters have shown that main features of the Denmark Strait Overflow can be reproduced in a model driven by buoyancy forcing only, but the modelling results of [Bjastoch *et al.*, 2003] show that wind stress might play a more important role than previously thought. Bjastoch *et al.* [2003] propose an interaction of large scale changes in the wind stress pattern such as the North Atlantic Oscillation with the overflow transport across the Greenland-Scotland Ridge (GSR). Moreover, the overflows through Denmark Strait (DS) and the Faroe Bank Channel (FBC) seem to be correlated and respond as a coupled system to forcing changes [Nilsen *et al.*, 2003; Zhang *et al.*, 2004]. Unfortunately, today's coarse resolution climate models cannot resolve these processes, which complicates model based estimates of deep water formation and export from the Nordic Seas to the North Atlantic. This is especially important when assessing climates different from today's where one of the gateways was almost closed, e.g. for an iceberg blocking of the Denmark Strait during Heinrich Events. To circumvent this problem a high resolution regional ocean model is used to study the Northern Overflows under present-day (PD) and Last Glacial Maximum (LGM) conditions. From sensitivity experiments using idealised forcing changes the governing dynamics controlling the exchange across the ridge are investigated addressing the following key questions:

- What is the relation between the Denmark Strait overflow, the flow across the Iceland-Faroe Ridge (IFR) and the Faroe Bank Channel overflow in a hydraulic framework for both PD and LGM conditions? Is there a correlation/anti-correlation of DS, IFR and FBC?
- What is the relation between wind stress and transport? Is it reasonable to expect an effect of the NAO on the Denmark Strait overflow (DSO)? What changes can be assumed for glacial/interglacial climates? Does wind stress affect the individual overflows in a different way?
- What is the flow direction across the GSR for different buoyancy and wind forcing? What can be inferred for the dispersal of marine biota?
- What is the impact of a (partial) blocking of the DS during PD and LGM conditions? Are there implications for generating Dansgaard/Oeschger (D/O) cycles?

5.1. Present-day circulation

5.1.1. Model validation

The reference run for PD conditions employs the model set-up introduced in Section 2.2.2. The model domain is extended to include the full GSR with closed walls and restoring zones for temperature and salinity at the northern and southern wall. The buoyancy forcing is from idealised density profiles representing average conditions north and south of the GSR based on *Conkright et al.* [2003]. Additional forcing comes from surface wind stress which was derived from the mean winter (DJF) wind field of the ECMWF climatology [*Gibson et al.*, 1997]. Thus, the main difference to the previous modelling experiments is the extended domain and the application of wind stress as forcing. The reason to include the full GSR here is to allow for a wind driven barotropic circulation around Iceland and to include the FBC as a second deep gateway. As a consequence of the more complex set-up it takes 50 days for the model to reach equilibrium. Therefore, it is integrated for 150 days and days 70 to 150 are analysed. It is expected that the FBC overflow can possibly compensate changes in the DSO. In order to reduce the computational costs there is no seasonal cycle but the model is driven with PD winter and LGM summer conditions. This approach allows to compare times with active deep water formation in the Nordic Seas and should be best comparable [*Schäfer-Neth*, 1994]. The model is mainly analysed on specific cross-sections (Figure 2.3) splitting the Greenland-Scotland Ridge into the four sections: the Denmark Strait (DS), the Iceland-Faroe Ridge (IFR), the Faroe Bank Channel (FBC) and the Wyville-Thomson Ridge (WTR).

The transport rates of dense water in the model are fairly realistic (Figure 5.1). The transport of DSO of 3.4 Sv for $\sigma_\theta \geq 27.8$ in the model is at the upper end of the observed values, which vary between 2.7 Sv and 3.4 Sv [*Dickson and Brown*, 1994; *Girton et al.*, 2001; *Macrandar et al.*, *subm.*]. The FBC overflow is underestimated in the model with 0.8 Sv for $\sigma_\theta \geq 27.6$ whereas the observations are in the range of 1.4-1.9 Sv for $\sigma_\theta \geq 27.89$ [*Borenäs and Lundberg*, 1988; *Østerhus et al.*, 1999]. This too low value in the model is due to the coarse resolution of the bathymetry. The observed depth of the FBC is 840 m whereas it is only 660 m in the model. The overflows across the Iceland-Faroe Ridge are only approximately known from measurements and are less steady but occur in pulses. Overflow across the Iceland-Faroe Ridge takes place at various locations and may amount up to 1 Sv [*Meincke*, 1983]. Since it takes place through small gaps in the ridge which are not resolved by the model this part of the overflow is almost absent in the experiments. The WLK branch of the overflows was found to be weak in observations at about 0.3 Sv [*Ellett*, 1998]. In the model this transport is overestimated at 0.8 Sv for $\sigma_\theta \geq 27.6$. Overall the results are comparable to that of observations and to similar modelling studies [e.g. *Biastoch et al.*, 2003].

The structure of the dense water reservoir and the overflows becomes apparent when looking at the depth and velocity structure of the 27.8 isopycnal (Figure 5.2). The descending overflows through DS and FBC can be clearly seen in the velocity field. The spatial structure of the overflows attached to the continental slope is evident in the depth of the isopycnals. The downstream connection of FBC and DS through the Charlie-Gibbs Fracture is not included and hence the flow of ISOW from the Iceland Sea to the Irminger Basin is not realistically included.

The reference experiment for PD is consistent with observations [*Girton et al.*, 2001; *Girton and Sanford*, 2003] and model experiments with a similar set-up [*Biastoch et al.*, 2003]. However, as a consequence of closed walls no net volume transport across the GSR

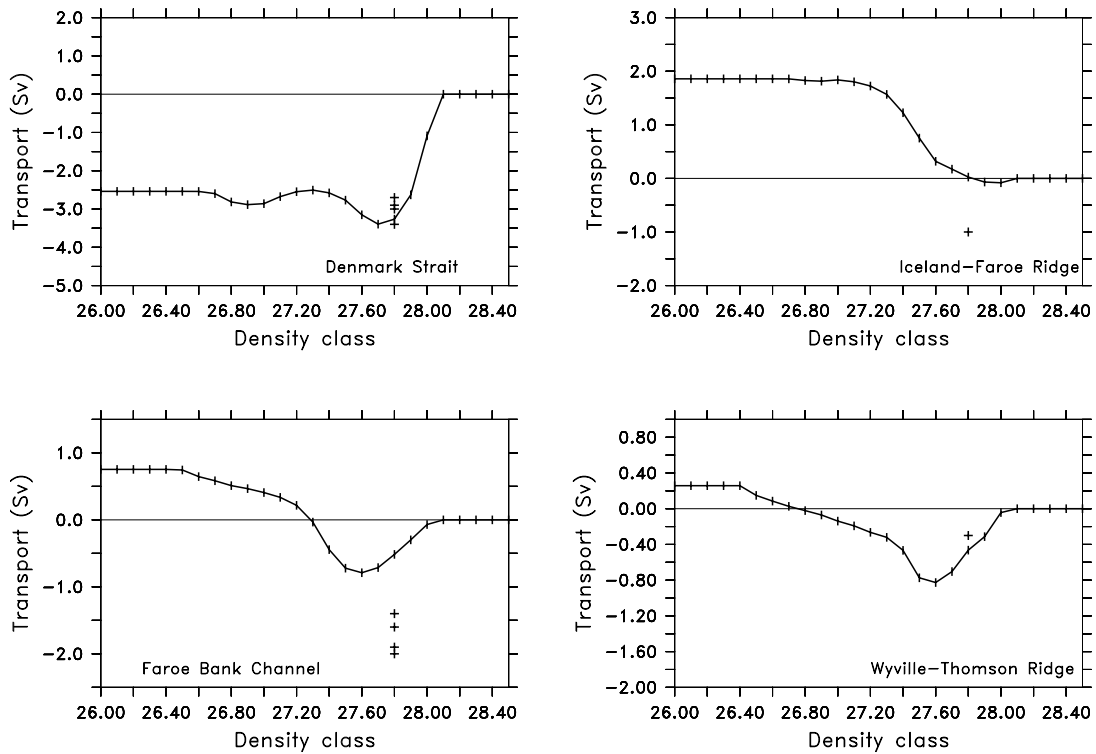


Figure 5.1.: Cumulative volume transport of water in density classes across the Denmark Strait, the Iceland-Faroe Ridge, the Faroe Bank Channel and the Rockall Trough. Positive values correspond to northward (eastward) and negative values to southward (westward) transport. The transport is integrated from high to low densities and the density class is associated to the lower bound. The midpoint of the $0.1 \sigma_\theta$ wide density bins is indicated as vertical line. Observed values (plus signs) are shown for comparison [Dickson and Brown, 1994; Girton *et al.*, 2001; Macrander *et al.*, *subm.*].

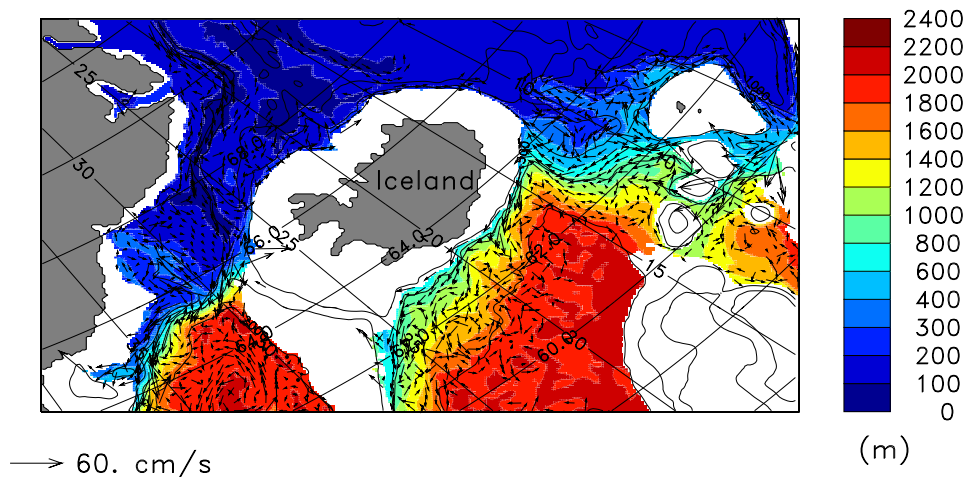


Figure 5.2.: Depth of the 27.8 isopycnal (shading) and velocity structure on that isopycnal (vectors). The 500 m, 1000 m, 2000 m, 3000 m isobaths are overlain. Note the increasing depth of isopycnal surfaces south of the GSR.

is permitted as would be possible with Bering Strait and Davis Strait open. Despite these limitations, the model is consistent with the circulation pattern in the Nordic Seas and the origin of DSOW as the lower part of the EGC as proposed by *Rudels et al.* [2002] based on observational evidence. The direct path of DSOW from the Iceland Sea to Denmark Strait as identified from measurements [*Jónsson and Valdimarsson, 2004*] can be observed in the model as well (Figure 5.3). In contrast to their conclusion that this path indicates deep

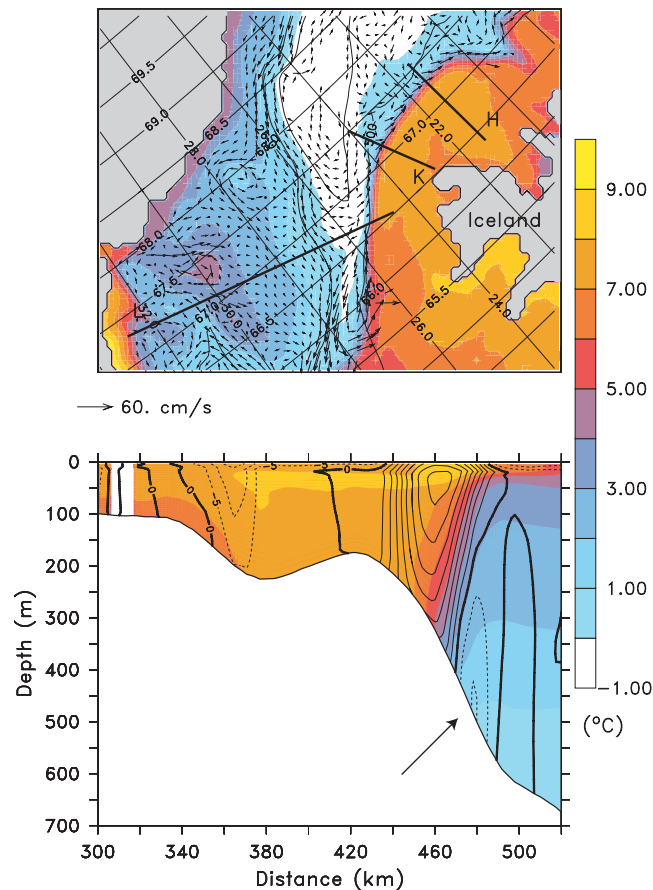


Figure 5.3.: *Upper panel:* Temperature (shading) and velocity field (vectors) on the $\sigma_\theta = 27.8$ isopycnal. The longitude and latitude grid is overlain, with 0.5° spacing in latitude and 2° in longitude. The standard sections Latrabjarg (L), Køgur (K) and Hornbanki (H) of the Icelandic marine research institute in Reykjavik are indicated as lines. *Lower panel:* Temperature (shading) and velocity (contours) at the Hornbanki section. The velocity contour interval is 5 cm/s. Note the westward flow at 450 m depth (indicated by the arrow) at the same location as observed by *Jónsson and Valdimarsson* [2004].

water production in the Iceland Sea feeding the overflow, it can be identified in the model as a branch of the southward flowing lower EGC. However, it should be noted that this is the case for an idealised situation and it might be different under variable forcing. Further studies are necessary with models using seasonal cycling, surface net heat flux and ice cover. From preliminary experiments it appears that both paths are active depending on the exact state of the surface forcing [R. Käse 2004, pers. comm.].

5.1.2. Changing wind forcing

Model GSR, validated for PD in the previous chapter, is used here with different magnitudes of wind stress to investigate the dependence of overflow transport on local wind stress (Table 5.1).

Experiment	Time slice	Buoyancy	Wind stress
GSR-0ka-A	0 ka BP	Levitus	x 0
GSR-0ka-B	0 ka BP	Levitus	x 1
GSR-0ka-C	0 ka BP	Levitus	x 2
GSR-0ka-D	0 ka BP	Levitus	x 4

Table 5.1.: Overview of experiments with average density profiles and wind forcing. The surface stress for PD winter was then linearly scaled by factors of 0,1,2 and 4 to test the sensitivity for changes in the surface stress.

For simplicity the scalar field of wind stress curl is taken in the following instead of the vector components of the wind stress. Wind stress curl is defined as

$$\nabla_h \times \tau = \frac{\partial \tau_y}{\partial x} - \frac{\partial \tau_x}{\partial y}. \quad (5.1)$$

The difference between maximum and minimum wind stress curl in the area of the GSR (45° W - 5° E and 58° N - 66° N) is defined as Δ_τ henceforth.

In the case of no wind the transport is solely buoyancy forced, with increasing wind stress the transport of DSOW increases whereas the transport across the Wyville-Thomson ridge (WTR) decreases. The overflow transports across FBC and IFR are almost constant (Figure 5.4; left panel). The increase of DSOW transport is a consequence of the enhanced

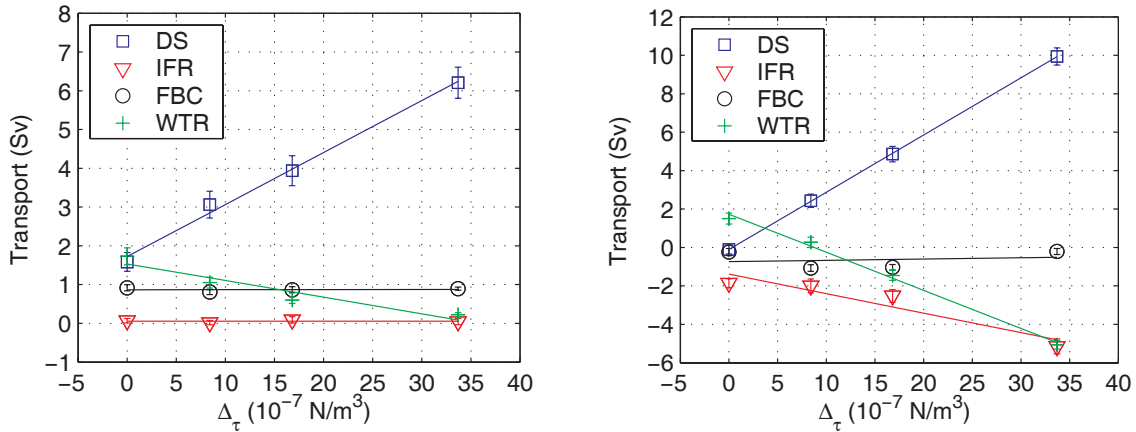


Figure 5.4.: *Left panel:* Relation between wind forcing and overflow transport ($\sigma_\theta \geq 27.8$). Δ_τ is the difference between maximum and minimum wind stress curl in the area of the GSR (45° W - 5° E and 58° N - 66° N). The transport is averaged over model days 70 to 150 and the error-bars indicate the 95% confidence bounds for the mean.

Right panel: Relation between wind forcing and barotropic transport.

cyclonic circulation around Iceland, which enhances the barotropic transport through Denmark Strait [Bjostoch *et al.*, 2003]. The stronger outflow is compensated by stronger inflow

through the IFR and the WTR (Figure 5.4; right panel). In turn the dense water transport across the WTR diminishes. Note that the resolution of ≈ 6 km in the model employed here cannot capture the FBC properly and hence some portion of ISOW which should pass through the FBC is leaving across the WTR. Nevertheless, the results are in agreement with *Biastoch et al.* [2003] and the anti-correlation of ISOW and DSOW they found is corroborated here. With increasing wind stress the transport of DSOW increases and ISOW (FBC and WTR) decreases as a results of the increased barotropic circulation around Iceland. In addition to the conclusions drawn by *Biastoch et al.* [2003], who suggested that the shelf in the Denmark Strait may play an important role for transport changes under varying wind stress, it is found here that the transport also changes in the deep part of the DS (not shown).

In Figure 5.4 it can be seen that the transport of DSOW depends linearly on Δ_τ . A linear regression of Δ_τ and the transports listed in Table 5.2 yields

$$Q_{\text{DSOW}} = 1.92 \text{ Sv} + 0.1292 \frac{\text{Sv}}{10^{-7} \text{ N/m}^2} \cdot \Delta_\tau, \quad (5.2)$$

which relates transport of DSOW and wind stress (with $R^2 = 0.97$). Equation (5.2) can be

Experiment	Time slice	Δ_τ (10^{-7} N/m^2)	Q_{DSOW} (Sv)	Q_{barotrop} (Sv)
GSR-0ka-A	0 ka BP	0.0	1.6 ± 0.3	0.0 ± 0.3
GSR-0ka-B	0 ka BP	8.4	3.5 ± 0.4	2.9 ± 0.4
GSR-0ka-C	0 ka BP	16.8	4.0 ± 0.6	4.9 ± 0.5
GSR-0ka-D	0 ka BP	33.6	6.2 ± 0.5	10.2 ± 0.6

Table 5.2.: Mean volume transport for varying wind stress from the GSR-0ka experiments with Q_{DSOW} as the transport of dense water and Q_{barotrop} as the total depth integrated transport. The error estimate is for the 95% confidence bounds of the mean transport over days 70 to 150.

interpreted as a buoyancy forced transport of 1.92 Sv plus the wind driven transport, but a theoretical justification of this interpretation is not straightforward. In Section 3.3.3 the coupling of hydraulic and barotropic transport was briefly discussed. For a small barotropic fraction the hydraulic framework seems to be acceptable but if as in case GSR-0ka-D with four times the average wind stress the wind driven transport (4.6 Sv) exceeds the hydraulic transport (1.6 Sv) by large, and the hydraulic assumptions becomes questionable. However, the transport does not exceed the hydraulic limitation (6.7 Sv for GSR-0ka-D as derived from Equation (3.7)) and an analysis of the plume Froude number (not shown) reveals that the position where the composite Froude number G (cf. Equation (3.14)) becomes unity is nearly unchanged for the experiments with different wind stress. The increased transport rate for higher wind stress is accomplished only from higher advections speeds at the sill, i.e. the transport at the shelf (depth < 200 m) contributes only a small amount to the total dense water transport. Note that the minimum depth is 100 m in the model and thus shallower depth are not realistically included. This affects a small area only and the differences in circulation on the shelf due to the slightly too deep model bathymetry are expected to be small. Interestingly, the effective height upstream is not increasing but slightly decreasing and reduces the hydraulic limitation from 7.6 Sv in GSR-0ka-A to 6.7 Sv in GSR-0ka-D. Note that for all cases considered the actual transport is submaximal ($Q_{\text{DSOW}} < Q_{\text{WLK}}$).

The experiments with systematic variations of wind stress demonstrate that the DSO can only be described as a superposition of pressure gradient force and wind driven parts. The pressure gradient forced flow has been described as limited by hydraulic constraints, this estimate will be altered if wind driven barotropic flow is present. So far there is no theory combining rotating hydraulic theory and barotropic flow. However, the model results indicate that the simple addition of barotropic wind forced motion and pressure gradient driven transport is a valid assumption. The brief discussion on the effects of barotropic transport on rotating hydraulic included here is descriptive only and this is certainly a point which deserves further investigation from a theoretical perspective. Interestingly, the expected interannual variability over the time span of NCEP/NCAR reanalysis data (1948-2004) due to the momentum input by wind stress forcing based on Eq. (5.2) has a standard deviation of ± 0.2 Sv. This should be large enough to be recognised in measurements.

The barotropic nature of the overflow highlights the need to more accurately measure this component in observations. The measurement of SSH from remote sensing is potentially useful for monitoring the overflows but with an error of 5 cm for individual tracks and 2 cm between tracks [Hoyer and Quadfasel, 2001] is still not good enough.

5.1.3. Application to the North Atlantic Oscillation

The effects of variable wind forcing investigated in the previous chapter are applied below to understand the direct, wind forced effects of the NAO on the Nordic Seas and North Atlantic. The inflow of Atlantic water to the Nordic seas is increased for a positive phase of the NAO [Blindheim *et al.*, 2000] and the subpolar gyre expands [Bersch, 2002; Curry and McCartney, 2001]. There is a fast barotropic (3 days) response due to changes in Ekman transport and a delayed (6-8 years) baroclinic transport [Eden and Willebrand, 2001]. Marshall *et al.* [2001] found that during a positive NAO phase the barotropic circulation around Iceland increases, which may in turn increase the transport of DSOW [Biastoch *et al.*, 2003]. Moreover, it has been suggested that the NAO influences the northerlies and Arctic Sea ice export [Hilmer and Jung, 2000].

The variability of wind stress curl is assessed from reanalysis data and model experiments. The values of minimum, maximum and difference between maximum and minimum of the winter wind stress curl over the GSR are listed in Table 5.3. Comparing positive and negative phases of the NAO shows that the difference between both is comparable to the difference between one- and two-times wind stress. The atmospheric general circulation mode (AGCM) modelling results of Lorenz and Lohmann [2001, pers. comm.] for PD generally agree with the reanalysis data but slightly underestimates the maximum wind stress curl. The LGM model results indicate enhanced wind stress for glacial conditions similar to two times PD wind stress. As forcing for the LGM model experiments below the difference LGM-PD was added to the reference field to reduce a possible model bias. The original field is kept here for completeness and to show that the difference between LGM model and anomalies from NCEP are small.

The results of the experiments with varying wind stress can be combined with the information of Table 5.3 to assess the direct influence of wind stress changes for different phases of the NAO. Observations [Blindheim *et al.*, 2000] and previous modelling experiments [Nilsen *et al.*, 2003] show a strengthening of the inflow of Atlantic Water with the FSC for a positive phase of the NAO. This strengthening of the FSC corresponds to a strengthening of the eastern branch of the NwAC at the Svinøy Section as observed by Orvik and Skagseth [2003].

Experiment	Min.	Max.	Max.-Min.
Reference	-1.9	6.5	8.4
NAO +	-4.4	13.0	17.4
NAO -	-1.4	8.5	9.9
WINDx2	-3.8	13.0	16.8
WINDx4	-7.6	26.0	33.6
Model PD	-2.0	4.9	6.9
Model LGM	-8.9	9.7	18.6
Model LGM 2	-9.8	9.8	19.6

Table 5.3.: Minimum, maximum and difference of wind stress curl (in 10^{-7}N/m^2) in region (45°W - 5°E , 58°N - 66°N). Reference is the mean over the NCEP/NCAR period (1948-2003), NAO + and NAO - are taken from winter period (DJFM) time-slices characteristic for the respective condition (1991-1994 for NAO+, and 1976-1979 for NAO-), in WINDx2 and WINDx4 the wind stress is doubled and quadrupled, respectively. The model data is from atmospheric general circulation model (AGCM) results of *Lorenz and Lohmann* [2001, pers. comm.] in unaltered form (LGM-2) and taken as anomalies from the NCEP/NCAR reanalysis (PD and LGM) from *Paul and Schäfer-Neth* [2003].

The western branch of the Norwegian Atlantic Current (NwAC), which corresponds to the IFR inflow, weakens. In the model, an increased wind stress leads to a stronger barotropic northward flow across the WTR and hence agrees with an enhanced FSC. The observed anti-correlation of IFR and FSC (WTR) cannot be reproduced in the model. The northward transport across the IFR is increasing as well for stronger wind stress. This emphasises that the analogy of NAO high and wind stress increase is limited because the southeastward shift of the current system during a positive phase of the NAO is missing in the wind stress experiments. However, the exact contributions to the NwAC are of minor importance here. The main result is a generally increased inflow into the Nordic Seas for a positive NAO phase. On the other hand an increase in barotropic southward transport through the DS can be expected [*Biastoch et al.*, 2003]. This will increase the transport of DSOW. The question arises if the inflow is stronger because the wind driven outflow has risen or vice versa. *Furevik and Nilsen* [2004] argues based on a regression with mean winter sea-level pressure that the inflow is compensating the outflow. In this study the outflow through DS is enhanced and across the WTR is reduced. As explained earlier some portion of the WTR outflow in the model should be attributed to the FBC. Thus it is reasonable to expect an decreased FBC as well even though this could not be shown in the model. In summary, a positive NAO will increase the FSC inflow and DS outflow and decrease the IFR inflow and FBC outflow. Following this argument, the recent reduction in the NAO amplitude from winter 2000 to winter 2003 should lead to an increase of the FBC overflow and a decrease of the DSO. That this exhibits some realism can be seen from the yet unpublished record of again rising transport rates through the FBC [*Hansen* 2004, pers. comm.].

Orvik and Skagseth [2003] successfully predicted the Norwegian Atlantic Slope Current based on wind stress curl. In a similar approach the annual mean wind stress changes are applied here to predict the effect of the NAO on the transport of DSOW. The idea here is to employ the relation of changing wind stress and overflow transport (Equation 5.2) to the wind stress from reanalysis data (NCEP/NCAR) in order to estimate the expected overflow response to NAO variability. In Figure 5.5 the NAO index is shown together with the standardised amplitude of wind stress averaged over the northern North Atlantic (45°W - 5°E , 58°N - 66°N). The annual mean¹ wind stress amplitude is correlated to the winter

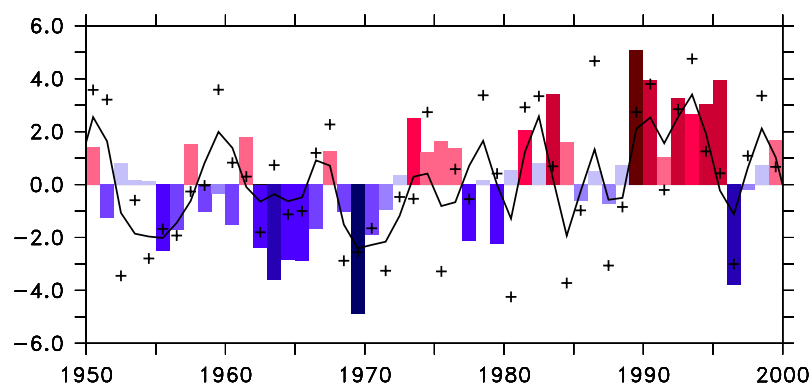


Figure 5.5.: Annual mean amplitude of standardised wind stress averaged over northeastern North Atlantic (plus signs for individual amplitude and solid line smoothed over three years with a Hanning window) and DJFM NAO index of *Hurrell [1995]* (shaded bars).

NAO index with $R^2=0.41$. If the influence of wind stress on the overflows shown before is valid this implies a direct influence of NAO controlled wind stress changes on the overflows on interannual timescales.

The wind stress curl difference Δ_{tau} was calculated for the whole NCEP/NCAR period (1948-2003) and then used to derive the annual mean DSOW transport based on Equation (5.2 (Figure 5.6). The obtained transport time-series has a mean of 3.0 Sv, a standard

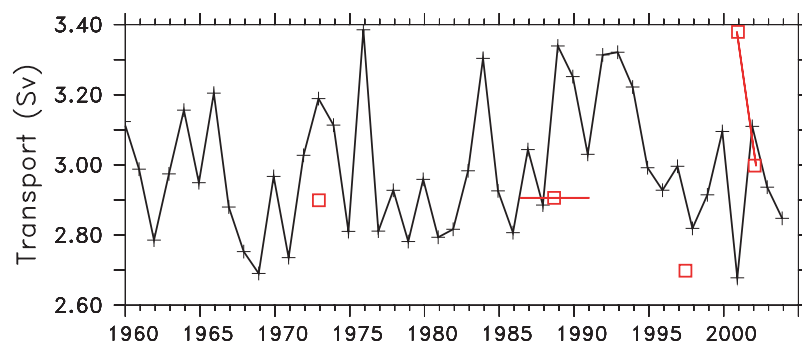


Figure 5.6.: Transport of DSOW as predicted from NCEP/NCAR wind stress anomaly (plus signs and solid line) and assuming Eq. (5.2) to be valid. Observations of the transport are shown as squares [*Ross, 1973; Dickson and Brown, 1994; Girton et al., 2001; Macrander et al., subm.*]. Repeat measurements [*Dickson and Brown, 1994*] or continuous measurements [*Macrander et al., subm.*] are indicated as lines.

deviation of 0.2 Sv and a maximum (minimum) of 3.4 Sv (2.7 Sv). The mean value compares well with previous observational estimates of 2.9 Sv [*Dickson and Brown, 1994*] and 2.7 Sv [*Girton et al., 2001*], which was expected since Eq. 5.2 is based on a tuned model. The measurements may underestimate the actual transport slightly due to the missing overflow contribution from the transport along the shelf. The recent (1999-2003) measurements of *Macrander et al.* [subm.] indicate both higher transport rates and a wider range of interannual variability between 3.0 Sv and 3.9 Sv. The observed variability is influenced by both changes in the density contrast, the reservoir height and the barotropic forcing.

¹The annual average was taken from July to June in order not to separate the winter (DJFM) NAO signal into different years.

However, the calculated transport variations (Figure 5.6), only due to changes in the wind forcing, are in the range of ± 0.2 Sv, which is still less than the observed variability of *Macranders et al.* [subm.].

5.1.4. Comparison of Faroe Bank Channel and Denmark Strait overflow

The Denmark Strait and Faroe Bank Channel overflows can be seen as hydraulically coupled system fed from the same reservoir. In this section two aspects are further investigated. At first the coupling of FBC and DS is determined purely based on hydraulic theory. The second point is the coupling on short timescales in the numerical model, which was validated for PD in Section 5.1.1.

At first, the transient behaviour of FBC and DS in a spindown experiment is considered. The time rate of change of the reservoir height h_{eff} is proportional to the flux down the channel as computed by steady theory [*Whitehead et al.*, 1974] for the Denmark Strait follows

$$A \frac{dh_{\text{eff}}}{dt} = -\frac{h_{\text{eff}}^2 g'}{2f} \quad (5.3)$$

and for the Faroe Bank Channel one obtains

$$A \frac{dh_{\text{eff}}}{dt} = -\frac{2^{3/2}}{3} b g'^{1/2} \left(h_{\text{eff}} - \frac{1}{8} \frac{f^2 b^2}{g'} \right)^{3/2} \quad (5.4)$$

with A being the upstream area, which was chosen to resemble the Nordic Seas. The upstream reservoir can be approximated as the area of 30° W - 20° E and 66° N - 80° N limited by the 720 m isobath, which yields an area of $1.638 \cdot 10^{12}$ m² based on the ETOPO5 bathymetry [*NGDC*, 1988]. With an effective height of 580 m for the DS and 400 m for the FBC and $2.9 \cdot 10^{-3}$ and $4.9 \cdot 10^{-3}$ as the respective density contrasts the coupled effect was calculated by integrating Equations (5.3) and (5.4) forward in time (Figure 5.7). The

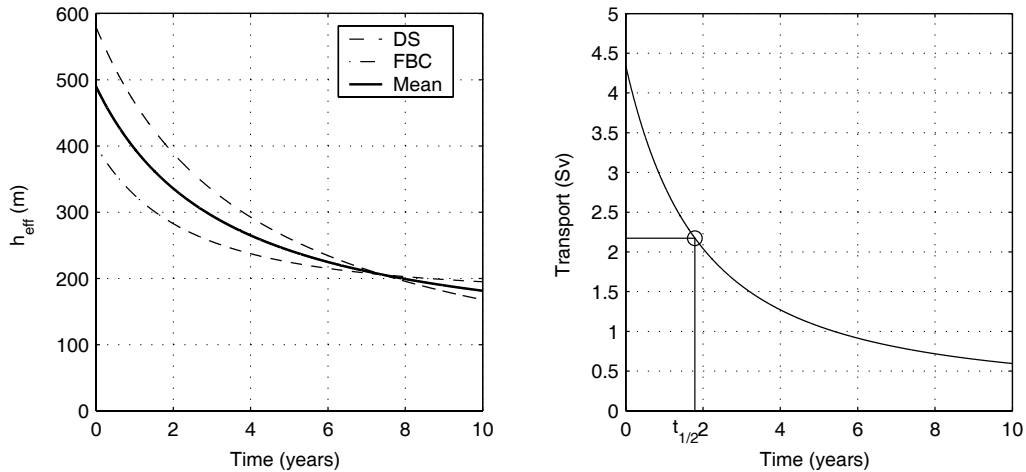


Figure 5.7.: The change of reservoir height for the DS and FBC separately and combined and the spin-down of the overflow transport for a given reservoir.

spin-down reveals that the time for the reservoir to decrease to half the initial height takes almost two years. The transport changes for one year without restoring the reservoir would cause a decrease in transport of 1.75 Sv for DS and FBC together. Thus the interannual

timescale for the reservoir depletion reduces the seasonal and inter-annual variability in the overflows and may explain the relatively constant transport estimates from observations as suggested in *Whitehead et al.* [1974]. Moreover, the seasonal signal might be reduced due to the fact that density changes on seasonal time scales will occur north and south of the Denmark Strait and thus partly cancel each other out.

The above results suggest that changes in reservoir height are expected to give an in-phase signal for DS and FBC overflows if fed from the same reservoir. Therefore, one would expect an in-phase behaviour of DS and FBC for NAO related upstream changes (reservoir height, density contrast). This would be consistent with the modelling results of [*Nilsen et al.*, 2003] who obtained such an in-phase relation but in contrast to the results of [*Biastoch et al.*, 2003] who showed an anti-correlation. However, these results on the correlation of the overflows should be taken with caution since the effect of wind stress would alter the theoretical relation (Eq. 5.3).

Apart from the long-term correlation, there is a pronounced short term variability of DSOW transport in the range of 2-10 days [*Saunders*, 2001], which could be correlated to the FBC overflow as well. The time series of the volume transport in the density class with the highest export of dense water (Figure 5.8 A) reveals the short term correlations of the transports across the separate parts of the GSR (Figure 5.8 B). The analysis yields a statistical significant² negative correlation for DS and IFR of $\rho_{xy}=-0.60$ at zero time lag but a positive correlation of $\rho_{xy}=0.58$ at time lag +1 days. This could be interpreted as a barotropic oscillation around Iceland with a period of one day. This would be closely linked to the theory of *Fristedt et al.* [1999] who explained the evolution of eddies at the Denmark Strait with the help of instable barotropic waves with a period of 1-2 days. The correlation of FBC and DS is rather weak at zero time lag with $\rho_{xy}=-0.16$ and slightly increases in amplitude to -0.29 at -1 days time lag. In principle a short term correlation could be accomplished via barotropic waves adjusting the surface elevation gradient, but the observed correlation seems to weak to justify the idea of a short term coupling of the deep overflows. IFR and FBC are weakly positive correlated with $\rho_{xy}=0.17$ and $\rho_{xy}=0.26$ at time lag zero and +2 days, respectively. In the model the FBC outflow is partly leaving through the WTR, which has a negative correlation with DS of $\rho_{xy}=-0.27$ and the IFR of $\rho_{xy}=-0.22$ but positive with the FBC with $\rho_{xy}=0.24$.

Overall the short term (O (days)) correlation between the individual overflows is quite weak in the model. The strongest and most plausible correlation is between DS and IFR. On long-term timescales, representing changes in the upstream basin, e.g. density contrast across GSR and reservoir height, the behaviour is different. *Nilsen et al.* [2003] find for the net-flux for a 3 year low-pass filtered time series a negative correlation of DS and IFR of $R=-0.80$ and positive with the FSC of $R=0.74$. The IFR and FSC are correlated with $R=-0.59$ in their study.

5.2. Last Glacial Maximum Circulation

5.2.1. LGM experiments

A second series of sensitivity experiments (Table 5.4) was carried out to investigate the effects of a change from PD to LGM conditions for hydrography, bathymetry and wind

²The statistical significance arises from the rejection of the null hypothesis $\rho_{xy} = 0$ based on a t-test on the 95% confidence interval with 70 degrees of freedom (cf. Equation 8.7 in *von Storch and Zwiers* [1999]).

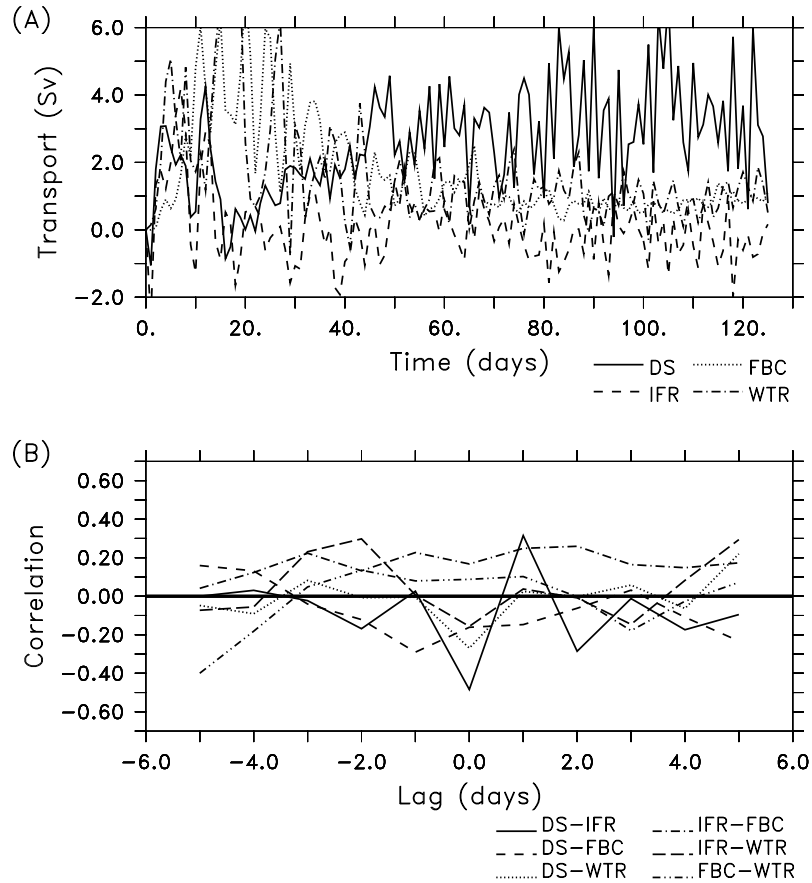


Figure 5.8.: (A) Time series of transport in the density class of maximum transport of dense water for Denmark Strait (DS), Iceland-Faroe Ridge (IFR), Faroe-Bank channel (FBC) and Wyville-Thomson Ridge (WTR) and (B) lagged correlation between the different time series. A positive correlation of e.g. +1 for DS-IFR means that IFR is leading DS by one day.

stress. The model GSR was configured to represent LGM summer conditions by using the bathymetry from the isostatic rebound model (Chapter 1) and boundary conditions for the hydrography from global model results of *Paul and Schäfer-Neth* [2003] and *Meissner et al.* [2003]. The wind stress AGCM-2 [S. Lorenz and G. Lohmann 2001, pers. comm.] is from a revised version of the AGCM of *Lohmann and Lorenz* [2000] employing the latest GLAMAP SST reconstructions [*Sarnthein et al.*, 2003b]. AGCM-1 uses the anomalies of the aforementioned model results added to the reanalysis of NCEP/NCAR.

Experiment	Time slice	Buoyancy	Wind stress
GSR-21ka-A	21.5 ka BP	LGM-1	none
GSR-21ka-B	21.5 ka BP	LGM-1	AGCM-1
GSR-21ka-C	21.5 ka BP	LGM-2	AGCM-1
GSR-21ka-D	21.5 ka BP	LGM-1	AGCM-2

Table 5.4.: Overview of experiments with average density profiles and wind forcing. Buoyancy profile LGM-1 is based on *Paul and Schäfer-Neth* [2003] and LGM-2 on *Meissner et al.* [2003].

The transport in density classes (Figure 5.9) was analysed on the same cross-sections as for PD. The LGM transport can be compared to PD (Figure 5.1) when taking into account for the global shift in density by ≈ 0.86 due to the salinity raise of 1.07^3 . For PD the overflow density can be derived by examining the velocity shear and identifying the overflow plume from the zone of maximum shear. The same approach for LGM conditions is more difficult due to the enhanced barotropic fraction of the velocity field and the core of the overflow plume is not as well defined as for PD. Based on the PD overflow definition but adding the global density increase one obtains a value of 28.75 as glacial overflow density.

For Denmark Strait (upper left panel in Figure 5.9) it becomes apparent that the wind stress is a crucial element for the volume transport across the sill. If wind stress is absent (GSR-21ka-A) the pressure gradient causes a small northward transport. Once wind stress is applied (GSR-21ka-B,C,D) the net flow in all density classes is southward as for PD. The transport differences due to different wind stress estimates (compare GSR-21ka-B and D) amounts to 0.5 Sv. The hydrography from different global LGM models (compare GSR-21ka-B and C) agrees qualitatively showing a southward flow of comparable magnitude (≈ 1.5 Sv). (Table 5.5).

Experiment	Time slice	Q_{DSOW} (Sv)	Q_{barotrop} (Sv)
GSR-21ka-A	21.5 ka BP	0.00 ± 0.00	-0.16 ± 0.02
GSR-21ka-B	21.5 ka BP	0.30 ± 0.00	1.33 ± 0.02
GSR-21ka-C	21.5 ka BP	0.00 ± 0.00	1.83 ± 0.05
GSR-21ka-D	21.5 ka BP	0.21 ± 0.00	0.86 ± 0.02

Table 5.5.: Volume transport from the GSR-21ka experiments with DSOW being the transport of dense water only and total is the full, depth integrated transport. Note that the forcing is constant and that there is almost no variability in transport.

The robust results of these very different initial conditions and forcings is that the total LGM overflow was strongly reduced to not more than 0.3 Sv. The exchange across the IFR

³In GSR-21ka-C the density class was artificially increased by 0.86 because the global salinity increase was not taken into account in the experiments of *Meissner et al.* [2003].

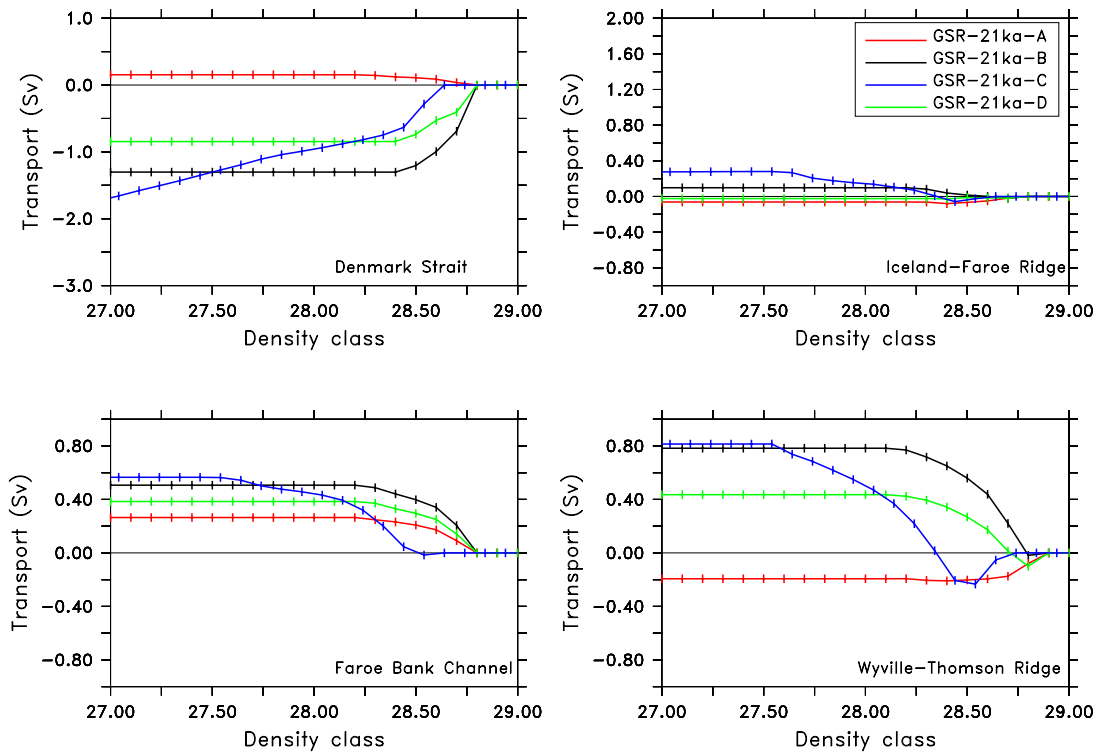


Figure 5.9.: Cumulative transport of dense water across the Denmark Strait, the Iceland-Faroe Ridge, the Faroe Bank Channel and the Rockall Trough. Positive values correspond to northward (eastward) and negative values to southward (westward) transport. The transport is integrated from high to low densities and the density class is associated to the lower bound. The midpoint of the $0.1 \sigma_\theta$ wide density bins is indicated as vertical line.

has nearly ceased, with only weak northward advection in GSR-21ka-B and C and very weak southward flow in GSR-21ka-A and D. The outflow through the FBC has vanished in this LGM simulation instead there is inflow from the Atlantic into the Nordic seas. However, the FBC is not well represented and the outflow of dense water across the WTR should be at least partly attributed to the FBC. Nevertheless, there is advection at depth of warm water through both FBC and WTR towards the north (Table 5.6). The reference temperature for the LGM was kept at 0°C to be consistent with present-day even though a lower value might be more appropriate [Labeyrie *et al.*, 1987]. However, when using a reference temperature of -2°C instead of 0°C the difference between present-day and LGM heat transport is almost the same (+1 TW).

Exp.	DS		IFR		FBC		WTR		Sum	
GSR-0ka-A	33	(44)	74	(78)	34	(44)	-15	(-3)	125	(163)
GSR-0ka-B	3	(32)	74	(77)	40	(48)	30	(37)	148	(194)
GSR-0ka-C	-26	(31)	88	(91)	51	(59)	78	(83)	191	(264)
GSR-0ka-D	-92	(22)	126	(122)	50	(59)	207	(210)	292	(412)
GSR-21ka-A	5	(5)	2	(2)	8	(8)	-3	(2)	12	(17)
GSR-21ka-B	-7	(3)	4	(5)	11	(11)	34	(36)	43	(54)
GSR-21ka-C	-2	(0)	8	(7)	13	(5)	13	(15)	32	(27)
GSR-21ka-D	-3	(3)	1	(2)	10	(10)	11	(15)	19	(30)

Table 5.6.: Estimates of heat fluxes (relative to 0°C) in TW (1 TW=10¹² W) for the Greenland-Scotland ridge split into Denmark Strait (DS), Iceland-Faroe Ridge (IFR), Faroe Bank Channel (FBC) and Wyville-Thomson Ridge (WTR). The values in brackets are calculated for the heat transport associated to water warmer than 4.5°C in order to estimate the inflow of Atlantic Water at the surface.

The heat transport in the reference run (GSR-0ka-B) yields 3 TW net northward heat transport through DS. This can be split into a cold southward flow and a warm northward flow. The flow of water warmer than 4.5°C provides an estimate of the heat transport with the Irminger Current, which is 32 TW in the model for DJF as compared to 25 TW as annual mean in observations [Hansen and Østerhus, 2000]. The heat transport with the North Icelandic Irminger Current was observed to be variable on seasonal timescales with a minimum in March and a maximum in May [Kristmannsson, 1998]. The winter estimate (DJF) taken here should be quite close to the annual mean. The total heat transport in the model relative to 0°C is 148 TW across the GSR which underestimates the actual transport due to the closed domain. From observations [Bacon, 1997] the annual mean total heat transport through 60°N is about 280 TW but is further reduced when reaching the GSR. Thus the Irminger Current is overestimated whereas the transport with the Faroe Current and Shetland Current is underestimated.

After the discussion of the main forcing mechanisms for PD the experiments were extended to glacial times. First one should take into account for the fact that the LGM experiments heavily depend on the glacial SST and SSS reconstructions of the GLAMAP project [Sarnthein *et al.*, 2003a]. GLAMAP updates the older CLIMAP [1981] reconstructions by better representing glacial cooling in the tropics [cf. Crowley, 2000] and ice-free Nordic Seas [Weinelt *et al.*, 1996]. However, there are different SST reconstructions. Based on the modern analogue techniques on dinoflagellate cysts *de Vernal and Hillaire-Marcel* [2000] predict a more extensive sea-ice cover than GLAMAP. In joined interpretation with vertical density profiles based on $\delta^{18}\text{O}$ values the reconstructed SSTs indicate that deep water formation north of 50°N was absent [de Vernal *et al.*, 2002]. These reconstructions

might be less reliable due to a likely redepositions of the dinoflagellate cysts [Sarnthein 2002, pers. comm.] since most other studies find a less extensive sea-ice cover and indications for deep water formation within the Nordic Seas [Weinelt *et al.*, 1996; Trend-Staid and Prell, 2002; Sarnthein *et al.*, 2003b].

The LGM heat transport across the GSR varies dependent on the wind stress and density structure employed in the range of 19 to 43 TW, which is 13-29% of PD (29% comparing the reference experiments GSR-0ka-B and GSR-21ka-B). Weinelt *et al.* [2003] suggest a heat transport across the IFR and WTR between 110 and 130 TW or 50% of the modern value during D/O interstadial and almost zero during stadial/full glacial conditions. From the model the heat transport for LGM conditions across IFR, FBC and WTR is reduced from 145 TW to 50 TW or 34% of the modern value for D/O interstadials (glacial summer) conditions. It has to be stressed that the reconstructions of heat transport are subject to considerable uncertainty and therefore the modelling results and reconstructions are in agreement. This is not too surprising since the model GSR-21ka-B was forced with the GLAMAP reconstructions, which are the basis for the heat transport estimates of Weinelt *et al.* [2003]. However, further corroboration comes from the LGM model driven by the output of the coupled model (GSR-21ka-C) which arrives at a similar glacial heat transport across IFR, FBC and WTR of 34 TW.

The wind field obtained by Lorenz and Lohmann [2001, pers. comm.] based on the GLAMAP reconstructions shows increased wind velocities in the North Atlantic during glacial times. From the Sverdrup balance one would expect a stronger subtropical and subpolar gyre in contrast to reconstructions of a weaker Gulf Stream [Lynch-Stieglitz *et al.*, 1999b] but in harmony with suggestions of Wunsch [2003]. This points out that the barotropic flow component might have played a more important role in glacial times, which will be inspected more closely in the next chapter. Moreover, the relative strengthening of the transport through DS as compared to the FSC with increasing wind stress can potentially help to interpret the sediment records in the area of the FSC. Rasmussen *et al.* [1996] found that during cooling intervals benthic foraminifera reflect the gradual cooling as does the record of magnetic susceptibility whereas for planktic foraminifera the change is rather abrupt. In light of the experiments with varying wind forcing this can be explained as a nearly constant inflow of Atlantic Water into the Nordic seas but an increased outflow through the DS and a reduction for the FSC.

The advection of Atlantic Water into the Nordic Seas during glacial times based on reconstructed SST gradients has been assumed to occur as an Irminger Current equivalent through the Denmark Strait [Weinelt *et al.*, 1996; Sarnthein *et al.*, 2003b]. This view is not consistent with our modelling results (Figure 5.10), which indicate a rather weakened Irminger Current and inflow as ongoing North Atlantic Current. This view can be strengthened when using a map based on objective analysis mapping [Schäfer-Neth and Paul, 2003] of the core-based SSTs instead of the subjectively interpolated map (isoline maps in Pflaumann *et al.* [2003]).

Moreover, the interpretation of a still existent NAC is supported by the fact that the large-scale time mean flow follows contours of f/H [Nøst and Isachsen, 2003] which is consistent with the flow path proposed here. This is essentially similar to the modern surface flow and is further supported by observations of an ice-free Fram Strait [Norgaard-Pedersen *et al.*, 2003] which would be quite difficult to obtain with inflow of Atlantic Water through Denmark Strait only. An inflow of warm Atlantic Water across the eastern part of the GSR during LGM summer is corroborated by yet unpublished results of the MARGO project [M. Weinelt 2004, pers. comm.].

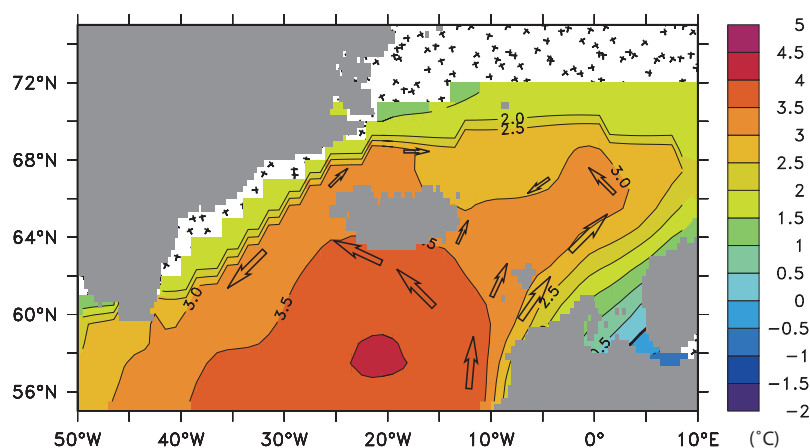


Figure 5.10.: Glacial summer (JJA) sea-surface temperature [Schäfer-Neth and Paul, 2003] and schematic surface circulation (superimposed vectors) and heat transport (size of vectors). The hashed area indicates sea-ice.

The strong reduction of DSOW as modelled for glacial conditions is consistent with reconstructions based on sedimentological evidence [Kuijpers *et al.*, 1998, 2003]. The hypothesis of a reversed overflow [Vogelsang, 1990] based on reconstructed ventilation rates is not supported. Even though nearly stagnant conditions can be expected from a vanished density contrast the wind driven part will have led to a net southward export.

As the model employed here is too limited in spatial extent and integrated for a too short time it cannot reproduce the deep water formation but depends on the correct representation of the main hydrographic structure as derived from the global models [Paul and Schäfer-Neth, 2003; Meissner *et al.*, 2003]. The exact location of the deep water formation sites might not be as crucial as initially assumed since the experiments employ both a global model with deep water formation in the Nordic seas [Paul and Schäfer-Neth, 2003] and without [Meissner *et al.*, 2003] and both yield comparable results concerning the cross-sill density contrast and inferred overflow transports.

5.2.2. The role of wind driven heat transport for ice free glacial Nordic Seas

The previous sections have repeatedly pointed out the importance of the wind driven transport. In the following a brief comment is given on the general implications of the glacial wind field as it is of special importance to the northern North Atlantic. First, it should be pointed out that an increase of wind stress over the North Atlantic, as found in model results for the last glacial [Lorenz and Lohmann 2001, pers. comm.] (Figure 5.11), would cause an increased horizontal gyre circulation, i.e. a stronger subpolar and subtropical gyre. A simple model of the wind driven circulation is to consider the Sverdrup relation [Ohshima *et al.*, 2004]. The volume transport streamfunction Ψ is calculated from the Sverdrup relation

$$\Psi = -\frac{1}{\beta \rho} \int_x^{x_e} \nabla_h \times \tau dx, \quad (5.5)$$

with $\beta = \frac{\partial f}{\partial y}$ as the meridional gradient of f . The Sverdrup relation is integrated from the eastern boundary (x_e) to the west where a value of 0 is set at the coast in regions shallower than 300 m. In Figure 5.12 the Sverdrup transport is shown for the PD wind field as derived

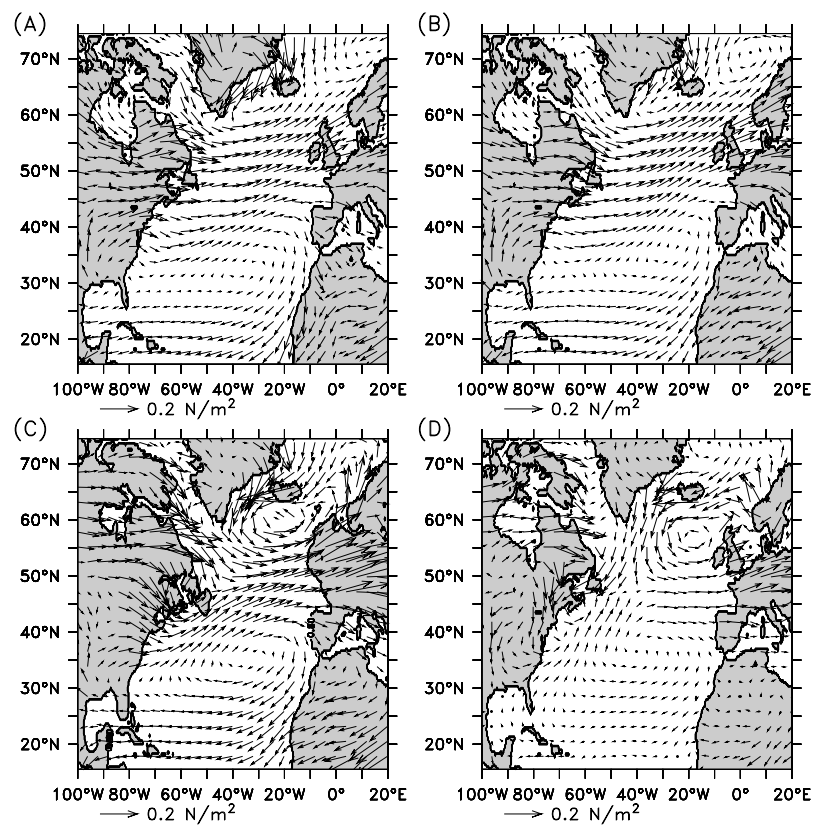


Figure 5.11.: Wind stress as derived from NCEP/NCAR (A), from AGCM-1 for PD (B) and LGM (C) and in (D) the anomaly LGM-PD. Comparison of (A) and (B) suggests that the AGCM wind fields are very similar to the ones from the reanalysis based on observations.

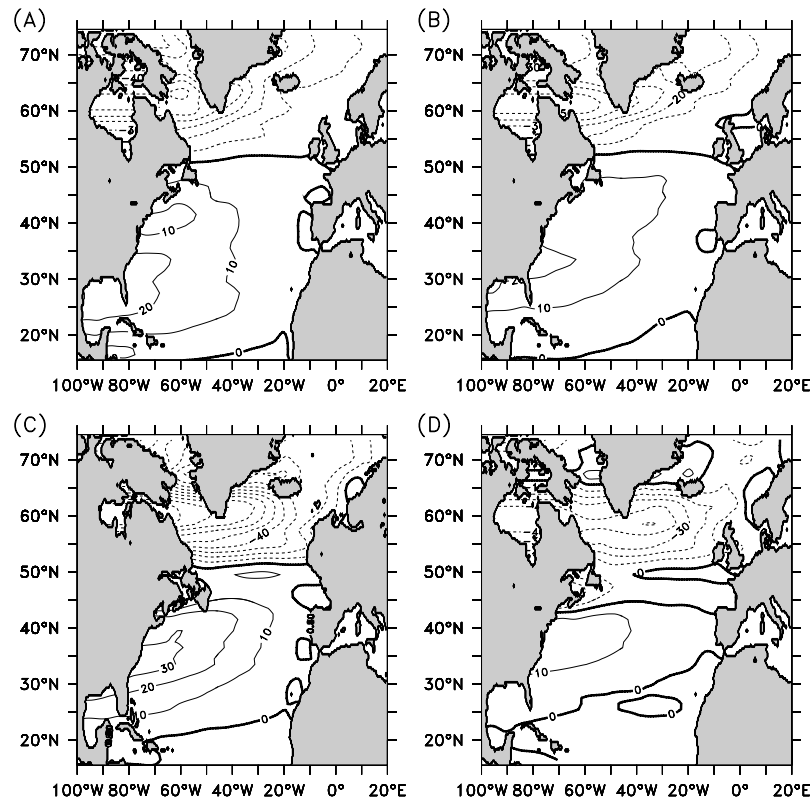


Figure 5.12.: The Sverdrup volume transport streamfunction as derived from NCEP/NCAR (A), from AGCM-1 for PD (B) and LGM (C) and in (D) the anomaly LGM-PD. Solid contours indicate anti-cyclonic circulation and dashed contours cyclonic circulation. The contour interval is 10 Sv. Note that the Sverdrup balance account for western boundary currents.

from a long term mean (1948-2003) of NCEP/NCAR and from a LGM atmospheric model driven by GLAMAP SST data [Paul and Schäfer-Neth, 2003].

The connection between heat transport and wind driven circulation is not straightforward and depends on the exact way of calculating or decomposing the mass transport. Bryden and Imawaki [2001] arrive at a gyre contribution to the northward heat transport in the North Atlantic of 10% from decomposing hydrographic sections whereas [Talley, 2003] obtains a gyre contribution of 50% from a mass balance analysis. Despite these discrepancies it is likely that the relative gyre contribution was more important for the LGM due to the increase in the horizontal mass transport (Figure 5.12) and a decreased MOC. The wind driven heat transport can help to explain the advection of warm Atlantic Water to the Northern North Atlantic and thus provides a potential energy source of ice free Nordic seas during the LGM.

The importance of wind stress and associated Ekman transport becomes apparent when comparing the LGM wind stress curl with PD values and the amplitude of positive and negative NAO phases (Table 5.3). Assuming a continuous stratification with no pressure gradient driven transport the purely wind driven transport would result in almost 2 Sv for the LGM compared to 1.1 Sv for PD. A rough estimate on the strength of the wind driven part of the Irminger Current can be obtained from a direct calculation of Ekman transport from the NCEP/NCAR data (45° W - 20° E, 65° N) which yields 0.4 Sv northward flow for PD and 0.3 Sv for the LGM data of Lorenz and Lohmann [2001, pers. comm.].

5.3. Blocking Denmark Strait

van Kreveld *et al.* [2000] have proposed based on paleoceanographic data that icebergs could have blocked Denmark Strait during the last glacial period creating a pacing mechanism for D/O events. The hypothesis of an iceberg blocking is supported by evidence from iceberg ploughmarks [Kuipers *et al.*, 2003], which indicate that icebergs reached as far down as to a depth of 900 m in the Iceland-Faroe Ridge, 350 m in the West Shetland margin and about 600 m in Scoresby Sund. The orientation of plough marks close to the Denmark Strait (Kangerlussaq region) is interpreted in the sense that massive icebergs were transported south with the EGC. However, the timing of these events is uncertain and they could have originated from paleo-ice sheet margins.

Assuming that the Denmark Strait was blocked the effect of such a closure of Denmark Strait is examined by artificially closing or partially blocking Denmark Strait in the model (Table 5.7). The effect of a partial blocking was assessed by the distribution of four idealised, large icebergs (12 km diameter⁴) across Denmark Strait.

Experiment	Time slice	Denmark Strait
GSR-0ka	0 ka BP	open
GSR-0ka-part	0 ka BP	partially blocked
GSR-0ka-block	0 ka BP	closed
GSR-21ka	21 ka BP	open
GSR-21ka-part	21 ka BP	partially blocked
GSR-21ka-block	21 ka BP	closed

Table 5.7.: Overview of experiments assessing the influence of closing or partially blocking DS. The set-up for PD is that of GSR-0ka-B and that for the LGM is taken from GSR-21ka-B.

⁴The size of the icebergs corresponds to two closed grid boxes in the model and is similar to the 10 km diameter icebergs used in Schäfer-Neth and Stettger [1999].

The volume transport in density classes for PD conditions (Figure 5.13) reveals the main effects of a closed DS. The missing overflow transport through DS is partly compensated by an increase in the dense water transport across the IFR, the FBC and the WTR. The

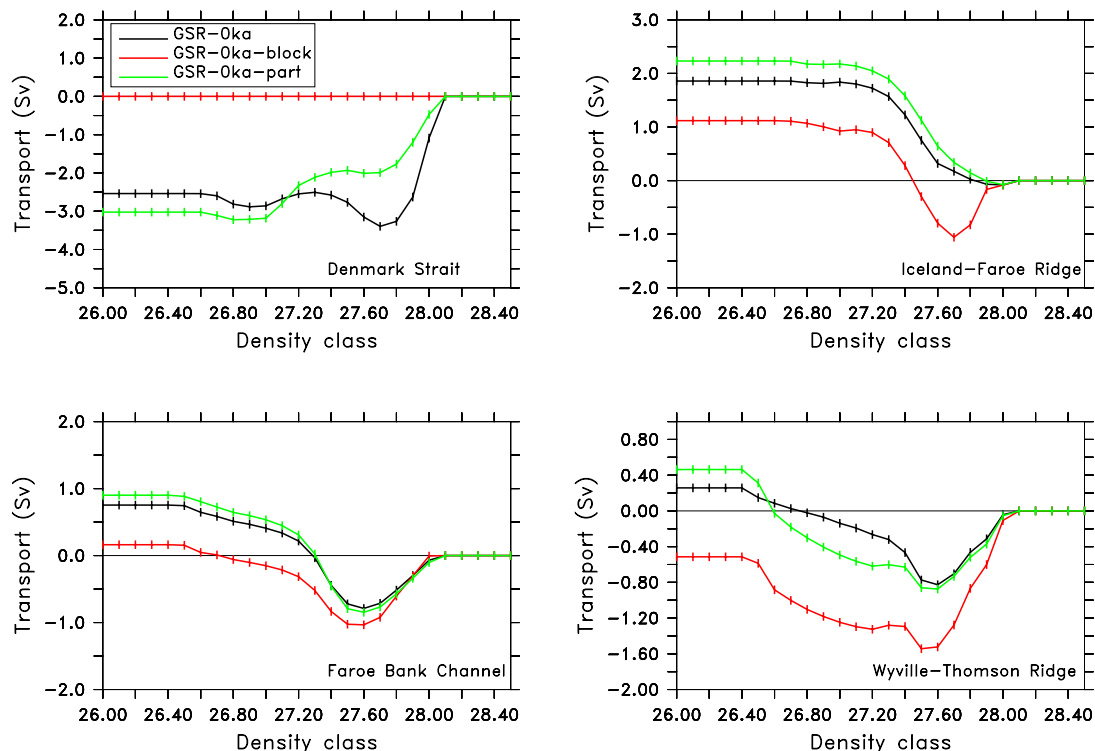


Figure 5.13.: Transport in density classes for open, partially blocked and fully blocked Denmark Strait for PD conditions.

total dense overflow transport reduces from 5.1 Sv to 3.6 Sv if DS is blocked and to 3.8 Sv if it is only partly blocked. The surprisingly strong effect of the partial blocking is due to an increased entrainment. The constrictions in the strait cause stronger mixing and enhanced entrainment of the overflow water leading to a reduction of overflow transport from 3.4 Sv to 2.0 Sv, even though the net outflow through DS is slightly increasing due to a reduced southward flow. In the IFR section the closed DS is compensated by a pronounced increase in dense water transport by 1 Sv. The combined effect of WTR and FBC is approximately of equal importance and increases by 0.9 Sv.

For LGM conditions the response to a closing of DS are qualitatively similar but of smaller magnitude. If DS is open or only partially closed virtually all of the dense overflow across the GSR leaves through the DS. If DS is closed there are small (up to 0.5 Sv) but distinct dense outflows for the remaining parts of the GSR. The net northward flow through IFR and FBC changes to a net southward flow.

The changes in the flow structure as a response to the closure of the DS are shown as the velocities on the isopycnals defining dense water and the depth of that isopycnal. For the PD reference run (Figure 5.15) it is fairly easy to identify the two main pathways of dense water. One passes through DS following the Greenland shelf break and the second passes through the FBC and the WTR. A partly blocked DS causes disturbances in DS and reduces the transport. A remarkable feature of the experiments with a closed DS is the additional

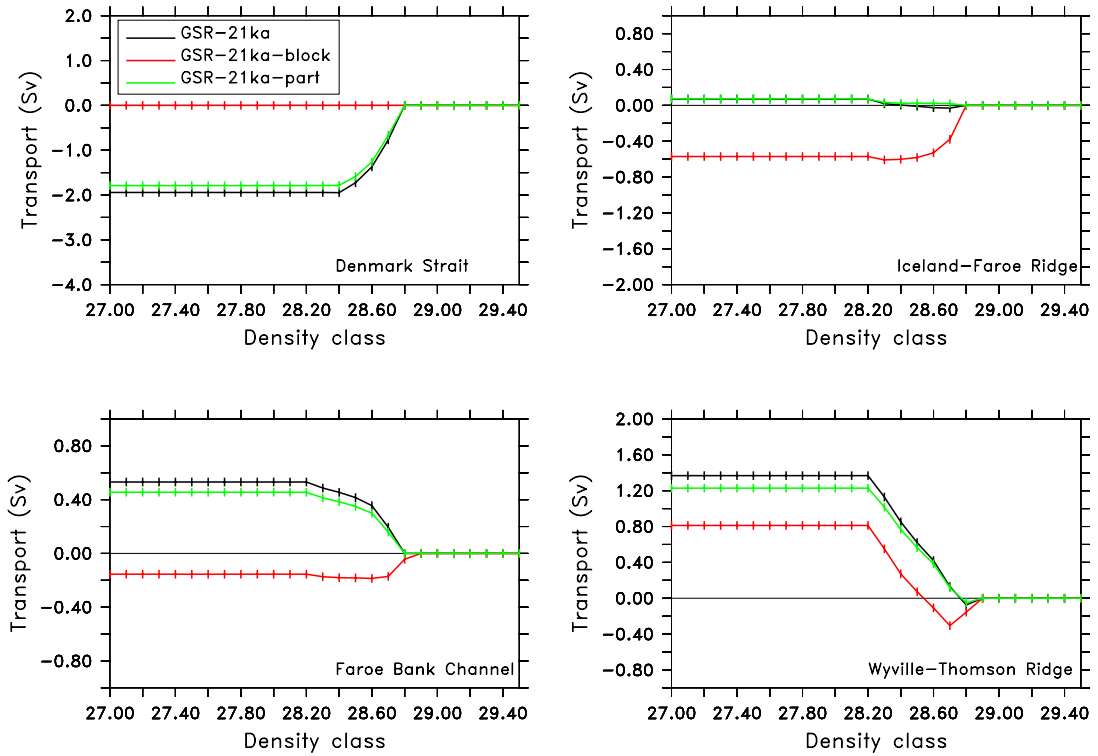


Figure 5.14.: Transport in density classes for open, partially blocked and fully blocked Denmark Strait for LGM conditions.

pathway for dense water across the IFR. It crosses the Reykjanes Ridge (RR) at shallower depth (<1000 m) as before (~ 1500 m). Interestingly, this new path comes very close to the now closed DS outflow and resembles the transport of DSOW. In the other two experiments ISOW would cross through the Charlie-Gibbs Fracture Zone (CGFZ), which is not included in the model domain. The LGM pathways (Figure 5.16) are essentially similar and the glacial equivalents to DSOW and ISOW can be easily identified. Comparing modern and glacial circulation there are a number of remarkable differences. For PD conditions the circulation of dense water in the Iceland Basin is dominated by the outflows of WTR and FBC whereas for LGM conditions a flow along the Scottish shelf break has developed circulating through the northeastern North Atlantic. To some extent these differences arise from the different depths of the isopycnals but the enhanced circulation along the Scottish Shelf break can be traced to deeper depths (not shown).

A consequence of a closed DS and the increased dense water export through the FSC is that the northward advection of warm water is diminished and hence the heat transport of the experiments with an open and (partially) blocked DS yield quite different results (Table 5.8).

A full blocking of the DS obviously stops the heat transport through it, but it strongly influences the whole GSR. Under PD conditions a closure of Denmark Strait would cause an 19% decrease in northward heat transport and for LGM conditions it would result in a reduction by 63%. Primarily, this is due to the increased southward flow of cold water across the IFR and a strong reduction of northward heat transport through the Faroe-Shetland Channel. Since the Denmark Strait is a region of net outflow, closing it leads to

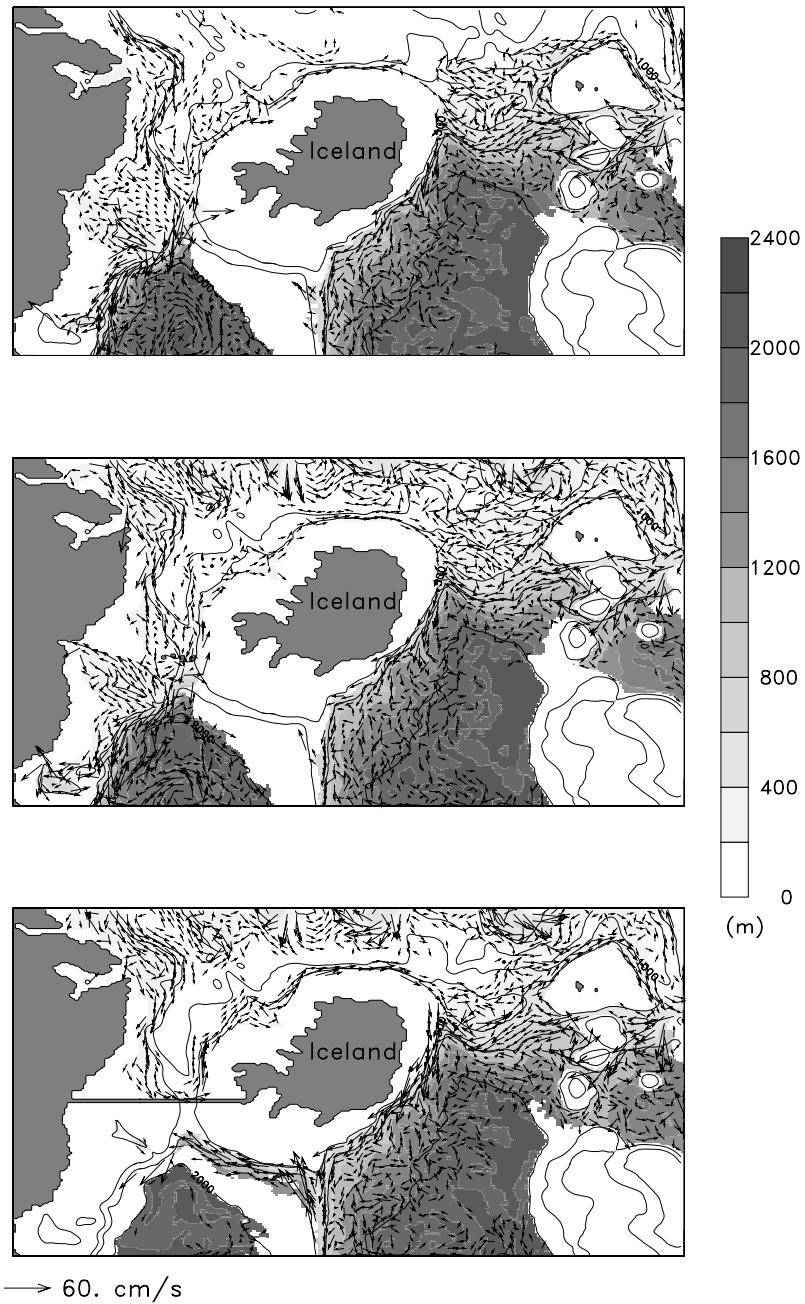


Figure 5.15.: Depth (shading) and velocity (vectors) of the 27.8 isopycnal for PD winter conditions. The top row is for a free exchange through the Denmark Strait, the middle row represents the partially blocked case and in the bottom row the DS is fully blocked. Note the increasing depth of the isopycnal surfaces south of the GSR.

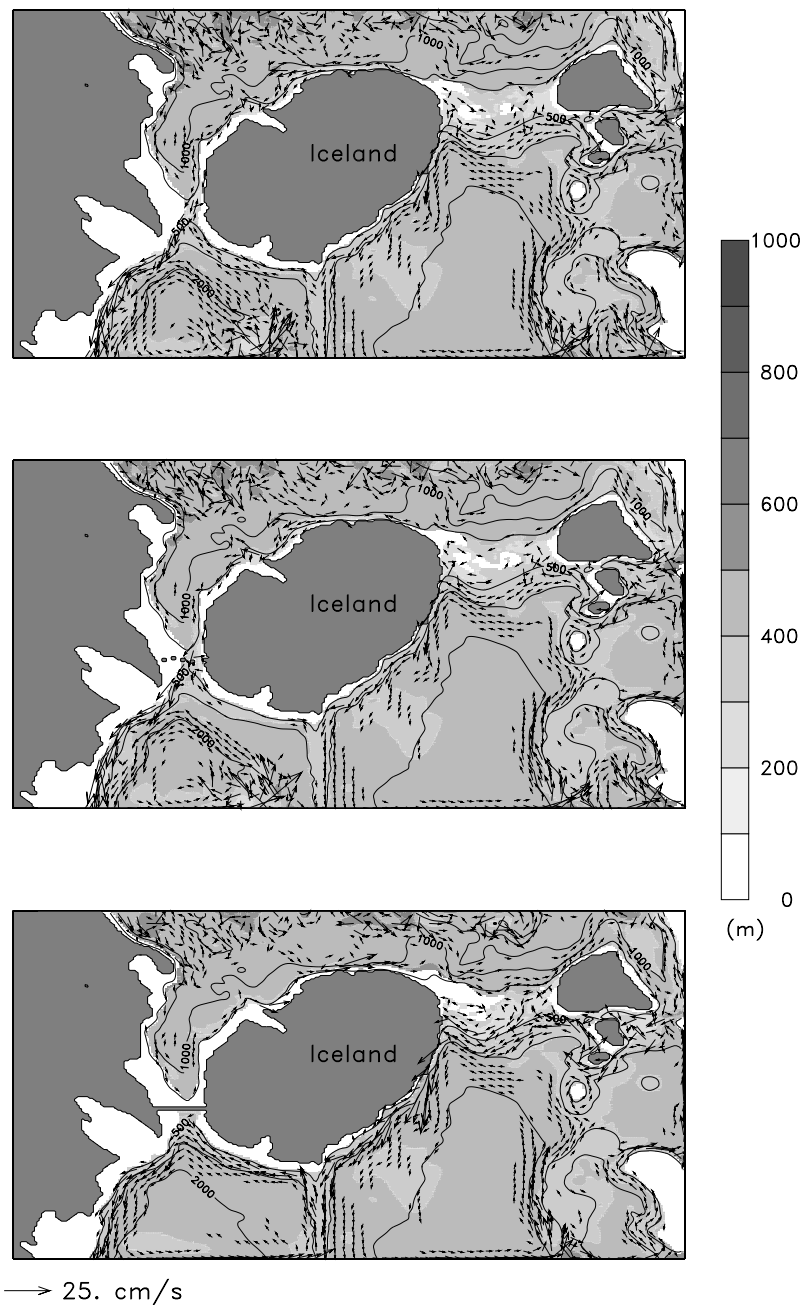


Figure 5.16.: Depth (shading) and velocity (vectors) of the 28.75 isopycnal for LGM summer conditions. The top row is for a free exchange through the Denmark Strait, the middle row represents the partially blocked case and in the bottom row the DS is fully blocked. Note that the increasing depth of isopycnal surfaces south of the GSR for PD conditions is absent for LGM conditions.

Exp.	DS		IFR		FBC		WTR		Sum	
0ka	3	(32)	74	(77)	40	(48)	30	(37)	148	(194)
0ka-part	-23	(8)	85	(87)	41	(51)	55	(61)	157	(207)
0ka-block	0	(0)	62	(83)	31	(40)	28	(38)	120	(160)
21ka	-7	(3)	4	(5)	11	(11)	34	(36)	43	(54)
21ka-part	-6	(1)	4	(5)	10	(10)	33	(34)	41	(49)
21ka-block	0	(0)	-2	(3)	0	(0)	18	(25)	16	(28)

Table 5.8.: Estimates on heat fluxes (relative to 0°C) in TW (1 TW=10¹² W) for the Greenland-Scotland Ridge split into Denmark Strait (DS), Iceland-Faroe Ridge (IFR), Faroe Bank Channel (FBC) and Wyville-Thomson Ridge (WTR). The values in brackets are calculated from the transport of water warmer than 4.5°C.

increased outflow over the remaining GSR and hence reduced inflow of warm water in order to close the volume export balance. With an open DS the deep overflows are compensated by surface inflow, for a closed DS this surface inflow across the IFR is reduced and it is increased at mid depth across the WTR, where less heat is advected northward.

A remarkable feature is the consistently high northward flow across the WTR compared to the other parts of the GSR. One could speculate that this will lead to a damping of millennial scale climate signals at locations recording this inflow as found by *Risebrobakken et al.* [2003]. Moreover, a positive feedback mechanism was identified as resulting of stronger overflow across the IFR once the DS is closed further reducing the northward heat transport which supports the hypothesis of *van Kreveld et al.* [2000].

5.4. Dispersal of marine biota

Active dispersal of benthic foraminifera through self-locomotion is considered not to be important but the dispersal is made possible by passive mechanisms through release of juveniles and the transport at various growth stages [*Alve*, 1999]. In experiments GSR-0ka-B and GSR-21ka-B Lagrangian drifters were deployed to simulate the cross-ridge transport of planktic and benthic foraminifera by passive advection for PD and glacial conditions. A total of 900 drifters were released at three different locations and advected horizontally and vertically following the modelled velocity field. Firstly, north of the Denmark Strait randomly distributed over a depth range of 0 m - 1400 m centred at 410 m to follow the dense water pathway. Secondly, south of the DS at a depth range of 140 m - 1100 m centred at 450 m to trace the Irminger Current. And thirdly, east of Iceland to monitor the IFR water masses at a depth range of 0 m - 560 m centred at 250 m. In Figure 5.17 the density of float trajectories is shown for PD winter and LGM summer conditions and for the different release areas.

The pathways for PD conditions reflect the surface circulation scheme as described in *Hansen and Østerhus* [2000]. The floats released south of the DS are advected anticyclonic around Iceland within the model's North Icelandic Irminger Current, whereas the floats released in north of the DS mainly follow the Denmark Strait overflow. The northward advection with the NAC of the floats released at the IFR is not pronounced enough due to a too weak NAC in the model as a result of the closed boundaries. Nevertheless, the wind forced inflow to the Nordic seas along the shelf break north of the Faroes appears realistic compared to observations [*Orvik and Niiler*, 2002]. In the area around Iceland, which is most important for this study, the model can reproduce the main features of drifter observations

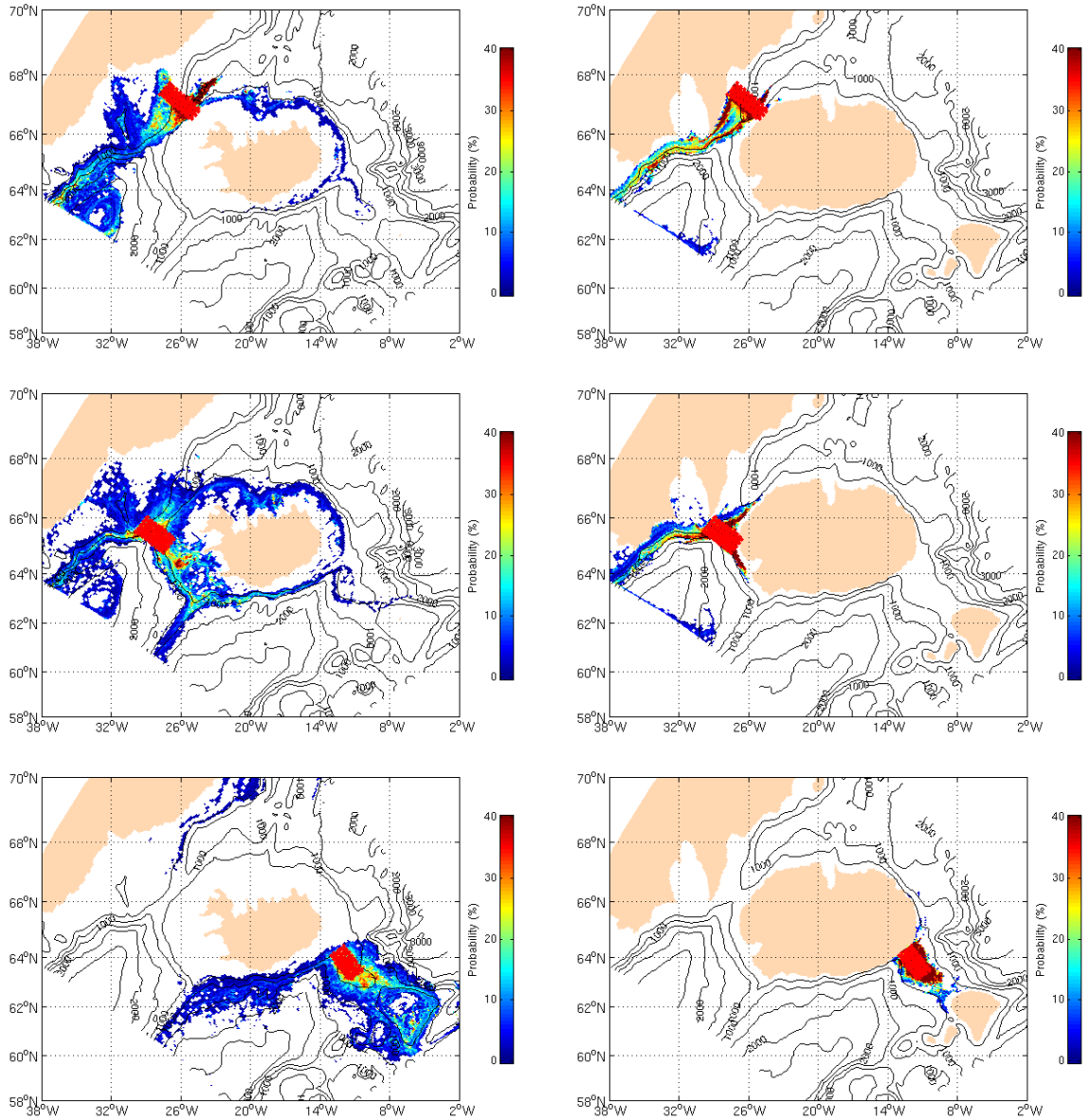


Figure 5.17.: Float distribution for PD winter (left column) and LGM summer (right column) conditions for different areas of release (first row: north of DS, second row: south of DS and third row: east of Iceland). The release area is marked by red dots. The shading indicates the probability that all particle reach this area within 110 days after release. A value of for instance 10% would mean that 10% of the particles released reach that particular spot.

[*Jakobsen et al.*, 2003], such as the anti-cyclonic circulation around Iceland.

Concerning the differences between PD and LGM conditions the most apparent result is a general reduction of particle advection for glacial conditions. The Irminger Current is strongly reduced and most drifters are transported southwards from DS. The drifter released north of the Denmark Strait cross the sill in a narrow band bound to the shelf break. East of Iceland there is only a very sluggish circulation and there are indications of a weak cyclonic circulation around Iceland as shown in Figure 5.18.

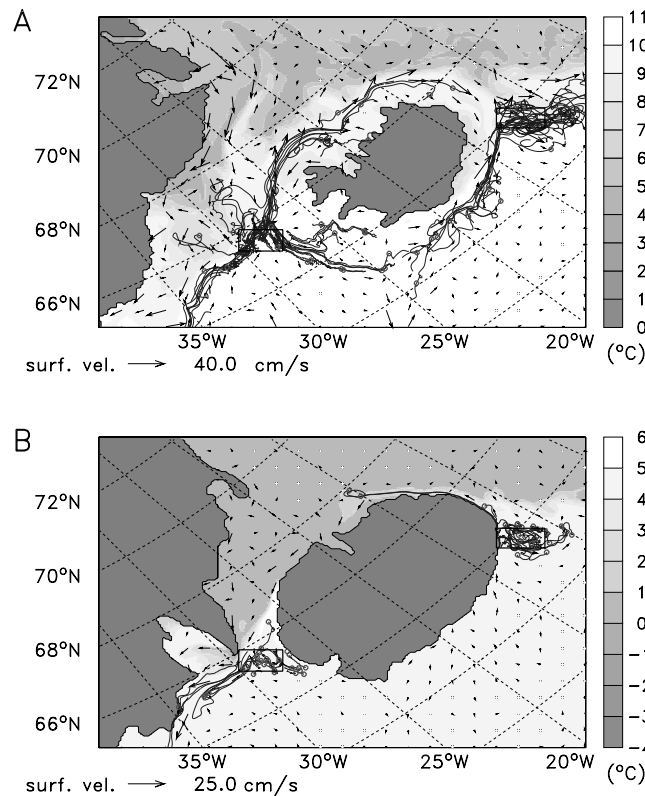


Figure 5.18.: Surface temperature, circulation and Lagrangian drifter pathways for modern conditions from experiment GSR-0ka-B (A) and for glacial conditions from experiments GSR-21ka-B (B).

For modern conditions 17% of the surface drifters released south of the DS follow the Irminger current along the western Icelandic coast, whereas for glacial conditions the northward particle transport is almost (2%) absent. For glacial conditions the results suggest a reversed flow instead, i.e. along the east Icelandic coast towards the north. Between 2% to 6% of the released floats are advected to the north-west of Iceland. One implication of the LGM model experiments is that subpolar planktic foraminifera found at the Northern Denmark Strait [*Völker*, 1999] do not necessarily indicate that there was a northward transport through Denmark Strait but that these organisms could have arrived there via the cyclonic route along the east of Iceland.

The dispersal of marine biota was additionally influenced by a changed tidal structure. As discussed in Section 3.3.3 a net mass or particle exchange can occur without a volume flux by tidal currents. From a global tidal model based on the paleo-topography reconstructions of *Peltier* [1994] an increase by up to 50% of tidal amplitudes has been estimated [*Scourse*

and Uehara 2003, pers. comm.] for times with a lowered sea-level and glaciated shelves (Figure 5.19). In the Denmark Strait the M2-tidal amplitude decreased from 1.2 m at 12 ka

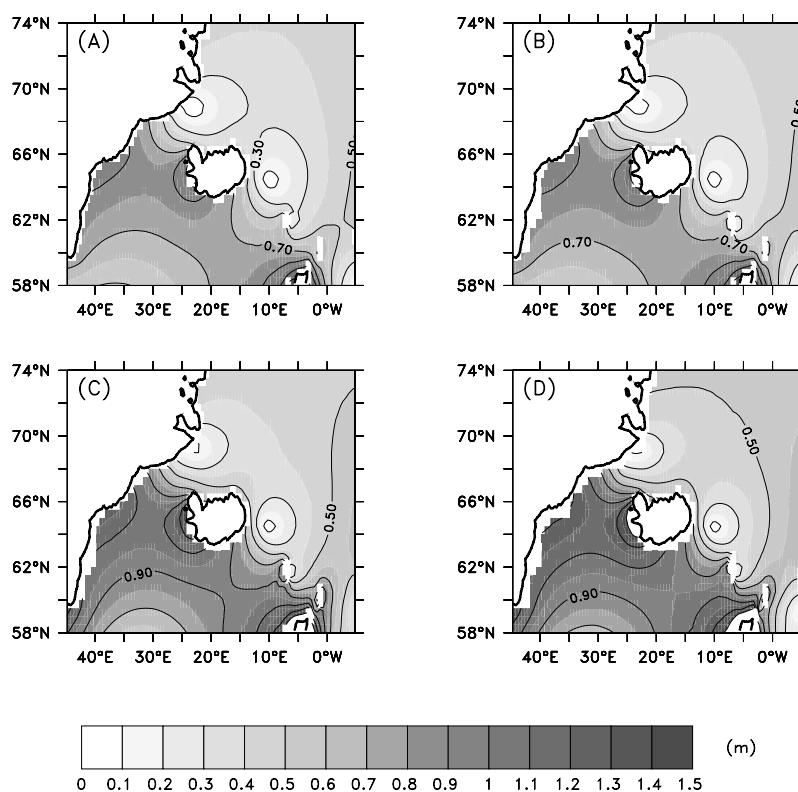


Figure 5.19.: The M2 tidal amplitude for PD (A), 2ka BP (B), 10ka BP (C) and 12ka BP (D) [Scourse and Uehara, unpublished data]. The difference between 2ka BP and PD is small but significantly increased tidal amplitudes are found for 10 ka BP and 12 ka BP, which assume glaciated shelves.

BP to about 0.8 m at 2 ka BP. The reconstructions do not go back to the LGM but 12 ka BP already assumes glaciated shelves and is therefore taken as an approximation for the LGM here. The implications of a higher tidal amplitude are an increased mixing rate due to higher tidal dissipation energy and in turn reduced stratification. Especially for the Denmark Strait this may have led to an additional reduction of sedimentation rates and a reduced stability of the shelf-ice. Even if the tidally induced transport is small it may become important at times with a reduced along-stream density difference and no transport driven by the pressure gradient. Then it may affect the distribution of marine biota as outlined above and can provide a mechanism for faunal cross-strait exchange. The effect of tides has not been taken into account in the model and should certainly be addressed in future model studies examining the dispersal of marine biota in more detail.

The distribution of marine biota from the Lagrangian drifter experiments indicates that the Denmark Strait is certainly not a barrier for the exchange of surface dwelling planktic foraminifera. But even for bottom dwelling foraminifera the results indicate potential dispersal routes both for modern and LGM conditions. These results are in harmony with other results of the research unit Ocean Gateways as outlined below. The potential of the Denmark Strait as a migration barrier for benthic foraminifera was investigated with a morphometric approach [A. Lorenz 2004, pers. comm.]. She compared specimen of the epibenthic

foraminifera *Cibicidoides wuellerstorfi* distributed north and south of the Denmark Strait which typically lives in a depth of 1000 m and might therefore not be able to cross the 600 m deep Denmark Strait. From an oceanographic point of view the sill cannot be a barrier because Bernoulli streamlines easily reach up from 1000 m depth to 600 m and could thus carry organisms from greater depth across the strait. Nevertheless, these currents might not be sufficient to contribute to the cross sill exchange. She found differences in morphometry of the species north and south of the Denmark Strait but such differences are most likely due to different current velocities affecting the net food supply. A high current velocity increases the amount of available food for the suspension feeder *Cibicidoides wuellerstorfi*. A. Lorenz [2004, pers. comm.] concluded that the Denmark Strait cannot be seen as migration barrier and is thus in harmony with the modelling results presented above and with oceanographic consideration.

A second approach was to determine genetic species and potential genetic differences in foraminifera with the same morphotype, similar to the study of *Bauch et al.* [2003] on planktic foraminifera. First results of a station close to Fram Strait indicate that there are benthic foraminifera which were characterised as *Cibicidoides wuellerstorfi* based on their morphotype but which show distinct differences in their 18S rDNA sequence indicating different genotypes [*M. Blümel* 2004, pers. comm.].

5.5. Summary and conclusions

A regional ocean model of the Greenland-Scotland Ridge has been utilised to investigate the dense northern overflows for PD and LGM conditions. The model yields realistic results for PD compared to observations. The sensitivity to wind stress changes was determined and a relationship of wind stress curl and the DSO is suggested. This was applied to the NAO to obtain an artificial overflow transport time series, which reproduces observed transport estimates and some of the trends suggested from observations. The coupling between the Denmark Strait and Faroe Bank channel overflows on short time-scales (O (days)) is not evident, whereas Denmark Strait outflow and Iceland-Faroe Ridge inflow are in phase. The coupling is further studied by closing the Denmark Strait partially and partially. The missing DSO cannot be fully compensated by additional outflow across the Iceland-Scotland ridge but the total transport of dense water is reduced by 30% compared to the case with an open Denmark Strait. Next, the sensitivity study was extended towards LGM conditions investigating volume and heat transport for different density profiles and wind stress. The LGM wind field implies a strengthening of the subpolar gyre and an increased northward heat transport as a possible explanation for the reconstructed ice-free conditions in the Nordic Seas. Finally the dispersal of marine biota was simulated by Lagrangian drifters.

From these experiments the following key results were obtained:

- The PD winter circulation is consistent with the observations of *Rudels et al.* [2002]. There is a direct path from the Iceland Sea to the Denmark Strait as found by *Jónsson and Valdimarsson* [2004] but without the necessity of deepwater formation in the Iceland Sea.
- The transport of DSOW can be described as the superposition of buoyancy and wind driven transport (Eq. 5.2).
- For stronger wind stress the inflow of AW into the Nordic Seas through the FSC

and IFR and the outflow of dense water through the DS are increasing. In turn the combined outflow over the WTR and through the FBC is lower.

- Changes in the wind stress due to NAO variability are expected to give rise to variations in the overflow transport on the order of 0.2 Sv.
- The spin-down time for the dense water reservoir of the northern overflows to be reduced to its half is almost two years, which strongly reduces seasonal and interannual signals.
- On short time scales (O(days)) the Denmark Strait and Faroe-Bank Channel overflows are weakly negatively correlated and Denmark Strait and Iceland-Faroe Ridge overflows are negatively correlated.
- Increased glacial wind stress yields a stronger northward heat transport. It is potentially the driving force for ice-free Nordic Seas.
- The glacial summer conditions the Denmark Strait overflow was strongly reduced from 3.5 Sv for present-day to less than 0.3 Sv with nearly no buoyancy driven overflow and a small wind driven southward transport.
- The total LGM heat transport across the Greenland-Scotland ridge was reduced to about 30% of its PD value.
- Blocking the Denmark Strait has a strong impact on the northward heat transport. It is reduced by 18% for PD and even stronger by 63% for LGM conditions.
- The exchange of marine biota during the Last Glacial Maximum was most likely reduced but still possible across the Greenland-Scotland ridge. Denmark Strait may have been reached by a cyclonic circulation around Iceland.
- The influence of tides on the exchange across the sill was probably enhanced due to higher tidal amplitudes at times with glaciated shelves.

6. Long-term, Basin Scale Impact of the Denmark Strait overflow

Overflow dynamics act on Rossby Radius length scale (10 km) which cannot be resolved by present-day climate models (resolution \sim 100 km). Even in eddy-permitting regional North Atlantic models the representation of overflows, especially through Denmark Strait, is still an unresolved issue [Willebrand *et al.*, 2001]. The sensitivity of z-level ocean models to bathymetry variations is well known [Roberts and Wood, 1997] and in coarse-resolution climate models one hardly obtains realistic transport rates for the Denmark Strait overflow without unphysical tuning of the model bathymetry [Gerdes, 1993b]. These bathymetry changes are not only subjective decisions but also model dependent, e.g. sigma versus z-level models, which may cause serious problems since the exact overflow representation presumably has not only local impact but can change the large scale vertical and horizontal circulation patterns [Beismann and Barnier, 2004].

In the following, a new approach for an improved overflow representation is proposed. The lack of a physical basis for the bathymetry tuning provided the rationale for an overflow parameterisation based on hydraulic transport estimates [R. Käse 2001, *pers. comm.*]. The idea is to diagnose the hydraulic transport from the upstream conditions and then impose this value on the exchange in a coarse resolution model. Technically, this can be done by having a shallow sill and pipe connecting the deeper regions across the Denmark Strait. Then the transport through the pipe is set to be the hydraulic estimate.

The main objectives of this chapter are to

- validate the overflow parameterisation based on hydraulic constraints with high- and medium-resolution sigma model experiments,
- test the parameterisation in a coupled climate model for long-term integrations and to identify changes in the large scale circulation due to the changed overflow representation, and
- determine the influence of the overflow representation on the stability of the AMOC.

6.1. Evaluation of an overflow parameterisation based on hydraulic constraints

6.1.1. Artificial overflow in the high-resolution Denmark Strait model

As a first step towards a hydraulic control based overflow parameterisation in coarse-resolution climate models, the parameterisation is evaluated in a high-resolution model. For these experiments the high-resolution sigma-coordinate model SCRUM is used. In this version the implementation of the advection scheme and point sources is more suitable to include the parameterisation. The general model set-up is taken from the dam-break experiments with two water masses as described and tested by *Käse and Oschlies* [2000]. Apart from the advection scheme and point source implementation it is equivalent to the sensitivity experiments described in Chapter 3. Note that there is no wind stress forcing in these experiments.

The parameterisation was tested by artificially closing the sill to a depth of 100 m and prescribing a virtual flow through the wall at sill level. The transport was diagnosed from the hydraulic relation $Q = \frac{1}{2} \frac{g'}{f} h_{eff}^2$ (Equation (3.7)) which yields the hydraulic constraint of 4.2 Sv. This value is then scaled with the factor 0.46 found in Section 3.2.4 relating maximum hydraulically controlled and actual transport. The resulting 1.9 Sv are then prescribed as transport through the sill via a point sink north and a point source south of it, yielding a net southward flow which is compensated by northward advection of warm water in the top 100 m. This experiment is compared to a reference case where the bathymetry is unchanged and neither sink nor source terms are applied at the sill, it is identical to DS-Res0ka-100 (Chapter 3).

The thickness of the plume and the transport properties downstream of the sill in the experiment with the parameterised overflow closely match those of the reference case (Figure 6.1). The parameterised version preserves the overflow properties slightly better due to less entrainment at the sill but overall, the amount of dense water as a function of distance from the sill agrees well between both experiments.

6.1.2. A northern North Atlantic test case

After the successful initial test in the previous section, the parameterisation is applied to a coarse-resolution northern North Atlantic model (Section 2.2.3) based on ROMS 2.0. The resolution is approximately 0.5° (50 km in zonal and meridional direction) and hence closer to that of global climate models ($\approx 2^\circ$ resolution). Under present-day conditions, the model is integrated for 11 years starting from rest. It reaches a quasi-equilibrium state after about one year.

After various tests on the technical implementation of the overflow parameterisation (not shown) it was included as a restoring term to the momentum equation in the lowest five layers above the sill. The transport was derived as before based on Eq. (3.7) but it was dynamically calculated at each time step and thus accounts for varying upstream conditions. Note that wind stress driven overflow transport is not taken into account when applying Eq. (3.7). Instead of taken into account for the wind stress here, the hydraulic transport is not rescaled by a factor to yield the actual transport but the upper limitation is used directly. Thus the maximum impact of the Denmark Strait overflow can be evaluated. As expected the parameterisation yields an increased Denmark Strait transport (Figure 6.2) and enhanced transport of cold water to the south. The most pronounced changes are located

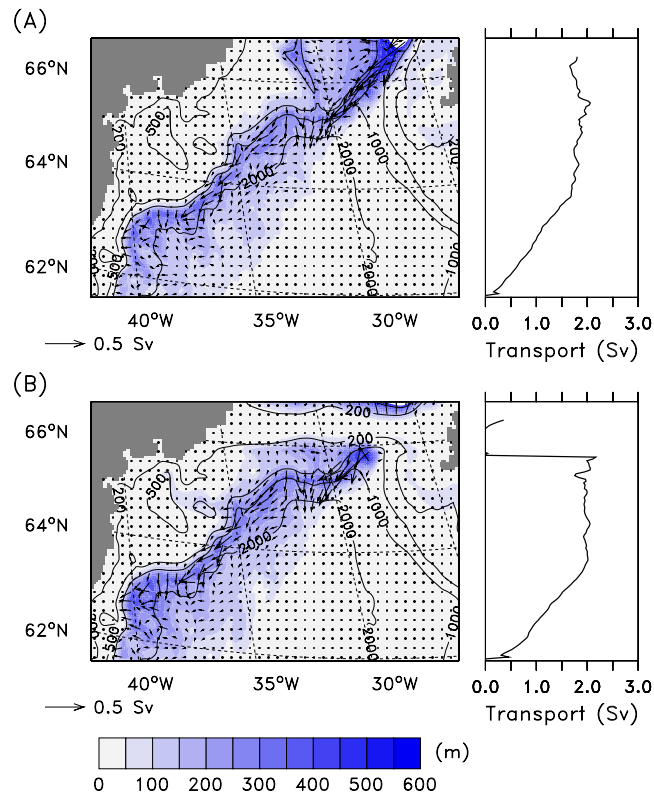


Figure 6.1.: Evaluation of the overflow parameterisation comparing reference case (A) and the parameterised version (B). Thickness (shading) and velocity (vector field) of the overflow water mass as defined from a passive tracer are shown on the left. The transport associated to the overflow plume is shown on the right. Note the decreasing transport in southward direction which is due to recirculating water from the south. Ideally one would expect a constant transport in steady state.

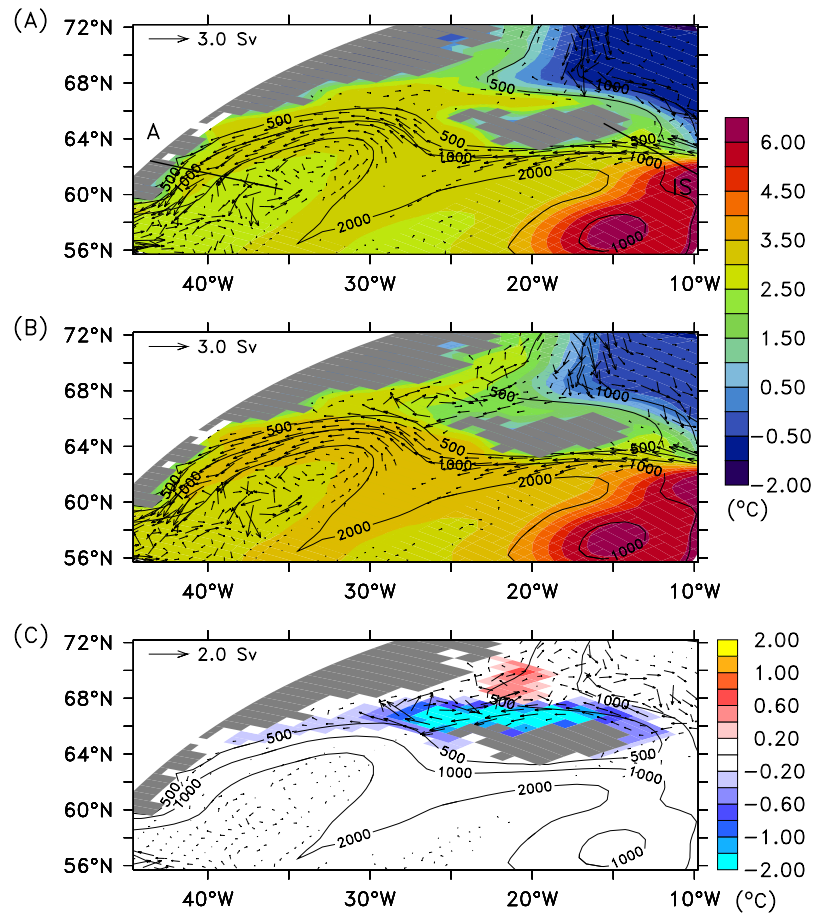


Figure 6.2.: Average temperature of the lowest 6 σ -layers (shading) and transport (vector field) for water masses colder than 3.5°C of the reference experiment (A), the parameterised version (B) and the difference param-ref (C). In (A) the Angmagssalik section of *Dickson and Brown* [1994] is indicated (labelled A) and a section between Iceland and Scotland (labelled IS). Note that a significant fraction of dense water comes from the Iceland-Scotland overflow.

in the vicinity of Iceland with strong cooling at the sill area and a warming north of the Denmark Strait. The warming is due to a recirculation cell driven by the strong southward flow forced from the parameterisation which to some extent cannot propagate further south but is forced northwards again. This recirculating cell transports warm Irminger Current water northwards, closely following the east Greenland coast. The additional southward transport of dense water is largely restricted to the area close to the sill, which is due to the representation of the topography in the model. The Faroe-Shetland Channel is too deep compared to the Denmark Strait and hence the transport through this part of the GSR is too strong. This problem arises from the limitation on the maximum slope in σ -models and it will be less important in z-level models.

A time series of the transport across a section from Iceland to Scotland and through the location of the current meter array at Angmagssalik¹ of *Dickson and Brown* [1994] shows that the transport is in a dynamical equilibrium after five years with seasonal variations by about 1 Sv on a seasonal timescale (Figure 6.3). The diagnosed DSO transport is 2 Sv

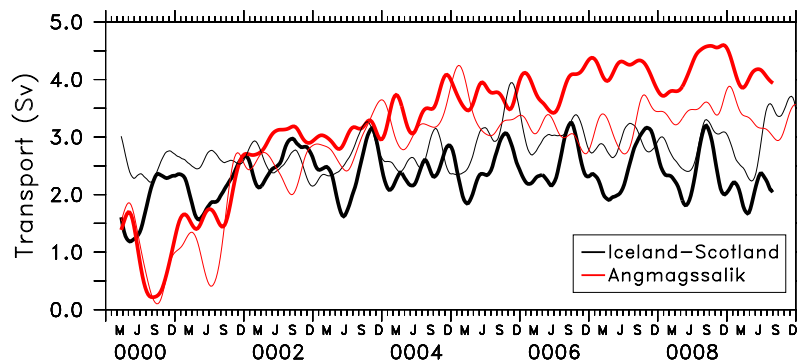


Figure 6.3.: Time-series of the transport of water colder than 3.2°C through the Iceland-Scotland section and the Angmagssalik section. The thin lines are from the reference run, the heavy lines from the experiments with a DSO parameterisation. Note that the time-series was smoothed with a 21 day Hanning filter for better clarity.

on average with less seasonal variability of 0.2 Sv (not shown), which only slightly reduces the variability in the Angmagssalik section. This seasonal variability of the overflows is a common feature in coarse-resolution models, in which the transport decreases to a minimum in late summer and increases to a maximum in late winter when new dense water is formed and the wind stress is stronger. The reason that there is variability of the DSO remaining in the parameterised version is due to the fact that only the overflow core is parameterised. There can be changes at shallower depth and laterally neighbouring points. Therefore, the bulk of the overflow transport is prescribed but a certain degree of freedom is left.

Table 6.1 lists mean values for the transports together with estimates from observations from *Dickson and Brown* [1994] for the Denmark Strait and Angmagssalik and from *Hansen and Østerhus* [2000] for the Iceland-Scotland section. The water masses in the model are not well represented and the overflows are too warm and not dense enough. For this reason, the density class based overflow definition is different for observations and model. A comparison of the modelled overflow equivalents shows that the parameterisation yields a strengthened Denmark Strait overflow as well as higher transport at Angmagssalik but reduced transport through the Iceland-Scotland section. In comparison to observations, the volume trans-

¹Location is shown in Figure 6.2.

Section	Reference	Parameterisation	Observations
Denmark Strait	0.5	2.0	2.9
Iceland-Scotland	2.9	2.4	3.0
Angmagssalik	3.3	4.1	10.7

Table 6.1.: Transport of the modelled overflow water mass with water colder than 3.2°C in Sverdrup averaged over years 9 and 10 of the experiment. The observations refer to the common water mass definition for overflows of $\sigma_\theta \geq 27.8$.

port for the Denmark Strait reaches more realistic values but entrainment and transport at Angmagssalik is still underestimated. Moreover, the transport through the Iceland-Scotland section is reduced towards too low values.

The validation of the parameterisation with high-resolution sigma-coordinate models gave promising results and yielded confidence that the representation of overflow transport can be successfully parameterised. Initial tests with the coarse-resolution sigma-coordinate model were not that convincing, showing only slight improvements for the Denmark Strait transport. This increased DSO transport was at cost of an unrealistic recirculation north of the Denmark Strait, carrying warm water to the north along the east Greenland coast. These problems can be largely attributed to the bathymetry of the GSR. Due to limitations on the maximum topographic slope, which arise from the pressure gradient problem in sigma coordinate models (Section 2.1), Denmark Strait was too wide and too shallow, a problem which does not occur in z-level models, where a better performance can be expected.

6.2. Evaluation of the overflow parameterisation in a global model

6.2.1. Including the overflow parameterisation

The effect of the overflow parameterisation, which has been evaluated in the high and coarse-resolution sigma-coordinate models on a regional scale, is investigated in the global coupled climate model UVic ESCM (for a general description see Section 2.3). In a series of seven long-term (2000 years) equilibrium experiments the effect of the parameterisation was assessed for different set-ups (Table 6.2).

Experiment	Parameterisation	Remark
Ref	none	Reference run
Ref-noGSR	none	GSR deepened
Ref-BBL	none	BBL included
Hyd-DS	DS	
Hyd-deepDS	DS	deepened DS
Hyd-FBC	DS + FBC	
Hyd-BBL	DS	BBL included

Table 6.2.: Overview of global model experiments employing different topographies and overflow parameterisations.

Focus of the experiments is the circulation in the North Atlantic for different depths of the GSR and strengths of the overflows. The spatial resolution in the GSR area in the global model is about 200 km in zonal and meridional direction, which is too coarse to

resolve topographic features such as the Faroe-Shetland Channel properly. In the standard configuration (Experiment Ref-noGSR) of previously published experiments [e.g. *Weaver et al.*, 2001; *Schmittner et al.*, 2002a] large parts of the ridge are set to a depth of 2000 m and Iceland is removed, whereas in the reference experiment presented here the GSR has been included again with a realistic sill depth of 600 m for the Denmark Strait and 1012 m for the FSC (Experiment Ref). These experiments are then compared to model runs with a parameterised DSO and with a realistic sill depth of 600 m (Experiment Hyd-DS), a deeper DS with a sill depth of 1012 m (Experiment Hyd-deepDS) and a version with both overflows, DS and FBC, parameterised (Hyd-FBC). As a step towards a better representation of the descent of dense water, a BBL scheme was included in two experiments (Experiments Ref-BBL and Hyd-BBL).

Technical remarks The parameterisation was included as a momentum source term during the computation of the internal mode velocities. Technically, this was done by replacing the advective and diffusive fluxes with the diagnosed hydraulic transport [*P. Herrmann* 2004, pers. comm.]. The hydraulic transport estimate is based on the integral form of Equation (3.7) [*R. Käse* 2004, pers. comm.]

$$Q_{WLK} = \frac{g}{f \rho_0} \int_h^0 (\rho_N(z) - \rho_S(z)) z dz. \quad (6.1)$$

The integral is evaluated from the sill depth $z = h$ to the surface $z = 0$, with ρ_N and ρ_S being the laterally averaged but depth dependent potential densities north and south of the sill, respectively (Figure 6.4). g is the gravitational acceleration, f is the Coriolis parameter and ρ_0 is the mean density. A virtue of the integral form is that it is easy to implement in

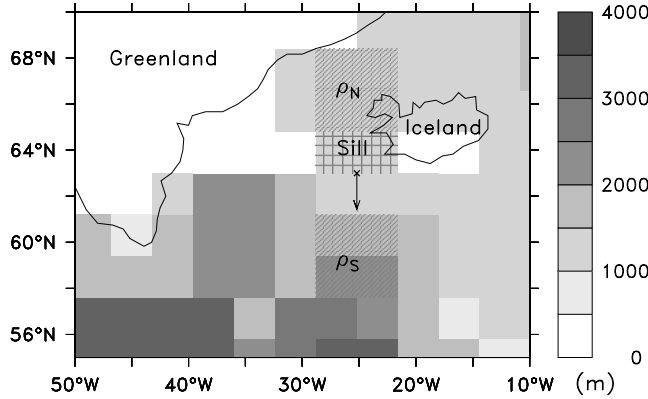


Figure 6.4.: Schematic representation of the overflow parameterisation. The across-sill density contrast is diagnosed from the hatched areas ρ_N and ρ_S from sill level to the surface. The hydraulic transport derived from Equation (6.1) is distributed between sill depth and bottom at the sill as indicated by the vector.

z-level models because no explicit effective height needs to be determined. This minimises jumps in the hydraulic transport estimate, which would otherwise result from shifts in the upstream height by one depth level. The hydraulic transport diagnosed from Equation (6.1) is then distributed between sill level and bottom. For a realistic depth of the DS this is just the bottom cell, but in case of an artificially deepened DS it includes three grid cells in the vertical. In order to account for unresolved entrainment downstream of the sill the

prescribed transport was taken to be the maximum hydraulic transport. Consequently, the wind stress driven part was not taken into account as before since the maximum impact of the overflow is assessed by using the unscaled hydraulic limitation.

6.2.2. Sensitivity experiments

The Denmark Strait overflow transport (defined from $\sigma_\theta \geq 27.8$) in the reference experiment (Ref) has a rate of 0.7 Sv, directed to the north. When the hydraulic parameterisation is applied (Hyd-DS) the flow is southward and strongly enhanced with an overflow transport of 6 Sv. The structure of the thermohaline circulation is commonly described by the meridional overturning circulation, defined as the annually averaged zonally and vertically integrated velocity above a certain geopotential height z as

$$\Psi(\phi, z) = \int_{\lambda_W}^{\lambda_E} d\lambda a \cos \phi \int_z^0 dz' v(\lambda, \phi, z'), \quad (6.2)$$

where v is the meridional velocity, a is the earth's radius, λ and ϕ are longitude and latitude, respectively. As a response to the increased overflow transport, the AMOC increases from less than 19 Sv to 20 Sv (Figure 6.5). Thus the local increase of dense water transport, changes the basin wide overturning by more than 6%.

For the discussion whether the influence of the overflows on the overturning is large or not one needs to define the meaning of large. *Dengg et al.* [1999] include a BBL scheme in their model and find an increase in overturning from 15 to 16 Sv which they call “*hardly a change at all*”. Their modelled change in overturning agrees quantitatively with the results obtained here for including the parameterisation. However, their view that this change is too small cannot be supported here and it will be shown that such a change is large. For this reason the scaling arguments² of *Nilsson et al.* [2003] are considered, which show that the strength of the AMOC is set by the vertical diffusivity A_v and the equator-to-pole density contrast $\Delta\rho$ by $AMOC \propto \Delta\rho^{1/3} A_v^{2/3}$. To find the upper bound on the changes which can be expected dependent on the overflow representation the experiments with and without BBL of *Dengg et al.* [1999] are taken. They find a difference of the maximum potential densities of 0.2 kg/m³ at 64° N. This has to be compared to the mean density contrast equator-to-pole calculated as the difference between the average density in the top 1000 m at 30° S and over the full water column at 65° N as in *Prange et al.* [2003] but from climatological data [*Conkright et al.*, 2003] one obtains 1.1 kg/m³. Thus based on scaling arguments one would expect a maximum overturning change of $\frac{1.3^{1/3}}{1.1^{1/3}} = 1.057$. With a more realistic, larger equator-to-pole density contrast the expected change would be smaller. Therefore, an increase from 15 to 16 Sv by 6.7% is large.

In the model deepwater is formed by cooling of the warm and saline water of the North Atlantic Drift south of the GSR (Figure 6.5). In the reference experiment convection mainly takes place west of Scotland, in the Irminger and Labrador Seas. Convection in the Nordic Seas is strongly underestimated as indicated by much deeper mixed layers in observations [*Monterey and Levitus*, 1997] (Figure 6.6). In the parameterised version additional convection occurs in the Iceland Sea down to a depth of 300 m and more pronounced convection in the Norwegian Sea reaching down to 700 m. In turn, the convection in the Irminger Sea is reduced. The effect of the parameterisation to increase the mixed layer depth north of the

²For a more extensive discussion on scaling arguments and the influence of the vertical diffusivity on the meridional overturning see Section 6.4.2

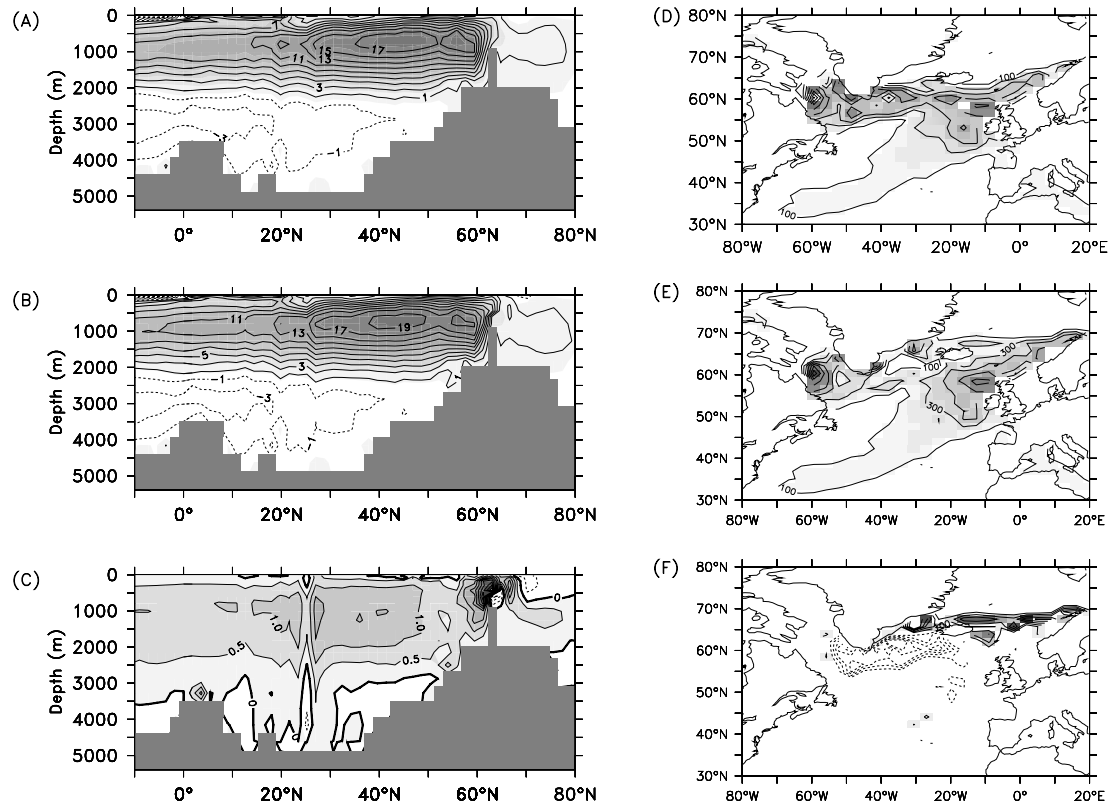


Figure 6.5.: *Left panel:* Atlantic meridional overturning streamfunction (Sv)(annual mean over years 1900 to 2000) for the reference experiment (A), the parameterised Denmark Strait overflow (B) and the difference between parameterised and reference experiment (C). The contour interval is 2 Sv in A and B and 0.5 Sv in C.

Right panel: Mixed layer depth (m) (long-term mean February conditions) for the reference experiment (D), the parameterised Denmark Strait overflow (E) and the difference between parameterised and reference experiment (F). The contour interval is 200 m in D and E and 100 m in F. The mixed layer depth was defined as the depth where the potential density has increased by more than 0.01 kg/m^3 .

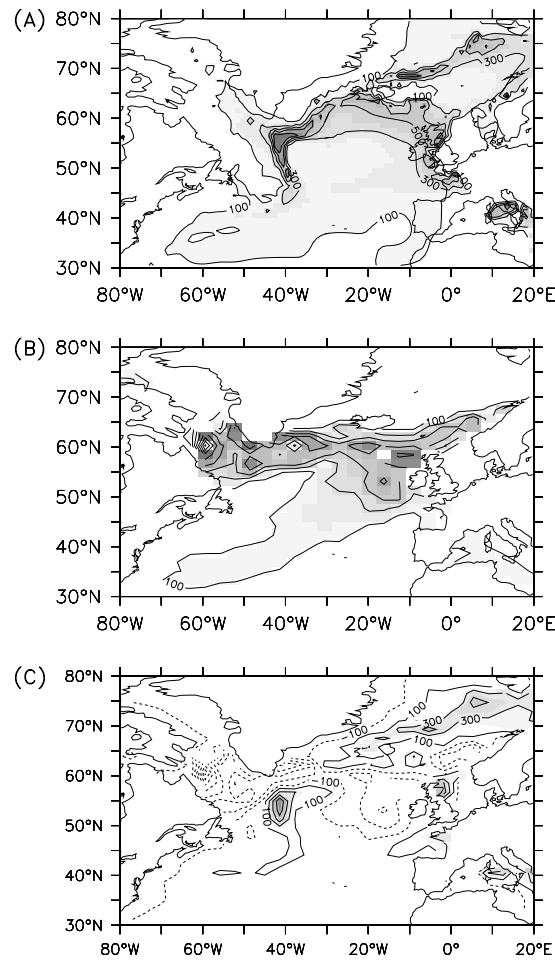


Figure 6.6.: Mixed layer depth (m) (long-term mean February, March, and April conditions) as found in observations [Monterey and Levitus, 1997] (A), for the reference experiment (B) and the difference between reference experiment and observations (C). The contour interval is 200 m in A and B and 100 m in C. The mixed layer depth was defined as the depth where the potential density has increased by more than 0.01 kg/m^3 .

GSR improves the model performance but is still too small in magnitude to provide realistic deepwater formation north of the GSR. However, the excessive sea-ice volume in the Nordic Seas of the reference experiment³ reduced in the experiment using the parameterisation.

The barotropic streamfunction in the experiment including the parameterisation shows a strengthening of the subpolar gyre by 2 Sv and of the subtropical gyre by 1 Sv compared to the reference experiment (Figure 6.7). The increased horizontal circulation as a result of

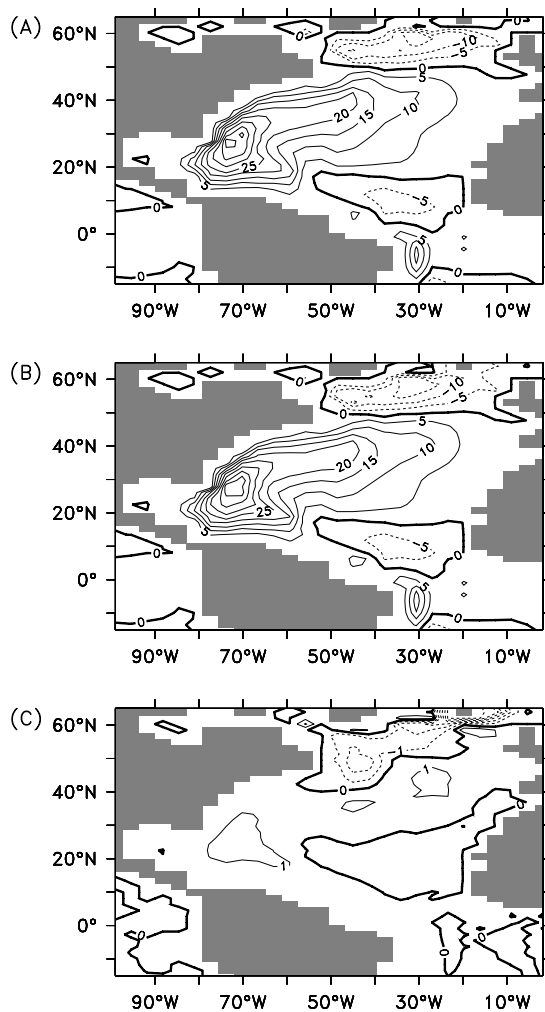


Figure 6.7.: Barotropic mass transport streamfunction (Sv) for the reference experiment (A), the parameterised Denmark Strait overflow (B) and the difference between parameterised and reference experiment (C). Solid lines indicate cyclonic and dashed lines anti-cyclonic circulation. The contour interval is 5 Sv in A and B and 1 Sv in C.

stronger overflows can be attributed to the Joint Effect of Baroclinicity and Relief (JEBAR) as discussed in *Döscher et al.* [1994]. The JEBAR term in the barotropic vorticity balance describes the effect of a changed bottom pressure torque on the horizontal circulation due to deep buoyancy driven flow.

Even though the relative strengths of the DS and FBC overflows change there is no

³For further discussion on the reference state in the UVic model see *Weaver et al.* [2001]. The sea-ice cover is shown in their Figure 19 C.

indication of a regime shift of the deep circulation as found in *Beismann and Barnier* [2004]. In a study with a regional ocean only model of 1° resolution *Gerdes and Köberle* [1995] found a more realistic path and separation of the Gulf stream when convection was forced in the Iceland Sea. Such changes in the overall path could not be reproduced here but the strength of the Gulf stream increases slightly.

As a further remote effect due to the increased overflow transport the deep western boundary current (DWBC) along the American continental slope intensifies by more than 10% (Figure 6.8). This result is similar to the sensitivity study of *Döscher et al.* [1994], which

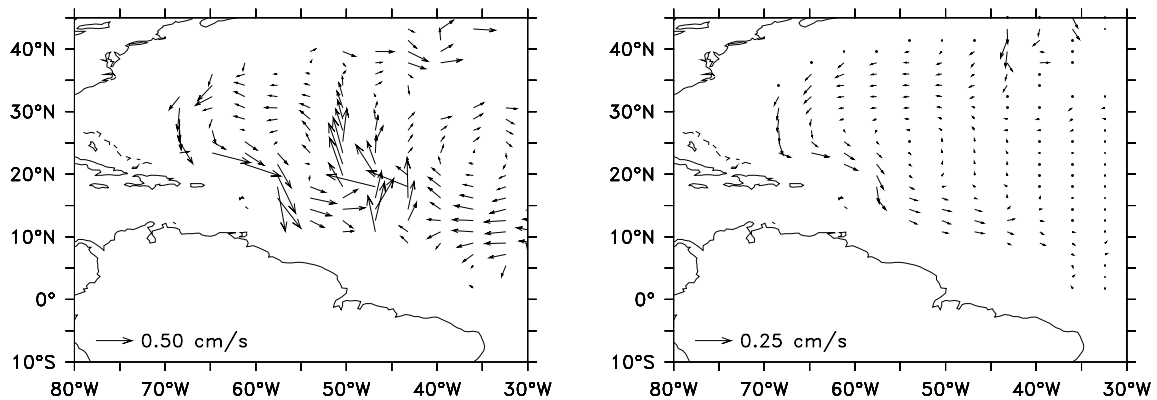


Figure 6.8.: Structure of the deep western boundary current (DWBC) in 3375 m depth of experiment Ref (left panel). Changes in the DWBC between the reference experiment (Ref) and the parameterised version (Hyd-DS). The difference Hyd-DS minus Ref indicates an intensified southward transport (right panel). Note the velocity scales are different in above figures.

investigates the response of a regional North Atlantic model to changes in the thermohaline forcing at the northern boundary at 65°N . In their study a change in buoyancy forcing from the Levitus climatology [*Levitus et al.*, 1994; *Levitus and Boyer*, 1994] to actual section data creates an increase in the NADW formation by 4 Sv and an increased AMOC by more than 3 Sv. They trace the temporal evolution of the change in boundary conditions as a coastal wave propagating along the path of the DWBC. The signal is qualitatively⁴ similar to the changes in the experiments presented here.

In contrast, the changes in AMOC due to the parameterisation are less than expected from previous studies [e.g. *Döscher et al.*, 1994; *Gerdes and Köberle*, 1995; *Döscher and Redler*, 1997]. *Döscher and Redler* [1997] found in a regional North Atlantic model with closed northern boundaries at 65°N a strong dependence between the overturning and the representation of the northern overflows. The experiments presented here suggest that the export of DSOW can be strongly increased (6 Sv) with less effect on the AMOC (1 Sv). Analysing the descent of the overflow plume revealed that this might be caused by too strong mixing of the overflow with ambient water.

Gerdes [1993b] have shown that the best representation of the DSO concerning deepwater export is obtained with a nominal sill depth of 1000 m for the Denmark Strait. To test if this is also applicable with a parameterised DSO, an experiment with a 1000 m deep sill was conducted (Experiment Hyd-deepDS), and is compared to the experiments with a realistic

⁴Absolute velocity changes cannot be reliably compared because the thickness and advection speed in the boundary layer is dependent on the grid resolution [e.g. *Hsieh et al.*, 1983].

sill depth (Experiments Hyd-DS and Ref) in Figure 6.9. There are no significant differences

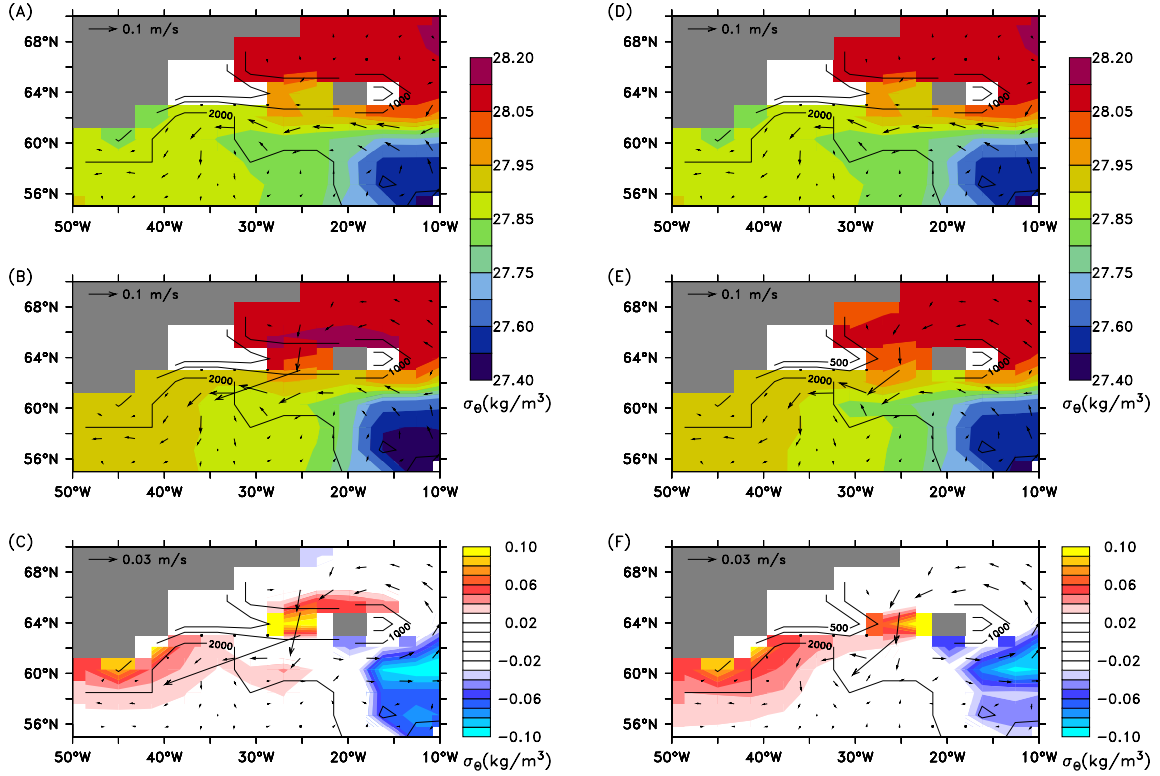


Figure 6.9.: Circulation and water mass properties at the GSR region in the overflow depth range of 550 m to 2000 m. The average potential density σ_θ (kg/m^3) is shaded for the reference experiment Ref (A,D), the hydraulic experiments (B,E) and in the difference Hydraulic - Reference (C,F). The velocity averaged over the overflow depth range is indicated by the vectors. The left panel is from experiment Hyd-DS and the right panel is from Hyd-deepDS.

in the water mass properties in the outflow region between the experiments with a different depth of the Denmark Strait. In both cases the Denmark Strait overflow is increased and the export of dense water is enhanced if the overflow parameterisation is used. Thus the main factor controlling the export of dense water is the parameterisation, while the varying sill depth neither alters the overflow transport at the sill nor the subsequent export further south significantly.

The strengthened overflow transport due to the parameterisation increases the northward heat transport in the North Atlantic by a maximum of 80 TW at the GSR and 20 TW at low latitudes (Figure 6.10). The northward heat flux was calculated based on the net surface heat flux over the Atlantic basin. The relation of overturning and heat transport as proposed by Böning *et al.* [1996] is an increase of 0.1 PW northward heat transport for an increase in MOC of 2 Sv both taken at 24° N. From the results presented here, a slightly higher sensitivity is obtained, with an increase of 0.058 PW for 0.83 Sv increase (0.1 PW/1.4 Sv).

The increase in heat transport has immediate effects on the climate in the North Atlantic realm (Figure 6.11). When including the parameterisation, the northward heat transport is increasing and in turn the surface air temperature (SAT) is rising, the amount of snow is decreasing and the sea-ice cover is shrinking. As an example, the annual mean surface

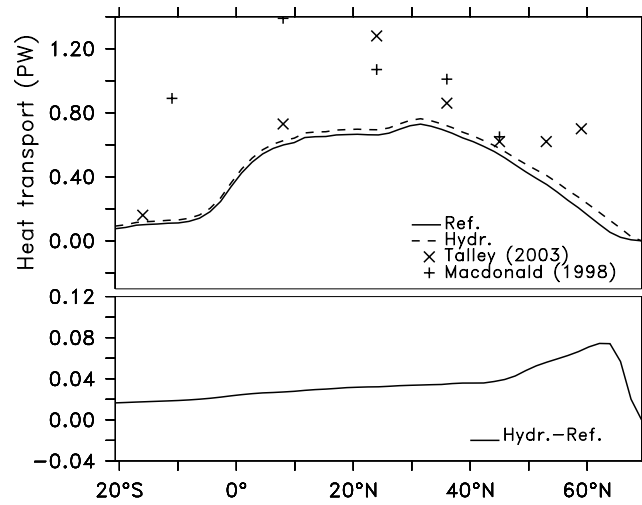


Figure 6.10.: Annual mean northward heat transport vs. latitude in PW ($1 \text{ PW} = 10^{15} \text{ W}$) as derived from an integration of the net surface heat flux comparing reference experiment (Ref.) and the parameterisation (Hydr.) with observations from *Talley* [2003](x) and *Macdonald* [1998](+). The net effect of the parameterisation is shown in the lower part of the graph as difference between parameterised and reference experiment.

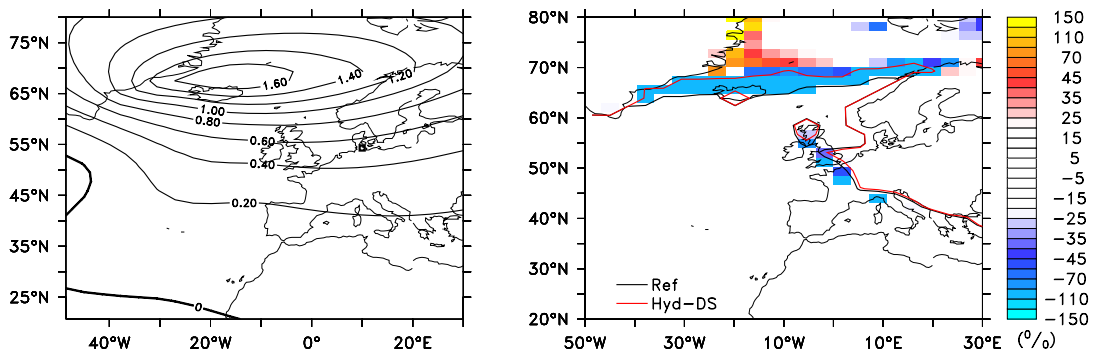


Figure 6.11.: *Left panel:* Difference in annual mean surface air temperature (in $^{\circ}\text{C}$) between reference experiment and parameterisation (Hyd-DS - Ref). The parameterisation leads to generally warmer temperatures in the northern North Atlantic. Northern Europe experiences a warming by about 0.5°C . As an example Kiel is shown as a square, where the temperature rises by 0.55°C .

Right panel: The relative change in snow coverage comparing experiments Ref and Hyd-DS. The shading indicates the change from Ref to Hyd-DS in per cent. In addition the area with an annual mean fraction of more than 10% of sea-ice is outlined. Note the differences especially in high latitudes.

air temperature in northern Germany would rise by 0.55°C comparing experiments Ref and Hyd-DS.

In comparison to the reference run the enhanced dense water export resulting from the parameterisation can be clearly seen in the zonal overturning streamfunction at a section across the North Atlantic at 58°N (Figure 6.12). The southward flow in the overflow density

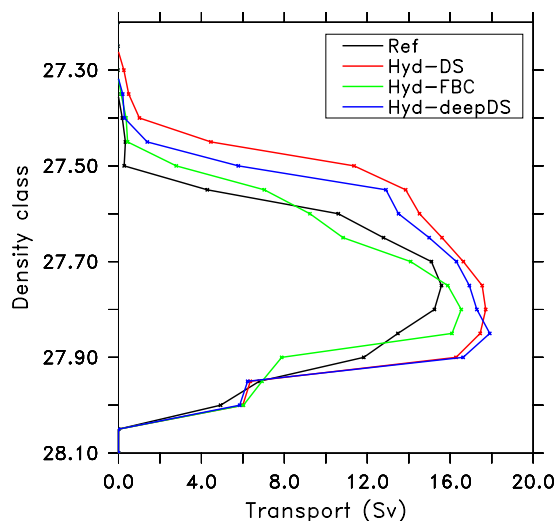


Figure 6.12.: Zonally integrated overturning streamfunction at 58°N with the vertical coordinate being in density rather than geopotential coordinates for experiments Ref, Hyd-DS and Hyd-deepDS. Positive values indicate southward flow. The transport was calculated as the maximum of the running sum from Canada to Scotland ($45^{\circ}\text{W} - 25^{\circ}\text{W}$) of water with a potential density σ_{θ} (kg/m^3) equal or exceeding that of the given density class.

classes is enhanced and in turn the northward flow of warm and less dense water is increased.

From observations [Dickson and Brown, 1994] the total transport at Cape Farewell of dense water with $\sigma_{\theta} \geq 27.8$ was estimated to be 13.3 Sv. From inverse modelling Lumpkin and Speer [2003] could refine this value by subtracting the recirculating part and found a net outflow in this density class of 9.8 ± 1.9 Sv. Comparison with observations shows that the overflow parameterisation improves the representation of the transport of dense water from 5 Sv in Ref to 7.1 and 7.7 in Hyd-DS and Hyd-deepDS, respectively (not shown). However, the dense water export is still underestimated compared to observations probably due to excessive mixing with ambient water. This will be addressed in the following section.

6.2.3. Including a bottom boundary layer

The experiments in the previous chapter suggest that although the transport at the sill is simulated realistically the descent of the overflow downstream of the sill remains a problem. It seems reasonable to assume that the effect of the parameterisation could be strengthened by including a BBL model, which more effectively transports the dense overflow water downstream away from the sill. Note that even though the deepwater formation is not well represented in the Nordic Seas a considerable amount is formed close to the GSR and will be affected from a BBL scheme. For this reason the BBL scheme of Campin and Goosse [1999] which was already included in a previous version of UVic ESCM by O. Saenko [2003,

pers. comm.] was re-implemented here. The scheme determines if the density in the bottom cell is higher than that of a neighbouring cell at a deeper level. If this is the case, it searches the full water column until a depth level with higher density or the bottom is found. Then additional fluid is transported into the cell above this level (or the bottom) with a downward advection speed which depends on the density contrast.

The effect of the BBL scheme becomes clearly visible in the bottom density field (Figure 6.13). In the reference experiment the dense water advected from the north is strongly

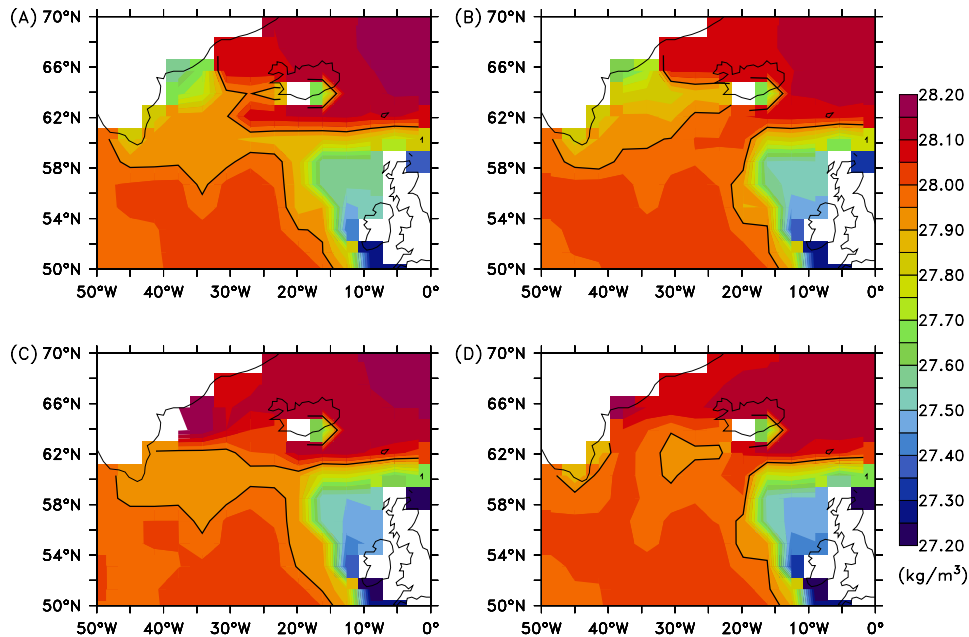


Figure 6.13.: Comparison of bottom cell densities for (A) the reference experiment, (B) with an BBL scheme included, (C) with a parameterised Denmark Strait overflow and (D) for the combined effect of parameterised Denmark Strait overflow and BBL scheme. The 27.95 isopycnal is additionally shown as contour line to highlight the differences in deepwater export.

mixed with ambient water and the core of the overflow water (here depicted as the 27.95 isopycnal) cannot be preserved as expected from observations [Dickson and Brown, 1994; Girton and Sanford, 2003]. The BBL scheme (Exp. Ref-BBL) reduces the amount of mixing and the dense water signal is transported further south. The hydraulic parameterisation (Exp. Hyd-DS) significantly increases the bottom density in the Irminger Sea and the Iceland Basin but cannot preserve the signal further south than 62° N. In a combination of BBL scheme and hydraulic parameterisation (Exp. Hyd-BBL) the density structure resembles that of two overflow cores reaching from the GSR to south-east Greenland, which is consistent with higher resolution eddy-permitting models [Redler and Böning, 1997].

The promising results for the dense water export might lead to the conclusion that the BBL scheme could significantly change the AMOC, which is supported by the model studies of the “Community Climate Effort” especially from Döscher and Redler [1997], who found a near linear relation between the AMOC⁵ (if between 15 and 22 Sv) and the mean Denmark Strait overflow density. However, these results cannot be confirmed here. In the model

⁵Inferred from their Figure 3.

study presented here, the AMOC only weakly changes (Figure 6.14) when the density of the Northern Overflows is better preserved (Exp. Ref-BBL) and more dense water is exported (Exp. Hyd-BBL).

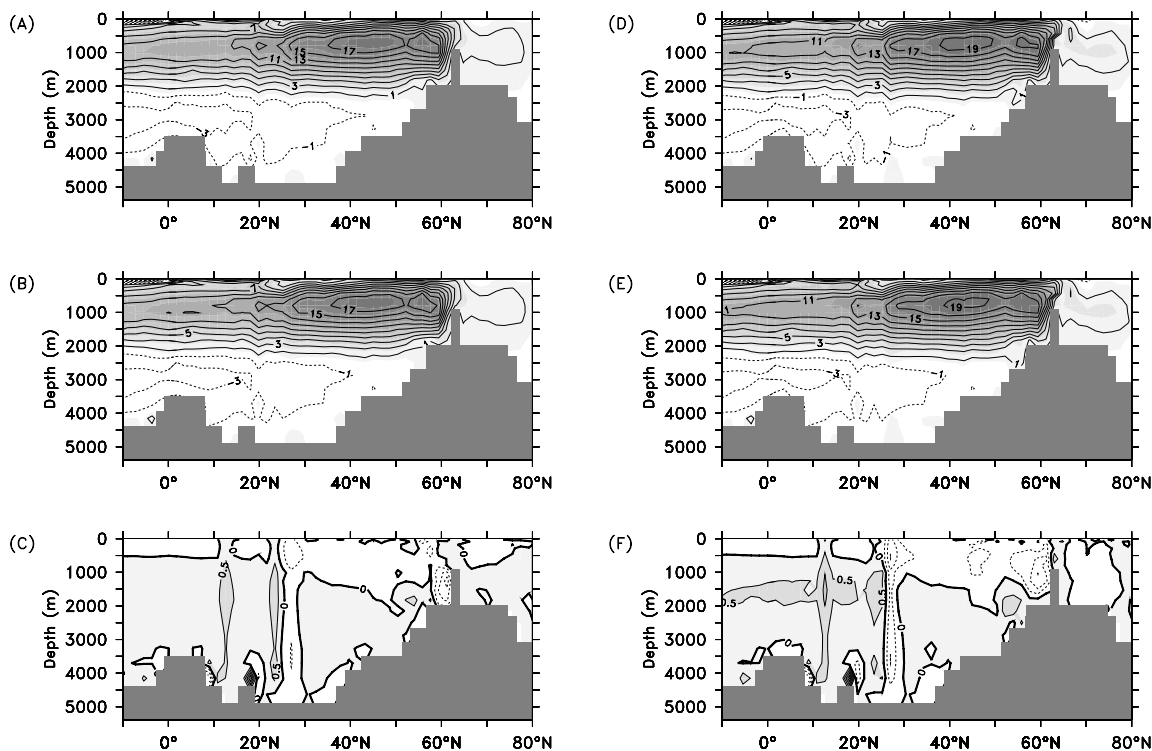


Figure 6.14.: *Left panel:* Atlantic meridional overturning streamfunction (annual mean over years 1900 to 2000) for the the reference experiment (A), with BBL scheme included (B) and the difference between the experiment with BBL and without (C). The contour interval is 2 Sv in A and B and 0.5 Sv in C.

Right panel: Overturning streamfunction as above but for the experiment with parameterisation (D), with parameterisation and BBL scheme included (E) and the difference between with BBL and without (F).

Comparing experiments Ref and Ref-BBL does not show any significant changes in the structure or strength of the AMOC. There are indications of minor local changes close to the sill essentially due to the individual volume fluxes through DS and FBC but this does not change the structure south of 55°N . If the hydraulic parameterisation is applied the BBL scheme reduces the maximum AMOC slightly (by 0.5 Sv) and the overturning cell's maximum shifts to a slightly deeper depth and extends further south. But all these changes are of small amplitude (< 1 Sv) compared to the increase of 4 Sv in *Döscher et al.* [1994] when they changed the buoyancy forcing at the northern boundary. This is quite surprising since the model experiments were especially designed to test the maximum impact of the DSOW transport. A likely explanation is due to the differences in the model set-up. Their regional ocean model cannot capture feedbacks arising from the coupling of atmosphere and ocean which are included in the UVic model used here. As seen above the northward heat transport has changed (Figure 6.10) and the water masses north of 58°N have become lighter (Figure 6.12) therefore the net freshwater flux changes which cannot be captured in an ocean only model. *Thorpe et al.* [2004] suggest that the global radiation budget is altered

in coupled models as a response to changes in the overflows. A limitation of the model results presented here is the cold bias in the reference experiment and a too weak dense water production north of the GSR.

A density profile of the central Labrador Sea (Figure 6.15) clearly shows the increase in bottom densities when the BBL scheme is included and a reduction in intermediate depth (800 m). Thus the BBL scheme causes a stabilisation of the water column in the Labrador Sea. In contrast, the hydraulic parameterisation leads to generally increased den-

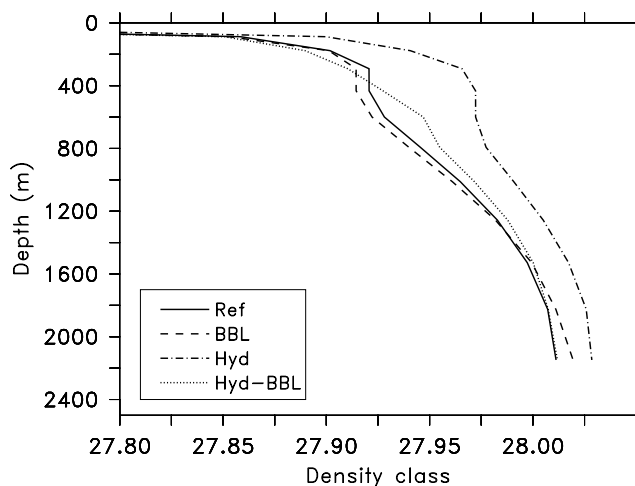


Figure 6.15.: Density profile of the central Labrador Sea (53° W - 57° W, 58° N - 61° N) comparing the reference experiment, the parameterised overflow version and the version with BBL scheme included.

sities throughout the water column. If BBL scheme and hydraulic parameterisation are combined the effect seen with only the hydraulic parameterisation active is reduced.

As these results might depend on the particular BBL scheme employed, an alternative approach the BBL scheme of *Beckmann and Döscher* [1997] was included into the UVic model [*P. Herrmann* 2004, pers. comm.]. The difference between *Campin and Goosse* [1999] and *Beckmann and Döscher* [1997] is essentially that the former scheme is designed only for downslope flows and advects fluid through the individual cells of the water column on the way downstream, whereas the latter is a pseudo-sigma-layer connecting neighbouring bottom cells⁶. The BBL model of *Beckmann and Döscher* [1997] can have both diffusive and advective fluxes. In the implementation in UVic model the advective transport was not divergence free, a feature that becomes visible only in global long-term studies. As it was implemented very carefully, the slight increase in globally integrated salinity might have been overlooked before. Anyhow, the parameterisation was restricted to diffusive transports only, as in MOM-4 in the revised *Beckmann and Döscher* [1997] scheme of Gnanadesikan [*Griffies et al.*, 2004]. However, compared to the reference run this BBL scheme does not significantly change the results (not shown).

An inclusion of the BBL scheme of *Campin and Goosse* [1999] helps to preserve the overflow properties when descending from the GSR. In fact, the bottom density distribution in the northern North Atlantic did show a sizeable difference between reference experiment and experiments with BBL in the order of a 0.1 kg/m^3 increase. Following the study of

⁶See review of *Killworth* [2003] for further details on bottom boundary layer models.

Döscher et al. [1994] this should increase the AMOC, however, the inclusion of the BBL did not result in any significant differences concerning the AMOC neither in the reference experiment nor when the hydraulic parameterisation was included. The slight decrease in overturning might be attributed to the increased stability of the water column in the Labrador Sea, which is an important location for deepwater formation in the model. This result is, even though initially not expected, in agreement with the coarse-resolution (2° grid) regional North Atlantic study of *Lohmann* [1998] who found a decrease from 24 to 20 Sv in overturning when including a BBL scheme. Moreover, it agrees well with results from the FLAME group [*Dengg et al.*, 1999], where in the comparable high-resolution models ($1/3^\circ$ and $4/3^\circ$) the BBL only slightly increased the overturning from 15 to 16 Sv.

6.2.4. Extension to include a parameterisation for the Faroe Bank Channel outflow

After the overflow parameterisation was tested for the Denmark Strait it is now extended and the Faroe Bank Channel overflow is parameterised as well. The relative strength of the FBC overflow in the reference experiment is too strong due to the deep and wide sill. This feature is common in coarse-resolution models which cannot resolve the small spatial scales of the Faroe Bank Channel and Faroe-Shetland Channel. Limiting these outflows by hydraulic constraints could potentially increase the DSOW export by altering the upstream reservoir height and result in a more realistic division of volume fluxes between the overflows. This is especially interesting because, as already mentioned before, *Beismann and Barnier* [2004] found in a regional ocean model study of the Atlantic two different modes of deep circulation in the subpolar North Atlantic depending on the relative strengths of DS and FBC overflows.

The implementation of the parameterisation essentially follows the one from the Denmark Strait using Equation (6.1), but at the location of the FSC. Equation (6.1) is for dynamically wide sill that is the sill is much wider than the Rossby Radius. Here the FBC is taken as wide sill as in *Whitehead* [1998] but one should probably treat it as narrow channel where rotation is not important. However, the difference between both Equation (3.7) and Equation (3.8) is only about 20% for realistic values which is small enough for the sensitivity study carried out here. The mean transport diagnosed for the FBC overflow is 8.5 Sv and for the DS overflow 3.6 Sv, but a large portion is directly recirculating. This yields a net transport of water with $\sigma_\theta \geq 27.8$ of 1.3 Sv for the DS and 3.8 Sv for the FBC, which is less than in the previous parameterisation approaches. However, one obtains a significantly increased AMOC compared to the reference experiment (Figure 6.16) and slightly more than in previous parameterisation approaches (not shown). The maximum overturning increases by more than 11% from 18.8 Sv to 20.9 Sv and the spatial structure clearly resembles the direct impact of the overflows as momentum source.

The mixed layer depth shows a reduction south of the GSR and an increase in Norwegian and Labrador Sea by more than 500 m. However, this is quite similar to Exp. Hyd-DS and the shift to convection sites north of the GSR is of smaller magnitude.

6.2.5. Summarising the thermohaline transports

The overturning circulations resulting from the individual experiments carried out before are summarised in Table 6.3, showing a good correlation between the formation of NADW and the AMOC except for experiment Hyd-FBC. If Hyd-FBC is neglected NADW and

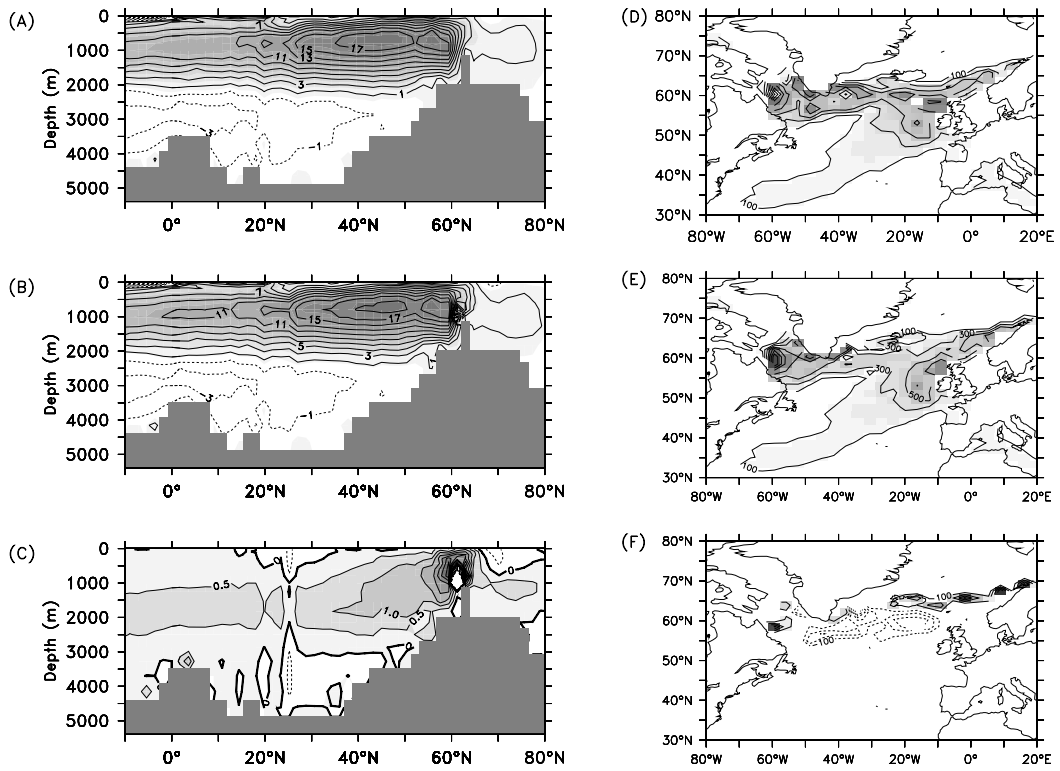


Figure 6.16.: *Left panel:* Atlantic meridional overturning streamfunction for the experiment Hyd-FBC with a parameterisation for both DS and FBC. In (A) the reference experiment is shown, the parameterised version in (B) and the difference between parameterised and reference experiment in (C). The contour interval is 2 Sv in A and B and 0.5 Sv in C.

Right panel: Mixed layer depth (mean February conditions) for the reference experiment (D), the parameterised DS and FBC overflows (E) and the difference between parameterised and reference experiment (F). The contour interval is 200 m in D and E and 100 m in F. The mixed layer was defined as the depth where the potential density has increased by more than 0.01 kg/m^3 .

Experiment	AMOC (Sv)	NADW 48° N(Sv)	NADW 60° N	DSOW (Sv)	ISOW (Sv)
Ref	18.8	17.1	13.1	0.0	1.4
Ref-noGSR	19.8	18.4	17.9	13.9	-2.0
Ref-BBL	18.5	16.8	10.9	-0.1	2.6
Hyd-DS	20.0	18.2	18.3	6.1	1.2
Hyd-deepDS	20.0	18.2	19.2	6.1	1.0
Hyd-FBC	20.9	17.6	13.9	1.3	3.8
Hyd-BBL	19.5	18.2	16.0	5.9	1.5

Table 6.3.: Strength of the Atlantic meridional overturning circulation (AMOC), export of North Atlantic Deep Water (NADW), Denmark Strait (DS) and Faroe-Shetland channel (FSC) overflow water masses in the global model for different parameterisations. NADW export is defined as the transport of water with $\sigma_\theta \geq 27.8$ at the given latitude intergrated over the basin width. At 60° N the NADW of DSOW and ISOW is taken into account wheres the NADW export at 48° N includes the contribution from the Labrador Sea as well. The overflow water masses follow the same density class definition.

AMOC can be linearly correlated ($R^2 = 0.99$). The correlation between the overflows and AMOC is weaker but statistically significant ($R^2 = 0.64$), between NADW and the overflows ($R^2 = 0.62$) there is also a significant correlation. The production of NADW is slightly higher compared to observations and results from a global inverse model. Based on observations *Ganachaud and Wunsch* [2000] found a rate of NADW production of 15 ± 2 Sv consistent with the findings of the inverse model of *Lumpkin and Speer* [2003] where NADW export through 48°N amounts to 15.6 ± 1.2 Sv.

The structure of the overturning cell agrees well with that of higher resolution eddy resolving models [*Willebrand et al.*, 2001] with respect to the location and depth of the overturning cell. For z -level models *Willebrand et al.* [2001] obtain NADW export of 12 Sv and a maximum overturning of 16 Sv at 40°N . The estimate of NADW production and AMOC is less than what is found in the modelling experiments presented here. However, the maximum AMOC in coarse-resolution models differs substantially, for example, *Lambert and Boer* [2001] found in the CMIP1 intercomparison project of coupled models a mean AMOC of 21.1 ± 9.1 Sv.

The global model experiments with the parameterisation yielded an improved overflow representation and increased meridional overturning. The main results of the coupled global model experiments are summarised in Table 6.3. Even though the density structure at the GSR is locally significantly changed, the remote effects are rather small. The depth profiles of the zonally integrated transport across the Atlantic at 36°N (Figure 6.17) do not show pronounced structural differences. Observational data from this section [*Roemmich*

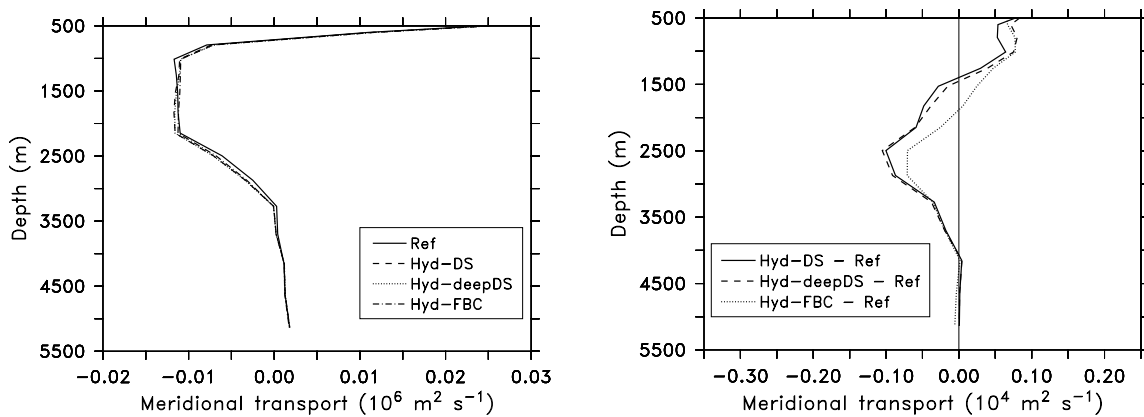


Figure 6.17.: Meridional transport in the Atlantic at 36°N for hydraulic parameterisations for the reference experiment (Ref), the Denmark Strait (Hyd-DS), the deep Denmark Strait (Hyd-deepDS) and Denmark Strait and Faroe Bank Channel both parameterised (Hyd-FBC)(left panel) and difference to the reference experiment (right panel).

and Wunsch, 1985] indicates two maxima of southward transport, located at 1700 m and between 2500 and 4000 m depth. The upper one, associated with the Labrador Sea (upper NADW), is fairly well presented in the model, whereas the lower (lower NADW) characteristic for overflow waters is not present. From the numerical study of *Döscher et al.* [1994] a strong influence of the representation of DSOW on the transport through this section is expected. When they changed the boundary conditions in the Denmark Strait from the Levitus climatology [*Levitus and Boyer*, 1994; *Levitus et al.*, 1994] to actual section data the transport of upper NADW decreased from $0.96 \cdot 10^4 \text{ m}^2/\text{s}$ to $0.07 \cdot 10^4 \text{ m}^2/\text{s}$ and the transport of lower NADW increased from $-0.2 \cdot 10^4 \text{ m}^2/\text{s}$ to $1.1 \cdot 10^4 \text{ m}^2/\text{s}$. In contrast, the hydraulic

parameterisation does not improve the representation of this water mass and the different experiments are hardly different with a maximum increase of about $0.1 \cdot 10^4 \text{ m}^2/\text{s}$ of upper NADW (Figure 6.17).

The location of convection areas does depend on the overflows as could be shown from the experiments with the overflow parameterisation. The main changes, when including the parameterisation, are an increase in mixed-layer depth off Norway and in the Iceland Sea. The deepwater formation area in the Iceland Sea does agree with recent observations [Jónsson and Valdimarsson, 2004], whereas the location close to Norway is too far east compared to the circulation scheme from observations of Mauritzen [1996a]. Overall, the parameterisation can be seen as successful in leading to a better representation of deepwater formation areas. Moreover, the excessive sea-ice cover is reduced, which further enhances the realism of the model results. Nevertheless, the amount of deepwater formed in the Nordic seas is still underestimated.

A benchmark for the parameterisation is whether it yields more realistic results than the standard UVic experiments previously published, where the GSR is completely removed. The difference between the parameterised version and the experiment without GSR is shown in Figure 6.18. Comparing the AMOC one finds that the removal of the GSR has surprisingly little effect on the large scale circulation. On the one hand this difference corroborates previous studies investigating the longterm climatic evolution [Schmittner *et al.*, 2002b; Meissner *et al.*, 2003] but on the other hand it is in contrast to the well established view that the AMOC has a strong dependence on the representation of the GSR overflows [e.g. Döscher *et al.*, 1994; Gerdes and Köberle, 1995; Redler and Böning, 1997; Roberts and Wood, 1997]. Roberts and Wood [1997] find a significant increase in AMOC when deep gateways are included in the Greenland-Scotland Ridge crudely representing the FBC. This result is questioned in a subsequent study with the same model but on a global scale, where it is found that the large-scale circulation is broadly insensitive to changes of mixing parameterisation and downstream bathymetry (sill depth remaining the same) at the Denmark Strait [Thorpe *et al.*, 2004]. The models showing a strong impact of the GSR overflows are regional ocean only North Atlantic models. In contrast to that the coupled model employed here can take into account for other processes important for the meridional overturning such as atmospheric tele-connections like the inter basin freshwater exchange [Latif *et al.*, 2000] or the moisture transport from subtropical to subpolar regions in the Southern Hemisphere [Saenko *et al.*, 2003]. Nevertheless, coarse resolution models in general and the UVic model in particular have problems to simulate realistic deep water formation. If the reference state of the UVic experiments would have more pronounced deep water formation in the Nordic Seas the impact of a better overflow representation on the AMOC might have been stronger.

6.3. Influence on the stability of the thermohaline circulation

6.3.1. Overview and experimental set-up

It has been suggested that the dense overflows might have a stabilising effect on the THC [Lohmann, 1998]. As shown in Section 5.1.4 the Nordic Seas can be seen as a reservoir of dense water, which cannot be rapidly flushed due to hydraulic constraints. If dense water production is shut off, the buoyancy driven overflow of dense water will continue at an exponentially decreasing rate. Below, the theory is tested whether this mechanism can provide a negative feedback for the AMOC, leading to a stabilisation. For this purpose,

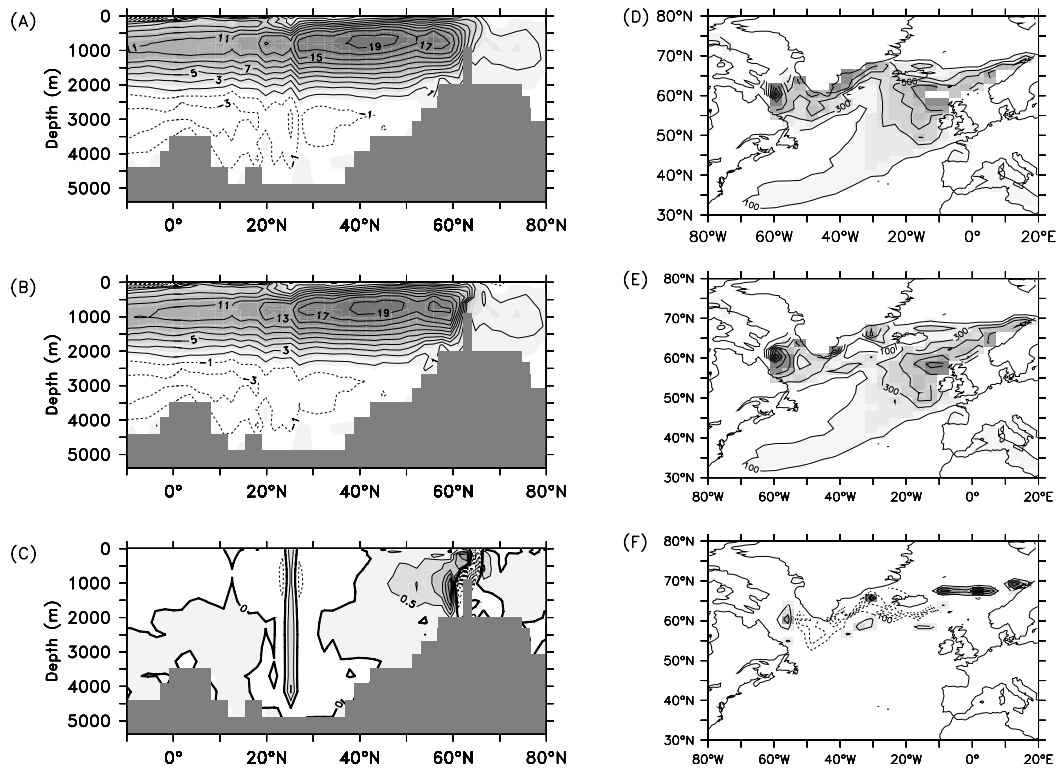


Figure 6.18.: *Left panel:* Atlantic meridional overturning streamfunction (annual mean over years 1900 to 2000) for the experiment without GSR (A), the parameterised Denmark Strait overflow (B) and the difference between hydraulic and no GSR experiment (C). The contour interval is 2 Sv in A and B and 0.5 Sv in C.

Right panel: Mixed layer depth (long-term mean February conditions) for the experiment without GSR (D), the parameterised Denmark Strait overflow (E) and the difference between parameterised and no GSR experiment (F). The contour interval is 200 m in D and E and 100 m in F. The mixed layer was defined as the depth where the potential density has increased by more than 0.01 kg/m^3 .

the Denmark Strait parameterisation was employed in experiments in which the freshwater balance of the North Atlantic was perturbed. Different experiments have been carried out (Table 6.4) varying the area and the amplitude of the freshwater forcing.

Experiment	FW ampl.	Duration (years)	Param.	FW area
FW1A-Ref	0.3 Sv	2000 (hyst)	no	A
FW1A-Hyd	0.3 Sv	2000 (hyst)	yes	A
FW1B-Ref	0.3 Sv	2000 (hyst)	no	B
FW1B-Hyd	0.3 Sv	2000 (hyst)	yes	B
FW1C-Ref	0.3 Sv	2000 (hyst)	no	C
FW1C-Hyd	0.3 Sv	2000 (hyst)	yes	C
FW1D-Ref	0.3 Sv	2000 (hyst)	no	D
FW1D-Hyd	0.3 Sv	2000 (hyst)	yes	D
FW2A-Ref	0.15 Sv	2000 (hyst)	no	A
FW2A-Hyd	0.15 Sv	2000 (hyst)	yes	A
FW2A-Wind	0.15 Sv	2000 (hyst)	no	A
FW3A-Ref	0.15 Sv	500	no	A
FW4B-Ref	0.3 Sv	500	no	B

Table 6.4.: Summary of the freshwater perturbation experiments using the UVic ESCM to test the effect of the DS parameterisation on the stability of the AMOC. The freshwater (FW) amplitude is given in Sv/500 years. It is applied to different areas (A, B, C, D; cf. Figure 6.19).

The general model set-up has been described in Section 2.3 and the implementation of freshwater perturbations is that of *Schmittner et al.* [2002b]. Most experiments follow a hysteresis loop (FW1, FW2 in Table 6.4) of initially 500 years increasing freshwater flux, then a 1000 year decrease and finally a 500 year increase again (Figure 6.19). Self recovery was tested by applying a freshwater perturbation which is suddenly switched off after 500 years (FW3,FW4 in Table 6.4). To insure conservation of salinity, the additional freshwater flux is extracted from the remaining ocean.

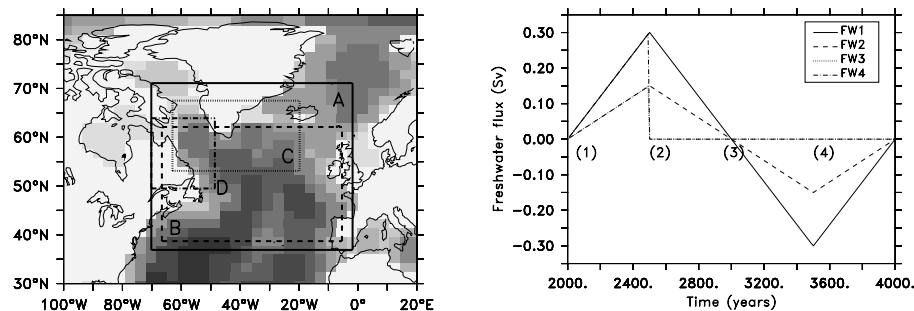


Figure 6.19.: Location (left panel) and magnitude (right panel) of freshwater perturbation experiments. The difference between the regions is exaggerated the actual region A extends from 74° W - 0° W, 36° N - 72° N, region B from 74° W - 0° W, 36° N - 63° N, region C from 74° W - 22° W, 52° N - 72° N and region D from 74° W - 47° W, 49° N - 65° N. Numbers 1 to 4 shown in the right panel are used in subsequent figures to indicate the freshwater flux amplitude.

The different freshwater perturbation areas (Figure 6.19) are the northern North Atlantic (area A), the North Atlantic up to the GSR (area B) and the area of northern North Atlantic

- Nordic Seas (area C). Finally, area D is located on the main deep water formation area in the model, namely the Labrador Sea. The rationale to test the different regions is that an additional freshwater flux south of the GSR might increase the density contrast across the sill and thus might enhance the deep water export from the Nordic seas.

6.3.2. Response of the overturning and hysteresis loops

Two stable circulation patterns exist in the model for present-day conditions (Figure 6.20) similar to previous studies [Stommel, 1961; Rahmstorf, 1996]. Starting from a state with active deepwater formation (on-state, 1) the AMOC gradually reduces with increasing freshwater flux until deep water formation is stopped (off-state, 2). Reducing the freshwater in-

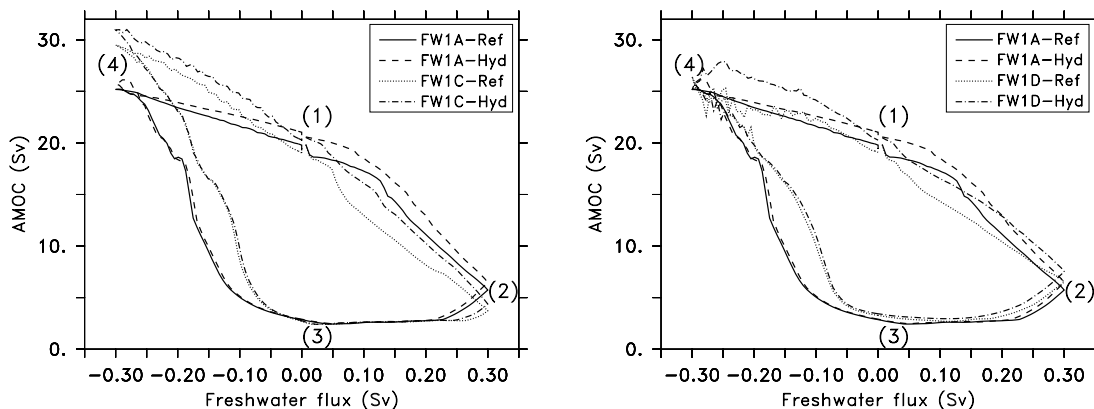


Figure 6.20.: *Left panel:* Hysteresis curves for a freshwater perturbation experiment with an amplitude of 0.3 Sv/500 yrs. comparing perturbation areas A and C and evaluating the effect of the parameterisation.

Right panel: Same as in left panel but comparing perturbation areas A and D.

put, the system stays in the off-state (3) until a threshold is passed and a rapid resumption of the circulation occurs (transition from (3) to (4)). These results are similar to earlier studies [Rahmstorf, 1995; Schmittner et al., 2002b]. In the following the focus will be on the differences between the individual hysteresis loops.

The difference at the starting point (labelled as (1) in Figure 6.20) is due to the slightly increased overturning when the hydraulic parameterisation is active. With the onset of the positive freshwater flux the experiments with perturbation areas A and C show different sensitivities. At a flux of +0.1 Sv the perturbation in area C had a much larger impact and the AMOC is reduced to 11 Sv whereas for area A it is still at 16 Sv. With further increasing freshwater flux this difference decreases continuously. At the maximum fresh water flux (0.3 Sv, labelled as (2)) the difference in the AMOC is reduced to 2 Sv for perturbations in area A relative to C. During the off-state, the same low level is reached for all experiments. When the freshwater flux changes sign (labelled as (3)), the experiment with perturbation area C recovers faster and reaches a higher maximum for the maximum negative freshwater flux (labelled as (4)) than the other experiments. The effect that can be attributed to the parameterisation is an increased overturning by about 2 Sv. In the starting phase of the freshwater anomaly there are indications for a potential stabilising feedback of the parameterisation but this effect is of small amplitude only.

If the freshwater is directly injected at the Labrador Sea (Area D) the overturning de-

creases faster but reaches almost the same value at the maximum freshwater flux as for area A (Figure 6.20). The almost linear decrease indicates that the freshwater flux might be too high in these experiments. However, since this behaviour is almost the same once the freshwater flux is decreased by half (Figure 6.21) it is probably more likely due to the fact that the freshwater is applied directly at the model's most important deep water formation area namely the Labrador Sea. Freshwater perturbation at this area also lead to oscillatory behaviour for large negative anomaly when cold and salty water is flushed periodically from the shallow parts of the Labrador Sea to depth.

In case of a smaller freshwater flux of 0.15 Sv/500 yrs. (right panel in Figure 6.21) the off-state has not yet been reached after 500 years. Therefore the recovery phase (points 3 to 4 in Figure 6.20) is different from the previous experiments. The transition back to the full on-state is more rapid and occurs earlier, and the response to the negative freshwater anomaly is fairly linear. With this smaller perturbation the role of the overflow parameterisation is more pronounced. The initial decline in AMOC is considerably slower, the minimum of 13.0 Sv is about 2 Sv larger than for reference state (11.1 Sv) and the transition back to the on-state happens earlier. The drop of 7.6 Sv from the initial AMOC (20.6 Sv) to the minimum AMOC of 13.0 Sv in experiment FW2A-Hyd is consistent with modelling results with the coupled Bergen Climate Model (BCM) of *Otterå et al.* [2003]. They find in the BCM a maximum weakening of the AMOC by 6 Sv as response to freshwater perturbation of 0.2 Sv to the Arctic Ocean.

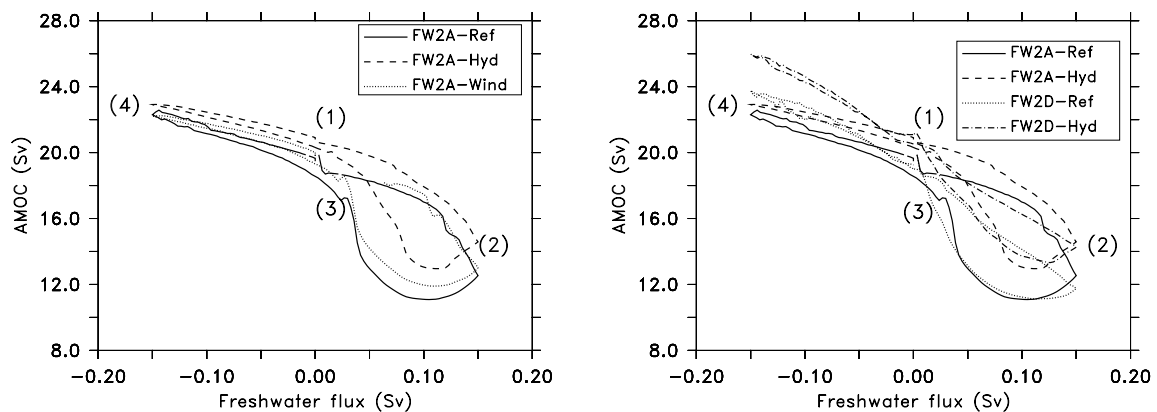


Figure 6.21.: *Left panel:* Hysteresis curves with 0.15 Sv/500 yrs. for area A comparing the reference experiment with parameterised version and with the wind feedback included. *Right panel:* Hysteresis curves for a perturbation of 0.15 Sv/500 yrs. comparing areas A and D.

It has been suggested that the response of the wind field acts as a positive feedback for the strength of the AMOC the so called wind stress feedback [*Mikolajewicz, 1996; Otterå et al., 2004*]. In response to the collapsed thermohaline circulation a cyclonic circulation over the Nordic Seas increases the freshwater export with the East Greenland Current and causes increased upwelling at low latitudes. Moreover, the northern hemisphere trade winds grow stronger over the Atlantic leading to enhanced Ekman transport. This feedback cannot be modelled with the UVic model because wind stress is prescribed. To evaluate the effect of wind stress changes the wind field from the coupled model results of *Otterå et al.* [2004] is taken as forcing (Exp.FW2A-Wind). The altered wind stress in the coupled model changes in response to the freshwater forcing resembling a phase of positive NAO. The experiment

is started from FW2A-Hyd during the initial phase of decreasing AMOC at year 210. From this it is found that the changes due to the different wind forcing are relatively small when the AMOC is weakening, but contribute to a faster recovery.

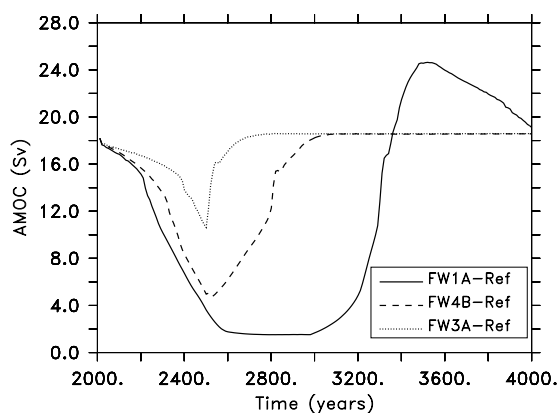


Figure 6.22.: Self recovery of the AMOC for a transient freshwater pulse, which is shut off after 500 years (FW3) for different strength (0.15 Sv/500 yrs. for FW3A-Ref, 0.3 Sv/500 years others).

Finally, the potential for a self recovery was examined by stopping the freshwater flux at its maximum after 500 years (Figure 6.22). With a 0.15 Sv/500 yrs. freshwater flux the maximum overturning reduces from 18.6 Sv to 10.6 Sv in 500 years and then fully recovers within 270 years. If the freshwater flux is doubled the maximum overturning reduces to 4.8 Sv in 500 years and the time for a full recovery more than doubles to 570 years.

Lohmann [1998] has shown that the improved representation of the overflows, by including a BBL scheme, had a stabilising effect on the meridional overturning. In the present study, it was tested if the same holds for the hydraulic parameterisations. The overall picture is that there was only little stabilising effect, and the model is rather sensitive to the site where the freshwater is injected. The straightforward explanation is that the proximity of the freshwater flux to the convective region is important. An interesting feature is that the overturning recovers in all cases once the freshwater perturbation is stopped independent of overflow parameterisation or wind stress. The wind stress feedback was found to be of minor importance, moreover, it was found to be not important at all concerning the recovery⁷.

6.4. Beyond the northern overflows - Other factors setting the North Atlantic Meridional Overturning strength

The main focus of the previous sections was to investigate the influence of the Denmark Strait on local to basin wide ocean circulation. As reviewed by *Griffies et al.* [2000] the representation of overflows is just one component important for ocean modelling and it is not independent of changes in other model components such as the equation of state, the parameterization of mesoscale eddies and the planetary boundary layer. During the course of these studies several experiments have been carried out to investigate the response of the Atlantic meridional overturning circulation (AMOC) to forcing and parameter changes others than the overflows, which will be briefly outlined below. The motivation for these

⁷See Section 6.4.1 for a more extensive description and the actual experiment.

additional experiments was the need to better understand processes that might act in concert or counteract the influence of the overflows on the overturning circulation. To rule out the possibility that the role of the dense northern overflows is overestimated, alternative ideas have been investigated on several questions most importantly the processes controlling the meridional overturning. The following brief overview will concentrate on the role of wind stress in driving the AMOC, the parameter sensitivity to values of vertical and horizontal diffusivities on the modelled overturning as well as the influence of solar irradiance.

6.4.1. The importance of wind stress

In a recent study *Timmermann and Goosse* [2004] have suggested that wind forcing is essential in driving the thermohaline circulation. In a multi-century experiment with the Earth model of intermediate complexity ECBILT(atmosphere)/CLIO(ocean) they showed that wind forcing is needed to maintain meridional overturning flow in the model. Initiated by their remark that this result needs further corroboration from other models, the same experiment was repeated with the UVic model (Section 2.3). The model was integrated for 2000 years reaching equilibrium with present-day wind forcing. From this reference experiment four sensitivity experiments have been carried out with no wind stress (1), no moisture advection (2), no wind stress and no moisture advection (3) and a hysteresis experiment perturbing the North Atlantic fresh water budget (4).

The missing wind stress does not result in a collapse of the thermohaline circulation here (left panel in Figure 6.23) but only in a modest reduction of the AMOC by 2.6 Sv from 19.4 Sv to 16.8 Sv AMOC.

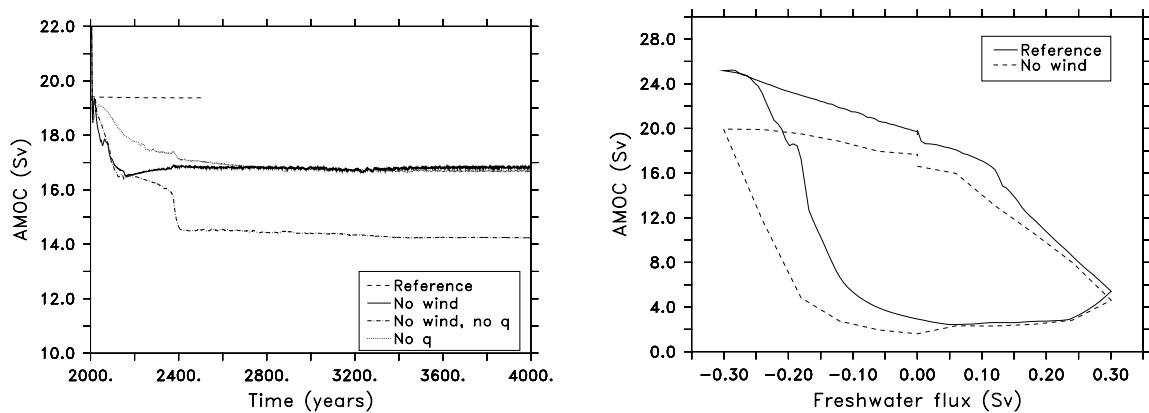


Figure 6.23.: *Left panel:* The Atlantic meridional overturning circulation for the reference experiment and for the experiment with zero momentum input to the ocean from wind stress (no wind). This is compared to experiments with neither moisture advection (no q) nor wind stress and no moisture advection (no wind, no q).

Right panel: Hysteresis loop for reference experiment and experiment with no wind stress. The freshwater forcing was 0.3 Sv/500 yrs.

It was found in previous studies that the moisture advection is important especially in the region of the ITCZ where it is advected against the gradient [*Weaver et al.*, 2001]. However, even the combination of no moisture advection and no wind stress does not result in a collapse of the overturning. Instead the individual reduction from the lack of wind stress (-2.6 Sv) and no moisture advection (-2.7 Sv) are combined (-5.1 Sv).

The possible role of the wind driven circulation during freshwater perturbations was assessed in a hysteresis experiment as FW1A-Ref (Section 6.3) but with no wind stress applied (right panel in Figure 6.23). The experiment starts from the reduced state of AMOC from the previous experiment and is then decreasing as in the reference experiment. It recovers later from the off-state as compared to the reference experiment, which is due to missing advective salt transport.

The sensitivity to a switch-off of wind stress was assessed in the UVic model. The results show that wind stress is not essential in driving the meridional overturning circulation in line with earlier studies [e.g. *Bryan and Cox*, 1967, Fig. 16] but in contrast to the recent study of *Timmermann and Goosse* [2004]. The shut down of NADW production, which they found as a consequence of the missing wind driven northward salinity transport, could not be reproduced. The reason for this discrepancy is not clear yet. Both models are of comparable complexity even though the quasi-geostrophic atmosphere of ECBILT is more realistic than the energy balance atmosphere of the UVic model. A possible explanation for the different model responses might be the parameter range of diffusivities the models act in. The explicit vertical diffusivity in CLIO ranges from $1\text{E-}5$ m^2/s at the surface to $1.1\text{E-}4$ m^2/s at the bottom but in addition there will be an increase in diffusion from the numerical scheme (hybrid scheme of centred differences and upwind). In UVic the numerical scheme is less diffusive, a centred differences scheme, but with higher explicit diffusivities ranging from $6\text{E-}5$ to $1.6\text{E-}4$ m^2/s . An additional sensitivity experiment (not shown) with half the diffusivity does result in a weaker overturning but still the THC does not break down.

There are certainly more differences in details but the question remains. Why should the overturning depend on the direct momentum input of wind stress? The preconditioning of deep convection by the wind stress driven northward salt transport seems to be necessary in the CLIO model. In contrast it is in the UVic model a consequence of the sinking in the north and hence a compensating northward flow is forced. As *Wunsch and Ferrari* [2004] point out using the Sandström theorem, cooling and heating at the same pressure cannot provide energy for a meridional overturning circulation without input of turbulent kinetic energy by winds and/or tides creating interior mixing. However, the vertical mixing is part of the hydrodynamic equations in the model and is prescribed independent of wind stress. Therefore, it is argued here that switching off the wind stress in a model without a turbulent kinetic energy closure is not suited to assess the importance of wind stress and second there is no theoretical reason why the overturning should break down when the momentum input is switched off but the vertical mixing is kept fixed.

6.4.2. Horizontal and vertical diffusion

The study of *Redler and Böning* [1997] has suggested a direct relation of the representation of the Denmark Strait overflow and the meridional overturning circulation in the North Atlantic. The question one should ask how this property relates to other variables setting the MOC strength. As already shown by *Gnanadesikan* [1999] simple scaling arguments can be found which relate the MOC to the density contrast between equator and high latitudes and the vertical diffusion. In their review of scaling arguments *Nilsson et al.* [2003] show that the strength of the AMOC is set by the vertical diffusivity A_v and the equator to pole density contrast $\Delta\rho$ by

$$AMOC \propto \Delta\rho^{1/3} A_v^{2/3}. \quad (6.3)$$

This scaling argument was assessed in the UVic model by systematically varying the vertical diffusivity profile to explore the parameter space (left panel in Figure 6.24). In a similar study

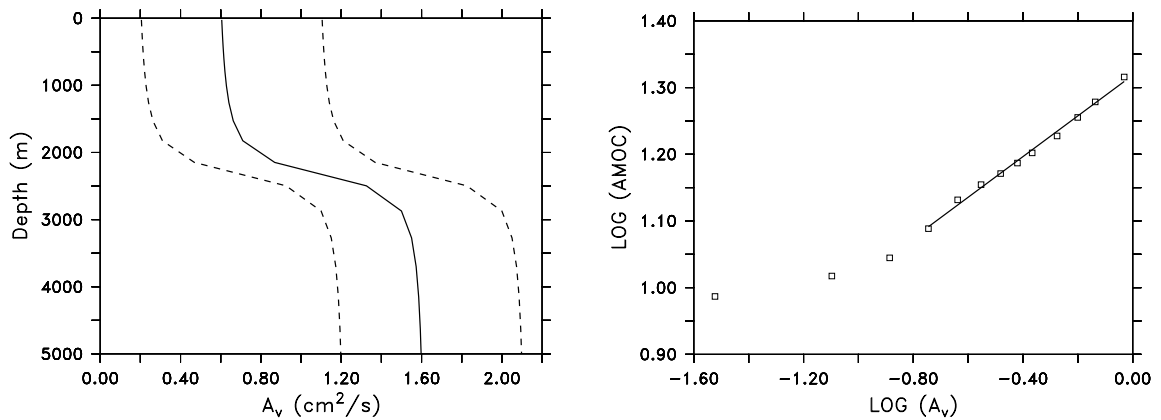


Figure 6.24.: *Left panel:* Depth profile of the vertical diffusivity with the standard profile as solid line and the dashed lines indicating the largest deviation from the reference profile considered in the sensitivity experiments. *Right panel:* AMOC strength versus vertical diffusion in the pycnocline on a logarithmic scale. The solid line represents a linear regression of the right branch of the curve (-0.8 to 0).

Prange et al. [2003] obtain from modelling results with the Hamburg large scale geostrophic model the expected $2/3$ power-law dependence by varying the vertical diffusivity mainly at pycnocline depth level, assuming that changes in diffusivity in the deep ocean do not have a strong effect. In the experiments presented here, the complete vertical diffusivity profile is shifted along the axis (Figure 6.24). From this an asymptotic behaviour for small diffusivities is obtained and a linear relationship for larger values of the diffusivity indicates a $1/3$ power-law. The $1/3$ power-law is in contrast to earlier studies of *Bryan and Cox* [1967] and *Prange et al.* [2003] but consistent with the study of *Schmittner and Stocker* [2001]. The difference is attributed to the set-up of the vertical diffusivity. Here the deeper levels are affected, whereas *Prange et al.* [2003] keep the value in the deep ocean constant. Since the results are different it is likely that it is not only the pycnocline level which affects the overturning but the deep ocean could play a role.

In an additional set of sensitivity experiments the isopycnal diffusivity A_h was changed to investigate the relation between horizontal diffusivity and overturning. The results (Figure 6.25) are presented in non-dimensional form to make it comparable to future studies with different grid resolutions. For this reason the grid Peclet number was defined as $Pe = \frac{v \Delta y}{A_h}$ with v as the zonal mean between 40° N and 50° N of the meridional maximum velocities in the depth range of 200-2000 m, which is the location of the maximum overturning circulation. Δy is the grid spacing in meridional direction (≈ 200 km). The experiments show an asymptotic behaviour for increasing Peclet number (decreasing diffusivity) and a rapid decrease for a Peclet number smaller than 18 ($A_h > 5 \cdot 10^6$). If the Peclet number is further decreased the model becomes finally unstable ($Pe < 10$).

The equator-to-pole density difference was not dealt with here separately but a general question arises from the scaling law (Equation 6.3). If this scaling holds, what does it imply for ocean models of different grid spacing? Assume that the resolution is doubled, then one would need a smaller numerical diffusion to obtain stable results and to get a realistic

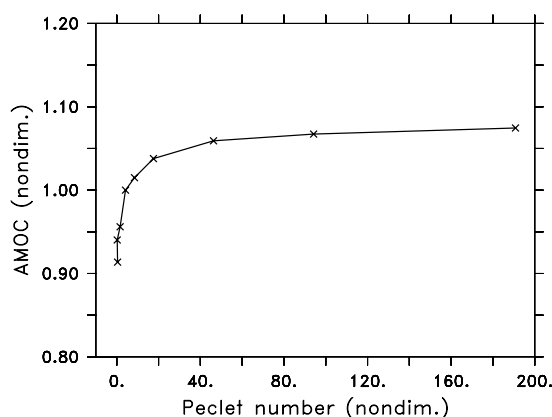


Figure 6.25.: AMOC strength normalised by the reference value versus horizontal grid Peclet number representing inverse isopycnal diffusivities.

overturning. One has to separate explicit diffusion and numerical diffusion here but it certainly changes with grid resolution. For simplicity let's assume that half of the diffusivity is taken. In order to obtain the same overturning the equator-to-pole density contrast would have to increase by a factor of 4 (cf. Eq. (6.3)). Thus, as the density difference is that between low and high latitudes one would expect that the overflow density becomes more important with higher grid resolution.

6.5. Summary and conclusions

An overflow parameterisation based on hydraulic constraints has been evaluated in high- and coarse-resolution sigma-coordinate models. This approach was extended from a regional to a global climate model testing different approaches to yield more realistic overflows. It was shown that the parameterisation has a significant but small effect on the meridional overturning circulation and closely linked quantities such as the sea-ice cover. However, a strong stabilising effect on the thermohaline circulation as could not be found. It was shown that the overflow representation was significantly improved using the parameterisation. The sea-ice cover in the Nordic Seas is reduced and the deep water formation north of the GSR is enhanced. The dense signal can be traced downstream of the Denmark Strait eventually strengthening the DWBC. The effect of these changes in a long-term integration using a coupled model is smaller than expected from previous studies based on ocean only, regional North Atlantic models [Döscher *et al.*, 1994; Böning *et al.*, 1996; Redler and Böning, 1997]. However, it was shown that changes in the overflow properties do have strong remote impact, e.g. the rise in annual mean surface air temperature by 0.5°C when using the parameterisation as compared to the reference experiments. This emphasises that there is no need for very pronounced changes in the overturning to yield a noticeable impact on Europe's climate.

The key features found in this chapter comprise:

- An overflow parameterisation based on hydraulic constraints could be successfully validated in a high-resolution σ -coordinate model. The implementation in a coarse-resolution version of the regional model had only minor effects.
- The long-term evaluation in the coupled climate model UVic ESCM did show significant differences when the parameterisation was active. The overturning was increased

by 6%, the mixed layer depth in the Iceland and Norwegian seas is increased and the sea-ice volume is reduced. However, remote effects on the circulation and stratification are small.

- The enhanced representation of the overflows does not contribute to an enhanced stability of the meridional circulation in this model if the freshwater input to the North Atlantic is increased.
- The self recovery of the overturning takes place independent of the overflow representation or wind stress feedback
- Including a bottom boundary layer scheme does lead to a better preservation of the overflow densities but has local effects on the circulation, only.

7. Summarising discussion

7.1. Regional dynamics

The focus of this study was on the Denmark Strait overflow and the dynamics that have determined its strength since the Last Glacial Maximum. Details of the overflow transport, such as the density structure and pathway found in, or derived from observations could be reproduced in idealised process studies treating the overflow as forced from buoyancy alone. The process model consists of an eddy resolving numerical model which can explicitly account for processes on Rossby length scale. Initially, it was set up with a density structure resembling a two-layer model and a wide parameter range concerning cross-sill density contrast ($\Delta\rho= 0.16 - 0.72 \text{ kg/m}^3$) and reservoir height of dense water above sill level (0 - 600 m) was covered. Based on a Froude number analysis it was shown that the transport is limited by hydraulic constraints within the parameter space. The flow reaches critical conditions 80km south from the sill independent of the reservoir height and only weakly dependent on the density contrast. For an increasing density contrast the flow reaches critical conditions more closely to the sill and vice versa for decreased density contrast farther away from the sill. These sensitivity experiments corroborate previous laboratory experiments [*Whitehead et al.*, 1974] and numerical studies [*Käse and Oschlies*, 2000] focusing on conditions representative for present-day.

For hydraulically controlled flow the volume transport is set by the density contrast and effective height. Different theoretical approaches estimating the maximum hydraulic transport of *Whitehead et al.* [1974], *Nikolopoulos et al.* [2003] and *Helfrich and Pratt* [2003] were compared. All theoretical estimates can be scaled to predict the modelled transport but they show good skills for different applications. The estimate of *Whitehead et al.* [1974] imposes an upper transport bound if taken far upstream and almost accurately predicts the variable transport at the sill. The theory of *Nikolopoulos et al.* [2003] provides upper and lower transport bounds whereas the estimate of *Helfrich and Pratt* [2003] yields the mean modelled transport without scaling and as the only estimate independent of the upstream circulation. It is very interesting to note that the upstream estimate of *Whitehead et al.* [1974] was refined in a study by *Stern* [2004]. They imposed a kinematic constraint on the along-stream velocity component and found that the actual transport should be 9/16 or 56% of the upstream limit. Taking further into account that *Nikolopoulos et al.* [2003] found a 10% decrease of the upstream limit if they account for realistic bathymetry, one obtains exactly the result found in this study that the actual transport is 46% of the upstream limit. The hydraulic transport limitation can be used to predict the overflow's response to changes in the upstream reservoir, e.g. the observed freshening of the Nordic Seas [*Dickson et al.*, 2002] leads to reduced density contrast by 0.033 kg/m^3 and should result in a decrease in overflow strength from 2.9 Sv to 2.7 Sv.

The same modelling approach was subsequently applied to a number of time-slices (11.3, 21.5, 30, 70 ka BP) to obtain an estimate for the paleo-overflow strength. Hydraulic theory could be corroborated for the different glacial-interglacial bathymetries and it was found

that the expected quadratic relation of sill depth and transport holds. Interestingly for geological applications the ice extent on the shelves did not have a strong effect. Comparing the expected changes in bathymetry and density contrasts for the LGM as obtained from global models it was shown that the density variations had a larger impact on the overflow strength than the restriction of the topography. The lowered sea-level alone will have reduced the overflow transport by 30% whereas the reduced density contrast will have lowered the overflow transport by more than 60% of the present-day value.

Classical hydraulic theory assumes an infinite upstream basin. Theoretically the circulation is initiated by a Kelvin wave travelling upstream along the eastern wall and setting up an anti-cyclonic circulation. This is in harmony with the model experiments driven by an interior downwelling source. In contrast to that the upstream circulation is primarily cyclonic for a boundary inflow in agreement with the description for a finite basin of *Helfrich and Pratt* [2003]. The modelled overflow does respond to the altered upstream circulation. The hydraulic estimate at the sill correctly predicts the transport whereas the upstream estimates cannot account for the changed circulation. This shows that one has to assume a constant upstream circulation when relying on the upstream estimate. The discussion on the upstream circulation could in principle help to clarify the origin of DSOW. Unfortunately this is not the case since the proposed origin of DSOW from the Iceland Sea [*Jónsson and Valdimarsson*, 2004] is in agreement with the interior downwelling source whereas the boundary inflow with the EGC as proposed by *Rudels et al.* [2002] yields to a cyclonic circulation. The regional model with windstress and a realistic density structure is in favour of an overflow originating from the EGC, but the model is restricted to a very specific wind stress situation and several full seasonal cycles would be needed for a more complete answer. This issue is left to future studies.

A possible limitation of the validity of hydraulic theory arises from the assumption that the potential vorticity is constant along a stream line. This is not the case in the model and emphasises that friction and the effects of diapycnal mixing influence the overflow as it was observed for the Faroe Bank Channel [*Saunders*, 1990]. However, for the Denmark Strait a Grashof number analysis has shown that that these effects are of minor importance only.

Apart from the overflow's transport its path was investigated. For present-day conditions the modelled descent of the overflow agrees well with observations. As a result of a reduced density contrast, as indicated for the LGM by global model results, it was found that the overflow path shifts upwards to shallower depth whereas it descends faster for increased density contrasts. The sedimentation patterns associated with the descending overflow were modelled to provide additional information for sediment cores obtained in this region. Material eroded along the path of the overflow is redeposited primarily downslope adjacent to coring locations investigating the overflow which yields confidence that the expected signal is recorded despite the spatial distance to the actual core of the overflow. As a drawback the admixture of Irminger Current water was almost certainly variable with time due to the relative change of the overflow's position and should be taken into account when interpreting the sediment records. A realistic entrainment of ambient water and the conservation of overflow properties downstream is dependent on a realistic background stratification. In the two-layer model the entrainment close to the sill is too strong whereas the observations are almost reproduced once a mean climatological background stratification is used.

Following the study focused on the Denmark Strait, the wind driven transport was more closely inspected in a regional model of the Greenland-Scotland Ridge. The results of these wind forced experiments indicate that the view on the Denmark Strait overflow as purely

buoyancy driven needs to be reconsidered. If present-day wind stress is applied, the buoyancy driven part is about 1.9 Sv and the wind driven part about 1 Sv. The direct influence of wind stress on the overflow is significant and a linear relation of local wind stress and overflow transport was obtained. As an application the influence of the NAO on the overflow transport was considered. It was found that transport fluctuations at least in the order of 0.2 Sv have to be expected for different phases of the NAO. For increased wind stress during a positive phase of the NAO the outflow through Denmark Strait is increased and the outflow through the Faroe-Shetland Channel is decreased. These modelling results are in contrast to observations which show neither seasonal nor interannual variability of the overflow [Dickson and Brown, 1994; Girton *et al.*, 2001]. However, recent observations of Macrander *et al.* [subm.] indicate that interannual variability might have been overlooked before. In addition, the influence of variable wind stress on the overflow transport found here is similar to the model study of Biastoch *et al.* [2003]. In an ocean model of slightly coarser resolution (about 9 km at the Denmark Strait) they found that the overflow transport is strongly dependent on the wind stress. In their study the most pronounced changes are at the shallower part of the shelf break whereas the wind stress in the experiments presented here changes in addition the barotropic fraction in the overflow core itself. This raises again the question how hydraulic control is accomplished in the presence of barotropic net flow. Sensitivity experiments with the Denmark Strait model with constant barotropic net flow suggest that baroclinic and barotropic component can be simply added as a first order assumption. However, this issue clearly needs to be reconsidered from a more theoretical perspective in future studies. The results indicating that wind stress does play a role question the approach to determine the absolute overflow transport purely based on hydraulic constraints. What remains valid is to determine relative changes due to variations in sill depth and density contrast.

The experiments for LGM conditions have been carried out as a comparison of present-day winter and LGM summer conditions, both times with active deep-water formation in the Nordic Seas as evident from observations and reconstructions. The LGM experiments with the GSR model have generally corroborated the previous experiments using the Denmark Strait set-up. The overflow from the Nordic Seas into the Atlantic was strongly reduced even though the increased wind stress could compensate for the decreased density contrast to some extent. The inferred strong reduction of DSOW but ongoing export of dense water from the Nordic Seas is in line with observations of decreased bottom water ventilation rates based on $\delta^{13}\text{C}$ [Dokken and Jansen, 1999; Sarnthein *et al.*, 2001]. The reliability of this estimate is limited by the ability of the global ocean circulation models to reproduce a realistic density stratification. As seen for the present-day reference experiment the density contrast is slightly underestimated and therefore the LGM estimate might be too low as well. However, this does not limit the conclusion that the strength of the Denmark Strait overflow for the LGM was strongly reduced relative to present-day. The most realistic scenario is that the overflow was in the range of 0 Sv to 0.5 Sv southward flow for glacial summer conditions. Glacial winter conditions were not explicitly considered and the situation was probably different since the sea-ice cover will have diminished the influence of wind stress and deep water formation by brine release could have played a role. As previously outlined the dense water reservoir north of the GSR has a spin down time to reduce the reservoir height by half in about 2 years. Thus it can be expected that the seasonal difference in buoyancy driven transport between glacial summer and winter have been similarly small as today. The maximum change to expect is a reduction in the overflow to zero transport for glacial winter.

The cyclonic circulation pattern proposed for the Nordic Seas for LGM summer conditions is different from the original interpretation of *Sarnthein et al.* [2003b]. They suggest a strong inflow through Denmark Strait and hence an anti-cyclonic circulation. This is not consistent with the modelling results, observational and theoretical evidence that the large scale flow is governed by f/H [*Nøst and Isachsen, 2003*], all suggesting a cyclonic circulation in the Nordic Seas.

The modelled northward heat transport in LGM summer is about 30% of the present-day winter value which is consistent with reconstructions based on planktic foraminifera [*Weinelt et al., 2003*]. They find a reduction of the poleward heat transport to values between 0-60% of present-day. Increased glacial wind stress as obtained in AGCM experiments [*Lohmann and Lorenz, 2000*] was suggested as a driving mechanism to keep the Nordic Seas ice free. Increased wind stress would also lead to a strengthening of the gyre circulation in the North Atlantic and to an increase in northward heat transport. The opposite effect is true for closing the Denmark Strait. This has a great impact on the overflow transports and more importantly on the heat transports. If Denmark Strait is closed, e.g. by icebergs, the net outflow from the Nordic Seas into the North Atlantic decreases and in turn the northward heat transport decreases, which can be seen as positive feedback to produce an even larger sea ice cover.

The distribution of marine biota was simulated by Lagrangian drifters. The dispersal pattern suggests that although the cross sill transport was significantly reduced exchange still took place. A cyclonic route around Iceland could be identified which could have carried surface dwellers from a location south of the Denmark Strait to the north crossing the Iceland-Faroe Ridge.

7.2. Basin wide impact

One of the main aims of the detailed study on the hydraulic constraints was to employ this relation as parameterisation in a global climate model. Initial tests with high- and medium-resolution models gave the necessary confidence that the overflow representation can be improved by using the hydraulic constraints as a sub-grid scale parameterisation to determine a physically consistent overflow transport.

The overflow parameterisation did indeed significantly improve the overflow representation in the global coupled climate model. The amount of dense water export could be increased towards more realistic values. The effect on the AMOC was an increase by 1 Sv, a strengthening of the DWBC and a reduction of the excessive sea-ice cover in the Nordic Seas.

In contrast to previous studies using ocean only models of the North Atlantic [*Döscher et al., 1994; Gerdes and Köberle, 1995; Redler and Böning, 1997*] the effect of the parameterisation in the coupled global model was smaller than expected. A comparison of the experiment with parameterised overflows and an experiment with deep Greenland-Scotland ridge without overflows does not show significant differences in meridional overturning. Furthermore, it is shown that the resumption of the AMOC from an off-state does neither depend on the representation of the overflows nor on the inclusion of a bottom boundary layer. In addition the importance of wind stress is assessed for the mean model state and for the resumption of the AMOC. It is found that there certainly is a wind driven circulation but the stability of the AMOC does not critically depend on the direct momentum forcing by winds.

The breakdown of the THC in response to freshwater anomalies is as expected from conceptual models [Rahmstorf, 1996] and in agreement with other coupled models [e.g. Rahmstorf, 1995; Schmittner *et al.*, 2002a]. The spatial distribution of the fresh water input affects the rate of decrease directly. If close to the areas of deep water formation the THC is more sensitive and the response is faster. Nevertheless, even an freshwater perturbation in the Labrador Sea leads in this model ultimately to a shutdown of convection in the Nordic Seas due to the advection of the anomaly with the subpolar gyre. This behaviour might be in part due to the relatively large rate of the freshwater perturbation used here, but some confidence that these results are reliable is gained from the experiments with half the freshwater perturbation rate. In contrast to other studies [Lohmann, 1998], it was found that the stability of the THC is neither enhanced through a better representation of the Denmark Strait overflow by using the parameterisation nor does it need a BBL scheme for better conservation of the overflow plume to recover.

The apparent differences between the model results presented here and previous model studies can be solved when considering that a different type of model is used. The studies showing an extremely high sensitivity to the northern overflows are regional ocean only models of the North Atlantic. In contrast to that a global coupled model of intermediate complexity was used here. This view is supported by results of Thorpe *et al.* [2004] based on sensitivity experiments with the coupled global model HadCM3. Their results are in good agreement with the present study. They have locally (60° N - 68° N, 45° W - 0° W) changed the convection scheme to that of Roether *et al.* [1994]. It essentially acts like a BBL scheme, better conserving the density properties of the overflow. In agreement with the results presented here they find regional effects as an increase in density at mid depth in the Labrador Sea and a slightly increased transport past Cape Farewell but the effect on the AMOC is small (their Figure 4). Moreover, they find that the representation of the Denmark Strait overflow does not play a role in climate change scenarios with increasing CO₂, which agrees with the freshwater perturbation experiments shown here. Overall, this suggests that the role of the Denmark Strait overflow seems to be overly emphasised in ocean only models where the atmospheric feedbacks [Latif, 2001; Vellinga *et al.*, 2002] are not taken into account.

8. Conclusions

The main findings of this study, based on results of a high-resolution ocean model and a global climate model, are:

- The Denmark Strait can be described as hydraulically controlled to a first order but an influence of wind stress on the Denmark Strait overflow has to be expected at least in the range of ± 0.2 Sv between positive and negative phases of the North Atlantic Oscillation.
- The overflow estimate using hydraulic theory is sensitive to the site where it is computed. It is strongly advised to derive estimates from the sill entrance region to take into account for changes in the upstream circulation.
- For Last Glacial Maximum summer conditions the overflow was in the range of 0 to 0.5 Sv southward flow. The ice extent on the shelves and the lowered sea-level were of minor importance, about 2/3 of the reduction in overflow was due to a decreased density contrast.
- The northward heat transport during Last Glacial Maximum summer was generally reduced compared to present-day winter. This reduction was especially pronounced at times when the Denmark Strait was blocked by icebergs. The advection of warm water into the Nordic Seas was similar to present-day but with a stronger inflow through the Faroe-Shetland Channel and a weaker inflow through the Denmark Strait.
- The overflow parameterisation yields an improved overflow representation in the coarse resolution model. The export of dense water is enhanced and the northward heat transport increases but the effect on the meridional overturning and stabilising effects during freshwater perturbations are rather weak.

Some of the results presented above need further attention. It would be desirable to apply the overflow parameterisation in a model of higher, e.g. one degree, resolution. If the results can be reproduced in models with better representation of the subpolar gyre and western boundary currents this would additionally corroborate the findings of this study. The same holds for the experiments with freshwater forcing, in a model with more realistic deep water production in the Nordic Seas the overflows could possibly have a stronger impact on the overturning.

A. Appendices

A.1. List of acronyms

The following acronyms are commonly used throughout this work. They are introduced in each chapter again out of convenience for the reader because it is assumed that many readers will skip certain chapters.

ACC:	Antarctic Circumpolar Current
AGCM:	Atmospheric General Circulation Model
AW:	Atlantic Water
D/O:	Dansgaard-Oeschger
DS:	Denmark Strait
DSO:	Denmark Strait overflow
DSOW:	Denmark Strait Overflow Water
DWBC:	Deep Western Boundary Current
EMIC:	Earth Model of Intermediate Complexity
FBC:	Faroe Bank Channel
FSC:	Faroe-Shetland Channel
GIN Sea:	Greenland-Iceland-Norwegian Sea
GSR:	Greenland-Scotland Ridge
IFR:	Iceland-Faroe Ridge
ISOW:	Iceland Scotland Overflow Water
LGM:	Last Glacial Maximum
MLD:	Mixed Layer Depth
NAC:	North Atlantic Current
NAO:	North Atlantic Oscillation
NwAC:	Norwegian Atlantic Current
NATL:	North Atlantic
O(...):	Order of (...)
OGCM:	Ocean General Circulation Model
PD:	Present-day
Q:	Transport
SSH:	Sea Surface Height
SST:	Sea Surface Temperature
WTR:	Wyville-Thomson Ridge

A.2. Model formulation

A.2.1. Equations of motion

The equations of motion take in Cartesian coordinates and for Boussinesq and hydrostatic approximations, the following form:

$$\frac{\partial u}{\partial t} + \mathbf{v} \cdot \nabla u - fv = -\frac{\partial \phi}{\partial x} + \mathcal{F}_u + \mathcal{D}_u \quad (\text{A.1})$$

$$\frac{\partial v}{\partial t} + \mathbf{v} \cdot \nabla v + fu = -\frac{\partial \phi}{\partial y} + \mathcal{F}_v + \mathcal{D}_v \quad (\text{A.2})$$

$$\frac{\partial \phi}{\partial z} = \frac{-\rho g}{\rho_0} \quad (\text{A.3})$$

The assumption of an incompressible fluid is stated by the continuity equation:

$$\frac{\partial u}{\partial x} + \frac{\partial v}{\partial y} + \frac{\partial w}{\partial z} = 0 \quad (\text{A.4})$$

The advective-diffusive equations which govern the temporal evolution of the potential temperature and salinity field are:

$$\frac{\partial T}{\partial t} + \mathbf{v} \cdot \nabla T = \mathcal{F}_T + \mathcal{D}_T \quad (\text{A.5})$$

$$\frac{\partial S}{\partial t} + \mathbf{v} \cdot \nabla S = \mathcal{F}_S + \mathcal{D}_S \quad (\text{A.6})$$

$$(\text{A.7})$$

The density is calculated from potential temperature and salinity using either the non-linear equation of state:

$$\rho = \rho(T, S, P) \quad (\text{A.8})$$

or a linear form, where density is dependent only on temperature (or only on salinity):

$$\rho = \rho(T) \quad \rho = \rho(S) \quad (\text{A.9})$$

(u, v, w) is the (x, y, z) -components of vector velocity \mathbf{v}

$S(x, y, z, t)$ is the salinity of the ocean

$T(x, y, z, t)$ is the potential temperature of the ocean

$\rho_0 + \rho(x, y, z, t)$ is the total in-situ density

$\phi = \frac{P}{\rho_0}$ is the dynamic pressure

$f(x, y)$ is the Coriolisparameter

g is the acceleration of gravity

$P \approx -\rho_0 g z$ is the total pressure

$\mathcal{F}_T, \mathcal{F}_S, \mathcal{F}_u, \mathcal{F}_v$ are the forcing terms

$\mathcal{D}_T, \mathcal{D}_S, \mathcal{D}_u, \mathcal{D}_v$ are the diffusive terms

A.2.2. Stretched vertical coordinate system and horizontal curvilinear coordinates

$$z = \zeta(1 + s) + h_c s + (h - h_c)\mathcal{C}(s), \quad (\text{A.10})$$

where h_c is a constant to be chosen as a typical surface mixed layer depth, and The ROMS σ -grid formulation uses the transformation function,

$$\mathcal{C}(s) = (1 - \theta_b) \frac{\sinh(\theta_s s)}{\sinh \theta_s} + \theta_b \frac{\tanh[\theta_s(s + \frac{1}{2})] - \tanh(\frac{1}{2}\theta_s)}{2 \tanh(\frac{1}{2}\theta_s)}, \quad (\text{A.11})$$

with the vertical coordinate s in the range of $-1 \leq s \leq 0$ and the the surface and bottom stretching parameters θ_s ($0 \leq \theta_s \leq 20$) and θ_b ($0 \leq \theta_b \leq 1$). This transformation allows a clustering of points close to the surface or close to the surface and to the bottom. It does not allow for clustering close to the bottom, which might be more useful for overflow problems. For large values of θ the resolution is increased at the surface for $b=0$ and equally increased at the bottom and at the surface for $b=1$, with a smooth transition between both .

The horizontal discretization is on an Arakawa C grid (Figure: A.1), following a second-order finite difference scheme. This method is well suited for problems with a horizontal resolution smaller than the Rossby radius [*Arakawa and Lamb, 1977*].

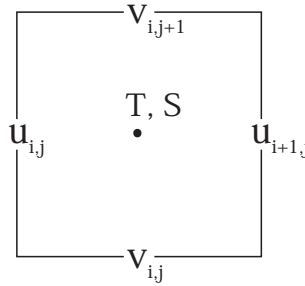


Figure A.1.: Schematic representation of the Arakawa C-grid.

In the horizontal curvilinear coordinates are used to allow for a coastline following grid and higher resolution in parts of particular interest. The new coordinates are obtained by a transformation from (x, y) to (ξ, η) , where the relationship of horizontal arc length to the differential distance is given by

$$(ds)_\xi = \left(\frac{1}{m}\right) d\xi \quad (\text{A.12})$$

$$(ds)_\eta = \left(\frac{1}{n}\right) d\eta \quad (\text{A.13})$$

with $m(\xi, \eta)$ and $n(\xi, \eta)$ are the scale factors which relate the differential distances $(\Delta\xi, \Delta\eta)$ to the physical arc length. Alternatively coastal boundaries can be specified as a finite-discretized grid via land/sea masking.

Bibliography

- Alley, R. B., Icing the north Atlantic, *Nature*, 392, 335, 1998.
- Alve, E., Colonization of new habitats by benthic foraminifera: a review, *Earth-Sci. Rev.*, 46, 167–185, 1999.
- Andrews, J. T., and S. Cartee-Schoolfield, Late Quaternary lithofacies, provenance, and depositional environments (12–30 cal ka), north and south of the Denmark Strait, *Mar. Geo.*, 199, 65–82, 2003.
- Andrews, J. T., T. A. Cooper, A. E. Jennings, A. B. Stein, and H. Erlenkeuser, Late Quaternary iceberg-rafted detritus events on the Denmark Strait-Southeast Greenland continental slope ($\approx 65^\circ$ N): related to North Atlantic Heinrich events?, *Mar. Geo.*, 149, 211–228, 1998.
- Appenzeller, C., T. F. Stocker, and M. Anklin, North Atlantic oscillation dynamics recorded in Greenland ice cores, *Science*, 282, 446–449, 1998.
- Arakawa, A., and V. R. Lamb, A primitive equation model, *Methods of computational physics*, 17, 174–265, 1977.
- Armi, L., The hydraulics of two flowing layers with different densities, *J. Fluid Mech.*, 163, 27–58, 1986.
- Bacon, S., Circulation and fluxes in the North Atlantic between Greenland and Ireland, *J. Phys. Oceanogr.*, 27, 1420–1435, 1997.
- Bacon, S., Decadal variability in the outflow from the Nordic seas to the deep Atlantic Ocean, *Nature*, 394, 871–874, 1998.
- Bauch, H., K. Darling, J. Simstich, H. A. Bauch, H. Erlenkeuser, and D. Kroon, Paleoceanographic implications of genetic variation in living North Atlantic *Negloboquadrina pachyderma*, *Nature*, 424, 299–302, 2003.
- Beckmann, A., and R. Döscher, A method for improved representation of dense water spreading over topography in geopotential-coordinate models, *J. Phys. Oceanogr.*, 27, 581–591, 1997.
- Beckmann, A., and D. B. Haidvogel, Numerical simulation of flow around a tall, isolated seamount. Part I: Problem formulation and model accuracy, *J. Phys. Oceanogr.*, 23, 1736–1753, 1993.
- Beismann, J. O., and B. Barnier, Variability of the meridional overturning circulation of the North Atlantic: sensitivity to overflows of dense water masses, *Oc. Dyn.*, 54, 92–106, 2004.
- Bennike, O., and Björck, Chronology of the last recession of the Greenland Ice Sheet, *J. Quat. Sc.*, 17, 211–219, 2002.
- Berger, A., and M. F. Loutre, Insolation values for the climate of the last 10 million years, *Quaternary Science Reviews*, 10, 297–317, 1991.
- Bersch, M., North Atlantic Oscillation-induced changes of the upper layer circulation in the northern North Atlantic Ocean, *J. Geophys. Res.*, 107, 3156, 2002.
- Biastoch, A., R. H. Käse, and D. B. Stammer, The sensitivity of the Greenland-Scotland Ridge overflow to forcing changes, *J. Phys. Oceanogr.*, 33, 2307–2319, 2003.
- Bitz, C. M., M. M. Holland, A. J. Weaver, and M. Eby, Simulating the ice-thickness distribution in a coupled climate model, *J. Geophys. Res.*, 106, 2441–2464, 2001.

- Blindheim, J., V. Borovkov, B. Hansen, S. A. Malmberg, W. R. Turrell, and S. Østerhus, Upper layer cooling and freshening in the Norwegian Sea in relation to atmospheric forcing, *Deep Sea Res. I*, *47*, 655–680, 2000.
- Bojariu, R., and L. Gimeno, Predictability and numerical modelling of the North Atlantic Oscillation, *Earth-Sci. Rev.*, *63*, 145–168, 2003.
- Bond, G., W. S. Broecker, S. Johnsen, J. McManus, L. Labeyrie, J. Jouzel, and G. Bonani, Correlations between climate records from North Atlantic sediments and Greenland ice, *Nature*, *365*, 143–147, 1993.
- Bond, G., et al., Persistent Solar Influence on North Atlantic Climate During the Holocene, *Science*, *294*, 2130–2136, 2001.
- Böning, C. W., and A. J. Semtner, *Ocean Circulation and Climate*, chap. High-Resolution Modelling of the Thermohaline and Wind-Driven Circulation, pp. 59–77, Academic Press, 2001.
- Böning, C. W., F. O. Bryan, W. R. Holland, and R. Döscher, Deep-water formation and meridional overturning in a high-resolution model of the North Atlantic, *J. Phys. Oceanogr.*, *26*, 1142–1164, 1996.
- Borenäs, K., and A. Nikolopoulos, Theoretical calculations based on real topography of the maximum deep-water flow through the Jungfern Passage, *J. Mar. Res.*, *58*, 709–719, 2000.
- Borenäs, K. M., and P. A. Lundberg, On the Deep-Water Flow Through the Faroe Bank Channel, *J. Geophys. Res.*, *93*, 1281–1292, 1988.
- Borenäs, K. M., and J. A. Whitehead, Upstream separation in a rotating channel flow, *J. Geophys. Res.*, *103*, 7567–7578, 1998.
- Borenäs, K. M., I. L. Lake, and P. A. Lundberg, On the intermediate water masses of the Faroe-Bank Channel overflow, *J. Phys. Oceanogr.*, *31*, 1904–1914, 2001.
- Boyle, E., Last Glacial Maximum North Atlantic deep water: on, off or somewhere in-between?, *Phil. Trans. R. Soc. Lond. B*, *348*, 243–253, 1995.
- Bruce, J. G., Eddies southwest of the Denmark Strait, *Deep Sea Res. I*, *42*, 13–29, 1995.
- Bryan, K., and M. D. Cox, A numerical investigation of the oceanic general circulation, *Tellus*, *19*, 54–80, 1967.
- Bryden, H. L., and S. Imawaki, Ocean heat transport, in *Ocean Circulation and Climate*, edited by G. Siedler, J. Church, and J. Gould, pp. 455–474, Academic Press, 2001.
- Bryden, H. L., J. Candela, and T. H. Kinder, Exchange through the Strait of Gibraltar, *Progr. Oceanogr.*, *33*, 201–248, 1994.
- Campin, J.-M., and H. Goosse, Parameterization of density-driven downsloping flow for a coarse-resolution ocean model in z-coordinate, *Tellus*, *51A*, 412–430, 1999.
- Cenedese, C., J. A. Whitehead, T. A. Ascarelli, and M. Ohiwa, A Dense Current Flowing down a Sloping Bottom in a Rotating Fluid, *J. Phys. Oceanogr.*, *34*, 188–203, 2003.
- Chassignet, E. P., et al., DAMEE-NAB: the base experiments, *Dyn. Atmos. Oceans*, *32*, 155–183, 2000.
- Clark, P. U., and A. C. Mix, Ice sheets and sea level of the Last Glacial Maximum, *Quaternary Science Reviews*, *21*, 1–7, 2002.
- CLIMAP, P. m., Seasonal reconstructions of the earth's surface at the last glacial maximum, 1981.
- Conkright, M. E., R. A. Locarnini, H. E. Garcia, T. D. O'Brien, B. T. P., C. Stephens, and J. I. a. Antonov, World Ocean Atlas 2001: Objective Analyses, Data Statistics and Figures, *CD-ROM Documentation*, National Oceanographic Data Center, Silver Spring, MD, 2003.

- Cook, E. R., R. D. D'Arrigo, and M. E. Mann, A Well-Verified, Multiproxy Reconstruction of the Winter North Atlantic Oscillation Index since A.D. 1400, *J. Clim.*, *15*, 1754–1764, 2002.
- Cottet-Puinel, M., A. J. Weaver, C. Hillaire-Marcel, A. de Vernal, P. U. Clark, and M. Eby, Variation of Labrador Sea Water formation over the Last Glacial cycle in a climate model of intermediate complexity, *Quaternary Science Reviews*, *23*, 449–465, 2004.
- Crowley, T. J., CLIMAP SSTs re-visited, *Clim. Dyn.*, *16*, 241–255, 2000.
- Curry, R., and M. S. McCartney, Ocean gyre circulation changes associated with the North Atlantic Oscillation, *J. Phys. Oceanogr.*, *31*, 3374–3400, 2001.
- Curry, R., B. Dickson, and I. Yashayaev, A change in the freshwater balance in the Atlantic Ocean over the past four decades, *Nature*, *426*, 826–829, 2003.
- Curry, W. B., J.-C. Duplessy, L. D. Labeyrie, and N. J. Shackleton, Changes in the distribution of $\delta^{13}\text{C}$ of deep water ΣCO_2 between the last glaciation and the Holocene, *Paleoceanogr.*, *3*, 317–341, 1988.
- Dansgaard, W., et al., Evidence for general instability of past climate from a 250-kyr ice-core record, *Nature*, *364*, 218–220, 1993.
- Darby, D. A., and J. F. Bischof, A Holocene record of changing Arctic Ocean ice drift analogous to the effects of the Arctic Oscillation, *Paleoceanogr.*, *19*, PA1027, 2004.
- DaSilva, A. M., C. C. Young, and S. Levitus, Atlas of surface marine data 1994, volume 1: Algorithms and procedures, *Techn. Rep. 6*, Department of Commerce, NOAA, 1994.
- de Vernal, A., and C. Hillaire-Marcel, Sea-ice cover, sea-surface salinity and halo-/thermocline structure of the northwest North Atlantic: modern versus full glacial conditions, *Quaternary Science Reviews*, *19*, 65–85, 2000.
- de Vernal, A., C. Hillaire-Marcel, W. R. Peltier, and A. J. Weaver, Structure of the upper water column in the northwest North Atlantic: Modern versus Last Glacial Maximum conditions, *Paleoceanogr.*, *17*, 2002.
- Dengg, J., C. Böning, U. Ernst, R. Redler, and A. Beckmann, Effects of an improved model representation of overflow water on the subpolar North Atlantic, in *Int. WOCE Newslett.*, vol. 37, pp. 10–15, unpublished manuscript, 1999.
- Denton, G., and T. Hughes (Eds.), *The Last Great Ice Sheets*, John Wiley and Sons, 1981.
- Dickson, B., J. Meincke, I. Vassie, J. Jungclauss, and S. Østerhus, Possible predictability in the overflow from the Denmark Strait, *Nature*, *397*, 243–246, 1999.
- Dickson, B., I. Yashayaev, J. Meincke, B. Turrell, S. Dye, and J. Holfort, Rapid freshening of the deep North Atlantic ocean over the past four decades, *Nature*, *416*, 832–837, 2002.
- Dickson, R. R., and J. Brown, The Production of North Atlantic Deep Water - Sources, Rates, and Pathways, *J. Geophys. Res.*, *C99*, 12,319–12,341, 1994.
- Dokken, T. M., and E. Jansen, Rapid changes in the mechanism of oceanic convection during the last glacial period, *Nature*, *401*, 458–461, 1999.
- Döscher, R., and R. Redler, The relative importance of northern overflow and subpolar deep convection for the North Atlantic thermohaline circulation, *J. Phys. Oceanogr.*, *27*, 1894–1902, 1997.
- Döscher, R., C. W. Böning, and P. Herrmann, Response of Circulation and Heat Transport in the North Atlantic to Changes in Thermohaline Forcing in Northern Latitudes: A Model Study, *J. Phys. Oceanogr.*, *24*, 2306–2320, 1994.
- Duplessy, J. C., N. J. Shackleton, R. G. Fairbanks, L. Labeyrie, D. Oppo, and N. Kallel, Deepwater source variations during the last climatic cycle and their impact on the global deepwater circulation, *Paleoceanogr.*, *3*, 343–360, 1988.

- Eden, C., and J. Willebrand, Mechanism of interannual to decadal variability of the North Atlantic circulation, *J. Clim.*, *14*, 2266–2280, 2001.
- Egbert, G., and S. Erofeeva, Efficient inverse modeling of barotropic ocean tides, *J. Atmos. Ocean. Technol.*, *19*, 183–204, 2002.
- Ellett, D. J., Norwegian Sea Deep Water overflow across the Wyville-Thomson Ridge during 1987–88, *ICES Cooperative Research Report*, *225*, 195–205, 1998.
- Ezer, T., H. Arango, and A. Shchepetkin, Developments in terrain-following ocean models: intercomparisons of numerical aspects, *Ocean Modelling*, *4*, 249–267, 2002.
- Farmer, D. M., and L. Armi, Maximal two-layer exchange over a sill and through the combination of a sill and contraction with barotropic flow, *J. Fluid Mech.*, *164*, 53–76, 1986.
- Fleming, K., Constraints on the Greenland Ice Sheet since the Last Glacial maximum from sea-level observations and glacial rebound models, *Quaternary Science Reviews*, *23*, 1053–1077, 2004.
- Fristedt, T., R. Hietala, and P. Lundberg, Stability properties of a barotropic surface-water jet observed in the Denmark Strait, *Tellus*, *51A*, 979–989, 1999.
- Funder, S., and L. Hansen, The Greenland ice sheet - model for its culmination and decay during and after the last glacial maximum, *Bulletin of the Geological Society of the Denmark*, *42*, 137–152, 1996.
- Furevik, T., and J. E. Ø. Nilsen, *Climate Variability in the Nordic Seas*, chap. Large-Scale Atmospheric Circulation Variability and its Impacts on the Nordic Seas Ocean Climate - a Review, Geophysical Monograph Series, AGU, 2004.
- Ganachaud, A., and C. Wunsch, Improved estimates of global ocean circulation, heat transport and mixing from hydrographic data, *Nature*, *408*, 453–457, 2000.
- Ganopolski, A., and S. Rahmstorf, Abrupt glacial climate changes due to stochastic resonance, *Phys. Rev. Lett.*, *88*, 2002.
- Ganopolski, A., S. Rahmstorf, V. Petoukhov, and M. Claussen, Simulation of modern and glacial climates with a coupled global model of intermediate complexity, *Nature*, *391*, 351–356, 1998.
- Garrett, C., and F. Gerdes, Hydraulic control of homogeneous shear flows, *J. Fluid Mech.*, *475*, 163–172, 2003.
- Gent, P. R., and J. C. McWilliams, Isopycnal mixing in ocean circulation models, *J. Phys. Oceanogr.*, *20*, 150–155, 1990.
- Gent, P. R., J. Willebrand, T. J. McDougall, and J. C. McWilliams, Parametrizing eddy-induced tracer transports in ocean circulation models, *J. Phys. Oceanogr.*, *25*, 463–474, 1995.
- Gerdes, F., C. Garrett, and D. Farmer, On Internal Hydraulics with Entrainment, *J. Phys. Oceanogr.*, *32*, 1106–1111, 2002.
- Gerdes, R., A primitive equation ocean circulation model using a general vertical coordinate transformation. 1. Description and testing of the model, *J. Geophys. Res.*, *C98*, 14,683–14,701, 1993a.
- Gerdes, R., A primitive equation ocean circulation model using a general vertical coordinate transformation. 2. Application to an overflow problem, *J. Geophys. Res.*, *C98*, 14,703–14,726, 1993b.
- Gerdes, R., and C. Köberle, On the influence of DSOW in a numerical model of the North Atlantic general circulation, *J. Phys. Oceanogr.*, *25*, 2624–2642, 1995.
- Gibson, J. K., P. Kallberg, S. Uppala, A. Hernandez, A. Nomura, and E. Serrano, Ecmwf re-Analysis Project Report Series - 1. ERA description, *Tech. rep.*, European Centre for Medium-range Weather Forecasting, 1997.

- Gill, A. E., The hydraulics of rotating-channel flow, *J. Fluid Mech.*, *80*, 641–671, 1977.
- Girton, J. B., Dynamics of transport and variability in the Denmark Strait overflow, Ph.D. thesis, University of Washington, Seattle, WA, 2001.
- Girton, J. B., and T. B. Sanford, Descent and modification of the overflow plume in the Denmark Strait, *J. Phys. Oceanogr.*, *33*, 1351–1364, 2003.
- Girton, J. B., T. B. Sanford, and R. H. Käse, Synoptic sections of the Denmark Strait overflow, *Geophys. Res. Lett.*, *28*, 1619–1622, 2001.
- Glueck, M. F., and C. W. Stockton, Reconstruction of the North Atlantic Oscillation 1429–1983, *Int. J. Climatol.*, *21*, 1453–1465, 2001.
- Gnanadesikan, A., A Simple Predictive Model for the Structure of the Oceanic Pycnocline, *Science*, *283*, 2077–2079, 1999.
- Griffies, S. M., C. Böning, F. O. Bryan, E. P. Chassignet, R. Gerdes, H. Hasumi, A. Hirst, A.-M. Treguier, and D. Webb, Developments in ocean climate modelling, *Ocean Modelling*, *2*, 123–192, 2000.
- Griffies, S. M., M. J. Harrison, R. C. Pacanowski, and A. Rosati, A technical guide to MOM4, *GFDL Ocean Group Technical report No. 5*, NOAA/Geophysical Fluid Dynamics Laboratory, 2004.
- Grootes, P. M., and M. Stuiver, Oxygen 18/16 variability in Greenland snow and ice with 10-3- to 10+5-year time resolution, *J. Geophys. Res.*, *102*, 26,455–26,470, 1997.
- Hagen, S., and M. Hald, Variation in surface and deep water circulation in the Denmark Strait, North Atlantic, during marine isotope stages 3 and 2, *Paleoceanogr.*, *17*, 1–16, 2002.
- Haidvogel, D. B., and A. Beckmann, *Numerical Ocean Circulation Modeling*, vol. 2 of *Series on environmental science and management*, Imperial College Press, London, 1999.
- Haidvogel, D. B., H. G. Arango, K. Hedstrom, A. Beckmann, P. Malanotte-Rizzoli, and A. F. Shchepetkin, Model evaluation experiments in the North Atlantic Basin: simulations in nonlinear terrain-following coordinates, *Dyn. Atmos. Oceans*, *32*, 239–281, 2000.
- Hankin, S., J. Callahan, A. Manke, K. O'Brien, and J. Sirott, *FERRET User's guide, Version 5.22*, NOAA/PMEL/TMAP, 2000.
- Hansen, B., and S. Østerhus, North Atlantic-Nordic Seas exchanges, *Prog. Oceanogr.*, *45*, 109–208, 2000.
- Hansen, B., W. R. Turrell, and S. Østerhus, Decreasing overflow from the Nordic seas into the Atlantic Ocean through the Faroe Bank channel since 1950, *Nature*, *411*, 927–930, 2001.
- Hansen, B., S. Østerhus, H. Hatun, R. Kristiansen, and K. M. H. Larsen, The Iceland-Faroe inflow of atlantic water to the Nordic Seas, *Progr. Oceanogr.*, *59*, 443–474, 2003.
- Hansen, B., S. Østerhus, D. Quadfasel, and W. Turrell, Already the Day After Tomorrow?, *Science*, *305*, 953–954, 2004.
- Hedström, K. S., *User's Manual for an s-coordinate Primitive Equation Ocean Circulation Model (SCRUM: Version 3.0)*, Institute of Marine and Coastal Sciences, Rutgers University, 1997.
- Heinrich, H., Origin and consequences of cyclic ice rafting in the Northeast Atlantic ocean during the past 130,000 years, *Quaternary Research*, *29*, 142–152, 1988.
- Helfrich, K. R., Time-Dependent Two-Layer Hydraulic Exchange Flows, *J. Phys. Oceanogr.*, *25*, 359–373, 1995.
- Helfrich, K. R., and L. J. Pratt, Rotating hydraulics and upstream basin circulation, *J. Phys. Oceanogr.*, *33*, 1651–1663, 2003.

- Henrich, R., Dynamics of atlantic water advection to the Norwegian-Greenland Sea - a time-slice record of carbonate distribution in the last 300 ky, *Mar. Geo.*, *145*, 95–131, 1998.
- Hermann, A. J., D. B. Haidvogel, E. L. Dobbins, and P. J. Stabeno, Coupling global and regional circulation models in the coastal Gulf of Alaska, *Progr. Oceanogr.*, *53*, 335–367, 2002.
- Hewitt, C. D., A. J. Broccoli, J. F. B. Mitchell, and R. J. Stouffer, A coupled model study of the Last Glacial Maximum: Was part of the North Atlantic relatively warm?, *Geophys. Res. Lett.*, *28*, 1571–1574, 2001.
- Hilmer, M., and T. Jung, Evidence for a recent change in the link between the North Atlantic Oscillation and Arctic sea ice export, *Geophys. Res. Lett.*, *27*, 989–992, 2000.
- Hogg, A. M., G. N. Ivey, and K. B. Winters, Hydraulics and mixing in controlled exchange flows, *J. Geophys. Res.*, *106*, 959–972, 2001.
- Høyer, J. L., and D. Quadfasel, Detection of deep overflows with satellite altimetry, *Geophys. Res. Lett.*, *28*, 1611–1614, 2001.
- Hsieh, W. W., M. K. Davey, and R. C. Wajsowicz, The free Kelvin wave in finite-difference numerical models, *J. Phys. Oceanogr.*, *13*, 1383–1397, 1983.
- Hurrell, J. W., Decadal trends in the North Atlantic Oscillation: Regional temperatures and precipitation, *Science*, *269*, 676–679, 1995.
- Hurrell, J. W., Y. Kushnir, G. Ottersen, and M. Visbeck, An overview of the north atlantic oscillation, in *The North Atlantic Oscillation: Climatic Significance and Environmental Impact*, edited by J. W. Hurrell, Y. Kushnir, G. Ottersen, and M. Visbeck, vol. 134 of *Geophysical Monograph 134*, pp. 1–36, American Geophysical Union, 2003.
- Huybrechts, P., Sea-level changes at the LGM from ice-dynamic reconstructions of the Greenland and Antarctic ice sheets during the glacial cycles, *Quaternary Science Reviews*, *21*, 203–231, 2002.
- Ingolfsson, O., A. Lysa, S. Funder, P. Möller, and S. Björck, Late Quaternary glacial history of the central west coast of Jameson Land, East Greenland, *Boreas*, *23*, 447–458, 1994.
- Jakobsen, P. K., M. H. Ribergaard, D. Quadfasel, T. Schmith, and C. W. Hughes, Near-surface circulation in the northern North Atlantic as inferred from Lagrangian drifters: Variability from the mesoscale to interannual, *J. Geophys. Res.*, *108*, 2003.
- Jiang, L., and R. W. Garwood Jr., Three-dimensional simulations of overflows on continental slopes, *J. Phys. Oceanogr.*, *26*, 1214–1233, 1996.
- Johnsen, S. J., et al., Irregular glacial interstadials recorded in a new Greenland ice core, *Nature*, *359*, 311–313, 1992.
- Johnson, G. C., and D. R. Ohlsen, Frictionally modified rotating hydraulic channel exchange and ocean outflow, *J. Phys. Oceanogr.*, *24*, 66–78, 1994.
- Jónsson, S., The circulation in the northern part of the Denmark Strait and its variability, *ICES Journal of Marine Science*, *L*, 1–9, 1999.
- Jónsson, S., and H. Valdimarsson, A new path for the Denmark Strait overflow water from the Iceland Sea to the Denmark Strait, *Geophys. Res. Lett.*, *31*, 2004.
- Jungclauss, J. H., and J. O. Backhaus, Application of a transient reduced gravity plume model to the Denmark Strait overflow, *J. Geophys. Res.*, *99*, 12,375–12,396, 1994.
- Jungclauss, J. H., J. Hauser, and R. H. Käse, Cyclogenesis in the Denmark Strait Overflow Plume, *J. Phys. Oceanogr.*, *31*, 3214–3229, 2001.
- Käse, R. H., and A. Oschlies, Flow through Denmark Strait, *J. Geophys. Res.*, *105*, 28,527–28,546, 2000.

- Käse, R. H., J. B. Girton, and T. B. Sanford, Structure and variability of the Denmark Strait Overflow: Model and observations, *J. Geophys. Res.*, *108*, art. no.-3181, 2003.
- Killworth, P. D., On hydraulic control in a stratified fluid, *J. Fluid Mech.*, *237*, 605–626, 1992a.
- Killworth, P. D., Flow Properties in Rotating, Stratified Hydraulics, *J. Phys. Oceanogr.*, *22*, 997–1017, 1992b.
- Killworth, P. D., On reduced-gravity flows through sills, *Geophysical Astrophysical Fluid Dynamics*, *75*, 91–106, 1994.
- Killworth, P. D., Hydraulic control and maximal flow in rotating stratified hydraulics, *Deep-Sea Research I*, *42*, 859–871, 1995.
- Killworth, P. D., On the rate of descent of overflows, *J. Geophys. Res.*, *106*, 22,267–22,275, 2001.
- Killworth, P. D., Inclusion of the bottom boundary layer in ocean models, in *Near-Boundary Processes and their Parameterization*, edited by P. Müller, Proceedings of the 13th 'Aha Huliko'a Hawaiian Winter Workshop, pp. 177–185, 2003.
- Kim, S. J., G. M. Flato, and G. J. Boer, A coupled climate model simulation of the Last Glacial Maximum, Part 2: approach to equilibrium, *Clim. Dyn.*, *20*, 635–665, 2003.
- Kitoh, A., S. Murakami, and H. Koide, A simulation of the Last Glacial Maximum with a coupled atmosphere-ocean GCM, *Geophys. Res. Lett.*, pp. 2221–2224, 2001.
- Kösters, F., Denmark Strait Overflow: Comparing model results and hydraulic transport estimates, *J. Geophys. Res.*, *109*, C10,011, 2004.
- Kösters, F., R. H. Käse, K. Fleming, and D. Wolf, Denmark Strait overflow for Last Glacial Maximum to Holocene conditions, *Paleoceanogr.*, *19*, PA2019, 2004.
- Krauss, W., A note on overflow eddies, *Deep Sea Res. I*, *43*, 1661–1667, 1996.
- Krauss, W., and R. H. Käse, Eddy formation in the Denmark Strait Overflow, *J. Geophys. Res.*, *103*, 15,525–15,538, 1998.
- Kristmannsson, S. S., Flow of Atlantic Water into the northern Icelandic shelf area, 1985-1989, *ICES Cooperative Research Report*, *225*, 124–135, 1998.
- Kuijpers, A., S. R. Troelstra, M. Wisse, S. H. Nielsen, and T. C. E. van Weering, Norwegian sea overflow variability and NE Atlantic surface hydrography during the past 150,000 years, *Marine Geology*, *152*, 75–99, 1998.
- Kuijpers, A., et al., Late Quaternary sedimentary processes and ocean circulation changes at the Southeast Greenland margin, *Mar. Geol.*, *195*, 109–129, 2003.
- Labeyrie, L. D., J. C. Duplessy, and P. L. Blanc, Variations in mode of formation and temperature of oceanic deep waters over the past 125,000 years, *Nature*, *327*, 477–482, 1987.
- Lambeck, K., C. Smither, and P. Johnston, Sea-level change, glacial rebound and mantle viscosity for northern Europe, *Geophysical Journal International*, *134*, 102–144, 1998.
- Lambert, S. J., and G. J. Boer, CMIP1 evaluation and intercomparison of coupled climate models, *Clim. Dyn.*, *17*, 83–106, 2001.
- Large, W. G., J. C. McWilliams, and S. C. Doney, Oceanic vertical mixing: A review and a model with a nonlocal boundary layer parameterization, *Reviews of Geophysics*, *32*, 363–403, 1994.
- Larsen, B., *Structure and development of the Greenland-Scotland Ridge*, chap. Geology of the Greenland-Iceland Ridge in the Denmark Strait, pp. 425–444, Plenum Publishing Corporation, 1983.

- Latif, M., Tropical Pacific/Atlantic Ocean interactions at multi-decadal time scales, *Geophys. Res. Lett.*, *28*, 539–542, 2001.
- Latif, M., E. Roeckner, U. Mikolajewicz, and R. Voss, Tropical Stabilisation of the Thermohaline Circulation in a Greenhouse Warming Simulation, *J. Clim.*, pp. 1809–1813, 2000.
- LeGrand, P., and C. Wunsch, Constraints from paleotracer data on the North Atlantic circulation during the last glacial maximum, *Paleoceanogr.*, *10*, 1011–1045, 1995.
- Levitus, S., and T. P. Boyer, *World Ocean Atlas 1994*, vol. 4 (Temperature), NOAA Natl. Environ. Satell. Data and Inf. Ser., Washington, D.C., 1994.
- Levitus, S., R. Burgett, and T. P. Boyer, *World Ocean Atlas 1994*, vol. 3 (Salinity), NOAA Natl. Environ. Satell. Data and Inf. Ser., Washington, D.C., 1994.
- Lohmann, G., The influence of a near-bottom transport parameterization on the sensitivity of the thermohaline circulation, *J. Phys. Oceanogr.*, *28*, 2095–2103, 1998.
- Lohmann, G., and S. Lorenz, On the hydrological cycle under paleoclimatic conditions as derived from AGCM simulations, *J. Geophys. Res.*, *D105*, 17,417–17,436, 2000.
- Lumpkin, R., and K. Speer, Large-scale vertical and horizontal circulation in the North Atlantic ocean, *J. Phys. Oceanogr.*, *33*, 1902–1920, 2003.
- Lynch-Stieglitz, J., W. B. Curry, and N. Slowey, Weaker gulf stream in the Florida Straits during the Last Glacial Maximum, *Nature*, *402*, 644–647, 1999a.
- Lynch-Stieglitz, J., W. B. Curry, and N. Slowey, A geostrophic transport estimate for the Florida Current from the oxygen isotope composition of benthic foraminifera, *Paleoceanogr.*, *14*, 360–373, 1999b.
- MacAyeal, D. R., A Low-Order Model of the Heinrich Event Cycle, *Paleoceanogr.*, *8*, 767–773, 1993a.
- MacAyeal, D. R., Binge/Purge Oscillations of the Laurentide Ice Sheet as a Cause of the North Atlantic’s Heinrich Events, *Paleoceanogr.*, *8*, 775–784, 1993b.
- Macdonald, A. M., The global ocean circulation: A hydrographic estimate and regional analysis, *Progr. Oceanogr.*, *41*, 281–382, 1998.
- Macrander, A., U. Send, H. Valdimarsson, S. Jónsson, and R. Käse, Interannual Changes in the overflow from the Nordic Seas into the Atlantic Ocean through Denmark Strait, *Geophys. Res. Lett.*, *subm.*
- Malanotte-Rizzoli, P., K. Hedstrom, H. Arango, and D. B. Haidvogel, Water mass pathways between the subtropical and tropical ocean in a climatological simulation of the North Atlantic ocean circulation, *Dyn. Atmos. Oceans*, *32*, 331–371, 2000.
- Marchesiello, P., J. C. McWilliams, and A. Shchepetkin, Open boundary conditions for long-term integration of regional ocean models, *Ocean Modelling*, *3*, 1–20, 2001.
- Marchesiello, P., J. C. McWilliams, and A. Shchepetkin, Equilibrium Structure and Dynamics of the California Current System, *J. Phys. Oceanogr.*, *33*, 753–783, 2003.
- Marshall, J., and F. Schott, Open-ocean convection: observations, theory, and models, *Rev. Geophys.*, *37*, 1–64, 1999.
- Marshall, J., Y. Kushnir, D. Battisti, P. Chang, A. Czaja, R. Dickson, M. McCartney, R. Saravanan, and M. Visbeck, North Atlantic climate variability: Phenomena, impacts and mechanisms, *Inter. Jour. Climatology*, *21*, 1863–1898, 2001.
- Matthiesen, S., and K. Haines, A hydraulic box model study of the Mediterranean response to postglacial sea-level rise, *Paleoceanogr.*, 2003.
- Mauritzen, C., Production of dense overflow waters feeding the North Atlantic across the Greenland-Scotland Ridge. 1. Evidence for a revised circulation scheme, *Deep Sea Res. I*, *43*, 769–806, 1996a.

- Mauritzen, C., Production of dense overflow waters feeding the North Atlantic across the Greenland-Scotland Ridge. 2. An inverse model, *Deep Sea Res. I*, *43*, 807, 1996b.
- McManus, J. F., R. Francois, J.-M. Gheradi, L. D. Keigwin, and S. Brown-Leger, Collapse and rapid resumption of Atlantic meridional circulation linked to deglacial climate changes, *Nature*, *428*, 834–837, 2004.
- Meincke, J., *Structure and Development of the Greenland Scotland Ridge, New Methods and Concepts*, chap. The modern current regime across the Greenland Scotland Ridge, Proc. NATO Adv. Res. Inst., Plenum Press, 1983.
- Meincke, J., B. Rudels, and H. J. Friedrich, The Arctic Ocean-Nordic Seas thermohaline system, *ICES Journal of Marine Science*, *54*, 283–299, 1997.
- Meissner, K. J., A. Schmittner, and A. J. Weaver, The ventilation of the North Atlantic Ocean during the Last Glacial Maximum—a comparison between simulated and observed radiocarbon ages, *Paleoceanogr.*, *18*, 2003.
- Mellor, G. L., L.-Y. Oey, and T. Ezer, Sigma coordinate pressure gradient errors and the seamount problem, *J. Atmos. Ocean. Technol.*, *15*, 1998.
- Mienert, J., J. T. Andrews, and J. D. Milliman, The East Greenland continental margin (65°N) since the last deglaciation: Changes in seafloor properties and ocean circulation, *Mar. Geo.*, *106*, 217–238, 1992.
- Mikolajewicz, U., A meltwater induced collapse of the 'conveyor belt' thermohaline circulation and its influence on the distribution of $\delta^{14}C$ and $\delta^{18}O$ in the oceans, *Max-Planck-Institut für Meteorologie, Report*, *189*, 1–25, 1996.
- Mix, A., E. Bard, and R. R. Schneider, Ice sheets and sea level of the last glacial maximum, *Quaternary Science Reviews*, *22*, 2002.
- Monterey, G., and S. Levitus, Seasonal variability of mixed layer depth for the world ocean, in *NOAA Atlas NESDIS 14*, p. 96, US Government Printing Office, Washington DC, 1997.
- Munk, W., and C. Wunsch, Abyssal recipes ii: energetics of tidal and wind mixing, *Deep Sea Res. I*, *45*, 1977–2010, 1998.
- Myers, P. G., An examination of wind-stress forcing and circulation in the sub-polar North Atlantic, *Quaternary International*, *99-100*, 89–98, 2003.
- NGDC, Data Announcement 88-MG-02: Digital Relief of the Surface of the Earth, *Cd-rom*, National Geophysics Data Center, NOAA, Boulder, 1988.
- Nikolopoulos, A., K. Borenäs, R. Hietala, and P. Lundberg, Hydraulic estimates of Denmark Strait overflow, *J. Geophys. Res.*, *108*, 2003.
- Nilsen, J. E. O., Y. Gao, H. Drange, T. Furevik, and M. Bentsen, Simulated North Atlantic-nordic seas water mass exchanges in an isopycnic coordinate ogcm, *Geophys. Res. Lett.*, *30*, 2003.
- Nilsson, J., G. Broström, and G. Walin, The Thermohaline Circulation and Vertical Mixing: Does Weaker Density Stratification Give Stronger Overturning, *J. Phys. Oceanogr.*, *33*, 2781–2795, 2003.
- Nof, D., The translation of isolated eddies on a sloping bottom, *Deep Sea Res. I*, *30*, 171–182, 1983.
- Norgaard-Pedersen, N., R. F. Spielhagen, H. Erlenkeuser, P. M. Grootes, J. Heinemeier, and J. Knies, Arctic Ocean during the Last Glacial Maximum: Atlantic and polar domains of surface water mass distribution and ice cover, *Paleoceanogr.*, *18*, 1063, 2003.
- Nøst, O. A., and P. E. Isachsen, The large-scale time mean ocean circulation in the Nordic Seas and Arctic Ocean estimated from simplified dynamics, *J. Mar. Res.*, *61*, 175–210, 2003.

- Ohshima, K. I., D. Simizu, M. Itoh, G. Mizuta, Y. Fukamachi, S. C. Riser, and M. Wakatuschi, Sverdrup balance and the cyclonic gyre in the Sea of Okhotsk, *J. Phys. Oceanogr.*, *34*, 513–525, 2004.
- Orvik, K. A., and P. Niiler, Major pathways of Atlantic water in the northern North Atlantic and Nordic Seas toward Arctic, *Geophys. Res. Lett.*, *29*, 1896, 2002.
- Orvik, K. A., and O. Skagseth, The impact of the wind stress curl in the North Atlantic on the Atlantic inflow to the Norwegian Sea toward the Arctic, *Geophys. Res. Lett.*, *30*, 1884, 2003.
- Orvik, K. A., O. Skagseth, and M. Mork, Atlantic inflow to the Nordic Seas: current structure and volume fluxes from moored current meters, VM-ADCP and SeaSoarCTD observations, 1995-1999, *Deep Sea Res. I*, *48*, 937–957, 2001.
- Østerhus, S., B. Hansen, R. Kristiansen, and P. Lundberg, The Overflow through the Faroe Bank Channel, in *Int. WOCE Newslett.*, vol. 35, pp. 35–37, unpublished manuscript, 1999.
- Otterå, O. H., H. Drange, M. Bentsen, N. G. Kvamstø, and D. Jiang, The sensitivity of the present-day Atlantic meridional overturning circulation to freshwater forcing, *Geophys. Res. Lett.*, *30*, 1898, 2003.
- Otterå, O. H., H. Drange, M. Bentsen, N. G. Kvamstø, and D. Jiang, Transient response of the Atlantic Meridional Overturning Circulation to enhanced freshwater input to the Nordic Seas-Arctic Ocean in the Bergen Climate Model, *Tellus*, *56A*, 342–361, 2004.
- Pacanowski, R., K. Dixon, and A. Rosati, *The GFDL modular ocean model user's guide*, Geophysical Fluid Dynamics Laboratory, Princeton University, Princeton, 1993.
- Paul, A., and C. Schäfer-Neth, Modeling the water masses of the Atlantic Ocean at the Aast Glacial Maximum, *Paleoceanogr.*, *18*, 1058, 2003.
- Peltier, W. R., Ice age paleotopography, *Science*, *265*, 195–201, 1994.
- Peltier, W. R., On eustatic sea level history: Last glacial maximum to holocene, *Quaternary Science Reviews*, *21*, 377–396, 2002.
- Penven, P., *ROMSTOOLS User's Guide*, Institut de Recherche pour le Developement, 213 rue Lafayette, Paris, France, 2003.
- Penven, P., J. R. E. Lutjeharms, P. Marchesiello, C. Roy, and S. J. Weeks, Generation of cyclonic eddies by the agulhas current in the lee of the agulhas bank, *Geophys. Res. Lett.*, *27*, 1055–1058, 2001.
- Penven, P., L. Debreu, P. Marchesiello, and J. C. McWillimas, Application of the ROMS embedding procedure for the Central California Upwelling System, *Ocean Modelling*, in revision.
- Perkins, H., T. J. Sherwin, and T. S. Hopkins, Amplification of Tidal Currents by Overflow on the Iceland-Faeroe Ridge, *J. Phys. Oceanogr.*, *24*, 721–735, 1994.
- Pflaumann, U., et al., Glacial North Atlantic: SEA-surface conditions reconstructed by GLAMAP 2000, *Paleoceanogr.*, *18*, 2003.
- Pickart, R. S., M. A. Spall, M. H. Ribergaard, G. W. K. Moore, and R. F. Milliff, Deep convection in the Irminger Sea forced by the Greenland tip jet, *Nature*, *424*, 152–156, 2003.
- Prange, M., V. Romanova, and G. Lohmann, The glacial thermohaline circulation: Stable or unstable?, *Geophys. Res. Lett.*, *29*, 2028, 2002.
- Prange, M., G. Lohmann, and A. Paul, Influence of Vertical Mixing in the Thermohaline Hysteresis: Analyses of an OGCM, *J. Phys. Oceanogr.*, *33*, 1707–1721, 2003.
- Pratt, L. J., Hydraulic Control of Sill Flow with Bottom Friction, *J. Phys. Oceanogr.*, *16*, 1970–1980, 1986.
- Pratt, L. J., and Chechelnitsky, Principles for capturing the upstream effects of deep sills in low resolution ocean models, *Dynam. Atmos. Oceans*, *26*, 1–25, 1997.

- Pratt, L. J., and S. G. Llewellyn-Smith, Hydraulically Drained Flows in Rotating Basins. Part I: Method, *J. Phys. Oceanogr.*, *27*, 2509–2521, 1997.
- Pratt, L. J., and P. A. Lundberg, Hydraulics of Rotating Strait and Sill Flow, *Annu. Rev. Fluid Mech.*, *23*, 81–106, 1991.
- Pratt, L. J., K. R. Helfrich, and E. P. Chassignet, Hydraulic adjustment to an obstacle in a rotating channel, *J. Fluid Mech.*, *404*, 117–149, 2000.
- Price, J. F., and M. O. Baringer, Outflows and Deep Water Production by Marginal Seas, *Progr. Oceanogr.*, *33*, 161–200, 1994.
- Rahmstorf, S., Bifurcations of the Atlantic thermohaline circulation in response to changes in the hydrological cycle, *Nature*, *378*, 145–149, 1995.
- Rahmstorf, S., On the freshwater forcing and transport of the Atlantic thermohaline circulation, *Clim. Dyn.*, *12*, 799–811, 1996.
- Rahmstorf, S., The current climate, *Nature*, *421*, 699, 2003.
- Rasmussen, T. L., E. Thomsen, T. C. E. van Weering, and L. Labeyrie, Rapid changes in surface and deep water conditions at the Faeroe margin during the last 58,000 years, *Paleoceanogr.*, *11*, 757–771, 1996.
- Redler, R., and C. W. Böning, Effect of the overflows on the circulation in the subpolar North Atlantic: A regional model study, *J. Geophys. Res.*, *102*, 18,529–18,552, 1997.
- Rew, R., G. Davis, S. Emmerson, and H. Davies, *NetCDF User's Guide*, Unidata, University Corporation for Atmospheric Research, Boulder, Colorado, 1996.
- Rimbu, N., G. Lohmann, J.-H. Kim, and R. Arz, H. W. annd Schneider, Arctic/north atlantic oscillation signature in holocene sea surface temperature trends as obtained from alkenone data, *Geophys. Res. Lett.*, *30*, 1280, 2003.
- Risebrobakken, B., E. Jansen, C. Andersson, E. Mjelde, and K. Hevróy, A high-resolution study of Holocene paleoclimatic and paleoceanographic changes in the Nordic Seas, *Paleoceanogr.*, *18*, 2003.
- Roberts, M. J., and R. A. Wood, Topographic sensitivity studies with a Bryan-Cox-type ocean model, *J. Phys. Oceanogr.*, *27*, 823–836, 1997.
- Roemmich, D., and C. Wunsch, Two transatlantic sections: Meridional circulation and heat flux in the subtropical North Atlantic Ocean, *Deep Sea Res. I*, *32*, 619–664, 1985.
- Roether, W., V. M. Roussenov, and R. Well, *Ocean Processes in Climate Dynamics: Global and Mediterranean Examples*, chap. A tracer study of the thermohaline circulation in the Eastern Mediterranean, pp. 371–394, Kluwer Acad. Pub., 1994.
- Ross, C. K., Temperature-salinity characteristics of the overflow water in the Denmark Strait during OVERFLOW 73. , *Rapp. P. V. Reun. Cons. Int. Explor. Mer.*, *185*, 111–119, 1973.
- Rudels, B., P. Eriksson, H. Grönvall, R. Hietala, and J. Launianien, Hydrographic observations in the Denmark Strait in fall 1997, and their implications for the entrainment into the overflow plume., *Geophys. Res. Lett.*, *26*, 1325–1328, 1999.
- Rudels, B., E. Fahrback, J. Meincke, G. Budéus, and P. Eriksson, The East Greenland Current and its contribution to the Denmark Strait overflow, *ICES J. Mar. Sci.*, *59*, 1133–1154, 2002.
- Rutberg, R. L., S. R. Hemming, and S. L. Goldstein, Reduced North Atlantic Deep Water flux to the Southern Ocean inferred from neodymium isotope ratios, *Nature*, *405*, 935–938, 2000.
- Saenko, O. A., A. J. Weaver, and A. Schmittner, Atlantic deep circulation controlled by freshening in the Southern Ocean, *GRL*, 2003.

- Sarnthein, M., E. Jansen, M. Arnold, J. C. Duplessy, H. Erlenkeuser, A. Flato, T. Veum, E. Vogelsang, and M. S. Weinelt, $\delta^{18}O$ Time-slice reconstruction of meltwater anomalies at Termination I in the North Atlantic between 50 and 80°N, in *the last deglaciation: Absolute and radiocarbon chronologies*, edited by E. Bard and W. S. Broecker, NATO ASI Series, Vol. 12, pp. 183–200, Springer Verlag, Berlin, 1992.
- Sarnthein, M., K. Winn, S. J. A. Jung, J. C. Duplessy, L. Labeyrie, H. Erlenkeuser, and G. Ganssen, Changes in east Atlantic deepwater circulation over the last 30,000 years: Eight time slice reconstructions, *Paleoceanogr.*, *9*, 209–267, 1994.
- Sarnthein, M., R. Gersonde, U. Niebler, S. annd Pflaumann, R. Spielhagen, J. Thiede, G. Wefer, and M. Weinelt, Overview of Glacial Atlantic Ocean Mapping (GLAMAP 2000), *Paleoceanogr.*, *18*, 2003a.
- Sarnthein, M., U. Pflaumann, and M. Weinelt, Past extent of sea ice in the northern North Atlantic inferred from foraminiferal paleotemperature estimates, *Paleoceanogr.*, *18*, 2003b.
- Sarnthein, M., et al., Fundamental modes and abrupt changes in North Atlantic circulation and climate over the last 60 ky - Concepts, reconstructions and numerical modeling, in *The Northern North Atlantic: A changing environment*, edited by P. Schäfer, W. Ritzrau, M. Schlüter, and J. Thiede, pp. 365–410, Springer Verlag, Berlin, 2001.
- Sarnthein, M., et al., Coring a sediment record of variations in the Denmark Strait Overflow, in *The Expedition ARKTIS XVIII/1 a,b of the Research Vessel Polarstern in 2002*, edited by P. Lemke, Ber. Polarforsch. Meeresforsch., pp. 22–36, 2003c.
- Saunders, P. M., Cold outflow from the Faroe Bank Channel, *J. Phys. Oceanogr.*, *20*, 29–43, 1990.
- Saunders, P. M., *Ocean Circulation and Climate*, chap. The Dense Northern Overflows, Academic Press, 2001.
- Schäfer-Neth, C., Modellierung der Paläoozeanographie des nördlichen Nordatlantiks zur letzten Maximalvereisung, *Berichte Sonderforschungsbereich 313*, *51*, 1–106, 1994.
- Schäfer-Neth, C., and A. Paul, Circulation of the glacial Atlantic: a synthesis of global and regional modeling, in *The Northern North Atlantic: A changing environment*, edited by P. Schäfer, W. Ritzrau, M. Schlüter, and J. Thiede, pp. 441–462, Springer Verlag, Berlin, 2001.
- Schäfer-Neth, C., and A. Paul, The Atlantic Ocean at the Last Glacial Maximum: 1. Objective mapping of the GLAMAP sea-surface conditions, in *The South Atlantic during the Late Quaternary: Material Budget and Current Systems*, edited by G. Wefer, S. Mulitza, and V. Ratmeyer, pp. 531–548, Springer Berlin, 2003.
- Schäfer-Neth, C., and K. Statterger, Icebergs in the North Atlantic: Modeling circulation changes and glacio-marine deposition, in *Computerized Modeling of Sedimentary Systems*, edited by J. Harff, W. Lemke, and K. Statterger, pp. 63–78, Springer Verlag, 1999.
- Schmittner, A., and T. F. Stocker, A seasonally forced ocean-atmosphere model for paleoclimate studies, *J. Clim.*, *14*, 1055–1068, 2001.
- Schmittner, A., K. J. Meissner, M. Eby, and A. J. Weaver, Forcing of the deep ocean circulation in simulations of the last glacial maximum, *Paleoceanogr.*, *17*, 2002a.
- Schmittner, A., M. Yoshimori, and A. J. Weaver, Instability of glacial climate in a model of the ocean-atmosphere-cryosphere system, *Science*, *295*, 1489–1493, 2002b.
- Schmitz, W. J., On the interbasin-scale thermohaline circulation, *Rev. Geophys.*, *33*, 151–173, 1995.
- Schulz, M., On the 1470-year pacing of dansgaard-oeschger warm events, *Paleoceanogr.*, *17*, 10.1029/2000PA000571, 2002.
- Schulz, M., and A. Paul, Holocene climate variability on centennial-to-millennial time scales: 1. Climate records from the North-Atlantic realm, in *Climate development and history of the North Atlantic Realm*, edited by G. Wefer, W. H. Berger, K.-E. Behre, and E. Jansen, pp. 41–54, Springer Verlag, Berlin, 2002.

- Schulz, M., A. Paul, and A. Timmermann, Relaxation oscillators in concert: A framework for climate change at millennial timescale during the late Pleistocene, *Geophys. Res. Lett.*, *29*, 2002.
- Seim, H. E., and M. C. Gregg, The importance of aspiration and channel curvature in producing strong vertical mixing over a sill, *J. Geophys. Res.*, *102*, 3451–3472, 1997.
- Severinghaus, J. P., T. Sowers, E. J. Brook, R. B. Alley, and M. L. Bender, Timing of abrupt climate change at the end of the younger dryas interval from thermally fractionated gases in polar ice, *Nature*, *391*, 141–146, 1998.
- Shapiro, R., Smoothing, Filtering, and Boundary Effects, *Reviews of geophysics and space physics*, *8*, 359–387, 1970.
- Shchepetkin, A. F., and J. C. McWilliams, A method for computing horizontal pressure-gradient force in an oceanic model with a non-aligned vertical coordinate, *J. Geophys. Res.*, *108*, 2003.
- Shchepetkin, A. F., and J. C. McWilliams, Quasi-monotone advection schemes based on locally adaptive dissipation, *Monthly Weather Review*, *126*, 1541–1580, 1998.
- Shchepetkin, A. F., and J. C. McWilliams, The regional ocean modeling system: A split-explicit, free-surface, topography-following coordinates ocean model, *Journal of Computational Physics*, *subm.*
- She, J., and J. M. Klinck, Flow near submarine canyons driven by constant winds, *J. Geophys. Res.*, *105*, 28,671–28,694, 2000.
- Shi, X. B., L. P. Roed, and B. Hackett, Variability of the Denmark Strait overflow: A numerical study, *J. Geophys. Res.*, *106*, 22,277–22,294, 2001.
- Shin, S. I., Z. Liu, B. Otto-Bliesner, E. C. Brady, J. E. Kutzbach, and S. P. Harrison, A Simulation of the Last Glacial Maximum climate using the NCAR-CCSM, *Clim. Dyn.*, *20*, 127–151, 2003.
- Skinner, L. C., and N. J. Shackleton, Rapid transient changes in the northeast Atlantic deep water ventilation age across Termination I, *Paleoceanogr.*, *19*, 2004.
- Smethie, W. M., and R. A. Fine, Rates of North Atlantic deep water formation calculated from chlorofluorocarbon inventories, *Deep-Sea Res. Part I-Oceanogr. Res. Pap.*, *48*, 189–215, 2001.
- Song, Y., and D. B. Haidvogel, A semi-implicit ocean circulation model using a generalized topography-following coordinate, *J. Comput. Phys.*, *115*, 228–244, 1994.
- Spall, M. A., Large-scale circulations forced by localized mixing over a sloping bottom, *J. Phys. Oceanogr.*, *31*, 2369–2384, 2001.
- Stern, M., Transport extremum through Denmark Strait, *Geophys. Res. Lett.*, *31*, L12,303, 2004.
- Stern, M. E., Comment on rotating hydraulics, *Geophys. Fluid Dyn.*, *6*, 127–130, 1974.
- Stewart, R. H., *Introduction to Physical Oceanography*, Open Source Textbook, 2002.
- Stommel, H., Thermohaline convection with two stable regimes of flow, *Tellus*, *13*, 224–230, 1961.
- Styles, R., and S. M. Glenn, Modeling stratified wave and current bottom boundary layers on the continental shelf, *J. Geophys. Res.*, *105*, 24,119–24,139, 2000.
- Swift, J. H., K. Aagaard, and S.-A. Malmberg, The contribution of the Denmark Strait overflow to the deep North Atlantic, *Deep-Sea Research*, pp. 29–42, 1980.
- Talley, L. D., Shallow, Intermediate, and Deep Overturning Components of the Global Heat Budget, *J. Phys. Oceanogr.*, *33*, 530–560, 2003.
- Thorpe, R. B., R. A. Wood, and J. F. B. Mitchell, Sensitivity of the modelled thermohaline circulation to the parameterisation of mixing across the Greenland-Scotland ridge, *Ocean Modelling*, *7*, 259–268, 2004.

- Timmermann, A., and H. Goosse, Is the wind stress forcing essential for the meridional overturning circulation?, *Geophys. Res. Lett.*, *31*, L04,303, 2004.
- Timmermann, A., H. Gildor, M. Schulz, and E. Tziperman, Coherent Resonant Millennial-Scale Climate Oscillations Triggered by Massive Meltwater Pulses, *J. Clim.*, 2003.
- Trend-Staid, M., and W. L. Prell, Sea surface temperature at the Last Glacial Maximum: A reconstruction using the modern analog technique, *Paleoceanogr.*, *17*, 2002.
- UNESCO, Tenth report of the joint panel on oceanographic tables and standards, *Tech. Papers in Marine Sci.* *36*, UNESCO, Paris, 1981.
- van Aken, H. M., and C. J. de Boer, On the synoptic hydrography of intermediate and deep water masses in the Iceland Basin, *Deep Sea Res. I*, *42*, 165–189, 1995.
- van Krevelend, S. A., M. Sarnthein, H. Erlenkeuser, P. Grootes, S. Jung, M. J. Nadeau, U. Pflaumann, and A. Voelker, Potential links between surging ice sheets, circulation changes and the Dansgaard-Oeschger cycles in the Irminger Sea, 60-18 kyr, *Paleoceanogr.*, *15*, 425–442, 2000.
- Vellinga, M., R. Wood, and J. Gregory, Processes governing the recovery of a perturbed thermohaline circulation in HadCM3, *J. Clim.*, *15*, 764–780, 2002.
- Vogelsang, E., Paläo-Ozeanographie des Europäischen Nordmeeres an Hand stabiler Kohlenstoff- und Sauerstoffisotope, *Ber. SFB 313, Univ. Kiel*, *23*, 1–136, 1990.
- Völker, A., Zur Deutung der Dansgaard-Oeschger Ereignisse in ultra-hochauflösenden Sedimentprofilen aus dem Europäischen Nordmeer, Thesis, Univ. Kiel., 1999.
- von Storch, H., and F. W. Zwiers, *Statistical analysis in climate research*, Cambridge Univ. Press, Cambridge, 1999.
- Wählin, A. K., Downward channeling of dense water in topographic corrugations, *Deep Sea Res. I*, *51*, 577–590, 2004.
- Warner, J. C., C. R. Sherwood, H. G. Arango, B. Butman, and R. P. Signell, Performance of Four Turbulence Closure Methods Implemented Using a Generic Length Scale Method, *Ocean Modelling*, *8*, 81–113, 2005.
- Weaver, A. J., et al., The UVic Earth system climate model: model description, climatology, and applications to past, present, and future climates, *Atmos. Ocean*, *39*, 361–428, 2001.
- Weinelt, M., M. Sarnthein, U. Pflaumann, H. Schulz, S. Jung, and H. Erlenkeuser, Ice-free Nordic Seas during the Last Glacial Maximum? potential sites of deepwater formation, *Palaeoclim. Data Model.*, *1*, 283–309, 1996.
- Weinelt, M., E. Vogelsang, M. Kucera, U. Pflaumann, M. Sarnthein, A. Voelker, H. Erlenkeuser, and B. A. Malmgren, Variability of North Atlantic heat transfer during mis 2, *Paleoceanogr.*, *18*, 1071, 2003.
- Whitehead, J. A., Topographic Control of oceanic flows in deep passages and straits, *Rev. Geophys.*, *36*, 423–440, 1998.
- Whitehead, J. A., Constant potential vorticity hydraulically controlled flow - Complexities from passage shape, *J. Phys. Oceanogr.*, *33*, 305–312, 2003.
- Whitehead, J. A., A. Leetmaa, and R. A. Knox, Rotating hydraulics of strait and sill flows, *Geophys. Fluid Dyn.*, *6*, 101–125, 1974.
- Willebrand, J., B. Barnier, C. Böning, C. Dieterich, P. D. Killworth, C. Le Provost, Y. L. Jia, J. M. Molines, and A. L. New, Circulation characteristics in three eddy-permitting models of the North Atlantic, *Progr. Oceanogr.*, *48*, 123–161, 2001.

Winton, M., R. Hallberg, and A. Gnanadesikan, Simulation of density-driven frictional downslope flow in z-coordinate ocean models, *J. Phys. Oceanogr.*, *28*, 2163–2174, 1997.

Worthington, L. V., An attempt to measure the volume transport of norwegian sea overflow water through the denmark strait., *Deep Sea Res. I*, *16*, 421–432, 1969.

Wunsch, C., Determining paleoceanographic circulations, with emphasis on the Last Glacial Maximum, *Quaternary Science Reviews*, *22*, 371–385, 2003.

Wunsch, C., and R. Ferrari, Vertical mixing, energy, and the general circulation of the oceans, *Annu. Rev. Fluid Mech.*, *36*, 281–314, 2004.

Zhang, J., M. Steele, D. A. Rothrock, and R. W. Lindsay, Increasing exchanges at the Greenland-Scotland Ridge and their links with the North Atlantic Oscillation and Arctic Sea Ice, *Geophys. Res. Lett.*, *31*, 2004.

Danksagung

Diese Arbeit entstand in der Forschergruppe Ozeanpassagen am Institut für Geowissenschaften der Universität Kiel. Von entscheidender Bedeutung für das Gelingen dieser Arbeit war die engagierte Betreuung durch Prof. Dr. Rolf Käse und Prof. Dr. Michael Schulz. Die motivierenden Diskussionen und praktischen Hilfestellungen von Dr. Andreas Schmittner möchte ich ausdrücklich betonen. Insbesondere möchte ich die Leistungen von Prof. Dr. Michael Sarnthein anerkennen die Forschergruppe zu leiten und mich für die Herstellung des Kontaktes zur Modelliergruppe von Dr. Helge Drange in Bergen (Norwegen) bedanken. Weiterhin danke ich meinen Modellierkollegen Maja Zuvela und Dr. Birgit Schneider für Hilfe, Diskussion und Fragen, die mich immer wieder dazu gebracht haben, die hier vorliegende Arbeit aus unterschiedlichen Perspektiven zu sehen und das Interesse an Regionen außerhalb der Dänemarkstraße nicht zu verlieren. Ich danke Andreas Macrander für die Informationen zur zwischenjährlichen Variabilität des Dänemarkstraßen-Transports, sowie Christian Millo und Mara Weinelt für das Füllen einiger Wissenslücken zur Paleoceanographie der Dänemarkstraße. Martina Blümel und Andrea Lorenz haben mit ihren Ergebnissen und Wissen dazu beigetragen, dass diese Arbeit auch biologische Aspekte enthält. Ich möchte mich bei Dr. Kevin Fleming und Prof. Dr. Detlef Wolf für die zur Verfügung Stellung der glazialen und interglazialen Topographie aus ihren Modellergebnissen. Weiterhin möchte ich Peter Herrmann für die Implementierung der Parameterisierung im UVic Model bedanken, sowie Dr. Oleg Saenko für seine Version des Bodengrenzschichtmodells. Dr. Helge Drange danke ich für die Möglichkeit die Modelliergruppe in Bergen kennen zu lernen, sowie Dr. Odd Helge Otterå und Dr. Yongqi Gao für die zur Verfügung Stellung der Ergebnisse des Bergen Climate Models. Weiterhin danke ich Dr. James Scourse and Dr. Katsuto Uehara für die Bereitstellung ihrer Gezeitenrekonstruktionen und Modellierung. Ich möchte anerkennen, dass ohne die Unterstützung der übrigen Kollegen aus der Forschergruppe diese Arbeit so nicht möglich gewesen wäre.

Besonders herzlich möchte ich mich bei meiner Familie und Eltern bedanken und insbesondere bei Katja für die Rücksichtnahme und Unterstützung in der Endphase dieser Arbeit.

Lebenslauf

Persönliche Daten

Frank Kösters
Hansastraße 18
24 118 Kiel
Tel.: (0431) 239 46 97
E-Mail: frank.koesters@gmx.de
Geb. am 16. 11. 1976 in Haselünne

deutsche Staatsangehörigkeit

Schulbildung

1983–1996 Grundschule und Gymnasium in Meppen, Abitur

Zivildienst

1996–1997 Zivildienst im Nationalpark Niedersächsisches Wattenmeer

Studium

1997–1999 Grundstudium der Geophysik an der Universität Münster

1999 Vordiplom in Geophysik

1999–2000 Hauptstudium der Geophysik mit den Wahlfächern Geoinformatik und Geologie

2000–2001 Studium in angewandter Geophysik an der Universität Birmingham, England
Master-Arbeit: Zum Nutzen kapazitiv gekoppelter Geoelektriksysteme für geologische, hydrogeologische, geotechnische und archäologische Anwendungen
Abschluss: MSc Applied Geophysics

ab 2001 Promotion in Ozeanographie an der Universität Kiel
Dissertation: Zur Variabilität des Tiefenwassertransports durch die Dänemarkstraße im letzten interglazialen Zyklus

Kiel, 20. September 2004